University of Alberta

Computer Simulation and Experimental Characterization of a Tubular micro- Solid Oxide Fuel Cell

by

Mohammad Saeid Amiri

A thesis submitted to the Faculty of Graduate Studies and Research
in partial fulfillment of the requirements for the degree of

Doctor of Philosophy
in
Chemical Engineering

Department of Chemical and Materials Engineering

Spring 2010
Edmonton, Alberta

Examining Committee

Dr. R. E. Hayes, Chemical and Materials Engineering

Dr. Jingli Luo, Chemical and Materials Engineering

Dr. Anthony Yeung, Chemical and Materials Engineering

Dr. Marc Secanell, Mechanical Engineering

Dr. Josephine Hill, Chemical and Petroleum Engineering / University of Calgary

To my parents.

Acknowledgments

I would like to thank my supervisors Professors R. E. Hayes and K. Nandakumar. The superb mentorship I received from Professor Hayes, his kind attention and encouragement, and his trust in me were essential for the completion of this work.

It is an honor for me to thank Dr. Partho Sarkar from the Alberta Research Council for his generous and extensive support of this work, by providing the experimental facilities, and by sharing his brilliant ideas. I would also like to thank Dr. Luis Yamarte and Mr. Lorne Johanson for their assistance and teaching me their technical know-how.

My gratitude extends to my colleagues Drs. Ali Abbaspour, Misha Monder, Mranal Jain, and Veeramani for their support and all our insightful discussions. I also like to thank Dr. Nemanja Danilovic and Mr. Ali Torabi for their help with some of the experiments, and Professors Jingli Luo and Tom Etsell for granting access to their experimental facilities.

I would like to thank Bob Barton and Jack Gibeau for their excellent support with the computing facilities. I am grateful to the Department of Chemical and Materials Engineering staff, especially Lily Laser and Marion Pritchard, for the outstanding job they have done every day.

My deepest appreciation goes to all my friends to whom I owe my most-beautiful graduate experience; I will cherish our sweet memories for the years to come. I would like to especially thank my brother, Sadegh, who was always there for me.

This work was financially supported by the Alberta Ingenuity Fund in Nanotechnology, and the Natural Science and Engineering Council of Canada (NSERC) strategic grant.

Abstract

This work is focused on a state-of-the-art tubular micro-solid oxide fuel cell (TμSOFC), ~3 millimeters in diameter and ~300 microns thick, with Ni/YSZ and LSM/YSZ composite electrodes and a YSZ electrolyte.

A 2D axi-symmetric, multi-scale CFD model is developed which includes the fluid flow, mass transfer, and heat transfer within the gas channels and the porous electrodes. The electrochemical reactions are modeled within the volume of the electrodes, enabling the model to account for the extent of the reaction zone. Thermodynamic expressions are developed to estimate the single-electrode reversible heat generation and the single-electrode electromotive force of a non-isothermal electrochemical cell.

The isothermal, non-isothermal, and transient models are each validated against the experimental results, and consistent with the physical reality of the TμSOFC. A novel approach is used to estimate the kinetic parameters, enabling the simulations to be used as a diagnostic tool.

The model is used to gain a thorough insight about the TμSOFC. The cathode electrochemical activity and the anode support ohmic loss are identified as the two major performance bottlenecks for this cell.

Including radiation is found to be essential for a physically meaningful heat transfer model. The thermoelectric effects on the cell overall electromotive force is found to be negligible. It is found that the anode reaction is always endothermic, while the cathode reaction is always exothermic, and that the temperature gradients across the cell layers are less than 0.05°C

The cell transient response is found to be fast, and dominated by the thermal transients.

Several physical properties used in the model are measured experimentally, indicating that that the correlations used in the literature are not always suitable, especially when new fabrication techniques are used. The conductivity of the anode support was measured to be several orders of magnitude lower than expected and very sensitive to temperature, which explains the lower than expected and occasionally degrading cell performance. A hypothesis is proposed to explain this

phenomenon based on the thermal expansion effects which result in the formation and disruption of particle to particle contacts within the composite electrode.

Table of Contents

Chapter 1. Introduction 1

- 1.1 Solid oxide fuel cells 1
- 1.2 Thesis Objectives 2
- 1.3 Thesis outline 3
- 1.4 Thesis contributions 5

Chapter 2. Experimental 6

- 2.1 Anode supported tubular micro SOFC 6
- 2.2 Cell fabrication 12
- 2.3 TµSOFC experimental setup and performance testing 15

Chapter 3. The isothermal model 19

- 3.1 Introduction 19
- 3.2 Model development 21
  - 3.2.1 Modeling the porous electrodes 23
  - 3.2.2 The electrochemical reactions kinetics 25
    - 3.2.2.1 The anode reaction rate 28
    - 3.2.2.2 The cathode reaction rate 29
  - 3.2.3 The electric charge flow 31
  - 3.2.4 Mass transfer 35
    - 3.2.4.1 Mass transfer in gas channels 35
    - 3.2.4.2 Mass transfer in porous electrodes 38
- 3.3 Model implementation and solution 43
  - 3.3.1 Domain equations and boundary conditions 43
  - 3.3.2 Model Parameters 47
  - 3.3.3 Domain discretization 49

3.3.4 Numerical solution scheme and initial solution 52

3.3.5 Numerical convergence and consistency 53

3.4 Experimental validation 55

3.4.1 OCV dependence on hydrogen flowrate 55

3.4.2 Parameter estimation 56

3.4.3 Performance curves 58

3.5 Results and Discussion 60

3.5.1 Assessment of the contributions to the cell performance loss 60

3.5.2 Sensitivity of the simulated performance curve to electrode properties 63

3.5.3 Simulated details of the cell performance 67

3.6 Conclusion 83

Chapter 4. The non-isothermal model 84

4.1 Introduction 84

4.2 Model development 87

4.2.1 Conductive and convective heat transfer 89

4.2.2 Radiative heat transfer 93

4.2.3 The thermodynamics of a non-isothermal electrochemical cell 96

4.2.3.1 The single-electrode reversible heat generation 96

4.2.3.2 The electromotive force of a non-isothermal electrochemical cell 103

4.3 Model implementation 106

4.3.1 Model parameters 106

4.3.2 Boundary conditions 107

4.3.3 Geometry discretization 109

4.3.4 Equation discretization 109

4.3.5 Numerical solution 110

4.4 Experimental validation 111

4.5 Results and discussion 114

4.5.1 Gas flow and concentration distribution 114

4.5.2 Volumetric current and heat generation within each electrode 115

4.5.3 Temperature distribution within gas channels and cell layers 118

4.5.4 Overall reversible and irreversible heat generation 123

4.5.5 The significance of modeling heat transfer 126

4.5.6 The significance of radiative heat transfer 128

4.5.7 Sensitivity analysis 131

4.5.8 The overall energy balance and the overall thermoelectric effect in the non-isothermal electrodes 136

4.6 Conclusion 140

Chapter 5. TμSOFC transient simulation 141

5.1 Introduction 141

5.2 Model development 144

5.3 Experimental validation 145

5.4 Results and discussion 150

5.5 Conclusion 164

Chapter 6. TμSOFC characterization and performance diagnostic 165

6.1 Introduction 165

6.2 Experimental 168

6.2.1 The cathode effective conductivity measurements 168

6.2.2 The cathode electrochemical performance measurements 170

6.2.3 The anode support layer effective conductivity measurements 170

6.2.4 The contact resistance measurement 172

6.3 Results and discussion 173

6.3.1 The cathode electrochemical polarization resistance and its degradation 173

6.3.2 Electronic conductivity of the cathode and its degradation 177

6.3.3 The contact resistance measurement 179

6.3.4 The anode support layer effective electronic conductivity 182

6.3.5 The anode functional layer effective electronic conductivity 202

6.4 The use of computer simulation as a diagnostic tool 207

6.5 Conclusion 209

Chapter 7. Concluding remarks 211

Bibliography 215

Appendix A. Physical properties 225

A.1 The gas mixture density 225

A.2 The gas mixture viscosity 226

A.3 The gas mixture thermal conductivity 228

A.4 The gas mixture specific heat capacity 229

A.5 The gas binary diffusion coefficients 230

A.6 The reaction specific enthalpy, entropy, and Gibbs free energy change 231

A.7 The thermal conductivity of solids 233

A.8 The specific heat capacity of solids 233

A.9 The emissivity of solids 234

A.10 The electric conductivity of solids 234

A.11 Temperature dependent reaction kinetic parameters 235

List of Tables

Table 2.1. The specifications of the precursor powders used for the TµSOFC fabrication. 12

Table 2.2. The cathode functional layer sintering program. 14

Table 2.3. The current collector layers sintering program. 14

Table 3.1. The physical properties of the porous electrodes. 47

Table 3.2. The overall elemental balance around the boundaries of the simulated TµSOFC. 54

Table 3.3. Open circuit voltage at various hydrogen flowrates, and the corrected values. 55

Table 3.4. The optimized parameters based on the experimental I-V data. 56

Table 4.1. The energy balance of the TµSOFC operating at 0.4V; units are all in watts. 139

Table A.1. The polynomial coefficients of the viscosity correlation. 227

Table A.2. The polynomial coefficients of the pure component thermal conductivity correlation. 228

Table A.3. The polynomial coefficients of the pure component heat capacity correlation.(Todd and Young, 2002). 229

Table A.4. The constants of the Chapman and Enskog relations for various components. 230

Table A.5. The polynomial coefficients of the ΔH_{rxn} and ΔS_{rxn} correlation polynomials. 232

Table A.6. Thermal Conductivity of the solids. 233

Table A.7. Specific heat capacity of the solids. 233

Table A.8. Emissivity of the solids. 234

Table A.9. Electric conductivity of the solids. 234

Table A.10. Temperature dependent kinetic parameters. 235

List of Figures

Figure 2.1. The anode supported TμSOFC: an incomplete cell fabricated by electrophoretic deposition (EPD), before adding the cathode functional layer, the current collectors, and the wiring (bottom); a complete cell after reduction (top). 7

Figure 2.2. An SEM micrograph of the anode supported TμSOFC cross section. 8

Figure 2.3. An SEM micrograph of the anode supported TμSOFC cross section. 9

Figure 2.4. A schematic of the anode TμSOFC: the cell within the furnace (bottom); the tip of the cell, indicating the injector tube (middle); the layers of the active length (top). 16

Figure 2.5. The thermocouples locations in the non-isothermal furnace. 17

Figure 3.1. A schematic of an SOFC with composite electrodes. 24

Figure 3.2. The structured mesh used to discretize the computational domain. 50

Figure 3.3. The effect of mesh size on the final solution obtained for the model. 51

Figure 3.4. The experimental and the simulated performance curves for the base case. 58

Figure 3.5. The experimental and the simulated performance curves at two hydrogen flowrates. 59

Figure 3.6. The contribution of various overpotentials and components of the cell to the overall performance loss. 61

Figure 3.7. The contribution of the anode and the cathode electrodes to the concentration overpotential. 62

Figure 3.8. The cell performance sensitivity to the electric properties of the porous electrodes. 64

Figure 3.9. The cell performance sensitivity to gas transport properties of the porous electrodes. 65

Figure 3.10. The cell performance sensitivity to the electrochemical activity of the electrodes. 66

Figure 3.11. The mole fraction of (a) oxygen on the cathode side and (b) hydrogen on the anode side at V_{cell}=0.4 V. Arrows indicate (a) air velocity and (b) fuel velocity vectors. 68

Figure 3.12. The mole fraction of hydrogen across the middle of the anode active length, within the anode gas channel and the anode. 69

Figure 3.13. The mole fraction of hydrogen along the AFL/electrolyte interface; zero on the x-axis corresponds to the edge close to the open end. 70

Figure 3.14. Mole fraction of oxygen across the middle of the cathode active length, within the cathode gas channel and the cathode. 71

Figure 3.15. The mole fraction of oxygen along the CFL/electrolyte interface; zero on the x-axis corresponds to the edge close to the open end. 72

Figure 3.16. Volumetric electron generation within the electrodes, in the cross section at the middle of the active length. 74

Figure 3.17. The volumetric electron generation along the AFL/electrolyte interface; zero on the x-axis corresponds to the edge close to the open end. 75

Figure 3.18. The volumetric electron generation along the CFL/electrolyte interface; zero on the x-axis corresponds to the edge close to the open end. 76

Figure 3.19. The ratio of convective to diffusive mass transfer of hydrogen within the anode, in the cross section at the middle of the active length. 77

Figure 3.20. The ratio of convective to diffusive mass transfer of oxygen across the cathode at the middle of the active length. 78

Figure 3.21. The (gauge) pressure distribution on the anode side, in the cross section at the middle of the active length. 79

Figure 3.22. The (gauge) pressure distribution along the AFL/electrolyte interface; zero on the x-axis corresponds to the edge close to the open end. 80

Figure 3.23. The (gauge) pressure distribution on the cathode side, in the cross section at the middle of the active length. 81

Figure 3.24. The (gauge) pressure distribution along the CFL/electrolyte interface; zero on the x-axis corresponds to the edge close to the open end. 82

Figure 4.1. A schematic of the surface to surface radiation within an enclosure. 94

Figure 4.2. The entropy change of the anode and the cathode reactions as a function of partial pressure of the components. 102

Figure 4.3. The overall performance prediction of the cell at various temperatures and the experimental results. 111

Figure 4.4. The temperature distribution prediction within the furnace versus the experimental. 113

Figure 4.5. The simulated concentration distribution and the velocity profile: (a) the hydrogen mole fraction on the anode side; (b) the oxygen model fraction on the cathode side. The arrows show (a) the hydrogen, and (b) the air velocity profile. 114

Figure 4.6. The volumetric electron generation within the anode and the cathode in the radial cross section at the middle of the active length. 115

Figure 4.7. The volumetric heat generation within the cell layers in the radial cross section at the middle of the active length... 116

Figure 4.8. The volumetric heat generation along the active length at the anode/electrode interface.. 117

Figure 4.9. The volumetric heat generation along the active length at the cathode/electrode interface.. 118

Figure 4.10. The predicted temperature distribution at various cell voltages. The adjacent contours are 5°C apart.. 119

Figure 4.11. The temperature distribution within the cell layers in the radial cross section at the middle of the active length... 120

Figure 4.12. The temperature distribution within the furnace in the radial cross section at the middle of the active length... 121

Figure 4.13. Temperature distribution along the active length at the cathode/air interface. 122

Figure 4.14. The cell overall electric power and heat generation rate. 123

Figure 4.15. The overall heat generation rate within the electrodes. 124

Figure 4.16. The temperature of the middle of the active length (TC-2) as current is drawn from the cell.. 125

Figure 4.16. The overall performance curves predicted by the isothermal model, the non-isothermal model, and the non-isothermal model without the effect of temperature gradients on the cell electromotive force... 126

Figure 4.17. The estimated furnace heat flux at various current loads. 127

Figure 4.18. The heat transferred away from the cathode by thermal radiation and thermal conduction at the cathode/gas interface. 128

Figure 4.19. The simulated temperature distribution when radiative heat transfer is not included; V_{cell} = 0.4V and no heat is provided by the furnace. 130

Figure 4.20. The sensitivity of the temperature distribution along the cell active length to the surfaces emissivities, when the furnace heat was re-estimated. 132

Figure 4.21. The sensitivity of the temperature distribution along the furnace wall to the surfaces emissivities, when the furnace heat was re-estimated. 133

Figure 4.22. The sensitivity of the temperature distribution along the cell active length to the surfaces emissivities, when the furnace heat was kept constant. 134

Figure 4.23. The sensitivity of the temperature distribution along the furnace wall to the surfaces emissivities, when the furnace heat was kept constant. 135

Figure 5.1. The temperature transients for a current step of 0 A to 1 A. 146

Figure 5.2. The temperature transients for a current step of 0 A to 0.5 A. 147

Figure 5.3. The temperature transients for a current step of 0 A to 1 A. Note that the second step from 1 A back to 0 A was only modeled for the case where Cp was multiplied by 100............ 148

Figure 5.4. The temperature transients for a current step of 0 A to 0.5 A. 149

Figure 5.5. The predicted fast and slow temperature transients; I= 0 to 1 A. 151

Figure 5.6. The sensitivity of the cell thermal transients to the furnace wall heat capacity; I= 0 A to 1 A.. 152

Figure 5.7. The sensitivity of the cell thermal transients to the cell heat capacity; I= 0 to 1 A. 153

Figure 5.8. The sensitivity of the cell thermal transients to the surface emissivity of components; I= 0 to 1 A. 154

Figure 5.9. The sensitivity of the cell thermal transients to the gas velocity; I= 0 to 1 A. 155

Figure 5.10. The sensitivity of the cell thermal transients to its thermal conductivity; I= 0 to 1 A. 156

Figure 5.11. The sensitivity of the cell thermal transients to the furnace thermal conductivity; I= 0 to 1 A. 157

Figure 5.12. The concentration transient at the anode/electrolyte interface; I= 0 to 1 A. 158

Figure 5.13. The concentration transient at the cathode/electrolyte interface; I= 0 to 1 A........ 159

Figure 5.14. The cell potential transient as the current stepped from 0 A. 160

Figure 5.15. The expanded cell potential transient; I= 0 to 0.5 A. 161

Figure 5.16. The expanded cell potential transient; I= 0 to 1 A. 162

Figure 5.17. The effect of gas flowrate on the cell potential transient; I= 0 to 1 A.................. 163

Figure 6.1. An experimental example of severe performance degradation in a TμSOFC. Each of the 176 I-V cycles lasted ~3 minutes, 1000 mA/min, with a 1 minute break after each cycle... 166

Figure 6.2. The two configurations used for the van der Pauw conductivity measurements method.. 169

Figure 6.3. A schematic of the four-probe measurement of the ASL and the AFL tubular samples.. 171

Figure 6.4. A schematic of the various contributions to the overall resistance of the contact resistance samples.. 172

Figure 6.5. The impedance spectra of the symmetric planar cell at various temperatures; the high frequency tail below x-axis is truncated. 174

Figure 6.6. The temperature dependence of the cathode polarization resistance, R_p. 175

Figure 6.7. The change in the polarization resistance of the LSM-YSZ cathode with time...... 176

Figure 6.8. The effective electronic conductivity of the LSM-YSZ electrode versus temperature. 177

Figure 6.9. The change in the effective electronic conductivity of the LSM-YSZ electrode at 800°C versus time.. 178

Figure 6.10. The experimental and simulated overall resistance of the contact resistance samples versus temperature. 180

Figure 6.11. The overall resistance changes in the contact resistance samples versus time...... 181

Figure 6.12. The conductivity of the ASL samples during the first cycle of heating and long-term testing. The samples were tested together under a humidified hydrogen atmosphere, and were initially unreduced. ASR87-1 and ASR87-2 were made from the same longer tube; same for ASR89-1 and ASR89-2.. 186

Figure 6.13. The conductivity of the ASL samples during the second cycle of heating and long-term testing. ASR87-1 and ASR87-2 were from the same longer tube; same for ASR89-1 and ASR89-2. 187

Figure 6.14. The conductivity of ASR89-1&2 during the cooling stage of the second cycle. They were from the same longer tube... 188

Figure 6.15. The conductivity of ASR89-1 as a function of temperature during the heating, long-term and cooling stages of the second testing cycle. 189

Figure 6.16. The conductivity of ASR89-2 as a function of temperature during the heating, long-term and cooling stages of the second testing cycle. 190

Figure 6.17. The conductivity of ASR40 during the heating and long-term testing. The sample was reduced for 2 hours prior testing... 191

Figure 6.18. The conductivity of ASR40 during the cooling stage of its first testing cycle (second heating cycle).. 192

Figure 6.19. The conductivity of ASR40 as a function of temperature during the heating, long-term and cooling stages.. 193

Figure 6.20. The conductivity of ASR39 during the heating and long-term testing stages. The sample was reduced for 2 hours prior testing. 194

Figure 6.21. The SEM microstructure of ASR39 after the conductivity measurements. 195

Figure 6.22. The SEM microstructure of ASR39 after the conductivity measurements. 196

Figure 6.23. The BSE microstructure of ASR39 after the conductivity measurements. 197

Figure 6.24. The SEM microstructure of ASR39 after the conductivity measurements. 198

Figure 6.25. The SEM microstructure of ASR39 after the conductivity measurements. 199

Figure 6.26. The SEM microstructure of ASR39 after the conductivity measurements. 200

Figure 6.27. The SEM microstructure of ASR39 after the conductivity measurements. 201

Figure 6.28. The conductivity of ASR40 during the heating and long-term testing. The sample was reduced for 2 hours prior testing.. 203

Figure 6.29. The SEM microstructure of AFR2 after the conductivity measurements. 204

Figure 6.30. The SEM microstructure of AFR2 after the conductivity measurements. 205

Figure 6.31. The outer surface of AFR2 after the conductivity measurements. 206

Figure 6.32. Model predictions resulting from the kinetic parameters based on various fitting points.. 208

List of Abbreviations

ACCL	Anode Current Collector Layer
AFL	Anode Functional Layer
AFR	Anode Functional Resistance measurement sample
ASL	Anode Support Layer
ASR	Anode Support Resistance measurement sample
BSE	Back-Scattered Electron Microscopy
CC	Current Collector
CCCL	Cathode Current Collector Layer
CFL	Cathode Functional Layer
DGM	Dusty-Gas Model
EIS	Electrochemical Impedance Spectroscopy
EPD	ElectroPhoretic Deposition
LSM	Lanthanum Strontium Manganate
MSM	Maxwell-Stefan Model
REV	Representative Elementary Volume
RHS	Right-Hand Side
SEM	Scanning Electron Microscopy
SOFC	Solid Oxide Fuel Cell
TC	Thermocouple
TPB	Three-Phase Boundary
TµSOFC	Tubular micro- Solid Oxide Fuel Cell
YSZ	Yttria-Stabilized Zirconia

Chapter 1. Introduction

1.1 Solid oxide fuel cells

Fuel cells are electrochemical devices that convert the chemical energy of fuels directly to electricity, with higher efficiency compared to almost any other energy conversion device. A fuel cell consists of an electrolyte, an anode, and a cathode. Electrolyte is an ion permeable medium which separates the fuel from the oxidant. The fuel cell electrochemically oxidizes the fuel to produce electric power and heat.

Solid oxide fuel cells (SOFCs) are based on oxygen-ion conducting electrolytes. A common material used as an SOFC electrolyte is Yttria-stabilized Zirconia (YSZ). YSZ becomes conductive to oxygen ions at high temperatures, hence YSZ based SOFCs typically operate around 800°C. A high operating temperature has drawbacks such as sealing problems, thermal stress issues, and reduced ideal efficiency of the fuel cell; however the advantages are significant. At high temperatures the activity of the anode and the cathode catalysts are much higher; hence cheaper catalysts can be used with an excellent performance. Nickel, the most common anode catalyst, catalyzes the reforming reactions as well; thus SOFCs are compatible with hydrocarbon fuels such as methane. These advantages distinguish SOFCs as one of the most promising types of fuel cells for both stationary and portable power generation applications.

A tubular micro-SOFC (TμSOFC) is few millimetres in diameter and has a very thin wall (hundreds of microns). It has several advantages over other designs of SOFCs. Compared to the planar design, a tubular design is much easier to seal. The tubular design is mechanically more robust; a critical factor for fabricating very thin SOFCs. The thinner electrode and electrolyte layers reduce the ohmic resistance performance losses, otherwise a major efficiency bottleneck for SOFCs. Thinner electrodes also reduce the barrier against the reacting components to diffuse into and from the active sites within the porous electrodes. In addition, thinner layers reduce the thermal stress caused by the temperature changes, and reduce the thermal mass of the cell. Therefore a stack of TμSOFCs is suitable for rapid start-up and shut-down cycles, which is a significant practical advantage, as it takes much longer for other designs of SOFCs to reach to their operating temperature. The small diameter of the TμSOFC allows for the ‘packing’ of more ‘active area’ within the same volume and therefore increases the volumetric power density of the stack. The latter two advantages are especially important for portable power generation applications.

1.2 Thesis Objectives

The focus of this thesis is a novel TμSOFC developed at the Alberta Research Council in Canada. The aim of this work is to utilize mathematical modeling to facilitate the experimental development and design of the TμSOFC system by providing a thorough insight into its performance. The main objectives of this thesis are:

- To simulate the performance of the single TμSOFC by developing a detailed multi-scale mechanistic model that includes the many phenomena occurring within its tens-of-micron-thin electrodes and electrolyte layers, as well as its centimeter-wide gas channels.
- To experimentally characterize the TμSOFC and measure the parameters used in the model.
- To validate the model and verify its predictions based on the experiments conducted on the TμSOFC specifically for this purpose.

- To use the model to gain a detailed insight into the TμSOFC operation, at steady-state and transient conditions.
- To use the model to facilitate the experimental development of the TμSOFC by identifying the performance bottlenecks.

1.3 Thesis outline

The initial intention of this work was to develop a 2-D axi-symmetric model for a single cell, experimentally validate it, and then extend it to further model the performance of a stack of TμSOFCs in 3-D. However, the modeling and validation of the single TμSOFC itself proved to be a quite challenging as the initial simulations were not consistent with the experiments, when the physical properties appearing in the model were assumed from the literature. This challenge introduced an opportunity to utilize the model as a diagnostic tool, which led to a thorough effort to experimentally characterize the physical and electrochemical properties of the cell components. The results showed that some of the properties were significantly different from the expected values. In addition, they could further explain some of the issues with the cell performance. Using the experimentally measured properties, the model was successfully validated and was then used to provide a detailed understanding about the TμSOFC performance.

In Chapter 2 the experimental procedures concerning the TμSOFC fabrication and performance testing are explained.

Chapter 3 is focused on the steady-state isothermal simulation of the TμSOFC. The mathematical models describing the various phenomena occurring in the SOFC are explained. Then the model implementation, numerical solution, and parameter estimation are explained. The model is validated against the experimental results, and the numerical consistency of the results is verified. The validated model is used to simulate the cell performance, understand various aspects of its performance, and to identify the contribution of the performance loss mechanisms. Finally, the sensitivity of the simulations to various model parameters is investigated.

Chapter 4 presents the steady-state non-isothermal model, which is an extension of the isothermal model. The heat transfer model is developed and discussed in details. Expressions are developed for modeling the thermodynamics of a non-isothermal electrochemical cell, which enables the model to predict the single-electrode reversible heat generation, as well as thermoelectric effects. The model predictions are validated against the experimental results, and used to investigate the thermal behavior of the cell and its sensitivity to various parameters.

Chapter 5 presents the TμSOFC transient model. The prediction results are compared with the experiments. Next, the model is used to study various aspects of the transient behavior of the cell performance and its time constants.

Chapter 6 focuses on the experimental characterization of the TμSOFC to identify the sources of its lower than expected performance. The issue of contact resistance, the electrochemical performance of the cathode, and the effective conductivity of the anode and the cathode composites are studied and their long-term changes are investigated. The anode support effective conductivity is found to be a major performance bottleneck due to its much lower than expected conductivity, and based on the experimental observations, a hypothesis is proposed to explain these phenomena.

1.4 Thesis contributions

The main contributions of this work include:

- One of the most comprehensive continuum level models is developed here to facilitate the development of a state-of-the-art fuel cell. The model includes mass, momentum, and heat transfer. The electrochemical reactions are modeled within the volume of the composite electrodes, which enables the model to account for the extent of reaction within the electrodes. Surface-to-surface radiation is modeled completely. A model of these details, for an actual cell, simulating its steady-state and transient behavior is unique.

- The simulation results provide a detailed insight about the cell performance. Most significantly, it pinpoints the major performance bottlenecks of the TµSOFC.

- The extent of the experimental validation of the model as a wholesome, in terms of the electrochemical performance, heat transfer, and the dynamic response of the cell is a unique aspect of this work.

- A consistent thermodynamic framework is developed which enables the calculation of single-electrode heat generation, as well as the electromotive force of non-isothermal electrodes.

- Several physical properties appearing in the model are measured experimentally and compared to values commonly reported in the literature.

- A novel approach is used for estimating the model’s unknown parameters, which enables the model to be used as a diagnostic tool.

- The immediate practical benefit of this work towards the development of the TµSOFC is unique.

Chapter 2. Experimental

In this chapter, the anode supported TµSOFC used for this study is introduced, its fabrication process is explained, and the experimental setups and testing procedures are presented.

2.1 Anode supported tubular micro SOFC

The anode supported TµSOFC was about 7 cm long, 2.5 mm in diameter, and about 300 µm thick; see Figure 2.1. The cell had one end open and the other closed. Hence, by the use of an alumina fuel injector tube inside the cell, it did not require any sealing. Only a 2.5 cm length near the closed end of the cell was active, participating in electrochemical reactions. The active length had six layers, see Figures 2.2 and 2.3. Ordered from the innermost, these layers were: anode current collector (ACCL), anode support (ASL), anode functional (AFL), electrolyte, cathode functional (CFL), and cathode current collector (CCCL).

Figure 2.1. The anode supported TμSOFC: an incomplete cell fabricated by electrophoretic deposition (EPD), before adding the cathode functional layer, the current collectors, and the wiring (bottom); a complete cell after reduction (top).

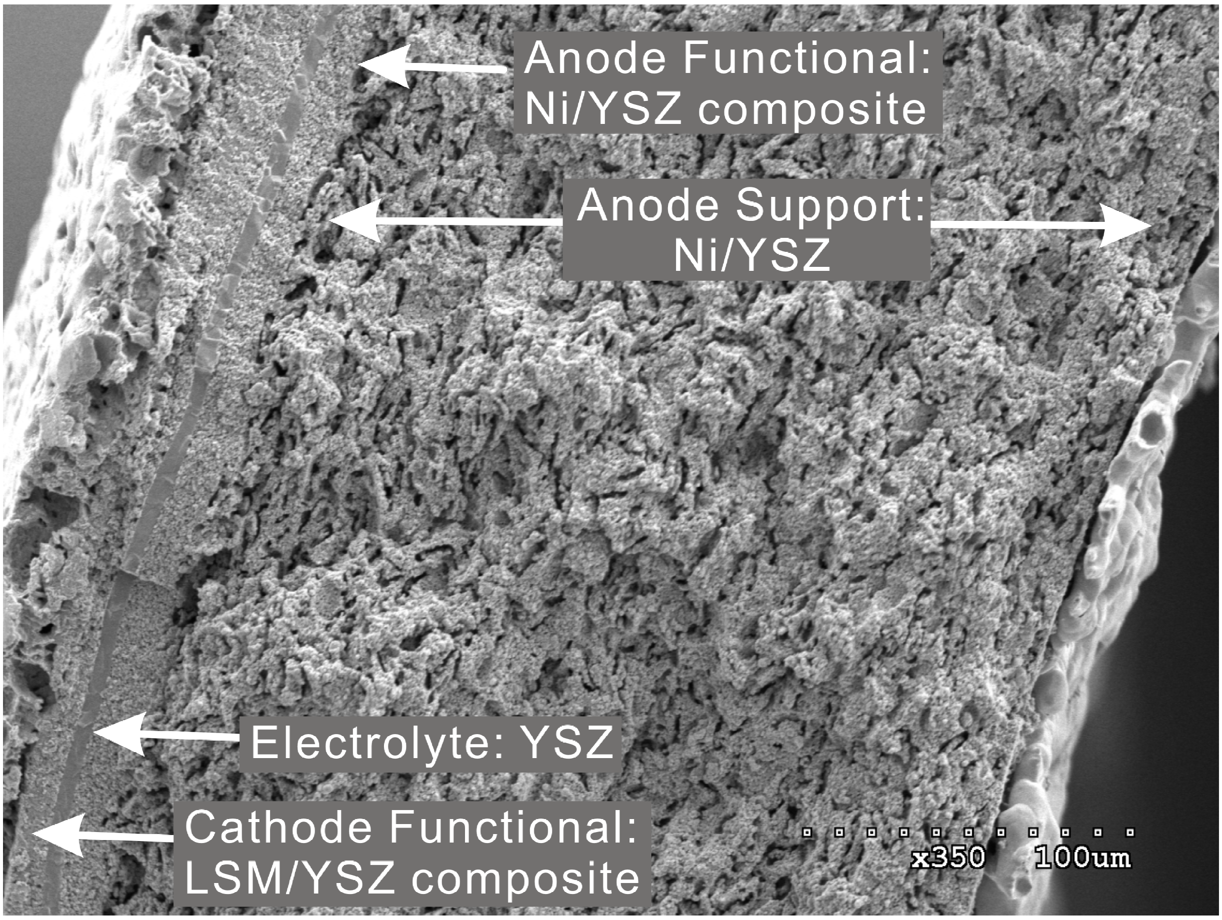

Figure 2.2. An SEM micrograph of the anode supported TμSOFC cross section.

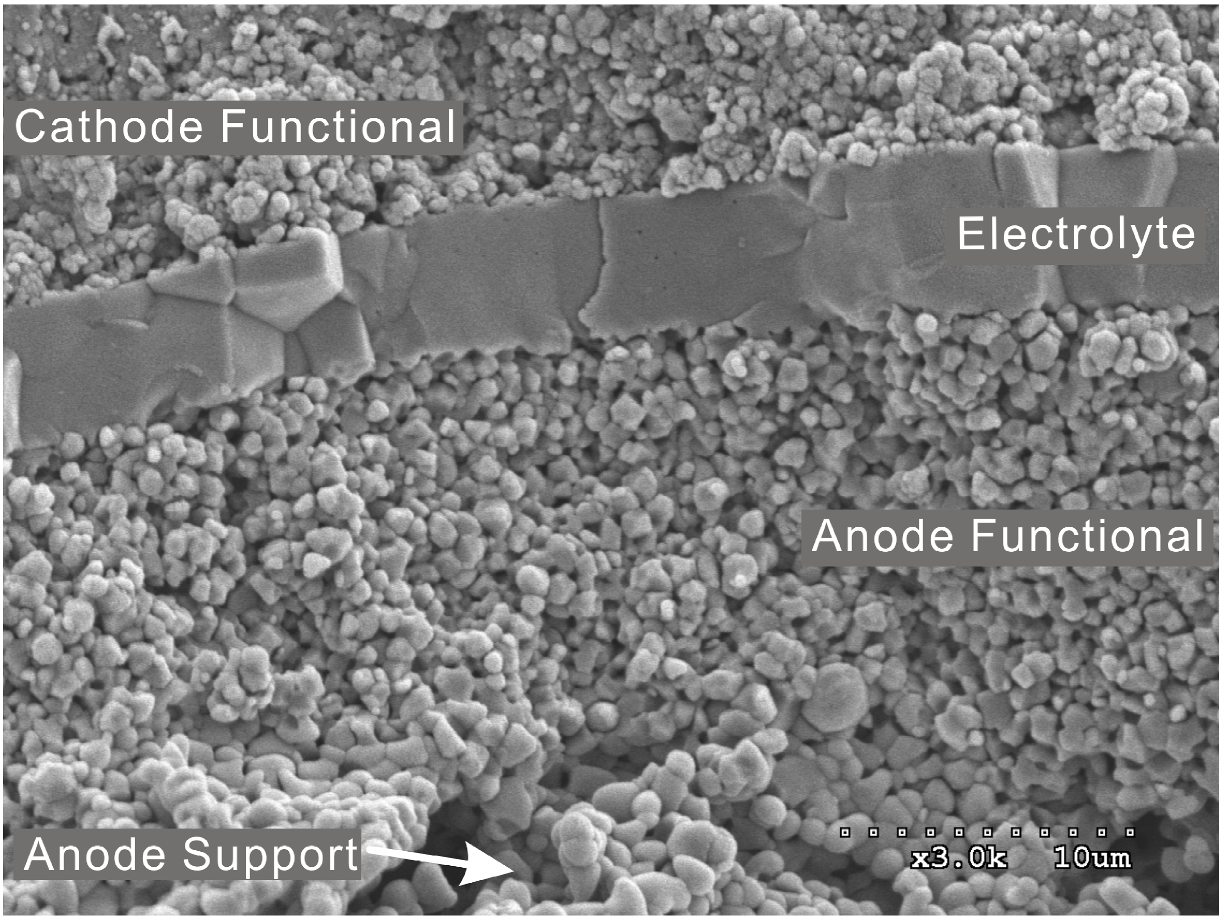

Figure 2.3. An SEM micrograph of the anode supported TμSOFC cross section.

The ASL was a porous Ni/YSZ composite, and as the thickest layer of all, it provided the mechanical strength of the cell. The gaseous reactants and products diffused through the ASL pores, to and from the electrochemical active sites within the AFL. At the same time, the electrons generated by the electrochemical reactions were conducted by the nickel particles to the current collector. The ASL was made to be more porous than the anode active layer to reduce the diffusion limitation for the gaseous components. There was a trade-off, however, as higher porosity reduces the effective electric conductivity of the solid structure.

The anode reactions occurred within the AFL. It had the same composition as the ASL, but to provide more reaction sites, it was made of a finer precursor powder without any pore former. The hydrogen molecules reacted with the oxygen ions provided by YSZ, to produce electrons and gaseous water. The Ni particles conducted these electrons to the ASL. Due to the low ionic conductivity compared to electric conductivity of the composite material, reactions mainly occurred close to the electrolyte layer. Although the ASL is electrochemically active, in a well designed electrode, reactions should mainly remain within the AFL to achieve an optimum performance.

The CFL was a porous composite of LSM (Lanthanum Strontium Manganate, $La_{0.8}Sr_{0.2}MnO_3$) and YSZ. LSM is an electron conducting ceramic which catalyses the oxygen reduction reaction. Oxygen molecules reacted to produce oxygen ions by consuming the electrons provided by the LSM particles; oxygen ions were then conducted by YSZ particles to the electrolyte and then to the anode side.

The electrolyte layer was a dense YSZ layer, completely impermeable to gaseous components on the cathode side and the anode side. YSZ is conductor to the oxygen ions but not to the electrons. It becomes conductive to the oxygen ions at high temperatures (600°C - 1000°C), but even at those temperatures its conductivity is still much less than nickel or LSM. In conventional SOFC designs where the electrolyte layer is thick, ohmic losses due to the low ionic conductivity of YSZ is a major performance bottleneck. It is desirable to have the electrolyte layer as thin as possible; however, it should be thick enough to avoid any cracks or pinholes. Cracks or pinholes significantly reduce the performance of the cell due to an electric short circuit between the anode and the cathode, and also due to mixing and direct reaction of the anode and the cathode side reactants.

Composite electrodes exhibit superior performance because they can provide more active sites for the electrochemical reactions. Most importantly, composite electrodes have the practical advantage of resolving the thermal expansion incompatibility of the electrolyte and the electrode materials. If electrodes are made from pure LSM or Ni, their different thermal expansion compared to YSZ will cause significant mechanical stress within the cell layers at high temperatures, which can lead to the delamination or cracking of the fuel cell layers.

The current collectors, the ACCL and the CCCL, covering the ASL and the CFL surfaces, were made of porous gold. They conducted electrons from/to electrodes, and were connected to the external current load. The CCCL covered only the active length of the cell. The ACCL was extended from the active length inside the cell, covering its entire inner surface of to the open end; it covered a small length on the outer surface of the cell as well, where the anode wire was wrapped around it.

The inactive length of the cell was not covered by the CFL or the CCCL, however it had all the remaining layers; the dense electrolyte layer prevented any mixing of the reactants on the cathode and the anode side.

2.2 Cell fabrication

The TμSOFC of this study was manufactured from ceramic powders. The specification of the precursor powders used is given in Table 2.1.

Table 2.1. The specifications of the precursor powders used for the TμSOFC fabrication.

Precursor powder	Type	Particle size (μm)
LSM	PRAXAIR, $(La_{0.8}Sr_{0.2})_{0.98}MnO_3$	0.85
YSZ	Tosoh, TZ-8Y	0.35
NiO (AFL)	J. T. Baker, NiO green powder	0.3
NiO (ASL)	Novamet, high purity green NiO - Type F	0.65

The ASL, the AFL, and the electrolyte were fabricated based on the sequential electrophoretic deposition (EPD) of several thin layers. In a typical EPD deposition process, a stable colloidal suspension of particles in an organic solvent is prepared. Colloidal particles are forced to migrate under an electric field, due to their surface charges, and deposit on a substrate with the opposite electric charge. The surface charge of the particles is induced by controlling the pH of the suspension. The thickness of the deposited layer can be conveniently controlled by manipulating the electric field strength and the time of deposition. The fabrication process of a single TμSOFC is discussed briefly in the following; a comprehensive description can be found elsewhere (Sarkar et al., 2007).

Three layers of the cell were deposited on a graphite rod by the EPD process. First the ASL was deposited from a stabilized suspension of NiO/YSZ (45/55 wt %) in absolute ethanol. The suspension contained some pore-former, corn starch, which burnt out after sintering to add extra porosity to the ASL. The deposition of the ASL was completed in less than 30 seconds. Next, the graphite rod was taken out and immersed in the AFL suspension which contained a finer NiO powder, without any pore former. Finally, the electrolyte layer was deposited on top of the AFL, from a suspension that contained YSZ solely. The cathode layer was not deposited at this stage because it would have reacted with YSZ at the sintering temperature required for fabricating a dense electrolyte layer.

The whole EPD process took less than 3 minutes, and was conducted by a semi-automated system. Using an in-house developed software, a computer controlled and monitored the applied voltage, the current passing through the suspension, and a robotic arm which dipped the graphite rod into and removed it from the suspension at a specified rate.

The cell was air dried for 12 hours, then sintered at 1380°C for 2 hours. The graphite rod substrate burnt out at that temperature, forming a hollow tubular cell with one end closed.

To ensure there were no cracks or pinholes in the electrolyte layer, a helium leak test was performed. The helium mass spectrometer leak detector, VARIAN 979, was used at a test port pressure of 1e-3 torr. The tube was pressurized to 2 psig through its open end by a helium/nitrogen gas mixture (1.2% He). A leakage below 1e-5 atm.cm^3/s was considered satisfactory.

The cathode functional layer was coated on the sintered YSZ electrolyte. A paste of LSM/YSZ (50:50 wt %) was prepared and brush-coated on top of the tube. The paste was made by first mixing YSZ, LSM, isopropyl alcohol, and 5 mm YSZ beads (YTZ grinding media, Tosoh) with a mass proportion of 1:1:4:20. It was then vibro-milled for 24 hours to ensure a homogenous mixture of LSM and YSZ particles. The mix was filtered to separate the beads and was dried at 60°C in an open bowl, while it was continuously stirred. It was then dried in an oven for 2 hours at 100°C to ensure the complete removal of the solvent. The dried material was passed through a 120 mesh sieve to break down chunks of the dried solids. A 2:1 weight proportion of the powder and a solution of 5 wt% ethyl cellulose (SIGMA) in alpha-terpineol (Fisher) was milled for 5 hours in a mortar grinder (Retsch with Zirconia mortar and pestle) to break down the agglomerates and to obtain a well-mixed paste.

The brush-coated cathode layer was air dried for 2 hours, and then sintered to obtain a porous CFL. It is well known that the sintering temperature and procedure can have a significant effect on the electrochemical performance of an SOFC electrode (Kim et al., 2001; Leng et al., 2003). The sintering program used for the CFL fabrication is shown in Table 2.2.

Table 2.2. The cathode functional layer sintering program.

Stage	Heating rate (°C/hr)	Set point (°C)	Dwell time (hr)
1	100	50	0.5
2	100	150	0.5
3	100	700	0.2
4	300	1140	2
5	300	25	-

The last stage of fabricating the TμSOFC was to put on the current collator layers. A gold paste was brush coated on top of the ASL inside the tube and the CFL outside the tube. The gold paste was prepared by mixing a 20:10:1 weigh ratio of gold powder, 5 wt% cellulose acetate in alpha-terpineol, and corn starch pore former. The paste was hand-mixed in an YSZ mortar and pestle to ensure homogeneity. The current collector layers were brush-coated, air dried for 2 hours, and then sintered to obtain the porous current collector layers. The process of painting and sintering of the current collector layers was repeated three times to ensure a uniform, thick enough current collector layer. The sintering program for the gold layer is shown in Table 2.3.

Table 2.3. The current collector layers sintering program.

Stage	Heating rate (°C/min)	Set point (°C)	Dwell time (hr)
1	3	75	2
2	1.5	800	2
3	5	25	-

Before the last current collector sintering step, the current collector wires were attached. Gold wires were wrapped around the cell for the cathode and the anode. For the cathode, the wire was wrapped on the edge of the active length near the closed end of the cell. For the anode, the gold layer that covered the interior of the cell was extended to the outer surface of the open end of the cell, creating a complete electric path. The anode wire, wrapped around the gold layer covering the outer surface of the cell at the open end, was covered with a non-porous gold paste to establish a firm electric connection after sintering. To ensure a good conductivity for the ACCL, the resistance from the close tip to the open end was measured and confirmed to be less than 0.03 ohms.

Cells without an electrolyte layer were used for the porometry experiments, using a CFP-1500-AEXL-I capillary flow porometer. Nitrogen gas was used to determine the permeability and the pore size distribution of the ASL and the AFL.

2.3 TµSOFC experimental setup and performance testing

Figure 2.4 shows a schematic of the isothermal experimental setup. The fuel cell was placed in the center of a tubular electric furnace such that the cell active length and the furnace tube were aligned at their middles. Air flowed against the cell's closed end, through a nozzle shaped diffuser. A ceramic injector tube, connected to the hydrogen source, was inserted inside the cell all the way to its closed end. Hydrogen flowed through the injector tube to the closed end, flowing back in the annular space between the injector tube and the cell's inner wall. The hydrogen flowed freely to the atmosphere through the open end of the cell. The setup dimensions used for the isothermal model are indicated on Figure 2.4. The only difference for the non-isothermal setup was the furnace diameter, which was 2.5 cm.

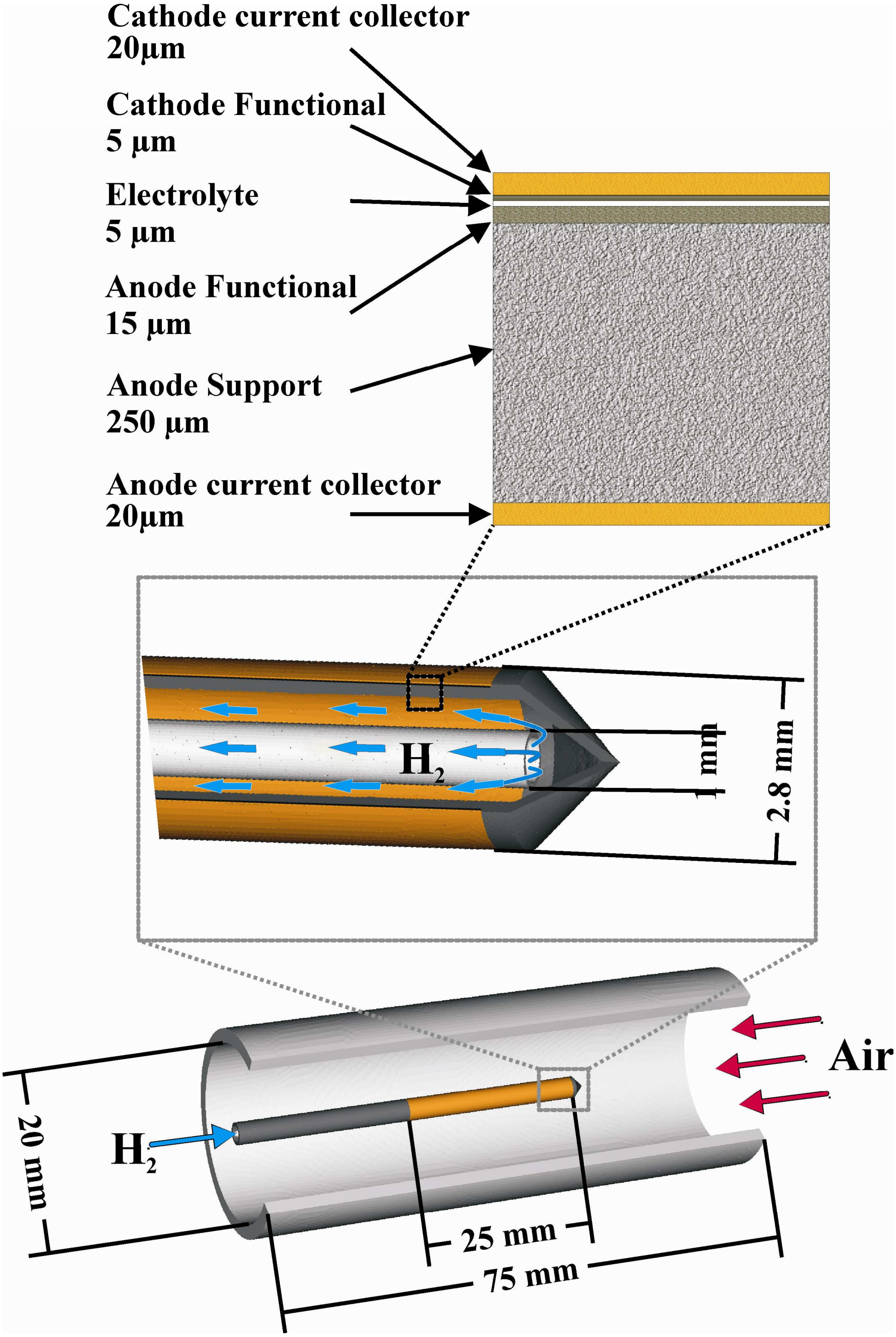

Figure 2.4. A schematic of the anode TµSOFC: the cell within the furnace (bottom); the tip of the cell, indicating the injector tube (middle); the layers of the active length (top).

Two different tubular electric furnaces were used for the isothermal and the non-isothermal experiments. For the non-isothermal setup, five thin thermocouples (type K, OMEGA) were used to measure the temperature distribution within the furnace, as shown in Figure 2.5. Three thermocouples, sheathed in alumina rods of 1.5mm OD, were attached along the cell to measure the temperature of the active length at its middle and the two ends (TC-1, TC-2, TC-3); another two thermocouple wires measured the temperature of the inlet air flow (TC-5), and that of the furnace inner wall at its middle (TC-4). A PID controller was used to keep TC-2 at the desired temperature. An Agilent 34970A DAQ switch equipped with a 34901A multiplexer module was used to collect the thermocouple measurements.

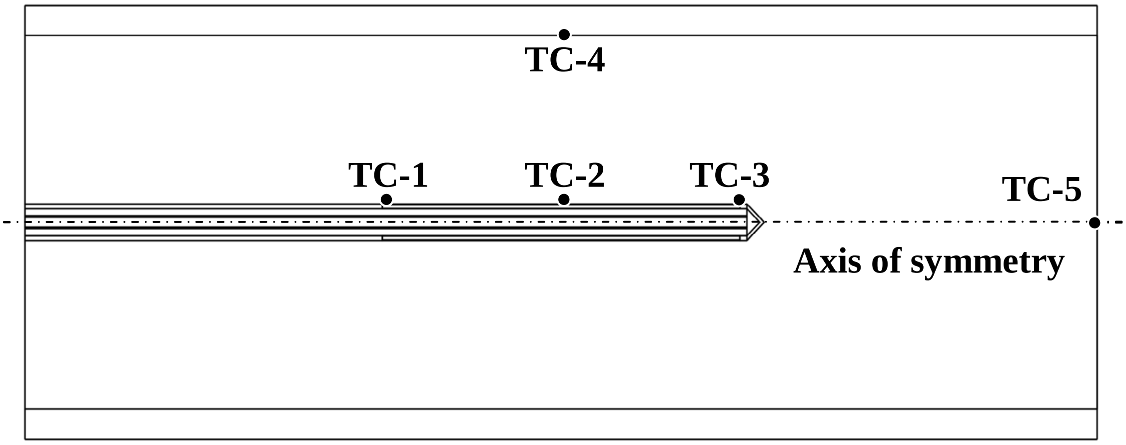

Figure 2.5. The thermocouples locations in the non-isothermal furnace.

The electric furnace used for the isothermal experiments had three separate heating coils along its tube, each controlled by a separate PID controller to maintain the cell active length (TC-1 TC-2, TC-3) at a uniform temperature.

The hydrogen and air flowrates were controlled by digital mass flow-meters (Alicat Scientific). Hydrogen was bubbled through water at the room temperature which added about 3 mol% moisture to the fuel gas. The hydrogen and air flowrates were set to 50 and 500 mL/min respectively. Note that the hydrogen gas velocity was much higher than the air velocity due to the much narrower cross section of the cell compared to the furnace tube.

The cell was heated to its operating temperature at a rate of 5°C/min. For a newly fabricated cell, the nickel oxide particles of the AFL and the ASL were reduced to metallic nickel during the first run. A physically reasonable cell voltage was observed around 600°C which was an indication that enough nickel was reduced to form a functioning anode. It was noticed in general that the performance of the cell did not remain constant for several hours after the operating temperature had been reached. Therefore the final data was collected about 30 hours after the cell had reached its operating temperature, when the changes in current vs. voltage plots (I-V curves) were settled.

The performance of the cell was measured by an Agilent N3301A electronic load, equipped with an Agilent N3302A cartridge. The cell was connected to the current load in a four-probe configuration to eliminate the resistance of connecting wires. An in-house developed computer program was used to collect data and control the cell performance as well as the temperature readings. The performance curves (I-V) were collected by sweeping the current drawn from the cell in steps of 10 mA, each step lasting for 10 seconds, when temperature and voltage measurements, pulled every second, settle to their steady value. The average of the last four readings of each step was used for the final analysis, to reduce the high frequency noise in the data.

Chapter 3. The isothermal model

3.1 Introduction

Mathematical modeling can provide a detailed insight about SOFCs, beyond the reach of any experiment. A valid mathematical model can significantly assist predicting, optimizing, controlling, and diagnosing the performance of the fuel cell system and therefore facilitate their development. Numerous models for SOFCs have been presented in the literature in recent years thanks to ever increasing access to high performance computing. These models can be categorized according to their specifics, i.e. level of detail, geometry, type of fuel, and simplifying assumptions. Excellent studies by Aguiar et al., (2002), Achenbach, (1994), Chan et al., (2001), Costamagna et al., (2004), Ferguson et al., (1996), and Yakabe et al., (2000) are most notable in the SOFC modeling literature. Kakac et al., (2007), and Bove and Ubertini, (2006) provide valuable reviews of the SOFC modeling efforts.

Modeling a fuel cell system is a challenging task, due to the various phenomena involved. The multi-scale model developed in this work includes micron-thin electrodes as well as centimetre-wide gas channels. Convective flow and mass transport within the gas channels and the porous electrodes are treated rigorously, instead of making simplifying assumptions. Reactions are assumed to occur within the volume of electrodes, not just at the electrode/electrolyte interface. All mechanisms of performance loss were accounted for in details. In addition, special attention was paid to numerical consistency and convergence of the simulation results.

In addition to developing an accurate model for the fuel cell, proper matching of the model with the experiments presents a new level of challenges. The reality of the experiments is reflected in the model through various parameters, i.e. physical properties. Some of these parameters can be measured directly, and some can only be estimated. There is a certain degree of uncertainty in any physical property measurement; however, for fuel cells this problem is more critical: some of the physical properties are significantly affected by factors such as fabrication techniques and degradation. This is a pronounced problem especially for composite electrodes due to their inherent randomness. Kakac et al., (2007) correctly point out the significant shortcomings in the treatment of these parameters in the fuel cell literature. In this work, some physical properties were measured and compared to the correlations commonly used in the modeling literature.

A novel method was used to estimate the model’s unknown parameters. The final model developed in this work was proven to be consistent with the physical reality of the TµSOFC. It was then used to gain a better insight into the TµSOFC’s operation and mechanisms that cause performance loss. In addition, the influence of uncertainty in physical parameters on final predictions was assessed. It was concluded that although the resulting error could be manageable, it eventually comes down to careful handling of the assumptions made, especially when novel fabrication processes are used.

3.2 Model development

Fuel cells are electrochemical cells that are continuously supplied with reactants. An electrochemical cell consists of the anode and the cathode electrodes, and an electrolyte. Electrochemical reactions occur at the electrodes, while the electrolyte transports ions between the electrodes. In the overall reaction that occurs in a hydrogen SOFC, hydrogen and oxygen react to produce water.

$$\begin{array}{ll} Anode: \quad H_2 + O^{2-} \longrightarrow H_2O + 2e^- & (a) \\ Cathode: \quad \frac{1}{2}O_2 + 2e^- \longrightarrow O^{2-} & (b) \\ \hline Overall: \quad H_2 + \frac{1}{2}O_2 \longrightarrow H_2O & (c) \end{array} \tag{3.1}$$

The chemical non-equilibrium between the anode and the cathode is the driving force for the electrochemical reactions, and creates an electric potential difference between the electrodes. A fuel cell can ideally deliver electric energy equivalent to the Gibbs free energy change of its reaction. The potential difference across electrodes at equilibrium, when no net reaction occurs, is called the open circuit voltage (OCV) of the cell. Thermodynamically, OCV is related to the maximum electrochemical work by the Nernst equation:

$$\varepsilon_{cell} = \varepsilon_{cathode} - \varepsilon_{anode} = \frac{-\Delta G_{cell}}{n_e F} \tag{3.2}$$

From basic thermodynamics, for an ideal gas system we have:

$$\Delta G_{cell} = \Delta G_{cell}^{\circ} + \sum \nu_i RT \ln\left(\frac{p_i}{p_i^{\circ}}\right) \tag{3.3}$$

Therefore:

$$\varepsilon_{cell} = \varepsilon_{cell}^{\circ} - \frac{RT}{n_e F} \sum \nu_i \ln\left(\frac{p_i}{p_i^{\circ}}\right) \tag{3.4}$$

where n_e is the number of electrons transferred in the reaction and is 2 for the overall reaction indicated in Eq.(3.1)(c). F is Faraday constant and is equal to 9648 (A s mol^{-1}). υ_i and p_i represent the stoichiometric coefficient and the partial pressure of component i, ε represents the equilibrium potential, R, T, and ΔG represent the ideal gas constant, the absolute temperature, and the change in the Gibbs free energy. The superscript ° represent the standard conditions.

By allowing the electrons to flow from the anode to the cathode, ideally the Gibbs free energy change of the cell's overall reaction can be harvested. In reality however, the voltage of a cell drops as current is drawn from it, because of the irreversible effects inherent to non-equilibrium processes. The effects that reduce the voltage of a cell from its ideal value are called the electrochemical overpotential. There are three types of overpotentials associated with the operation of an SOFC: the activation, the ohmic, and the concentration overpotentials. The activation overpotential is caused by the energy barriers that the reacting species have to overcome in order for the reactions to proceed. The ohmic overpotentials are cause by the resistance against the flow of ions and the electrons in various components of the cell. Finally, the concentration overpotentials are caused by the concentration change of the reacting species in the vicinity of the reaction sites within the electrodes, due to their depletion or production by the electrochemical reactions.

The magnitudes of all the aforementioned overpotentials increase as the net rate of the electrochemical reactions increases, i.e. at higher cell currents. Therefore the voltage of a fuel cell drops further as the current load is increased. The most important measure of a fuel cell's performance is its voltage at various current loads, which is called the I-V performance curves. It basically indicates how much performance is lost at any given current load. One of the objectives of this work is to predict and obtain the performance curve of a TμSOFC; hence, all the phenomena affecting the performance of the cell should be accurately accounted for.

To model and estimate overpotentials in a TμSOFC, an understanding of the phenomena underlying its operation is essential. On the cathode side, oxygen diffuses from the bulk gas phase to the surface of the current collector, and then through the porous current collector to the reaction sites within the CFL. Within the CFL, according to Eq.(3.1)(b), oxygen reacts and is converted to oxygen ions (O^{2-}) by consuming electrons. The oxygen ions are transported to the

AFL through a dense layer of the O^{2-} permeable electrolyte layer. On the anode side, hydrogen diffuses from the bulk gas to the anode surface, then through the ACCL and the ASL to the AFL. Within the AFL, hydrogen reacts with the oxygen ions to produce electrons and water according to Eq.(3.1)(a). These electrons are collected to pass through an outer electric circuit, an electronic load, and return to the cathode to complete the cycle.

Simulating the performance of the TμSOFC requires the mathematical modeling of the physical phenomena occurring in the cell. These include models for the electrochemical reactions kinetics, the transport of the neutral and the charged species, and the transport of energy. The models describing transport consist of balance equations coupled with phenomenological mathematical expressions that relate the rate of transport to the appropriate driving forces. The model developed in this chapter deals with an experimental setup that is designed to retain isothermal conditions within the system, therefore heat transfer was ignored.

As indicated in Figure 2.4, a TμSOFC testing setup involves dramatically different length-scales. The challenge of multi-scale modeling, to incorporate phenomena of various length scales efficiently, is discussed further in the numerical solution section. The overall model is a set of highly nonlinear interdependent mathematical equations that must be simultaneously solved by an appropriate numerical scheme.

3.2.1 Modeling the porous electrodes

In an SOFC, electrochemical reactions occur within the porous electrodes at locations called the three phase boundaries (TPBs). At a TPB, the reacting species in the gas phase, and the ions and the electrons in the solid phases are all available. Physically, a TPB is a line in the three-dimensional space at which the gas phase, the electronic conductor solid phase, and the ionic conductor solid phase intersect. A simplified two dimensional schematic of composite electrodes is shown in Figure 3.1. Due to surface diffusion, the electrochemical reactions are not limited only to the TPB lines but the surfaces in proximity to them are also active.

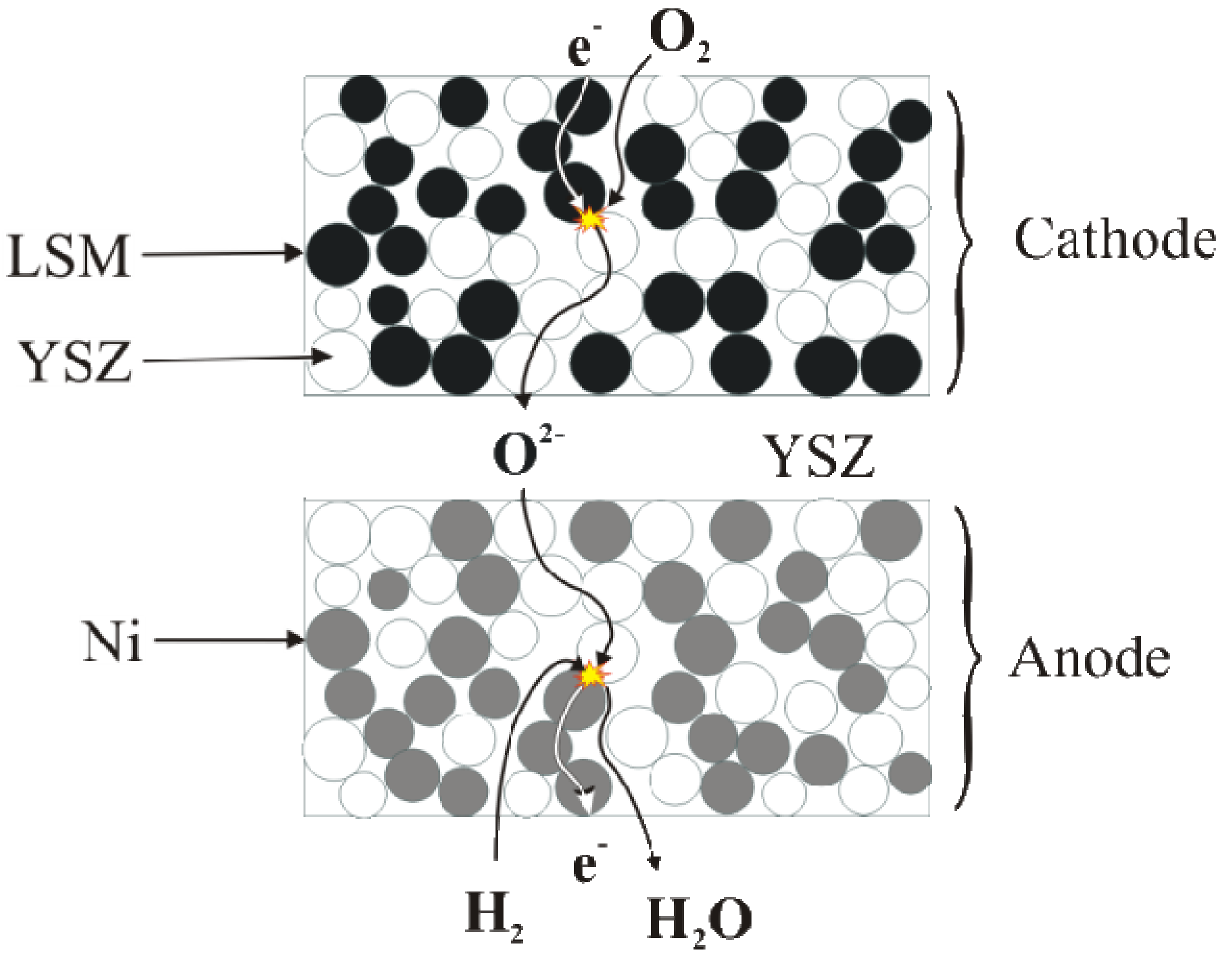

Figure 3.1. A schematic of an SOFC with composite electrodes.

In a composite porous electrode the TPBs are extended from the electrode/electrolyte interface to the electrode's volume, which enhances the electrode performance by providing more reaction sites. Note that only TPBs that consist of percolating particles participate in the electrochemical reactions. Percolating ionic conductor particles (YSZ in this case) are those that are connected to the electrolyte layer through a continuous path of YSZ particles. Similarly, the percolating electronic conductor particles are those that are connected to the current collector of their respective electrode through a continuous chain of electronic conductor particles. Therefore an active TPB is the intersection of the percolating ionic and the percolating electronic conducting phases, as they can host electrochemical reactions by providing or taking away ions and electrons. Non-percolating TPBs do not have any electrochemical function in an electrode. In a well designed composite electrode, among other factors, the percolation of particles is optimal.

Within the porous electrodes, where the electrochemical reactions occur, modeling the interaction of a gas phase and a solid phase is of critical importance. The most rigorous approach to model a porous electrode is to reconstruct the porous electrode theoretically (Abbaspour et al., 2006) or experimentally (Wilson et al., 2009; Wilson et al., 2006). The model equations are solved within each phase, with the appropriate boundary conditions. This approach yields a very detailed insight about the electrode performance. However, it requires extensive computational resources, and long execution times. Alternatively, the gas within the pores and the solid structure can each be homogenized into two superimposed continuous domains. The homogenized model of each phase includes the effects of the other phase in an averaged sense; the microscopic details are omitted in favor of the macroscopic characteristics of the porous medium. This approach is valid when the pore sizes are much smaller than the overall length scales of the domain, which is the case for the porous SOFC electrodes. The averaged equations for each phase can be developed through a rigorous mathematical manipulation of the transport equations (Vafai, 2005; Whitaker, 1999), or by a merely intuitive approach; nonetheless, the resulting equations often have a similar form. The resulting averaged equations are much simpler to solve to obtain quantities that are spatially continuous throughout the porous medium. In this work the electrodes were modeled by the latter approach; hence, the electrochemical reactions were modeled to occur within the volume of the electrodes, as it will be discussed further.

3.2.2 The electrochemical reactions kinetics

The rate of the electrochemical reactions occurring at the TPBs is closely related to the electric potential of its electronic and ionic conducting phases. An electric potential difference develops across the interface of the ionic and the electronic conducting particles in a TPB. According to the Nernst equation, this potential difference is directly related to the change in the Gibbs free energy of the half-reaction occurring at that electrode. The absolute values of the electrode potential (or $\Delta G^{\circ}_{half-rxn}$) cannot be determined. However, the electrode potential can be obtained relative to a reference electrode. In the electrochemical literature, the equilibrium electrode potentials for the reduction half-reactions are reported against a reference electrode, usually the hydrogen electrode at standard conditions. Therefore, according to the Nernst equation, expressions similar to Eqs. 3.2 to 3.4 can be written for the electrode potentials by assuming the electrode half-reaction in the reduction direction as the cathode, and the reference electrode as the anode.

As soon as the equilibrium of an electrode half-reaction is manipulated, for example by changing the electric potential difference between the ionic and electronic conductor, a net reaction starts occurring in a direction to return the electrode back to equilibrium. At this point, the electrochemical energy of the non-equilibrium electrochemical system can be harvested by means of the electrons passing through an external electric circuit. As it was mentioned earlier, the maximum energy deliverable by an electrochemical reaction would be equal to the change in the Gibbs free energy of the overall system, and that would be the case when the deviation from the equilibrium is infinitesimally small. However, in practice the system should generate a finite power; therefore some of the energy is lost due to the irreversibility of the non-equilibrium processes.

The more the electrochemical system deviates from its equilibrium, the faster the electrochemical reactions take place. Hence the electrochemical overpotential of the half-reaction, η_{act}, defined as the deviation of the potential of the electrode from its equilibrium potential, is a key concept in determining the electrochemical reactions rate:

$$\eta_{act} = V_{elec} - V_{ion} - \varepsilon_{electrode} \tag{3.5}$$

where $\varepsilon_{electrode}$ is the electrode's equilibrium potential. V_{elec} and V_{ion}, are the potentials of the electronic and the ionic conducting material respectively.

A mathematical relation can be developed for the rate of the electrochemical half-reactions as a function of the electrode overpotential, which is known as the Butler-Volmer equation:

$$i_{gen}^{TPB} = i_{\circ}^{TPB} \left(e^{(1-\alpha)\frac{n_e F}{RT}\eta_{act}} - \mathrm{e}^{(-\alpha \frac{n_e F}{RT}\eta_{act})} \right) \tag{3.6}$$

where i_{gen}^{TPB} is the rate of current generation per unit length of TPB, i.e. the rate of electrochemical reactions. $i_{\circ}^{TPB}$ is the exchange current density, α is the transfer coefficient, η is the activation overpotential, and n_e is the number of electrons transferred per reaction.

As the TPBs in reality are lines in space, the current generation in Eq.(3.6) is per unit length of the TPB. In our approach of homogenizing the porous electrode, the volumetric rate, $i_{\circ}$, is of interest which is defined as:

$$i_{\circ} = i_{\circ}^{TPB} \lambda_{TPB} \tag{3.7}$$

where λ_{TPB} is the active TPB length per unit volume of the composite electrode. Therefore the volumetric current generation, i_{gen}, is:

$$i_{gen} = i_{\circ} \left(\mathrm{e}^{(1-\alpha)\frac{n_e F}{RT}\eta_a} - \mathrm{e}^{-\alpha \frac{n_e F}{RT}\eta_a} \right) \tag{3.8}$$

For an electrochemical reaction occurring on a specific type of electrode, all the parameters appearing in Eq.(3.8), other than $i_{\circ}^{TPB}$, are relatively constant and can be found from the literature. $i_{\circ}^{TPB}$ can be affected by several factors such as the fabrication process, impurities, and such. λ_{TPB} is dependent on the microstructure of the electrode and is very sensitive to the fabrication process. Therefore the volumetric current density generation, $i_{\circ}$, can be regarded as the unknown kinetic constant, which encapsulates both the unknowns λ_{TPB} and $i_{\circ}^{TPB}$, and should be estimated for an electrode based on the experimental data.

Often a simplified version of the Butler-Volmer equation, called the Tafel equation, is used in the literature due to mathematical convenience:

$$\eta_a = \beta \ln\left(\frac{i_{gen}}{i_{\circ}} \right) \tag{3.9}$$

Clearly, unlike the Butler-Volmer equation, the Tafel equation is an explicit relation between the overpotential and the current generation. In this work however, we retain the full form of the Butler-Volmer equation to avoid any restriction that the simplifying assumption may impose.

It is worth noting that the above form of the Butler-Volmer equation is derived for a single step electrochemical reaction in which electrons are transferred all at once. In reality however, the overall half-reaction often occurs in multiple steps, which involves multiple intermediate reactions. For those cases the reaction kinetics are derived such that they account for all the intermediate steps. Therefore knowing the correct reaction mechanism is crucial for deriving a correct reaction rate expression. The resulting reaction rate expressions would be slightly different from the standard Butler-Volmer form. In our model, the mass transfer step from the bulk phase to the reaction sites are decoupled and are modeled separately, and the Butler-Volmer equation is calculated at local concentrations.

In this model, the anode and the cathode half-reactions are treated separately. In the following, the kinetics for each electrode will be discussed.

3.2.2.1 The anode reaction rate

At the anode, the hydrogen molecules react with the oxygen ions to produce water and electrons as in Eq.(3.1)(a). According to the Nernst equation, the anode equilibrium potential for the reduction reaction (in the reverse direction of Eq.(3.1)(a)) is:

$$\varepsilon_{An} = \varepsilon_{An}^{\circ} - \frac{RT}{2F}\ln\left(\frac{p_{H_2}}{p_{H_2O}}\right) \tag{3.10}$$

where ε_{An}° is the equilibrium potential of the anode electrode at the standard conditions. For convenience, the anode electrode at the standard conditions was assumed as the reference electrode, therefore ε_{An}° would be equal to zero:

$$\varepsilon_{An} = -\frac{RT}{2F}\ln\left(\frac{p_{H_2}}{p_{H_2O}}\right) \tag{3.11}$$

There are various mechanisms proposed for the oxidation of hydrogen reaction on a Ni/YSZ anode. A rate equation derived based on a detailed kinetic analysis (Zhu et al., 2005) is used here:

$$i_{gen,An} = i_{\circ,An}\left(\mathrm{e}^{\frac{1.5F}{RT}\eta_{An}} - \mathrm{e}^{-\frac{0.5F}{RT}\eta_{An}} \right) \tag{3.12}$$

$$i_{\circ,An} = i_{*,An} \frac{(p_{H_2} / p^*_{H_2})^{1/4} (p_{H_2O})^{3/4}}{1 + (p_{H_2} / p^*_{H_2})^{1/2}} \tag{3.13}$$

where $i_{gen,An}$ is the volumetric rate of electron generation within the anode. The exchange current density, $i_{\circ,An}$, is a function of the reacting components partial pressures, as shown in Eq.(3.13). Therefore, the kinetic constant to be determined is $i_{*,An}$. The parameter $p^*_{H_2}$ is calculated as:

$$p^*_{H_2} = 1.22 \times 10^8 T^{1/2}\, \mathrm{e}^{-\frac{88120}{RT}} \tag{3.14}$$

As before, the overpotential for the anode electrode is defined as:

$$\eta_{An} = V_{elec,An} - V_{ion,An} - \varepsilon_{An} \tag{3.15}$$

3.2.2.2 The cathode reaction rate

The oxygen molecules react on the cathode and are reduced to oxygen ions by consuming electrons, according to Eq.(3.1)(b). The equilibrium potential for the cathode is:

$$\varepsilon_{Ca} = \varepsilon^\circ_{Ca} - \frac{RT}{4F} \ln\left(\frac{1 \times 10^5}{p_{O_2}} \right) \tag{3.16}$$

Because the anode electrode at the standard conditions was selected as the reference electrode, the standard potential of the cathode would be equal to the equilibrium potential difference of a complete cell at the standard conditions:

$$\varepsilon_{Ca}^{\circ} = \frac{-\Delta G_{cell}^{\circ}}{2F} \tag{3.17}$$

There are several reaction mechanisms and rate expressions proposed for the oxygen reduction on an LSM/YSZ electrode. Again we take advantage of a rate expression derived based on a detailed kinetic study (Zhu et al., 2005):

$$i_{gen,Ca} = i_{\circ,Ca}\left(\mathrm{e}^{\frac{0.5F}{RT}\eta_{Ca}} - \mathrm{e}^{-\frac{0.5F}{RT}\eta_{Ca}}\right) \tag{3.18}$$

$$i_{\circ,Ca} = i_{*,Ca}\frac{(p_{O_2} / p_{O_2}^{*})^{1/4}}{1+(p_{O_2} / p_{O_2}^{*})^{1/2}} \tag{3.19}$$

where $i_{gen,ca}$ is the volumetric electron generation rate within the cathode; it is a negative value for the cathode, as electrons are consumed in a reduction reaction. The exchange current density of the cathode is a function of oxygen partial pressure, and the kinetic constant to be estimated is $i_{*,Ca}$. The parameter $p_{O_2}^{*}$ can be calculated as:

$$p_{O_2}^{*} = 4.96\times10^{13}\,\mathrm{e}^{-\frac{200000}{RT}} \tag{3.20}$$

And the activation overpotential for the cathode is defined as:

$$\eta_{Ca} = V_{elec,Ca} - V_{ion,Ca} - \varepsilon_{Ca} \tag{3.21}$$

3.2.3 The electric charge flow

To estimate the performance loss due to the electric resistance of the cell components, the electric current should be modeled. There are two types of electric currents in an SOFC, electron currents and oxygen ion currents (O^{2-}). Electrons flow through the electronic conductors which are nickel, LSM, and gold for the anode, the cathode, and the current collectors respectively. While YSZ is non-conducting to the electronic current, it conducts the oxygen ions in the electrolyte, the anode, and the cathode.

According to the Ohm's law, the electric currents are caused by the potential gradients within a conductor:

$$\mathbf{J}^q = -\sigma \nabla V \tag{3.22}$$

where $\mathbf{J}^q$ is a vector representing the flux of positive charges, and σ is the electric conductivity of the conductor.

The charge balance equation for each of the ionic and the electronic currents is:

$$\nabla \bullet \mathbf{J}^q = Q_{gen} \tag{3.23}$$

where the source term Q_{gen} is the generation of positive charges; it appears in the charge balance equation because of the electrode homogenization approach, where it is assumed that electrochemical reactions occur within the volume of the electrodes.

The charge balance equation should be solved for each type of conductor separately with the appropriate boundary conditions. In composite layers, i.e. ASL, AFL, and CFL, the ionic and the electronic currents are modeled as two superimposed domains with separate boundary conditions. These equations only affect each other through the current source term in their respective charge balance equation.

The electrolyte is a dense layer of pure YSZ which does not conduct electrons. YSZ transports oxygen ions through the oxygen ion defects in its crystal structure, i.e. the oxygen-ion vacancies.

The transport of oxygen ions in YSZ can be mathematically described similar to electron conduction:

$$\nabla \bullet (-\sigma_{io,electrolyte} \nabla V_{io,electrolyte}) = 0 \tag{3.24}$$

The source term is equal to zero within the electrolyte because there is no reaction occurring throughout the electrolyte.

For electronic current in the anode, AFL and ASL, Eq.(3.23) is written as:

$$\nabla \bullet (-\sigma^{eff}_{elec,An} \nabla V_{elec,An}) = -i_{gen,An} \tag{3.25}$$

$-i_{gen,An}$ is used as the source term because Q_{gen} on the right hand side of Eq.(3.23) should be a source of the positive charges, while $i_{gen,An}$ is the generation of negative charges.

For the ionic current in the anode, Eq.(3.23) is written as:

$$\nabla \bullet (-\sigma^{eff}_{io,An} \nabla V_{io,An}) = i_{gen,An} \tag{3.26}$$

For electrons being generated within the anode, negative charges (oxygen ions) disappear within the electrolyte. Therefore the rate of production of electrons, $i_{gen,An}$, has the same sign as the rate of generation of positive charges within the ionic conductor phase, as in Eq.(3.26).

The anode current collector is a porous gold layer, therefore there is no ionic current, and only the electronic current has to be modeled. Because no electrochemical reaction occurs within the current collector, the current source is zero:

$$\nabla \bullet (-\sigma^{eff}_{elec,An\,Cc} \nabla V_{elec,An\,Cc}) = 0 \tag{3.27}$$

Similar to the anode, the ionic and the electronic charge balance equations for the cathode are:

$$\nabla \bullet (-\sigma_{elec,Ca}^{eff} \nabla V_{elec,Ca}) = -i_{gen,Ca} \tag{3.28}$$

$$\nabla \bullet (-\sigma_{io,Ca}^{eff} \nabla V_{io,Ca}) = i_{gen,Ca} \tag{3.29}$$

And for the cathode current collector:

$$\nabla \bullet (-\sigma_{elec,Ca\,Cc}^{eff} \nabla V_{elec,Ca\,Cc}) = 0 \tag{3.30}$$

Because the electrodes are porous and composed of particles that only conduct either ionic or electronic charges, the overall conductivity of each phase is less than the intrinsic conductivity of a pure dense material. In addition, non-percolating particles do not contribute to current conduction. Therefore the effective conductivities should be used in the charge balance equation to take into account the reduced overall conductivity. The two major approaches for modeling conduction in a composite porous structure are the detailed modeling of the current flow in the structure, and the percolation theory (Costamagna et al., 2002). Naturally, the percolation theory is used here, as the detailed modeling of the porous microstructure was avoided.

According to the percolation theory, the probability of the particles of type *i* to be percolating, P_i, can be calculated as (Chan et al., 2004):

$$P_i = \left[1 - \left(\frac{4.236 - 6Z_{i-i}}{2.472}\right)^{2.5}\right]^{0.4} \tag{3.31}$$

P_i is the probability of the particles of the same type to form a complete chain, connecting two ends of the domain. Z_{i-i} is the average coordinate number of type *i* particles contacting the same type of particles in the random packing.

For a binary composite, where particles of type i and j are r_i and r_j in radius, $Z_{i\text{-}i}$ can be calculated as:

$$Z_{i-i} = \frac{6n_i}{[n_i + (1-n_i)(r_i / r_j)]} \tag{3.32}$$

There are two approaches used in the literature for calculating the effective conductivity based on the percolation theory. One is based on the percolation threshold of each type of conductor. Percolation threshold for the type i particles, n_c , is the critical fraction of those particles at which below that their network becomes non-percolating. Mathematically it is the particle fraction that makes P_i equal to zero, i.e. no chance for a complete chain of type i particles to form. According to this definition, there are two percolation thresholds, one for each type of conductor. When both types of particles are percolating, i.e. their fractions are above their percolation threshold, the effective conductivity of each type can be calculated as:

$$\sigma_i^{eff} = \gamma \frac{(n_i - n_c)^2}{(1-n_c)^2} \sigma_i \tag{3.33}$$

where σ_i and n_i are the intrinsic conductivity and the fraction of the type i particles, respectively. γ is a constant that takes into account the effect of necks between the particles on the overall conductivity. γ should be estimated based on the experimental data, however a value of 0.5 can be assumed when there is no data available (Chan and Xia, 2001).

The other approach to estimate the effective conductivity based on the percolation theory is to simply assume that the effective conductivity is directly proportional to the percolation probability (Chan et al., 2004):

$$\sigma_i^{eff} = (1-\phi) n_i P_i \sigma_i \tag{3.34}$$

where ϕ is the porosity of the composite electrode.

The effective conductivity estimations based on both Eqs. (3.33) and (3.34) is discussed and compared to the experimental values in the results section.

3.2.4 Mass transfer

The reactants are supplied to the fuel cell by the continuous flows of hydrogen on the anode side and air on the cathode side. On the anode side, hydrogen molecules are transferred from the bulk gas in the anode gas channel, through the porous anode, to the TBPs. The H_2O produced is transferred back from the TPBs to the gas channel. Similarly, the oxygen molecules are transported from the cathode gas channel to the TPBs throughout the porous cathode and react to produce oxygen ions. As a result of the electrochemical reactions, the concentration of oxygen, hydrogen, and H_2O in the vicinity of the TPBs are different from the bulk gas concentrations. The rates of reactions for the anode and the cathode electrodes are dependent on the concentration of species, as it can be noticed in the Butler-Volmer rate expressions. Therefore, to find the rate of current generation, the concentration of the species throughout their respective electrodes should be calculated by solving the mass transport and the mass balance equations. In this work, mass transport is modeled both within the porous electrode and within the gas channels. Again, modeling mass transfer in the porous electrodes is based the concept of homogenization of the transport equations for the gas phase. The resulting equations are then coupled with the mass transfer in the bulk gas via appropriate boundary conditions.

3.2.4.1 Mass transfer in gas channels

The mass balance equation for each component is:

$$\nabla \bullet (\mathbf{N}_i^m) = 0 \tag{3.35}$$

where $\mathbf{N}_i^m$ is the total mass flux of the component *i*. It is a result of two transport mechanisms, diffusion and convection; the total flux is conventionally decomposed into the diffusive and the convective flux terms:

$$\mathbf{N}_i^m = \mathbf{J}_i^m + \mathbf{c}_i^m \tag{3.36}$$

where $\mathbf{J}_i^m$ and $\mathbf{c}_i^m$ are the diffusive and the convective mass fluxes of the component *i*.

The convective flux results from the net flow of the bulk gas, and is related to its average velocity as:

$$\mathbf{c}_i^m = \rho \omega_i \mathbf{u} \tag{3.37}$$

where $\mathbf{u}$ and ρ are the bulk gas average mass velocity and mass density respectively. ω_i is the mass fraction of component i.

The gas flow within each channel was in the laminar regime. Therefore it was modeled by the continuity and the laminar flow momentum balance (compressible Navier-Stokes) equations.

$$\nabla \bullet (\rho \mathbf{u}) = 0 \tag{3.38}$$

$$\rho(\mathbf{u} \bullet \nabla)\mathbf{u} = \nabla \bullet [-p\mathbf{I} + \mu(\nabla \mathbf{u} + (\nabla \mathbf{u})^T) - \frac{2}{3}\mu(\nabla \bullet \mathbf{u})\mathbf{I}] \tag{3.39}$$

where μ is the dynamic viscosity. Dynamic viscosity for gas mixtures can be readily calculated based on the kinetic theory of gases, as explained in the appendix.

The diffusion of molecules in the gas phase has been studied comprehensively, and the two most well known models for diffusive mass transfer are the Fick's model and the Maxwell-Stefan model. The Fick's model is widely used because it is much simpler to solve, especially when an analytic solution is desired; however it has serious shortcomings for modeling more sophisticated diffusing systems where multiple components are present, and when driving forces are not limited to only concentration gradients. In contrast, the Maxwell-Stefan model has a more rigorous development, based on the balance of a generalized driving force and the friction forces between the diffusing molecules (Taylor and Krishna, 1993), or alternately based on irreversible thermodynamics (Curtiss and Bird, 1999). The Maxwell-Stefan approach can model diffusion in multi-component systems, and accounts for alternative driving forces for diffusion such as pressure and temperature gradients in addition to the conventional concentration gradients (Wesselingh and Krishna, 2000). According to the Maxwell-Stefan model, the diffusive mass flux of the component *i* in an ideal gas system, when only concentration and pressure driving forces are present, can be calculated as (Curtiss and Bird, 1999):

$$\mathbf{J}_i^m = -\rho\omega_i \sum_{j=1}^{n} D_{ij} (\nabla x_j + (x_j - \omega_j) \frac{\nabla P}{P}) \tag{3.40}$$

where ω_j and x_j are respectively the mass and the mole fraction of the component *i*, *P* is the total pressure of the gas, and D_{ij} is the binary diffusion coefficient between the components *i* and *j* ($D_{ii} = 0$).

The mass and mole fractions are not independent variables and are related as:

$$\omega_i = \frac{x_i M_i}{\sum_{j=1}^{n} x_j M_j} \tag{3.41}$$

For this work, the anode and the cathode side are both binary systems, hence:

$$x_2 = 1 - x_1 \tag{3.42}$$

By solving Eqs.(3.40)-(3.42), the mass transport in the gas channels can be modeled to obtain the concentration profile of each component.

It is worth mentioning that there are more sophisticated models proposed for multi-component mass transfer based on a comprehensive momentum balance of each component (Kerkhof and Geboers, 2005), however they are still under implementation and validation. Carefully designed fuel cell experiments would have a unique potential for studies on mutli-component transport especially in porous media due to two reasons; electrode potentials are dependent on concentration of species and can be accurately and conveniently measured. In addition, the amount of matter entering into the system can be accurately measured and manipulated by controlling the amount of current passing through it.

3.2.4.2 Mass transfer in porous electrodes

As the SOFC operates, the reacting components are transferred from the electrode/gas channel interface to the TPBs within the porous electrodes. Four mechanisms contribute to the overall mass transport in a porous electrode: free molecular diffusion, Knudsen diffusion, surface diffusion, and convective (viscous) transport. The Knudsen diffusion becomes significant when the mean free path travelled by the molecules is comparable to the pore dimensions; in that case the probability of the gas molecules hitting the solid walls of the porous medium becomes comparable to that of the gas molecules colliding each other. The convective transport, also known as the viscous or the Darcy flow, arises when pressure gradients exist within the porous medium. Surface diffusion plays a significant role in transport within the micro-pores – pores with a diameter smaller than 5 nm. The pore sizes in an SOFC electrode are significantly larger than 5 nm, therefore surface diffusion is ignored in this work. Surface diffusion was included by Shi et al., (2007), however it was not indicated whether it had a significant contribution to the overall transport or not. There are various approaches for coupling the four mechanisms of transport in the porous media, especially coupling the viscous flow with the rest (Keil, 1999; Noordman and Wesselingh, 2002), however it is still a matter of dispute (Kerkhof, 1996; Weber and Newman, 2005). In this work, it is assumed that the viscous flow acts parallel to the overall effect of the bulk and the Knudsen diffusion (Wood et al., 2002). Consequently, the total flux can be decoupled into the diffusive and the convective terms, similar to transport in the bulk gas.

Again, the concept of homogenization is employed to model the transport of gases within the porous electrodes. The components balance equation is:

$$\nabla \bullet (\mathbf{J}_i^m + \mathbf{c}_i^m) = R_i \tag{3.43}$$

Here $\mathbf{J}_i^m$ and $\mathbf{c}_i^m$ are the superficial diffusive and convective mass fluxes respectively. Note that the intrinsic velocity within the pores is higher than the superficial velocity. The use of the superficial fluxes instead of the pore fluxes simplifies the boundary conditions used at the electrode/gas interface. The volumetric source term, R_i,on the right hand side of Eq.(3.43) is the rate at which, due to the electrochemical reactions at the TPBs, component *i* is consumed or produced within the electrode. It can be related to the volumetric current generation according the stoichiometry of the electrode reaction. Every mole of electrons, one Faraday, is equivalent to 96485 coulombs of charge.

For the anode reaction, Eq.(3.1)(a), two electrons and one molecule of water are produced for every molecule of hydrogen consumed. Therefore the source terms are:

$$R_{H_2} = -\frac{i_{An}^{gen}}{2F} M_{H_2} \tag{3.44}$$

$$R_{H_2O} = \frac{i_{An}^{gen}}{2F} M_{H_2O} \tag{3.45}$$

Again, $i_{gen,An}$ is the rate of electron generation and is calculated according to the Butler-Volmer equation.

For the cathode reaction, Eq.(3.1)(b), four electrons are generated for each molecule of oxygen consumed:

$$R_{O_2} = -\frac{i_{Ca}^{gen}}{4F} M_{O_2} \tag{3.46}$$

Nitrogen does not participate in any reactions, therefore:

$$R_{N_2} = 0 \tag{3.47}$$

Within the current collectors R_i is zero for all the components because no reaction occurs there.

The convective mass transport in the porous medium is related to the average mass velocity of the gas:

$$\mathbf{c}_i^m = \rho \omega_i \mathbf{u} \tag{3.48}$$

Similar to the bulk gas, the velocity term is modeled by the continuity and the momentum balance equations. The averaged continuity equation keeps its original form. The averaged momentum equation however, after simplifications, turns into the much simpler form of the Darcy's law:

$$\nabla \bullet (\rho \mathbf{u}) = \dot{\mathrm{m}} \tag{3.49}$$

$$\mathbf{u} = -\frac{k}{\mu} \nabla p \tag{3.50}$$

where permeability, *k*, is a characteristic of the porous medium. $\mathbf{u}$ is the superficial velocity of the gas within the porous medium. The source term, $\dot{\mathrm{m}}$, is the rate at which mass is added or taken away from the gas phase due to electrochemical reactions. Permeability of an aggregated bed of spheres, at low Reynolds numbers, can be calculated based on the porosity of the packing according to the Kozeny-Carman equation (Krishna and Wesselingh, 1997):

$$\kappa = \frac{d_p^2 \varepsilon^3}{180(1-\varepsilon)^2} \tag{3.51}$$

The source term on the right hand side of the continuity equation, $\dot{\mathrm{m}}$, takes into account the net mass added to the gas phase within the pores due to the electrochemical reactions. Only oxygen reacts on the cathode and therefore the overall source term only includes the disappearance of oxygen:

$$\dot{\mathrm{m}}_{Ca} = \mathrm{R}_{Ca} = -\frac{i_{Ca}^{gen}}{4F} M_{O_2} \tag{3.52}$$

For each molecule of hydrogen consumed within the anode, one molecule of water is produced. Therefore the overall source term is:

$$\dot{\mathrm{m}}_{An} = R_{H_2O} + R_{H_2} = -\frac{i_{An}^{gen}}{2F} (M_{H_2} - M_{H_2O}) \tag{3.53}$$

There are several approaches for modeling diffusion in a porous medium. The volume averaged Fick model is not be the most accurate model, due to the inherent limitations of the Fick model itself. Another approach is to use the MS model with the effective diffusivities, to account for the effect the porous medium on diffusion. The more accurate model is the dusty-gas model (DGM), which elaborately accounts for the solid wall effects on the transport of gaseous components within a porous medium (Krishna and Wesselingh, 1997; Mason and Malinauskas, 1983). Mason manipulated the MS model into the DGM by assuming the solid structure as giant stagnant ‘dust’ molecules. The DGM has been extensively validated against the experimental data (Ho and Webb, 2006). For the SOFC electrodes, it has been shown that the Fick’s model is not a good approximation for the DG model, while the MS model without any general rule in some cases would be satisfactory (Suwanwarangkul et al., 2003). The DGM was used for modeling the diffusive mass transport in porous electrodes for this work.

The DGM for a system of ideal gases is (Krishna and Wesselingh, 1997):

$$-\frac{\nabla p_i}{RT}=\sum_{j=1}^{n}\frac{x_j\mathbf{J}_i-x_i\mathbf{J}_j}{D_{ij}^{e}}+\frac{\mathbf{J}_i}{D_{ik}^{e}} \tag{3.54}$$

where $\mathbf{J}_i$ is the molar diffusive flux of component *i*, and $p_i=x_iP$. D_{ik} is the effective Knudsen diffusivity and can be calculated based on the kinetic theory of gases:

$$D_{ik}=\frac{2}{3}r_o\sqrt{\frac{8RT}{\pi M_i}} \tag{3.55}$$

Because the pores within the electrodes are not straight cylinders, diffusion coefficients should be corrected to account for the tortuous path that the molecules diffuse through:

$$D_{ij}^{e}=\frac{\varepsilon}{\tau}D_{ij} \tag{3.56}$$

Tortuosity, τ, and porosity, ε, depend on the microstructure of the porous medium. It can be estimated for an aggregated bed of spheres as (Duplessis and Masliyah, 1988):

$$\tau = (1-(1-\varepsilon)^{2/3})/\varepsilon \tag{3.57}$$

The DGM for a binary ideal-gas system reduces to:

$$\mathbf{J}_1^m = -D\nabla(x_1P) \quad D = \frac{M_1}{RT}\left(\frac{1}{D_{12}^e}+\frac{1}{D_{1k}^e}\right)^{-1} \tag{3.58}$$

This is very similar to the Fick's law, however it includes the effect of Knudsen diffusion. One can conclude from Eq.(3.58) that the appropriate driving force for binary diffusion in a porous medium is the partial pressure of components ($p_i = x_iP$). That driving force includes the effect of pressure gradients on diffusion in addition to the concentration gradients.

3.3 Model implementation and solution

The geometry of the model included the furnace channel and the fuel cell within it. Due to the inherent symmetry of the cylindrical geometries involved, a solution for the real system could be obtained by solving the model equations on a 2-dimensional axi-symmetric domain, see Figure 3.2. This simplification did not imply any assumptions, and was exact for the three dimensional domain. The axi-symmetric geometry was reproduced in Comsol, a finite element solver, and the equations with appropriate boundary conditions were implemented and numerically solved.

3.3.1 Domain equations and boundary conditions

The charge flow equations were only implemented for the active length of the cell. The electronic current equation on the cathode side was implemented on the CFL and the CCCL domains. A Dirichlet boundary condition was used on the cross edge of the CCCL close to the fuel cell's tip, by specifying the voltage. This corresponded to the cathode current collector wire being wrapped on the top edge of the CCCL. The voltage on the boundary was specified as the desired cell potential (V_{cell}^*), which for a fuel cell could take a value between zero and the OCV. At the CFL/CCCL interface, a continuity boundary condition was used. A continuity condition for the electric current equations implies the continuity of the potential and the current passing across the boundary:

$$\mathbf{n}\bullet\left\{\mathbf{J}^q\right\}_1 = -\mathbf{n}\bullet\left\{\mathbf{J}^q\right\}_2 \tag{3.59}$$

$$\left\{V\right\}_1 = \left\{V\right\}_2 \tag{3.60}$$

where **n** is the unity vector normal the boundary.

The remaining boundaries were set as insulation, i.e. a zero flux condition:

$$\mathbf{n}\bullet\mathbf{J}^q = 0 \tag{3.61}$$

The electronic current equation on the anode side was implemented on the ACCL, the ASL, and the AFL. In reality, the current was carried by all those layers to the open end of the cell, beyond the active length. However, only the portion covering the active length was modeled, and the voltage boundary condition was set to zero at the cross boundary of the ACCL close to the cell's open end. The voltage drop along the cell, from the active length to the open end, was calculated analytically assuming parallel conduction in three cylindrical shells:

$$R_{leg,i} = \frac{L_{leg}}{2\pi d_i \sigma_{eff,i}} \quad i = \{ACCL, AFL, ASL\} \tag{3.62}$$

$$R_{leg} = \left(\frac{1}{R_{leg,ACCL}} + \frac{1}{R_{leg,ASL}} + \frac{1}{R_{leg,AFL}} \right)^{-1} \tag{3.63}$$

This way the unnecessary calculation of the current flow in the current collector was avoided; therefore the size of the computational domain was noticeably reduced, without implying any limiting assumption. After obtaining the numerical solution, the cell voltage defined as the boundary condition, V_{cell}^{*}, was modified to obtain the actual cell voltage that accounted for the voltage drop in the omitted part:

$$V_{cell} = V_{cell}^{*} - I_{cell} R_{leg} \tag{3.64}$$

Therefore, V_{cell} was comparable to the experimentally measured voltage across the cell wires.

Similar to the cathode, the continuity condition was used at the ACCL/ASL, and the ASL/AFL interfaces; the remaining boundaries were set as insulating boundaries.

The ionic current equation was implemented on the ASL, the AFL, the electrolyte, and the CFL. The continuity boundary condition was employed at their interfaces, and insulation condition for the remaining boundaries. The ionic current was the only domain that has no overall outflux of charges along its boundaries, among the three charge balance equations; all the ionic current was produced in the volume of the cathode was consumed within the volume of the anode domain.

Special attention must be paid to the fact that the use of continuity boundary condition for the flux and the potential variables across domains with different porosity was appropriate only because superficial fluxes and intrinsic (non-superficial) electric potentials were used in all the charge flow equations.

For the anode mass transfer model, Dirichlet boundary condition was used at the inlet of the injector tube by specifying the inlet composition of hydrogen. Similarly, the composition of air was specified at the inlet boundary of the air channel. Pure convective flux was assumed as the outlet boundary condition for the mass transfer models, by assuming zero diffusive flux:

$$\mathbf{n}\bullet\mathbf{J}^{m} = 0 \tag{3.65}$$

This boundary condition was valid because the convective velocity normal to the outlet boundary was much higher than the diffusive velocity.

A continuity condition of the component fraction and their mass fluxes was assumed across the gas channel/ porous electrode interfaces:

$$\mathbf{n}\bullet\left\{\mathbf{N}_i^{m*}\right\}_{porous\ electrode} = -\mathbf{n}\bullet\left\{\mathbf{N}_i^{m}\right\}_{gas\ channel} \tag{3.66}$$

$$\left\{x_i\right\}_{porous\ electrode} = \left\{x_i\right\}_{gas\ channel} \tag{3.67}$$

These conditions were valid because intrinsic concentration (concentration of the gas within the pores) and superficial mass fluxes were used in the porous media mass transfer equations.

Continuity boundary condition was implemented at the interfaces of the porous layers with each other, again valid for domains with different porosities as explained above. A zero flux was employed for the remaining boundaries.

For the momentum balance equations, the inlet velocity was specified as the fully developed laminar profile in a tube – a parabolic function:

$$u = 2u_{avg}\left[1-(r/R)^2\right] \tag{3.68}$$

where u is the normal velocity across the boundary, r is the radial position from the center of the tube, and u_{avg} is the average velocity of the gas in the tube (volumetric flowrate divided by the cross-sectional area of the tube).

The coupling of the momentum balance equations at the porous electrode / gas-channel interfaces was a more delicate issue. The differential equations for the momentum balance in the gas channel (the Navier-Stokes equation) is of second order in terms of velocity, but first order within the porous medium (Darcy's law). The velocity term in Darcy's law is the superficial velocity and the pressure is the intrinsic pressure of the gas within pores. For Darcy's law on the porous electrode side, the normal velocity at the gas-channel / porous electrode interface was equated to the normal velocity obtained from the Navier-Stokes equation:

$$\mathbf{n} \bullet \{\mathbf{u}\}_{porous\ electrode} = -\mathbf{n} \bullet \{\mathbf{u}\}_{gas\ channel} \tag{3.69}$$

This condition ensured the conservation of the overall mass flow across the porous medium and the gas channel. For the Navier-Stokes equation on the gas channel side, the normal stress at the boundary was equated to the pressure stress obtained from the Darcy's Law, while the tangential velocity was set to zero:

$$\mathbf{n} \bullet [-p\mathbf{I} + \mu(\nabla\mathbf{u} + (\nabla\mathbf{u})^T) - \frac{2}{3}\mu(\nabla \bullet \mathbf{u})\mathbf{I}] = -\{p\}_{porous\ electrode}\,\mathbf{n} \tag{3.70}$$

$$\mathbf{t} \bullet \mathbf{u} = 0 \tag{3.71}$$

where **t** is the unity vector tangent to the boundary.

The combination of the boundary conditions explained above did not necessarily imply that the tangential Darcy velocity across the boundary was equal to zero; while on the Navier-Stokes side it was forced to be zero. However, this inconsistency was minor because the tangential velocity at the intersection was very small, as it was later confirmed by the simulation results. Most importantly, these conditions conserved the mass exchanged across the electrode / gas-channel boundaries, and represented the physical reality of the system to a satisfactory degree.

3.3.2 Model Parameters

The physical properties appearing in the model equations were found either directly from the literature or were estimated based on the available mathematical correlations. The gas viscosity and density were calculated locally as functions of pressure, temperature and composition of the gas. Details of these calculations are presented in the appendix.

The properties related to the porous medium are presented in Table 3.1. The porosities were measured experimentally based on Archimedes principle, and were confirmed based on SEM image analysis. The pore size distribution and the permeability of the AFL and the ASL were measured by gas porometry. The permeability of the AFL and ASL were measured to be from 1e-14 m^2 to 1e-15 m^2 for the samples tested, about an order of magnitude higher than the theoretical values of ~1e-16 calculated from Eq.(3.51). This can indicate the effective use of pore former during fabrication, as well as a suitable sintering program which enhanced the permeability of the porous electrodes. The higher permeability of the reduced AFL and ASL samples could as well be due to the shrinkage of the nickel oxide particles after their reduction to nickel.

Table 3.1. The physical properties of the porous electrodes.

Parameter	Theoretical	Experimental	Used in the Model
permeability	5e-16, Eq.(3.51)	1e-14 to 1e-15	1e-14
$\log(\sigma_{elec,AFL}^{eff})$	5.07, Eq.(3.33) 5.90, Eq.(3.34)	3.84 ± 0.22	3.84
$\log(\sigma_{elec,ASL}^{eff})$	5.86, Eq.(3.33)	1.56 ± 0.40	1.56
$\log(\sigma_{elec,CFL}^{eff})$	3.65, Eq.(3.34)	2.39 ± 0.10	2.39
$\log(\sigma_{io,CFL}^{eff})$	-0.08, Eq.(3.34)	-	-0.11
$\log(\sigma_{io,AFL}^{eff})$,	-1.10, Eq.(3.33) -0.11, Eq.(3.34)	-	-0.11
$\log(\sigma_{io,ASL}^{eff})$	-0.19, Eq.(3.34)		-0.19
Porosity ASL, ACCL, CCCL	-	~ 0.4	0.4
Porosity AFL, CFL	-	~ 0.3	0.3

It was found that the effective conductivities calculated based on the percolation theory were significantly different from the experimental values, especially for the ASL. Eq.(3.33) could not be used for the ASL, because the composite was not within the percolation threshold of both the ionic and the electronic conducting particles. However, assuming percolation probability of 1 for Ni, a value of 0.2 was obtained for the ratio of the effective to intrinsic conductivity, based on Eq.(3.34). This value is drastically higher than the ~2e-5 value determined experimentally. It was also observed that the effective conductivity of the ASL varied significantly among the samples, and changed even for the same sample with time as well as at different testing cycles. The ASL effective conductivity values obtained experimentally were not normal for a Ni/YSZ composite. This could be due to agglomeration of nickel particles at high temperatures which is a well know phenomenon for SOFC electrodes. Agglomeration can influence the connectivity of particles and consequently the effective conductivity. In addition, the influence of the manufacturing technique, EPD, on the arrangement of the particles in the solid skeleton may have influenced the effective conductivity. The arrangement of particles can significantly influence the percolation of conductive chains. The experimental effective conductivities were used in the model for the values that were measured. The experimental results and more discussions on the effective conductivity of the anode and the cathode is presented in Chapter 6.

The main unknown parameters for the fuel cell were the kinetic constants of the anode and cathode reactions, namely $i_{*,Ca}$ and $i_{*,An}$. As it will be discussed further, a nonlinear least squares algorithm was used to tune these parameters to obtain simulations consistent with the experimental data.

3.3.3 Domain discretization

To solve the model equations numerically, the domain had to be discretized into elements by a numerical mesh. Length scales with several orders of magnitude difference were involved in the geometries modeled, the 5e-6 m thick electrolyte layer compared to the 7e-2 m long furnace tube, which made the meshing challenging. All the electrochemical phenomena occurred within the thickness of the electrodes; therefore resolving the large gradients across the electrode layer required a finer mesh. However that mesh size was unnecessarily fine for the gas channels and along the active length; using the same mesh size for the whole domain was computationally too expensive. An unstructured mesh was initially used, which was fine across but skewed along the electrodes, and which rapidly expanded within the gas channels. However, the required expansion ratio and the skewedness, introduced significant numerical errors to the FEM scheme, and severed the stability and the convergence behavior of the numerical solver. Therefore a skewed structured mesh was employed as the best option; see Figure 3.2.

The structured mesh was fine enough in the direction of the large gradients i.e. across the electrodes, but rather coarse along the gas channels. The mesh boundaries being aligned with the fluxes to be solved for (mass, momentum, charge), had the advantage of lower numerical error, and therefore required fewer nodes for the same accuracy. Therefore, the resulting mesh was optimized in terms of the computational requirements (time and memory), accuracy, and convergence properties. This is clearly indicated in Figure 3.3: the time required for solving the model on the finest structured mesh was less than half of that on an unstructured mesh, while the error was at least an order of magnitude smaller on the structured mesh.

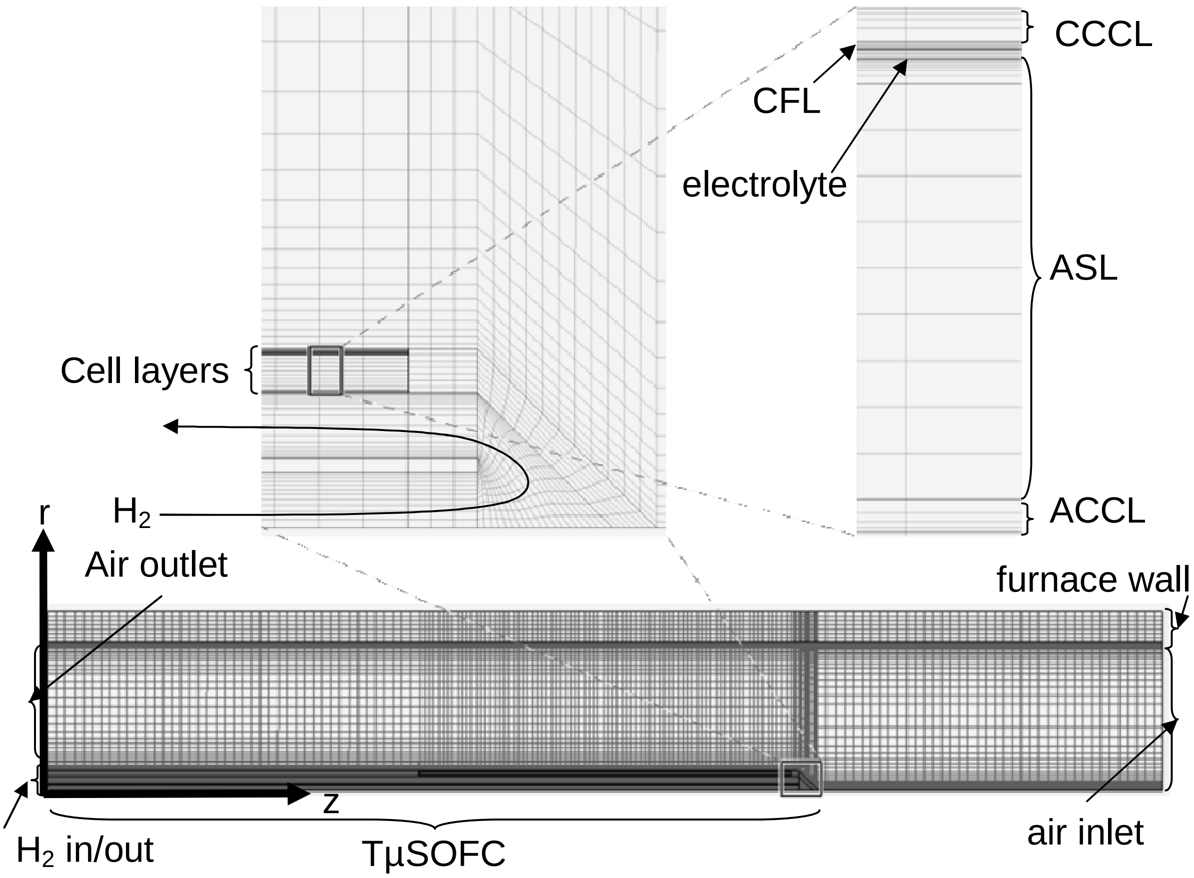

Figure 3.2. The structured mesh used to discretize the computational domain.

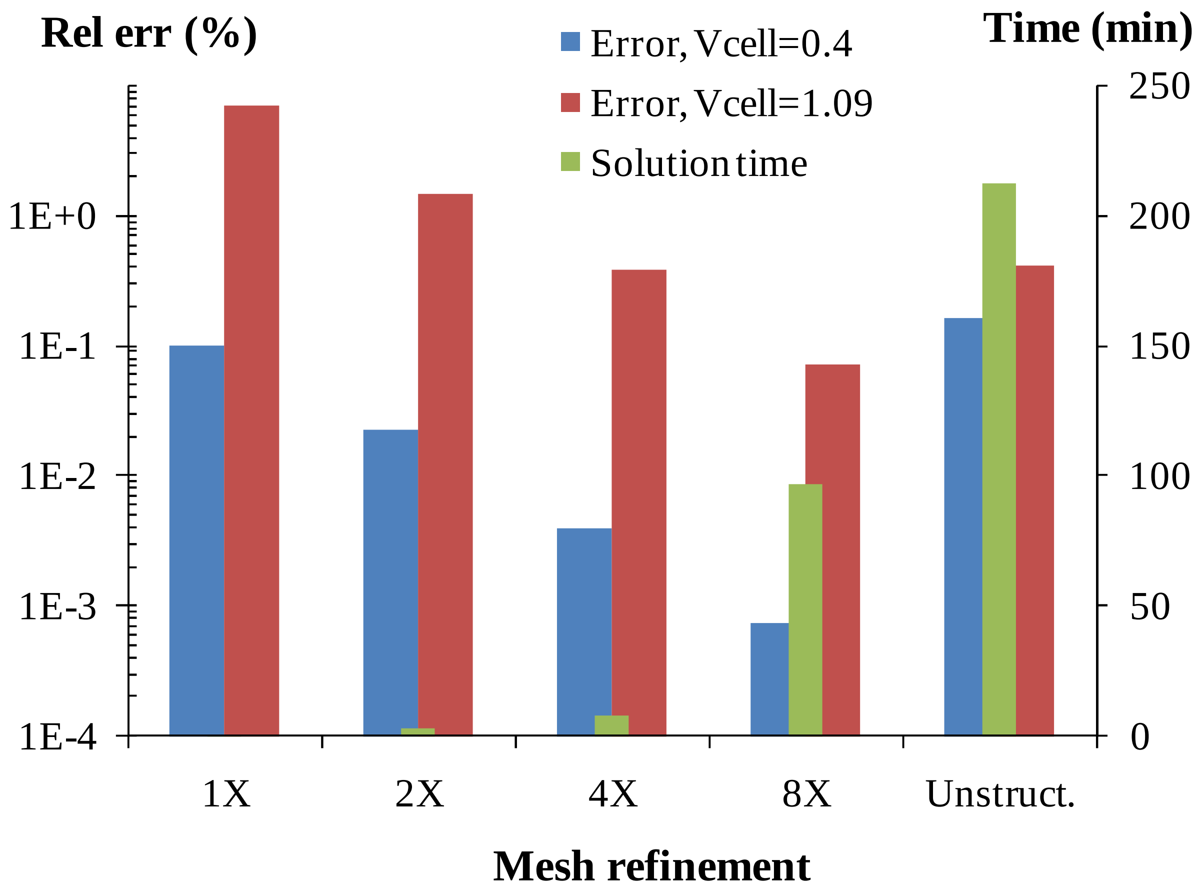

Figure 3.3. The effect of mesh size on the final solution obtained for the model.

3.3.4 Numerical solution scheme and initial solution

The final model consisted of a set of 9 interdependent partial differential equations. The solution was approximated by second-order Lagrangian polynomials on the numerical grid, except for pressure which a first-order Lagrangian polynomial was used. The resulting system of equations was solved by a nonlinear gradient based iterative solver (Newton) - which used a direct solver, UMFPACK, to solve the linearized system of equations. Numerical computations were performed on 12 Intel Xenon E5540 2.53GHz 64-bit CPUs which had access to 12GB of RAM.

The convergence to the final solution was challenging because of the nonlinearity of the equations involved. The initial solution was found to be fundamental to a stable convergence and the time required for it. For the hydrogen diffuser tube, the initial solution was chosen as the analytical parabolic velocity distribution. A similar concept was used for the air side; although the final solution in the air channel was not expected to be parabolic due to the presence of the fuel cell in the middle of the furnace. The initial solution for the concentrations on the air side and the fuel side were set equal to their respective inlet concentrations. The initial solution for the electronic potential of the anode side was set to zero. The initial solution for the ionic potentials was set to zero within the anode, the cathode and the electrolyte layers. The potential of the electronic conductor on the cathode side was set to the Nernst potential calculated for the cell inlet conditions. These initial solutions noticeably enhanced the convergence time and stability.

Even with the suitable initial conditions, it was found that convergence was still not guaranteed for all parameter values. This was especially problematic for the kinetic constants optimization algorithm, as a guaranteed convergence was essential. Therefore a segregated solution approach was adopted: the electric current equations were solved while the variables for the concentration and flow were kept constant at their initial solution values. The solution obtained was then used as an initial solution for solving all the equation simultaneously. This approach guaranteed convergence for a wide range of input parameter.

3.3.5 Numerical convergence and consistency

To ensure the numerical accuracy of simulation results, the sensitivity of the solution to mesh size was analyzed. The model equations were solved on a base case structured mesh. Then the mesh was systematically refined by adding nodes in the middle of the original nodes; hence halving the mesh size. This process was continued to obtain finer and finer meshes. The model was numerically solved for a cell voltage of 0.4 and 1.09 volts for each case - the range obtained experimentally. The main variable of interest, the current generated by the cell was calculated, and the values are shown in Figure 3.3; the case of an unstructured mesh is also included to compare it with the structured mesh results. The relative error was calculated for each case in comparison to the finest mesh case of 16X resolution. It is clear from Figure 3.3 that the relative error for a cell voltage of 0.4 V was smaller than 1.09 V. It was concluded that the 4X case was suitable enough for the purpose of this study, as the relative error for both voltages were less than 0.5%. The convergence error decreases monotonically, as the mesh was systematically refined. The discretization error, ΔY, which results from numerically solving the equations on a mesh, is a function of mesh spacing, ΔX, and can be approximated as $\Delta Y \sim (\Delta X)^{OC}$, where OC is the order of convergence. For a mesh independent solution, the order of convergence becomes close to the order of polynomials used in the numerical scheme. The order of convergence was estimated to be 2.02 and 2.00 based on the cell voltages of 1.09 and 0.4 volts. These values were close to the second order polynomials used in the FEM scheme; therefore the solution was indeed mesh independent.

Figure 3.3 clearly indicates the superiority of the structured mesh: the 4X mesh case, which was selected for the final simulation, had a convergence time 25 times less than the unstructured mesh, while having a smaller relative error.

To assess the numerical consistency of the simulation results, the overall species balance around the boundaries of the system was investigated. The inlet to the system was air and humidified hydrogen. The outlet was oxygen depleted air. The depleted oxygen, by combining with the hydrogen on the anode, had appeared as gaseous water in the anode exhaust stream. From the numerical point of view, the equations solved for the anode and the cathode sides were completely separate, connected only through the current source terms appeared in the charge balance equations. Therefore the oxygen atoms entered into the model as the boundary conditions, were transported by diffusion and convection to the CFL, numerically disappeared into the ionic conduction model, conducted to the anode side to numerically reappear within the anode gas phase, and from there they were transported through the porous electrode to the bulk gas and finally to the fuel outlet. In a numerical sense, values calculated at the outlet accumulated all the errors caused by the numerical solution scheme. Hence the consistent overall mass balance shown in Table 3.2 indicates that the numerical scheme was conservative and that the model was appropriately implemented.

Table 3.2. The overall elemental balance around the boundaries of the simulated TμSOFC.

Vcell=0.4 V	H_2	H_2O	O_2	H	O
In (mole/s)	3.54E-05	6.39E-05	1.48E-06	7.3825E-05	1.2928E-4
Out (mole/s)	2.43E-05	5.84E-05	1.25E-05	7.3826E-05	1.2931E-4
Difference				0.0014%	0.0191%

3.4 Experimental validation

The unknown parameters of the model were estimated based on the experimental data. Then the simulation results were examined to validate the ability of the model to describe and predict the physical reality of the system.

3.4.1 OCV dependence on hydrogen flowrate

It was observed experimentally that the cell OCV increased by changing the flowrate of hydrogen from 20 mL/s to 400 mL/s, as shown in Table 3.3. The model however did not predict this phenomenon. Although the model predicted the increase in the total pressure of the anode side at the higher flowrates, it did not predict an increase in the OCV. This is because for every mole of water vapor produced, equal number of hydrogen molecules are consumed; therefore according to the Nernst equation for the anode electrode, Eq.(3.11), OCV does not change with the total pressure, at constant concentration. In other words, at constant concentration ΔG_{cell} is not at all dependent on the total pressure of the anode gas mixture.

Table 3.3. Open circuit voltage at various hydrogen flowrates, and the corrected values.

Hydrogen flowrate (mL/sec)	OCV (experimental)	OCV(simulation)	H_2 mole fraction (modified)	OCV (refined simulation)
400	1.119652	1.095499	0.975885	1.119663
50	1.096697	1.095477	0.961001	1.096697
20	1.091864	1.095481	0.956885	1.091863

The discrepancy between the experimental and the simulation results can be explained by considering the effect of the hydrogen flowrate on the inlet concentration, in two ways. First, the bubbler may not saturate the hydrogen stream at higher flowrates because of the shorter residence time for the gas. Second, the bubbler temperature may decrease by increasing the flowrate of hydrogen. Note that, a change in the bubbler temperature from 30°C to 20°C can change the saturation mole fraction of hydrogen from 0.96 to 0.99. To ensure the consistency of the model with the experimental, the mole fraction of hydrogen was back calculated from the OCV values, hence using the fuel cell as a concentration sensor. The inlet concentration of hydrogen in the model was then modified accordingly, as shown in Table 3.3. Accurate OCV values were important because, as it will be discussed in the next section, the experimental data corresponding to very small current levels, i.e. small overpotentials, were used for estimating the unknown parameters. When overpotentials are small, small errors in OCV predictions introduce large relative errors, and compromise the accuracy of the predicted parameters.

3.4.2 Parameter estimation

The main parameters that had to be estimated were the current density generation of the cathode and the anode ($i_{*,Ca}$ and $i_{*,An}$). In addition, it was decided to estimate the effective conductivity of the anode support layer, because of the large variations observed in the effective electronic conductivity measured experimentally for several anode support samples. Nonetheless, it was kept in mind that the addition of an extra fitting parameter could result in a better numerical fit of the experimental results, without a physical significance. To find these parameters, a nonlinear parameter estimation procedure was employed in which the mean square difference of the model predictions and the experimental data were minimized at five points. The experimental data points were selected at very small currents, where the activation characteristics of the electrode would be the most distinct, relative to the effect of the ohmic and concentration overpotentials. The five points selected for fitting were evenly spaced from 4 to 20 mA, corresponding to experimental cell voltages ranging from 1.093 V to 1.081 V. The zero current point (OCV) was not used as it did not add any information about the activation parameters intended to be estimated, but it was assured that the OCV values predicted by the model were consistent with experimental data as explained earlier. The initial value of the optimization parameters for $i_{*,Ca}$, $i_{*,An}$, σ_{ASL}^{eff} were selected to be 1e8, 1e8 and 16.9 respectively. Table 3.4 shows results of parameter optimization.

Table 3.4. The optimized parameters based on the experimental I-V data.

Parameter	fitted	Other estimates
$i_{*,An}$ (A m^{-3})	2.64e9	3.23e9 (Shi et al., 2007)
$i_{*,Ca}$ (A m^{-3})	8.61e8	6.45e8 (Shi et al., 2007)
$Log(\sigma_{ASL}^{eff})$	1.08	$\log(\sigma) = 1.56 \pm 0.40$ (experimental)

To verify the numerical convergence of the estimated parameters, different initial guess values were tried. It was observed that values for $i_{*,Ca}$ and σ_{ASL}^{eff} remained essentially independent of the initial guess. However, the anode reaction constant, $i_{*,An}$, was dependent on the initial guess, and varied from ~1e9 up to ~1e13. As it will be discussed further, this was due to the very high activity of the anode catalyst which made the activation overpotential of the anode insignificant. This in turn prohibited an accurate estimation of $i_{*,An}$. In other words, in the context of this model and the TμSOFC under study, $i_{*,An}$ was masked and not readily identifiable. In fact, another group (Soderberg) also found it challenging to characterize the electrochemical performance of the anode, equivalent to $i_{*,An}$. Due to the high anode activity, measurements of its performance were significantly influenced by experimental errors. The estimated parameters for both the anode and the cathode ($i_{\circ,An}$ and $i_{\circ,Ca}$) were consistent with the values reported in the literature; see Table 3.4. The additional fitting parameter, σ_{ASL}^{eff}, was also consistent with the experimental measurements conducted separately for the ASL samples, as explained in Chapter 6.

3.4.3 Performance curves

The base case used for the fitting procedure was for the cell at 800°C with hydrogen and air flowrates of 50 mL/s and 500 mL/s respectively. At each cell voltage, the current generated by the cell was calculated from the integral of the volumetric current source term within the CFL:

$$I_{cell} = \int_{CFL} i_{gen,Ca} \mathrm{dv} \tag{3.72}$$

Figure 3.4 shows how the experimental and simulation performance curves compare. Note that only a small portion of the experimental curve was used for parameter estimation, and the rest was predicted by the model. Therefore the consistency of these two curves by itself was a model-validation measure.

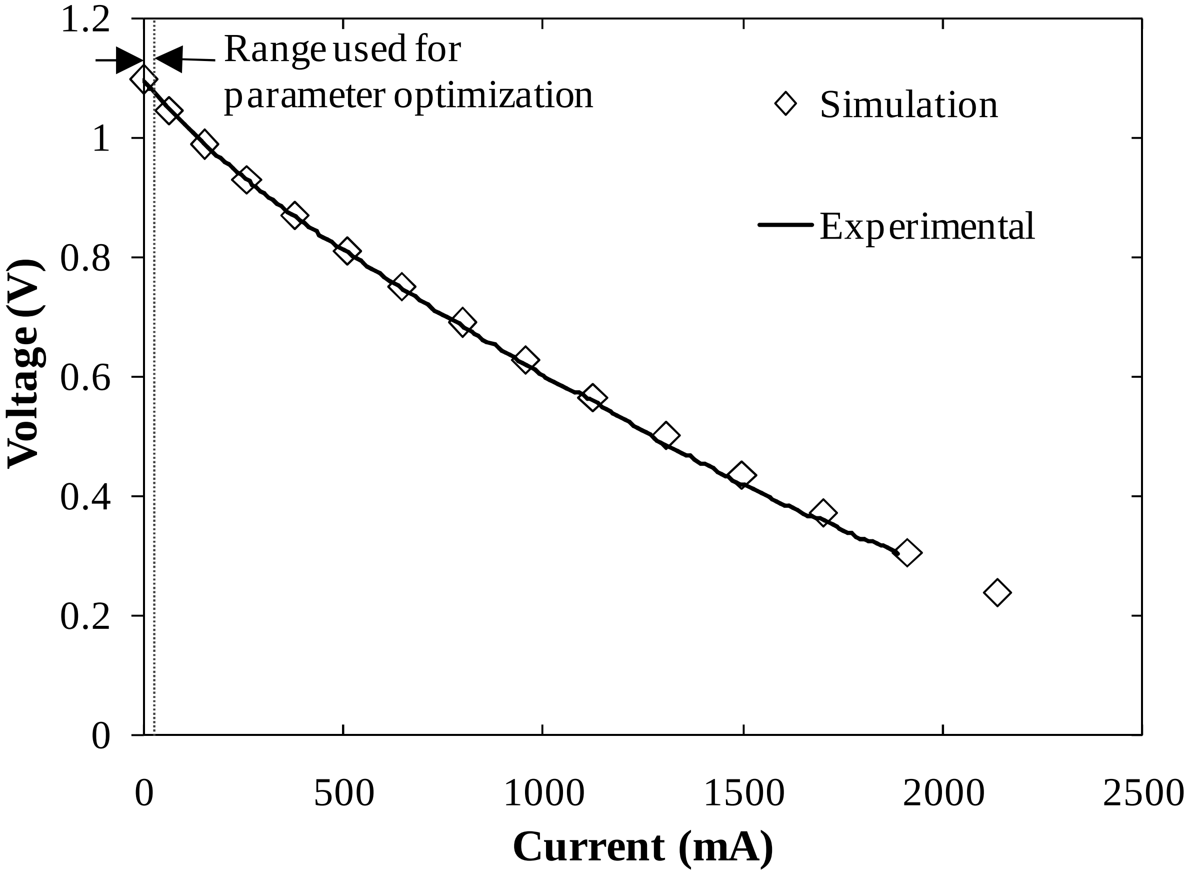

Figure 3.4. The experimental and the simulated performance curves for the base case.

Figure 3.5 shows the performance curves at two different flowrates of hydrogen. The simulation curves are predictions based on the parameters estimated for the base case. The consistency between the experimental and simulation results is an indicator of the proper modeling of the mass transport on the anode side. It is worth mentioning that to obtain the experimental data for the 20 mL.s^{-1} case, an accurate control and measurement of the hydrogen flowrate was critical. The shape of the curve, especially the sudden drop of the voltage at higher current levels was very sensitive to the flowrate of hydrogen. Initially a 500 mL/s mass flow controller was used which did not perform a satisfactory control at low flowrates. The problem was resolved by using a 50 mL/s mass flow controller. The use of a controller which was capable of controlling the mass flowrate, not just volumetric flowrate, was also an important factor to obtain accurate data; the controller measured and compensated for the pressure of the gas.

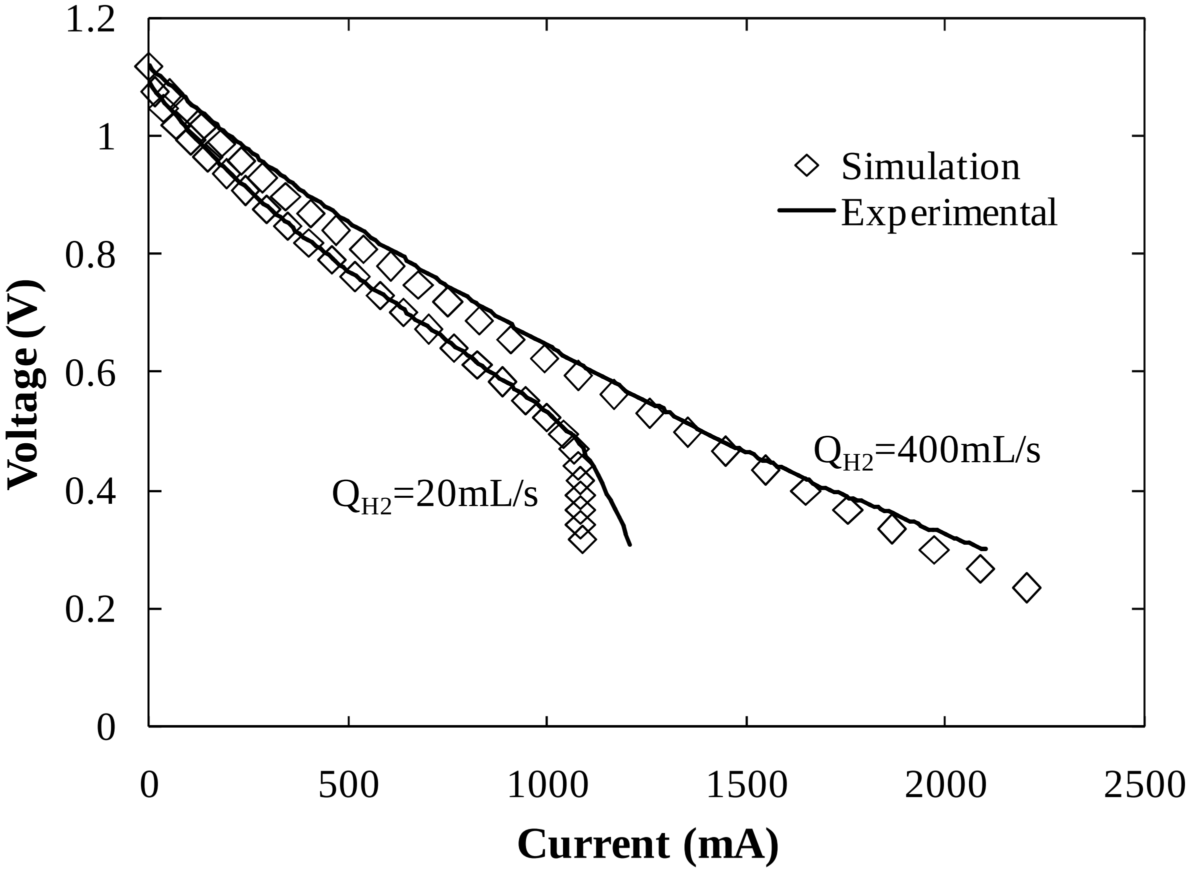

Figure 3.5. The experimental and the simulated performance curves at two hydrogen flowrates.

3.5 Results and Discussion

3.5.1 Assessment of the contributions to the cell performance loss

As it was mentioned earlier, there are three types of overpotentials (losses). The model predicted the local ohmic and activation losses were within the electrodes. The overall values for the contribution of each type of overpotentials was calculated by integrating the energy loss due to that overpotential divided by the total cell current. For the ohmic overpotential, the local energy loss is equal to the resistive heating in a conductor. Therefore, the average ohmic overpotential is calculated as:

$$\eta_{\Omega}^{avg} = \frac{\int \mathbf{J^q} \bullet \nabla V}{I_{cell}} \tag{3.73}$$

The ohmic loss of each component of the cell was calculated separately to identify the contribution of each to the total loss.

The energy loss due to the activation overpotential is the local activation overpotential (η_{act}) multiplied by the current generated at that point (Q_{gen}). Therefore the overall activation overpotential is:

$$\eta_{act}^{avg} = \frac{\int Q_{gen} \eta_{act}}{I_{cell}} \tag{3.74}$$

The concentration overpotential cannot be calculated in the same way, as there is no actual energy loss associated with it. Therefore it was calculated by subtracting the total loss from the activation and ohmic losses. This however did not distinguish the contribution of the concentration losses of the anode from the cathode side, and the electrodes from the gas channels.

Figure 3.5 shows the contribution of each type of overpotential to the overall performance loss, calculated from the simulation results. It is clear that the activation overpotential of the cathode was the biggest cause of performance loss in this cell. This is consistent with the well known fact that the reduction of oxygen on LSM is relatively slow. The ohmic loss due to the electrolyte layer was minimal, which is one of the advantages of the very thin electrolyte layer of the TμSOFC design. What is unusual for this cell is the large ohmic loss of the ASL, which was due to its unusually low electronic conductivity. The ohmic losses within the portion of the current collector layers covering the active length ($\eta^{avg}_{\Omega,ACCL+CCCL}$) were quite small. The sum of the losses due to the electronic and ionic current within the AFL and the CFL plus the activation loss of the AFL are all lumped as η_{etc}, and had a very small contribution to the total loss. In fact, the very small contribution of the anode activation loss compared to the overall loss explains the difficulty of obtaining an accurate estimate for the anode kinetic parameter, as discussed before.

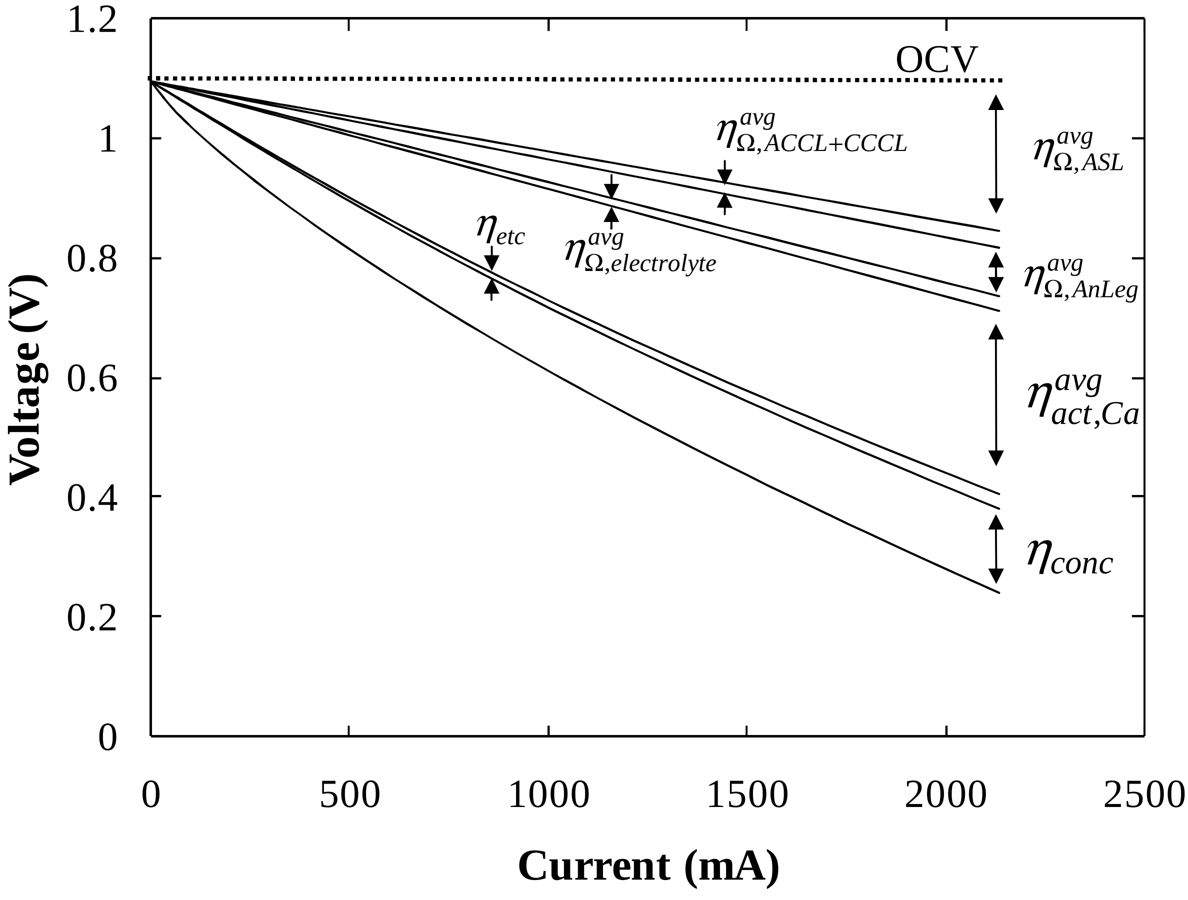

Figure 3.6. The contribution of various overpotentials and components of the cell to the overall performance loss.

To evaluate the share of the anode and the cathode to the concentration overpotential, a separate set of simulations was performed. The concentration overpotential of the anode porous electrode was artificially eliminated by numerically projecting the concentration of the gas channel/ACCL interface to the entire ACCL, ASL, and AFL domains (the curve $\eta_{conc}^{An}=0$). Therefore, the diffusion barrier of the porous electrode was artificially eliminated, as the concentrations of species were constant at each cross section of the electrode, while they changed along the electrode. Similar scheme was used for the cathode (the curve $\eta_{conc}^{Ca}=0$). The resulting performance curves are shown in Figure 3.7.

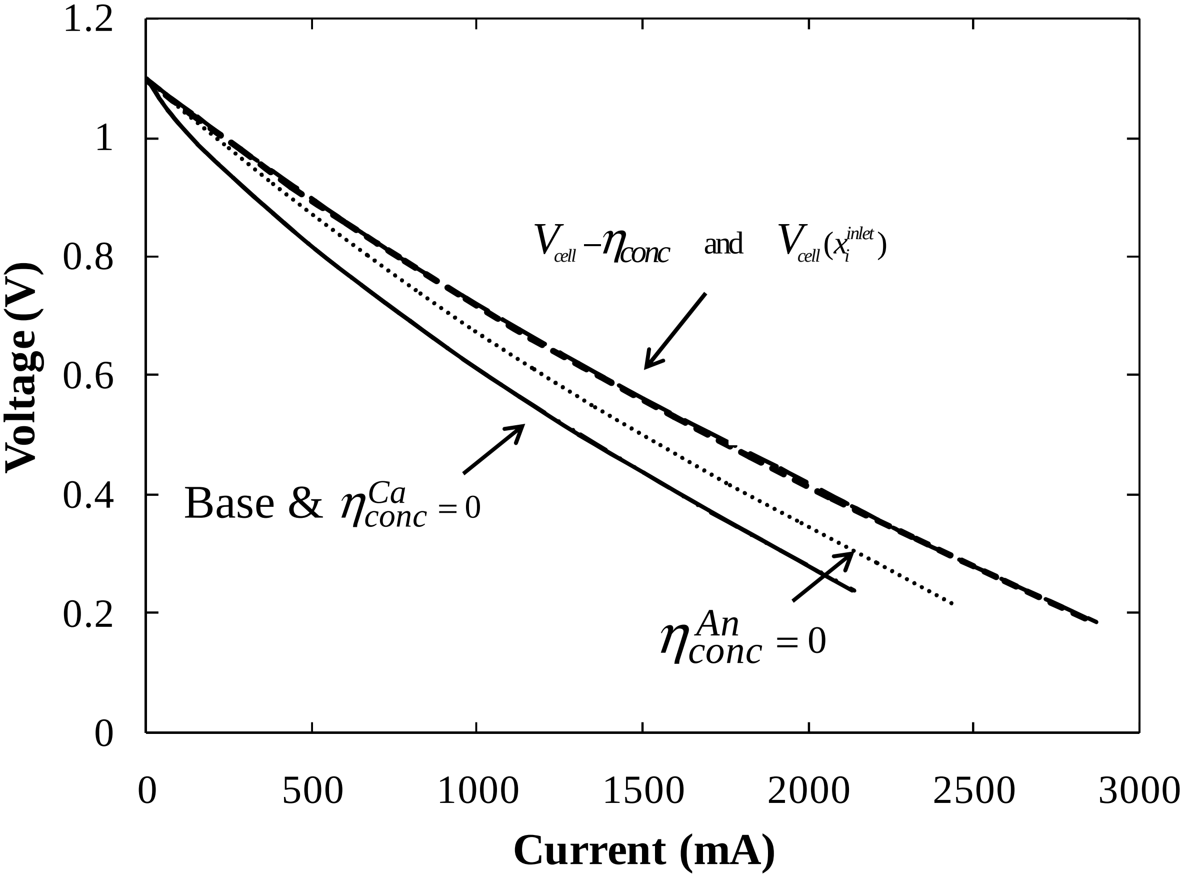

Figure 3.7. The contribution of the anode and the cathode electrodes to the concentration overpotential.

The concentration overpotential of the cathode was so small that the curve representing it is overlapping the base curve. This is because the cathode layer was very thin and introduced a very small concentration difference. On the other hand, the anode electrode had a significant contribution to the concentration loss, as its thickness was much higher. The contribution of both of the electrodes to the concentration overpotential does not add up to the concentration overpotential calculated indirectly $(V_{cell} - \eta_{conc})$ in Figure 3.7 Therefore, the difference between the curves for $\eta_{conc}^{An} = 0$ and $(V_{cell} - \eta_{conc})$ was not caused by the concentration gradients within the electrodes. It was inherent to the fact that the gases flowing within the channels were depleted from the reactants as they passed along the electrodes. Therefore the difference between the curves $\eta_{conc}^{An} = 0$ and $(V_{cell} - \eta_{conc})$ represents the concentration overpotential caused by the gas within the channels. A third hypothetical simulation was performed by keeping the concentration of all the species constant equal to the inlet values, within the gas channels as well as the electrodes, represented by the curve $V_{cell}(x_i^{inlet})$ in Figure 3.7. This way, the concentration losses was completely eliminated. It is clear that in Figure 3.7, the curve $V_{cell}(x_i^{inlet})$ almost overlaps with the curve that indicate the total concentration loss $(V_{cell} - \eta_{conc})$ obtained from Figure 3.7 This shows that our discussion about the flow inherent concentration loss was indeed valid.

3.5.2 Sensitivity of the simulated performance curve to electrode properties

As it was discussed earlier, some of the parameters required for the modeling of the electrodes varied from sample to sample, and in some cases were very different from the values calculated based on theoretical correlations or reported in the literature. It is well known that properties of the porous electrodes are very sensitive to their fabrication procedures. Therefore the sensitivity of the simulation results to variances in the electrode properties was analyzed.

The sensitivity of the cell performance to changes in the effective electric properties of the electrodes are shown in Figure 3.8. It is clear that the performance is very sensitive to the effective conductivity of the ASL. This is consistent with the findings from the overpotential contribution plot in Figure 3.6, where the ASL ohmic loss was found a key performance bottleneck. Changes in the effective conductivity of other layers did not affect the performance much, and the curves corresponding to a 10 time variance in those properties overlap with the base case. The only exception was the effective ionic conductivity of the CFL which noticeably reduced the performance when it was lower by a factor of 10.

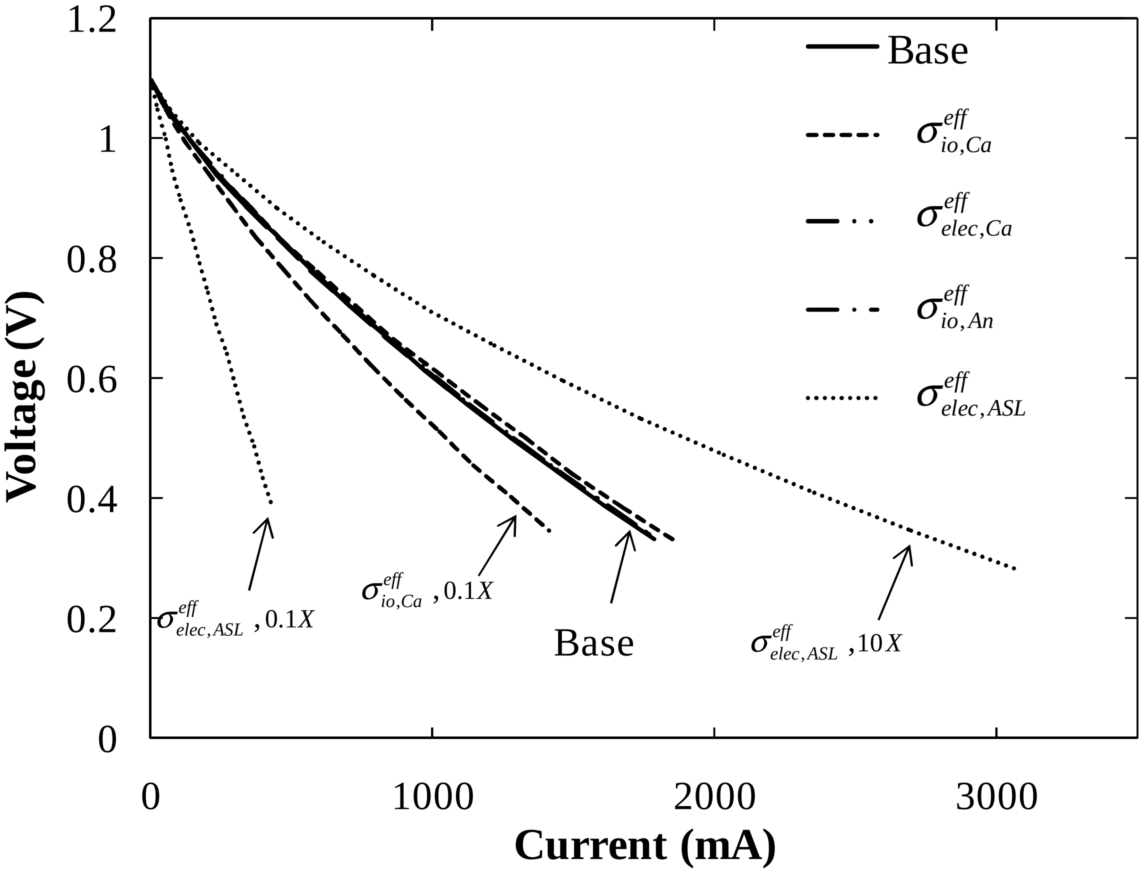

Figure 3.8. The cell performance sensitivity to the electric properties of the porous electrodes.

The cell performance sensitivity to the permeability and the effective diffusion coefficient of the gases within the porous electrodes was not significant, see Figure 3.9. Therefore the estimates used for the model were good enough to have a satisfactory prediction of the performance. Note that the sensitivity to these factors was analyzed by changing the values for all porous layers simultaneously. Naturally, most of the changes resulted from the anode electrode, and specifically the ASL, as it was much thicker than the other layers.

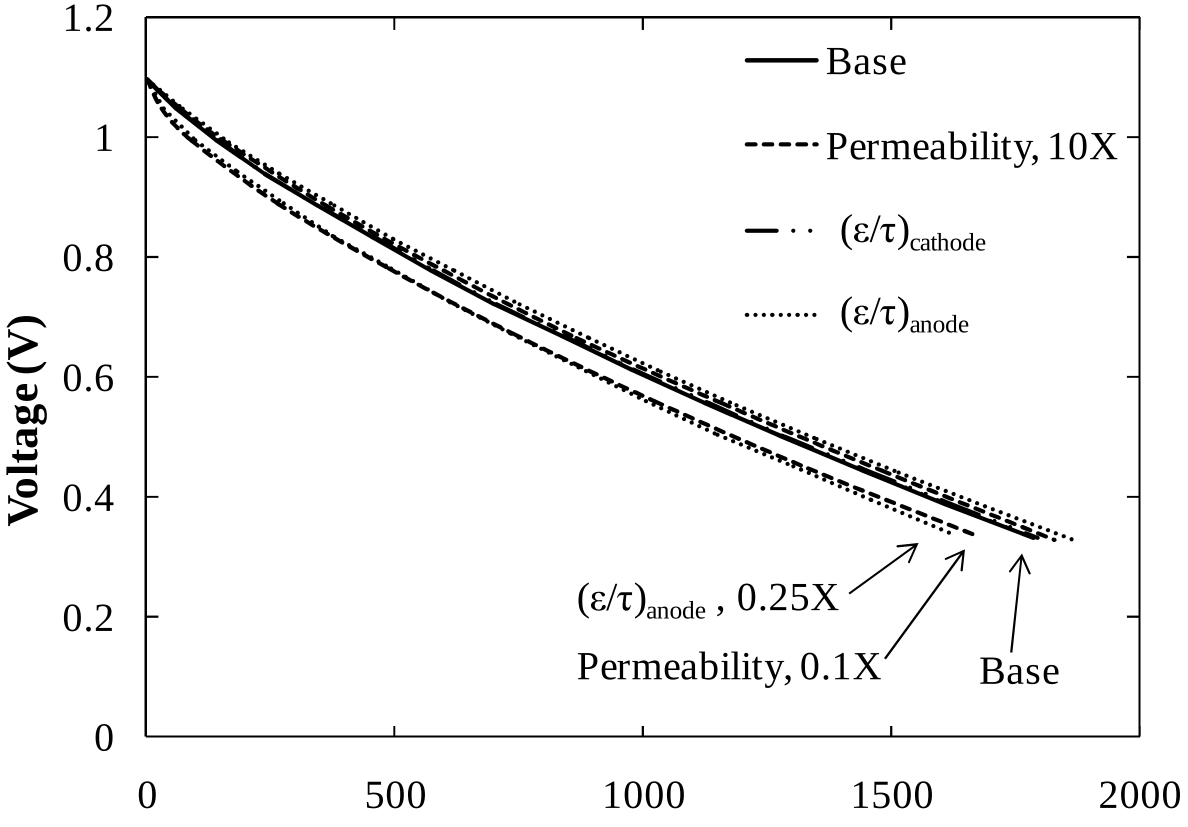

Figure 3.9. The cell performance sensitivity to gas transport properties of the porous electrodes.

Figure 3.10 shows the sensitivity of the cell performance to the kinetic parameters of the anode and the cathode reactions. These parameters reflect the catalytic activity of the electrodes. It is clear from Figure 3.10 that the cell performance prediction was very sensitive to changes in the cathode kinetic parameters. This is again consistent with the findings from Figure 3.6, where the cathode had the single most significant contribution to the overall performance loss. The changes in the anode kinetic parameter barely affected the performance curve, due to its superior performance and minimal contribution to the overall performance loss. Again, the fact that the performance is so insensitive to changes in anode kinetic parameter indicates that the optimization scheme could not extract much information from experimental data to make accurate estimation.

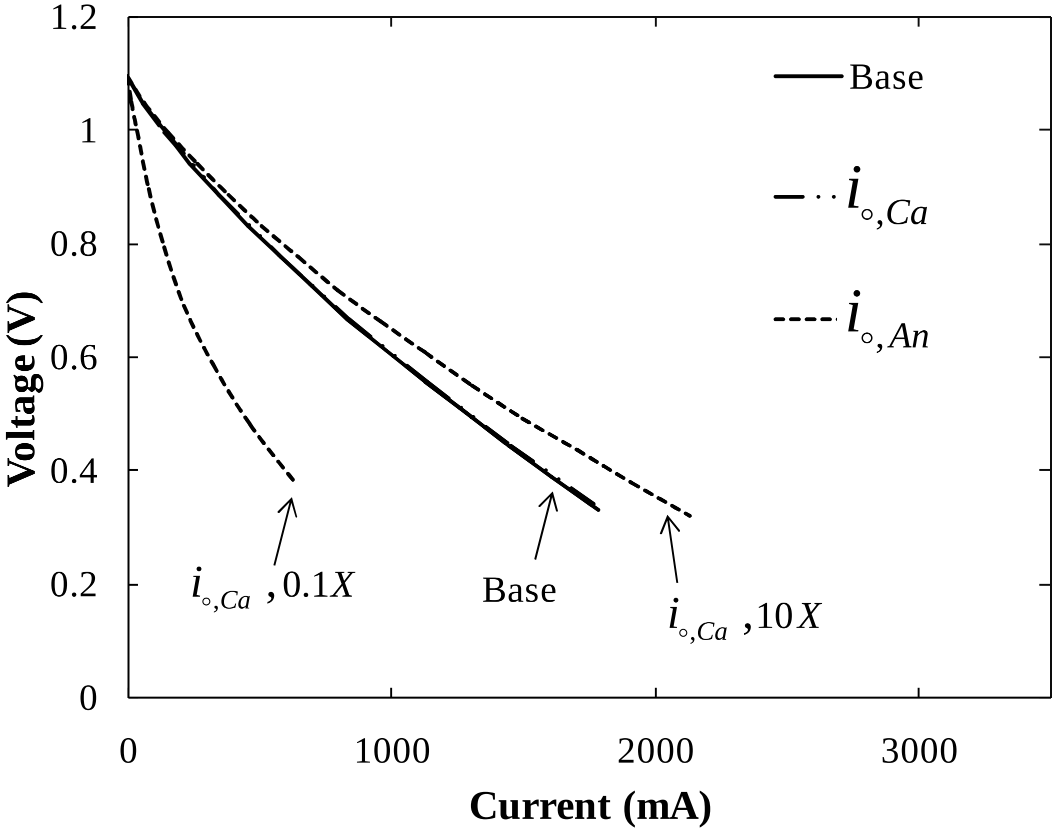

Figure 3.10. The cell performance sensitivity to the electrochemical activity of the electrodes.

3.5.3 Simulated details of the cell performance

By solving the mathematical model developed for the fuel cell, aspects of its operation can be studied that are often inaccessible to experiments. Therefore simulation results are an invaluable tool to gain insight about the cell performance. Here the results obtained from the base case simulation will be discussed.

The concentration distribution of oxygen in the gas channel had a boundary layer shaped region in which the gas was depleted from oxygen by the cathode; see Figure 3.11. For hydrogen, there was no such boundary layer shape, and the concentration of hydrogen decreased uniformly as it passes by the active length.

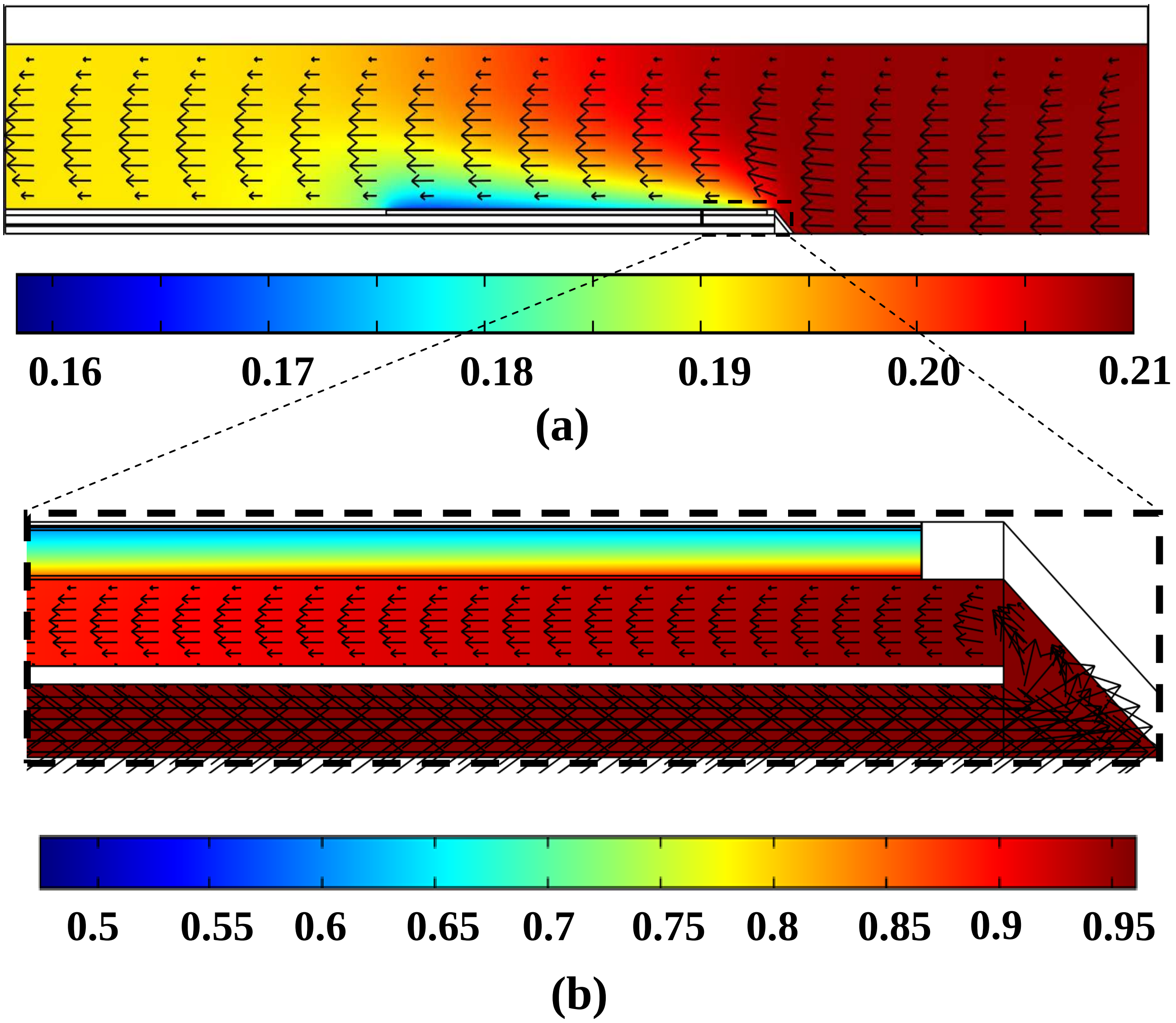

Figure 3.11. The mole fraction of (a) oxygen on the cathode side and (b) hydrogen on the anode side at V_{cell}=0.4 V. Arrows indicate (a) air velocity and (b) fuel velocity vectors.

The mole fraction of hydrogen in the cross section at the middle of the anode active length is shown in Figure 3.12. The concentration gradient across the gas channel was negligible, while it was noticeable within the AFL. The gradient is larger at higher current loads (lower cell voltages).

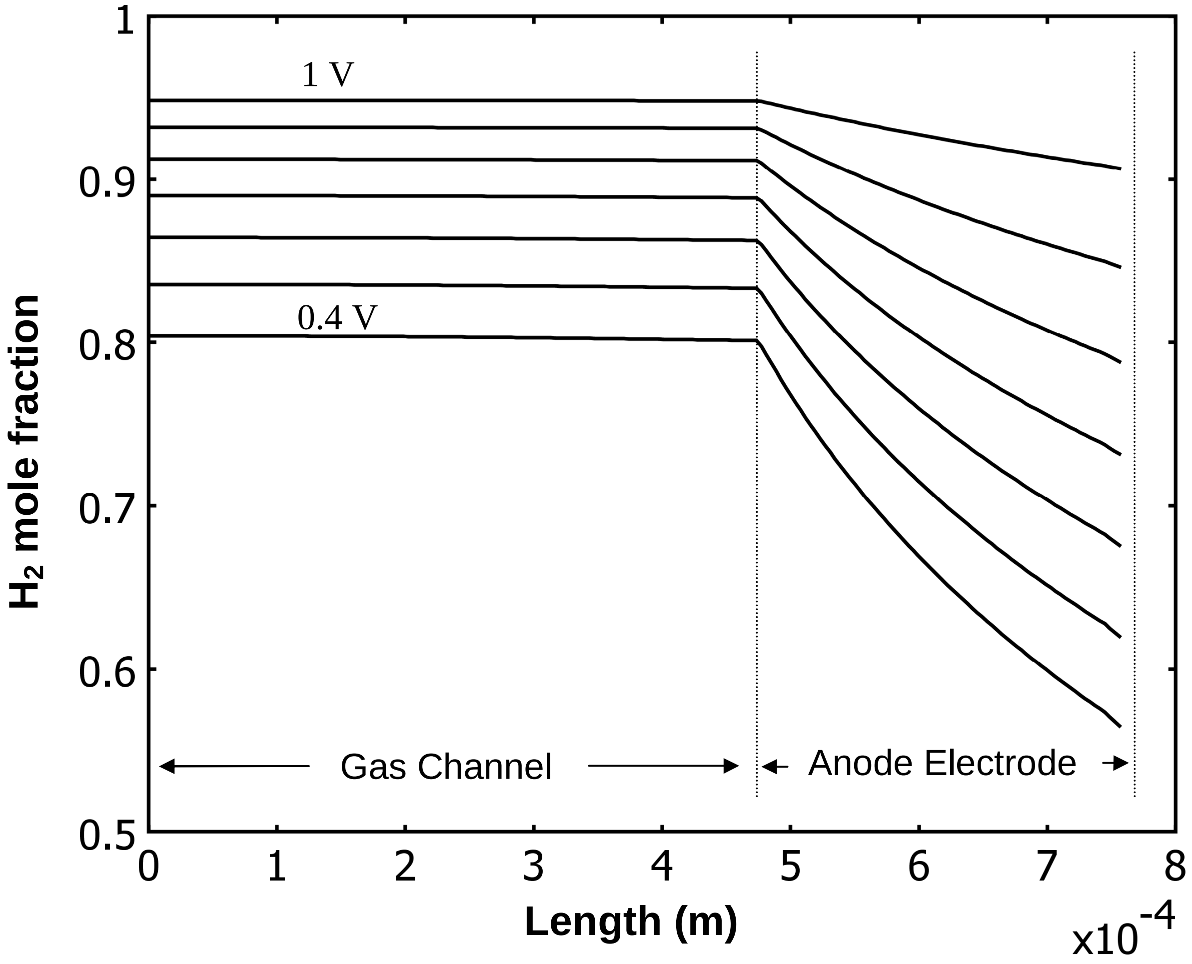

Figure 3.12. The mole fraction of hydrogen across the middle of the anode active length, within the anode gas channel and the anode.

The hydrogen mole fraction along the AFL/electrolyte interface is shown in Figure 3.13. The concentration gradients along the active length became larger at higher current loads.

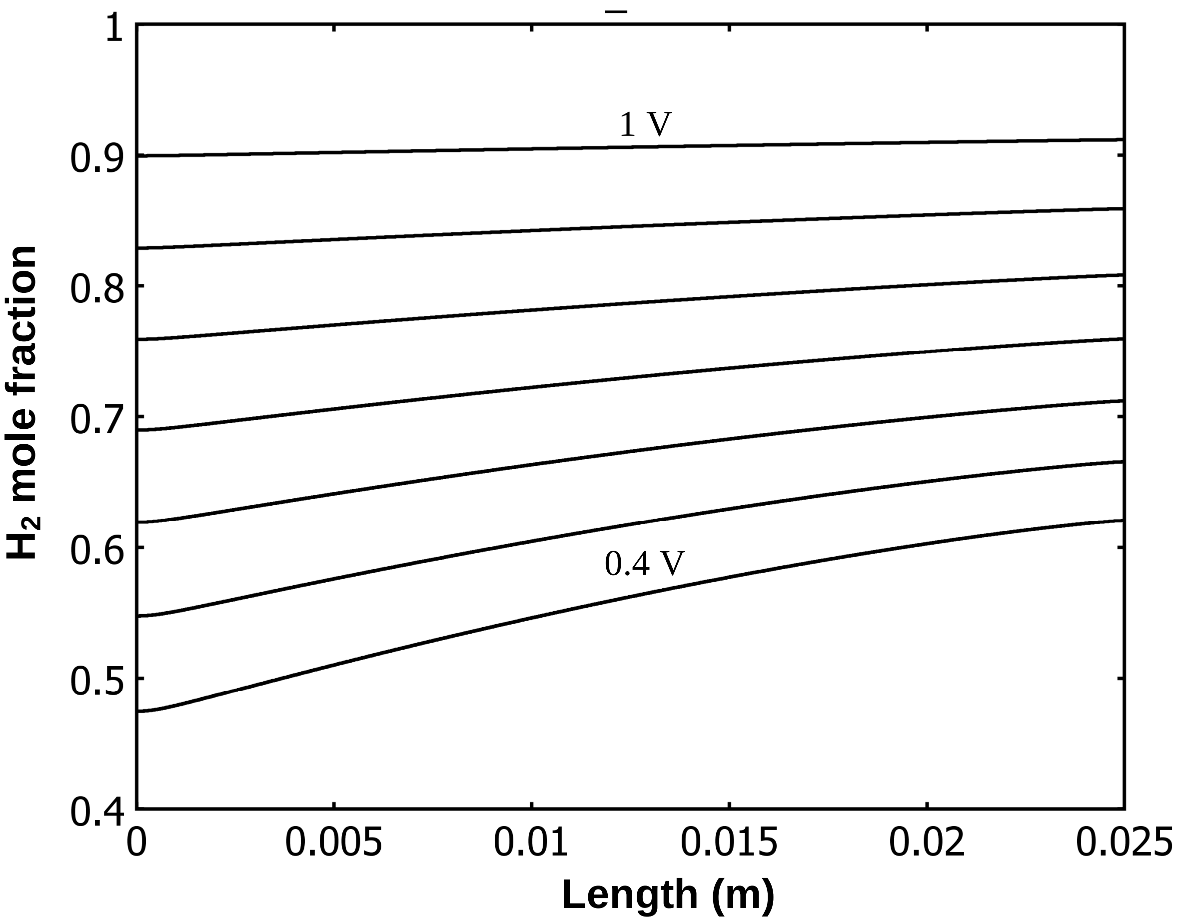

Figure 3.13. The mole fraction of hydrogen along the AFL/electrolyte interface; zero on the x-axis corresponds to the edge close to the open end.

Unlike the anode side, there was a noticeable gradient in the concentration of oxygen within the gas channel which was also observed in the color plot (Figure 3.11.(b)); see Figure 3.14. Although the gradients within the electrode were much higher compared to the gas channel, the very thin cathode layer did not cause a large difference in the concentration of oxygen.

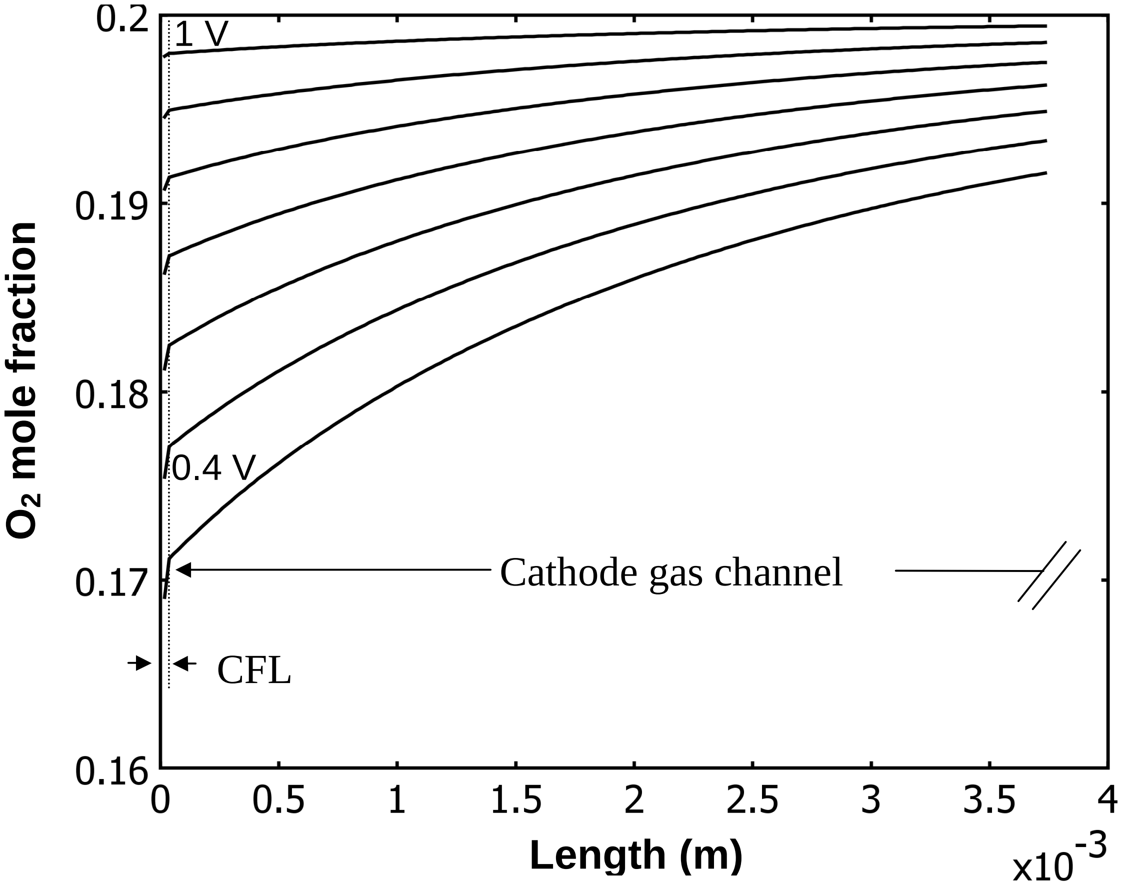

Figure 3.14. Mole fraction of oxygen across the middle of the cathode active length, within the cathode gas channel and the cathode.

The concentration of oxygen along the active length was higher at the two ends of the electrode: upstream of the air flow, where oxygen was still not consumed; and downstream where oxygen had the chance to diffusion axially within the gas channel from the bulk gas toward the electrode. See Figure 3.15.

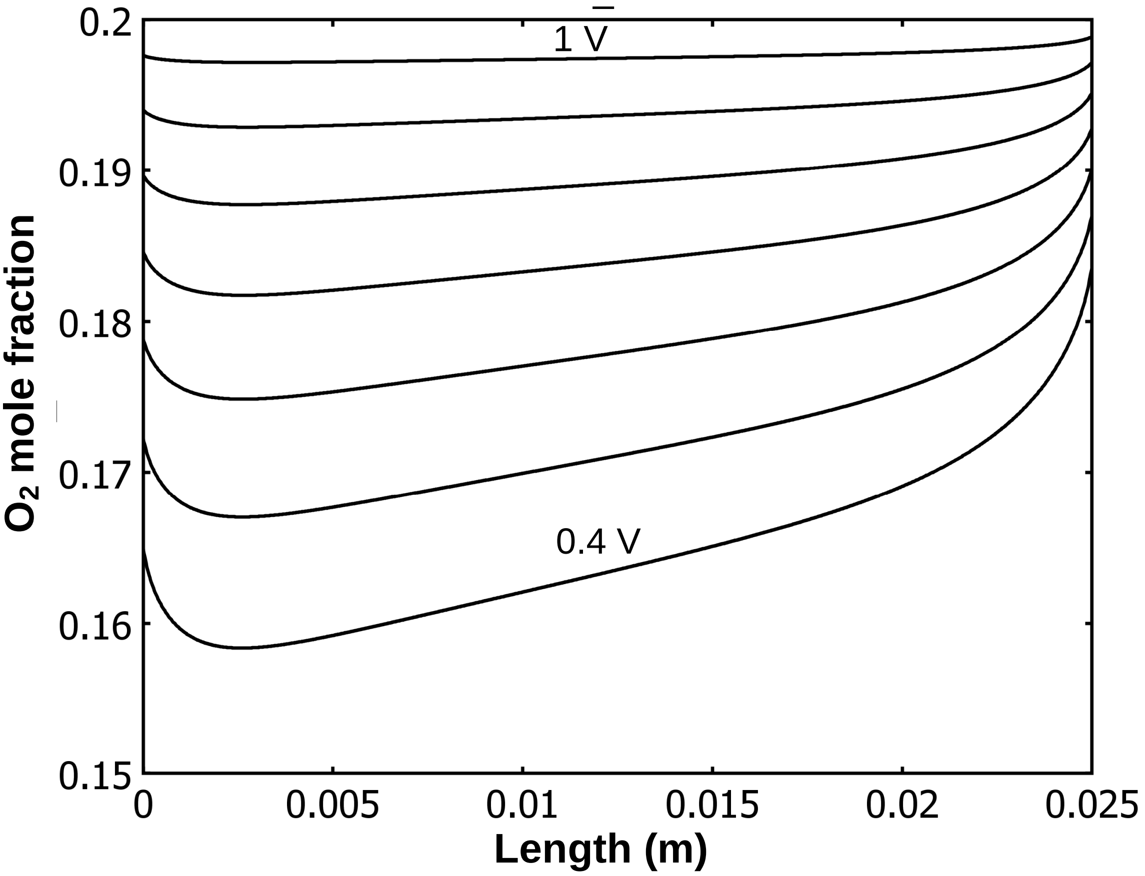

Figure 3.15. The mole fraction of oxygen along the CFL/electrolyte interface; zero on the x-axis corresponds to the edge close to the open end.

Figure 3.16 shows the rate of volumetric electron generation, i.e. the reaction rate, across the electrodes. Electrons were generated on the anode side while they were consumed on the cathode side; hence the sign of electron generation is positive and negative for the anode and the cathode respectively. The much higher activity of the anode is clear in this figure as the peaks are much higher for the anode compared to the cathode. Naturally, the peaks are higher at higher current loads. Notice that reactions were faster at the electrode/electrolyte interface, especially for the anode. This is because the ionic conductivity of YSZ particles within the composite electrode was much lower than the electronic conductivity of nickel or LSM particles. In fact, most of the AFL was not contributing to reactions, and therefore the anode could be fabricated thinner without any loss in the overall cell performance. This would have had the advantage of lower ohmic and diffusion resistance for the electrons and the reacting species. However there is a practical limitation: the AFL acts as a cushion for the very thin but dense electrolyte layer on top of the very porous ASL, and protects the electrolyte from cracking due to thermal and mechanical stresses. Unlike the AFL, most of the CFL was participating in reactions as the reaction rate did not drop significantly in its cross section; therefore there is a potential for enhancing the cell performance by increasing the thickness of the CFL.

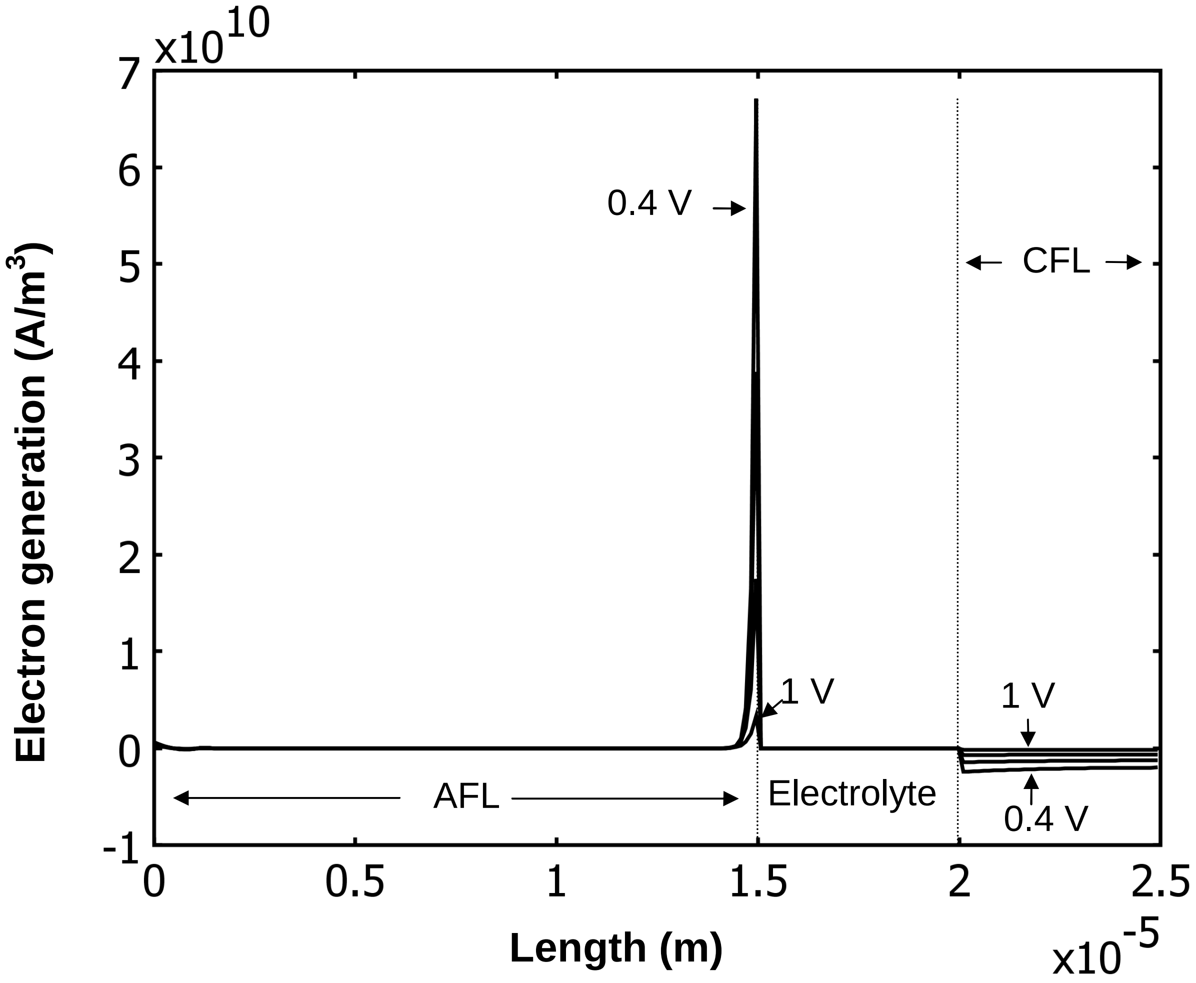

Figure 3.16. Volumetric electron generation within the electrodes, in the cross section at the middle of the active length.

Figure 3.17 shows the electron generation along the electrode/AFL interface, which corresponds to the peaks in Figure 3.16. The current generation was mostly uniform along the active length; however at high current loads it became concaved. The reason that the reaction rate is higher at the two ends of the active length is that the side close to the cell's open end (x=0.025) is where electrons were being pulled out and therefore the potential was less affected by ohmic losses. On the other end, upstream of the flow (x=0), higher hydrogen concentration enhanced the reaction rate.

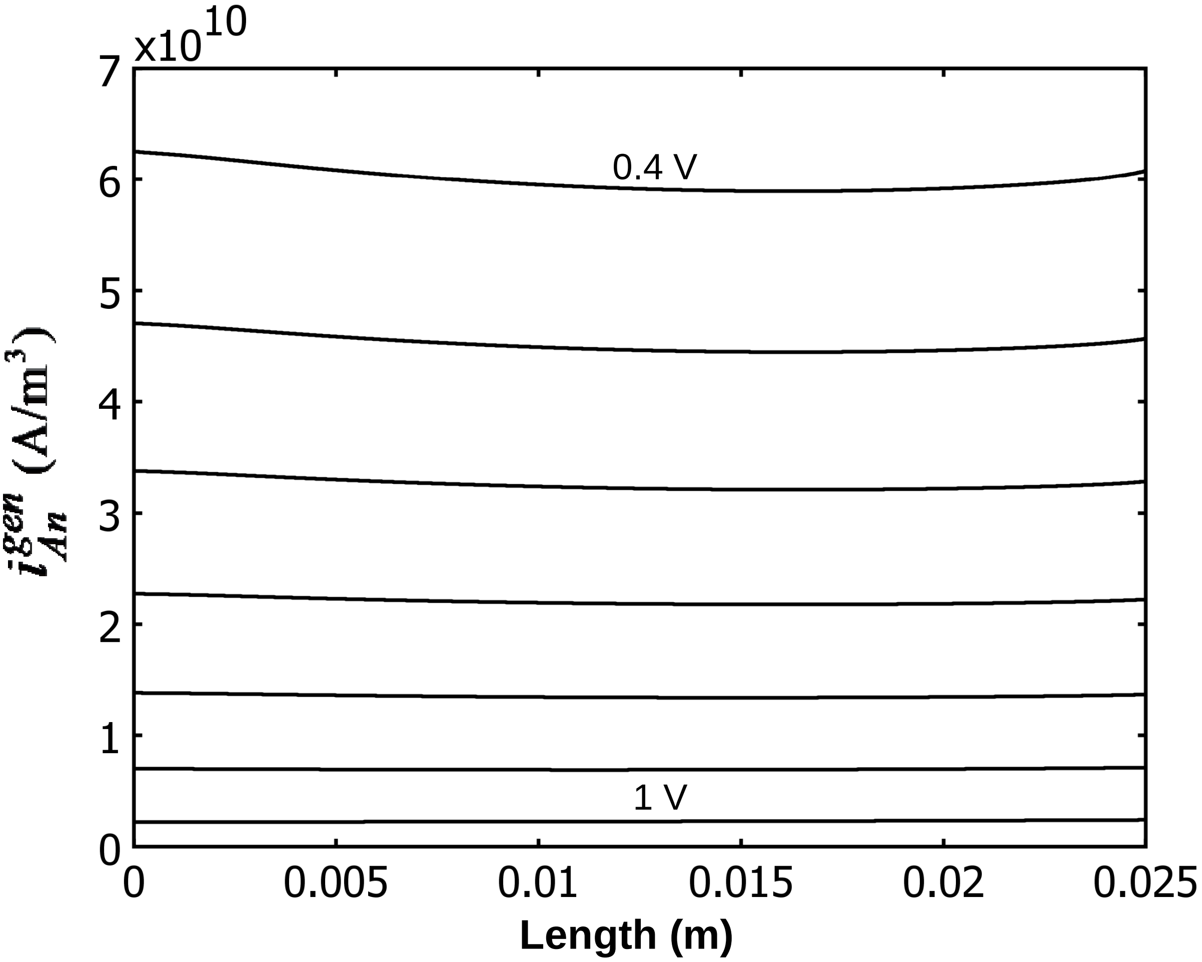

Figure 3.17. The volumetric electron generation along the AFL/electrolyte interface; zero on the x-axis corresponds to the edge close to the open end.

Figure 3.18 shows the rate of electron generation along the CFL/electrolyte interface. The rate of reaction was higher where the wire was connected to the current collector for the same reason as discussed for the anode. However in this case, the reaction at the other end (x=0) was not as high because it was downstream to the air flow and the concentration of oxygen was not much higher than the midsection, as it was seen in Figure 3.14.

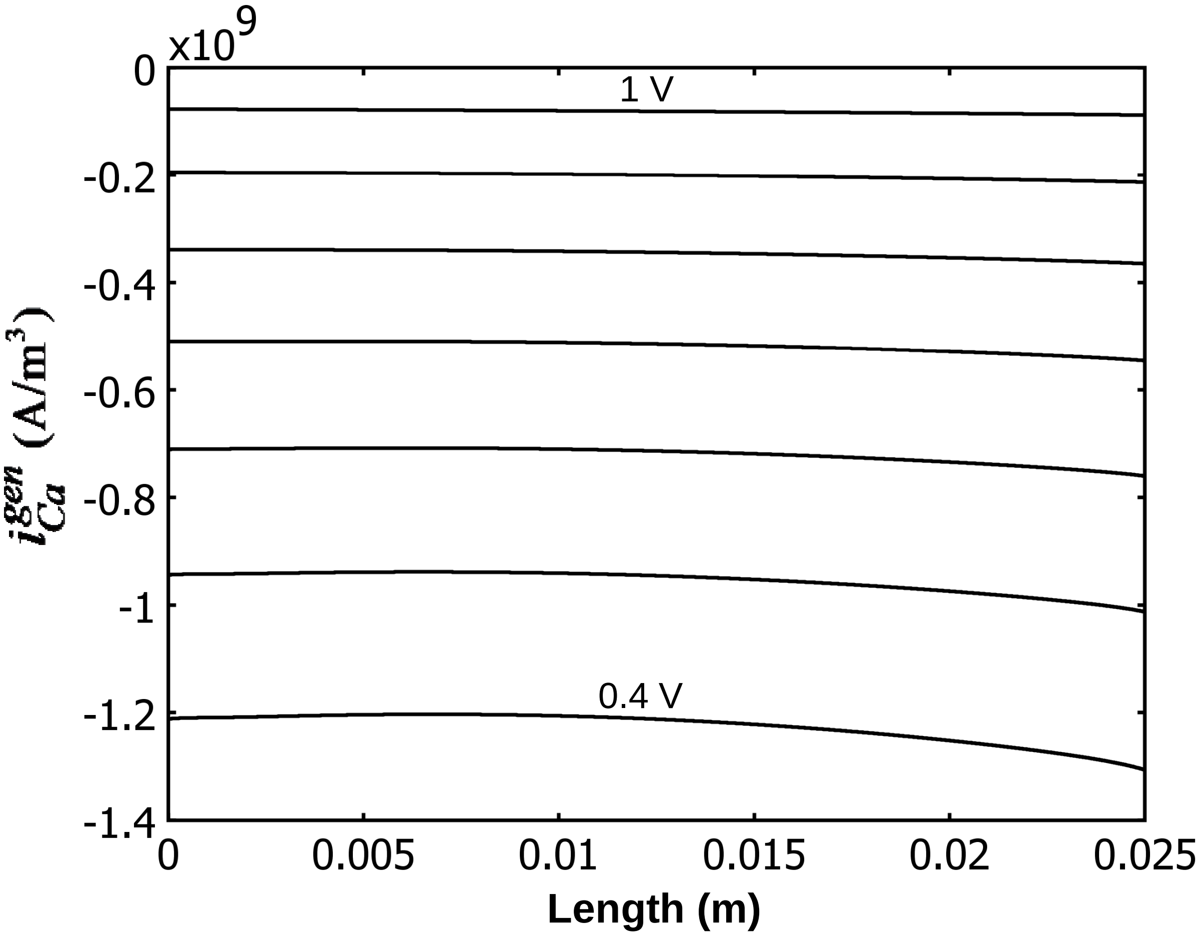

Figure 3.18. The volumetric electron generation along the CFL/electrolyte interface; zero on the x-axis corresponds to the edge close to the open end.

The relative magnitude of the convective to the diffusive mass transfer in the anode electrode is shown in Figure 3.19. The convective and the diffusive mass transport were of an equal importance. The effect of the diffusive mass transport became more significant at higher current loads due to larger concentration gradients developed within the electrode.

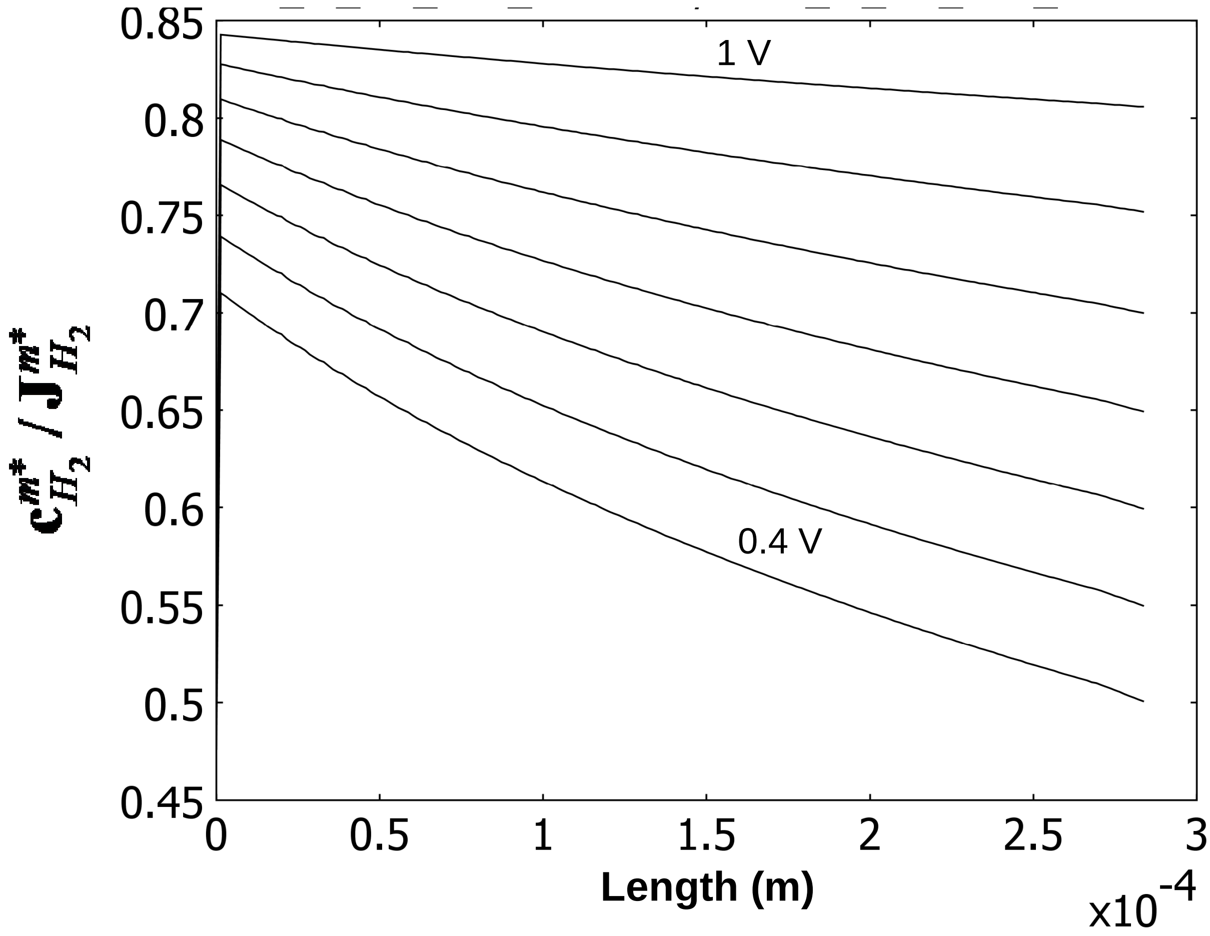

Figure 3.19. The ratio of convective to diffusive mass transfer of hydrogen within the anode, in the cross section at the middle of the active length.

The magnitude of the convective to the diffusive mass transport at a cross section of the porous cathode is shown in Figure 3.20. The convective transport was less significant for the cathode compared to the anode.

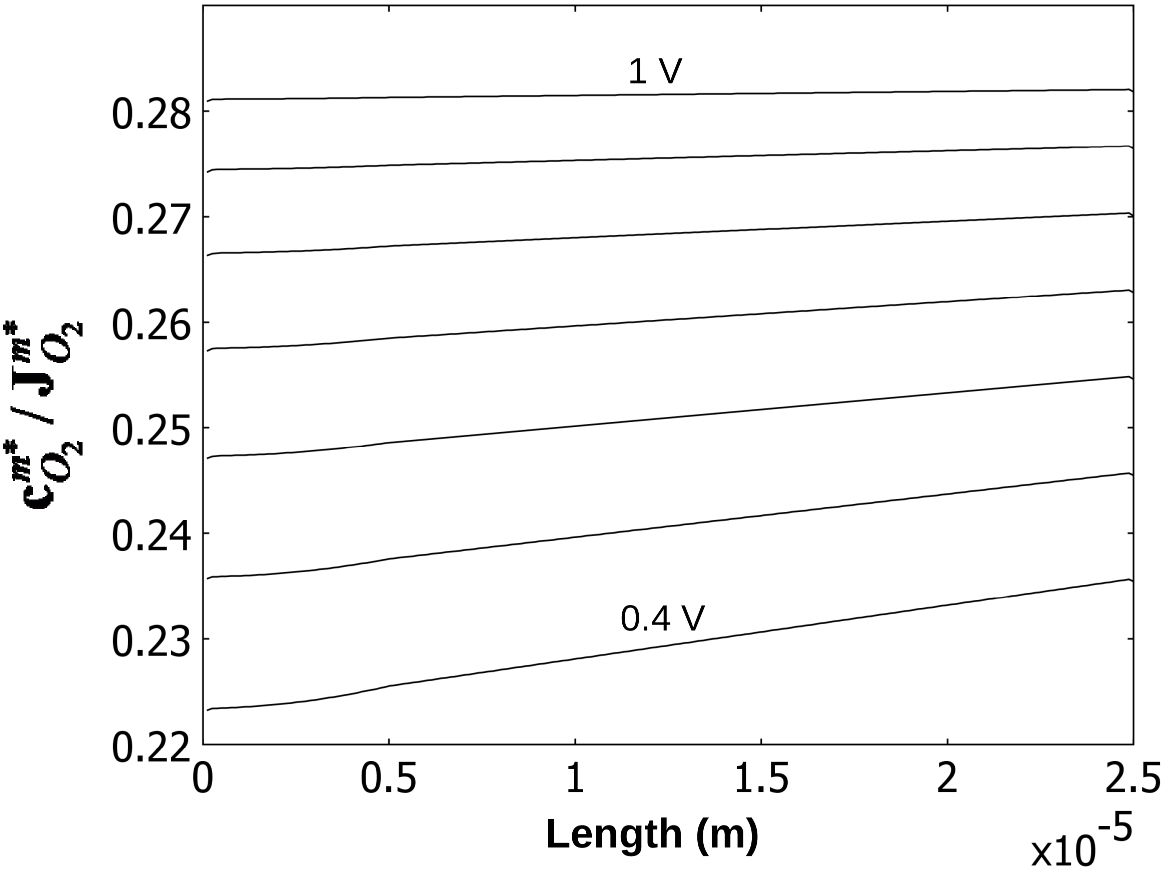

Figure 3.20. The ratio of convective to diffusive mass transfer of oxygen across the cathode at the middle of the active length.

The pressure distribution in the cross section of the anode is shown in Figure 3.21. There was a pressure buildup within the anode electrode. This is because water was produced while hydrogen was consumed within the porous electrode, which caused a net outflux of mass. The net outflux of mass created a pressure gradient within the anode electrode. Higher current generation obviously resulted in a higher pressure buildup within the electrode, which was as much as 10 kPa for V_{cell}=0.4V.

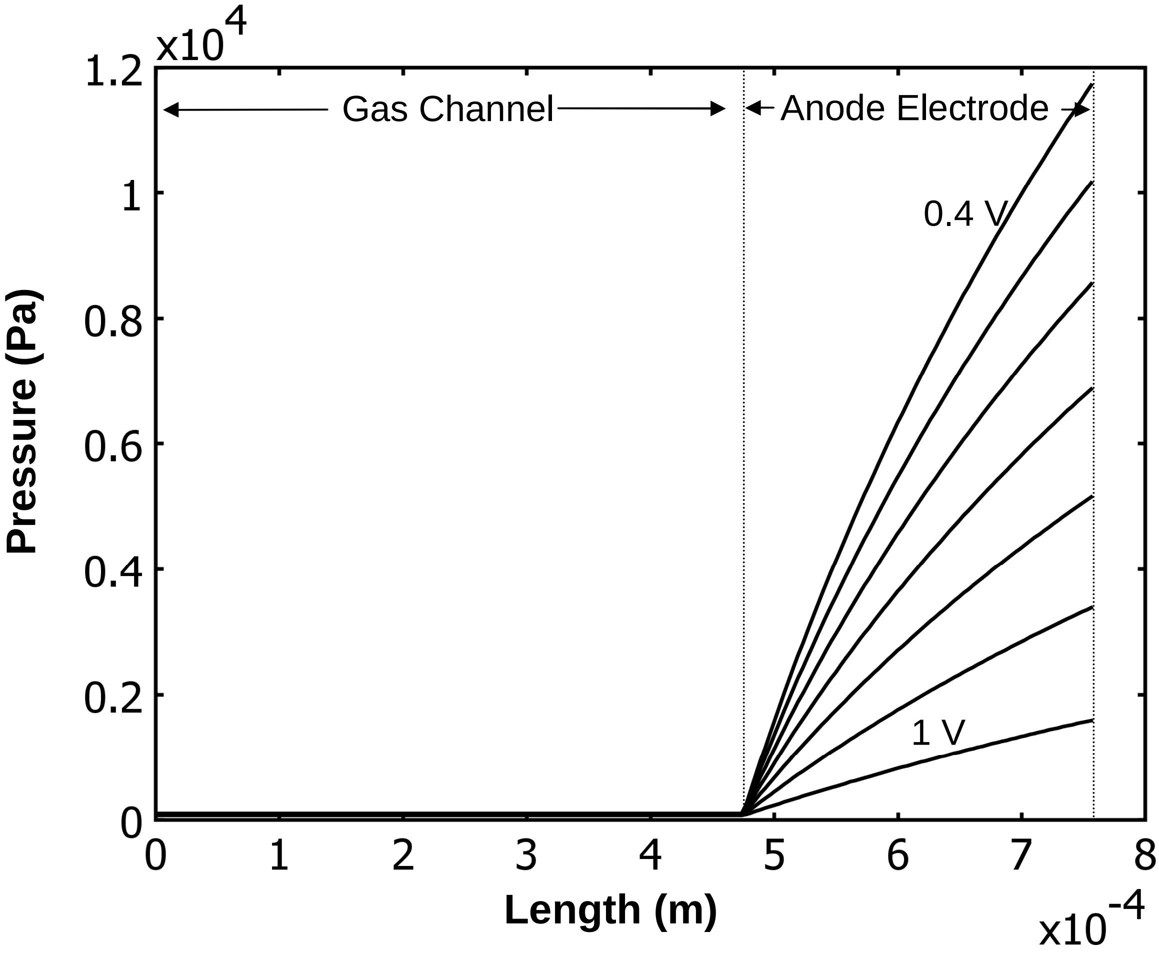

Figure 3.21. The (gauge) pressure distribution on the anode side, in the cross section at the middle of the active length.

Figure 3.22 shows the pressure distribution along the AFL/electrolyte interface. At higher current loads, there was a higher pressure gradient along the active length of the cell.

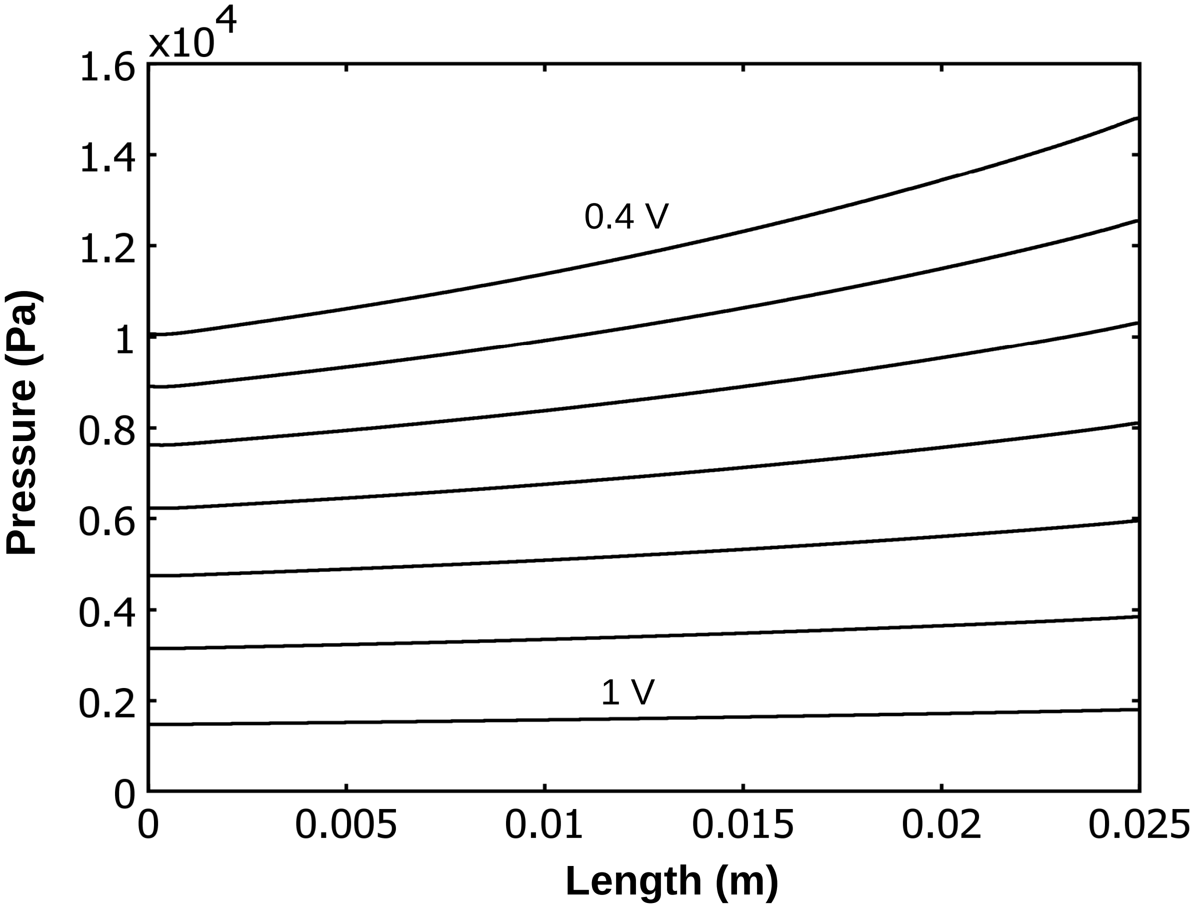

Figure 3.22. The (gauge) pressure distribution along the AFL/electrolyte interface; zero on the x-axis corresponds to the edge close to the open end.

The pressure distribution on the cathode side is shown in Figure 3.23. Contrary to the anode electrode, a net mass flux existed from the gas channel towards the electrolyte due to the consumption of oxygen within the CFL. Therefore a relative vacuum developed within the cathode electrode. Notice that the pressure difference was not as significant as the anode side because the cathode electrode was much thinner than the anode electrode.

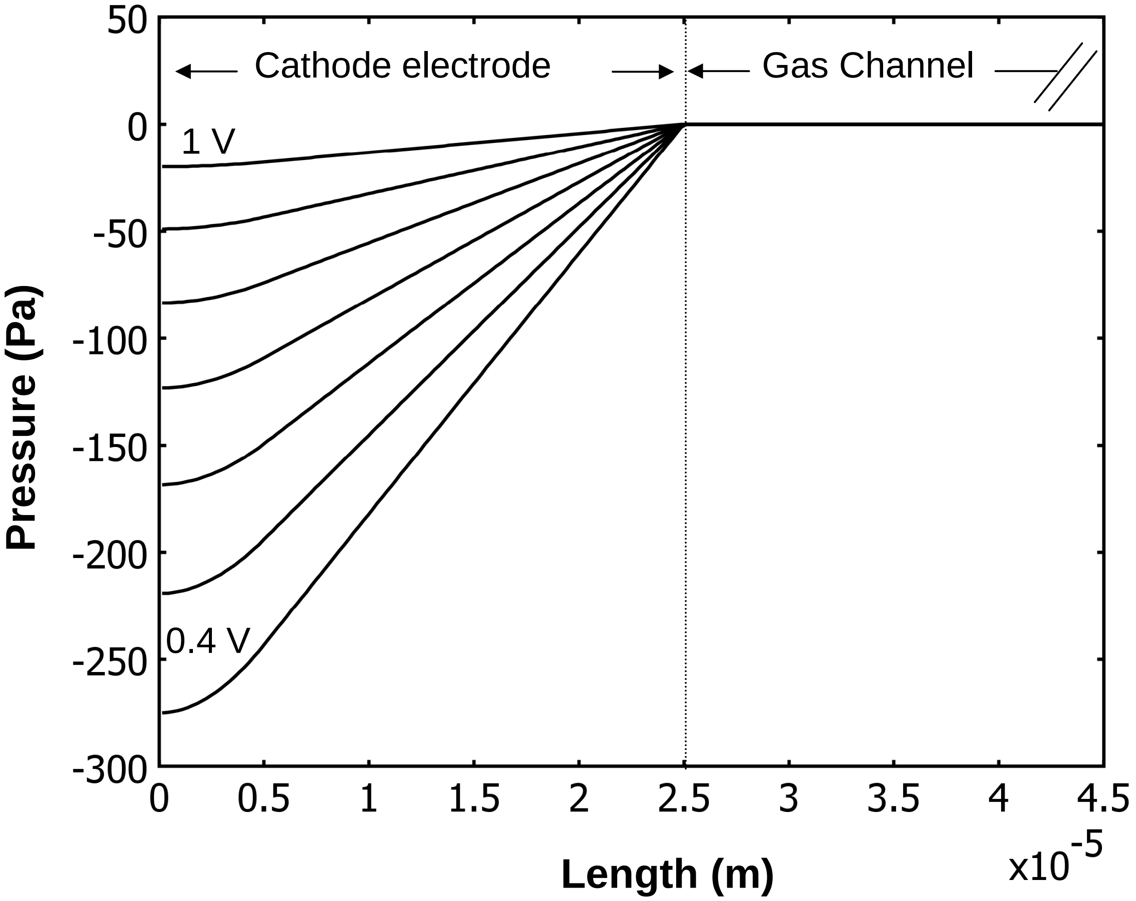

Figure 3.23. The (gauge) pressure distribution on the cathode side, in the cross section at the middle of the active length.

The pressure distribution along the CFL/electrolyte interface is indicated in Figure 3.24. A pressure gradient was developed along the cell at higher current loads, similar to but not as much as the anode electrode.

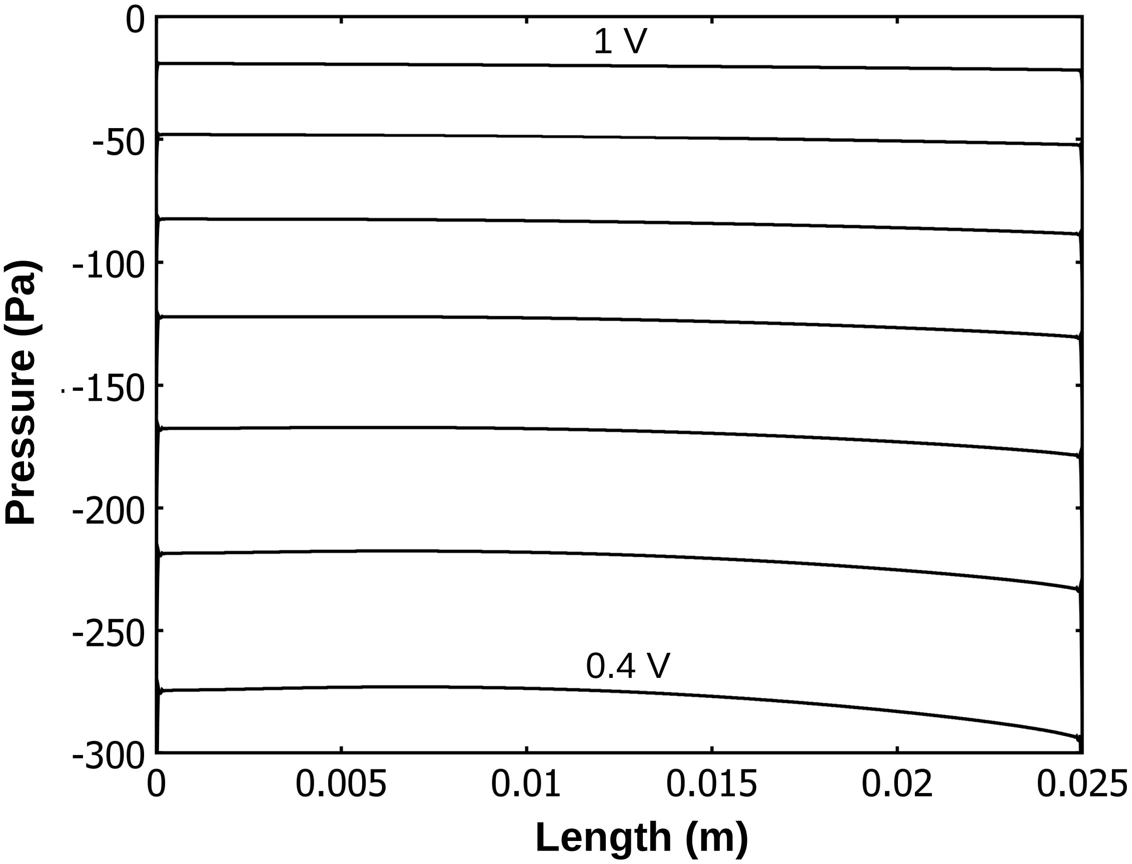

Figure 3.24. The (gauge) pressure distribution along the CFL/electrolyte interface; zero on the x-axis corresponds to the edge close to the open end.

3.6 Conclusion

A tubular micro solid oxide fuel cell was simulated based on detailed mathematical modeling of the physical phenomena occurring within the cell. The model was verified to be numerically consistent, and was successfully validated against the experimental data. The model was used to get a detailed insight into the TμSOFC performance. The simulation results were used to determine and distinguish the performance losses caused by various irreversible effects. It was found that due to the special design of this cell, i.e. the very thin electrolyte, significant losses commonly caused by low ionic conductivity of YSZ was minimal. The loss due to low activity of cathode was found to be the major performance bottleneck. In addition, the ohmic loss in the anode support layer was found to be significant, because of its unusually low effective conductivity. Therefore the two areas to focus on in order to enhance the performance of the cell are identified as: first, engineering the anode support microstructure to improve its electronic conductivity; second, improvement of the cathode catalyst. Obviously enhancing the conductivity of the anode support is a goal achievable with the available material knowledge, and should have a higher priority in further developing this fuel cell.

On the numerical aspect, it was found that models for estimating various properties for the cell, especially those for the porous electrodes should be used with special care. This was especially prominent in the case of electronic conductivity of the anode support layer, which was unusually low. This indicates the danger of assuming properties based on correlations, especially when novel fabrication techniques are employed; using invalid values can mislead the modeling results, and be inconsistent with the reality of the system.

Chapter 4. The non-isothermal model

4.1 Introduction

Solid oxide fuel cells (SOFC) typically operate around 800°C, and maintaining them at a uniform temperature is a major challenge of critical importance. Excessively high temperatures result in agglomeration effects within the electrodes, which leads to reduced performance, material degradation, and ultimately complete failure of the cell. High temperatures also increase the mechanical stresses caused by the thermal expansion mismatch of the SOFC components, which can lead to cracking, delamination, and mechanical failure of the cell. A more uniform temperature reduces the mechanical stresses caused by the temperature gradients. On the other hand, lower temperatures reduce the cell performance by decreasing the electrodes' electrochemical activity, and by increasing the electric resistance of the electrolyte. An SOFC generates heat as it operates and experiments have shown that the temperature differences between the cell surface and the gas inlet can reach up to hundreds of degrees Celsius (Zinovik and Poulikakos, 2009). Effective removal of the generated thermal energy is essential to avoid excessive temperatures, while a stack of SOFC is desired to be thermally self-sustained. Therefore, the thermal management is a delicate balance in the SOFC design and development.

For these reasons, it is essential to assess the temperature distribution within an SOFC, and assure that it remains within the acceptable limits. The experimental measurement of the temperature distribution within the SOFC systems and its layers, and assessing the effect of various parameters on it is quite difficult. Therefore, mathematical modeling can be a superior tool for gaining an accurate understanding of the heat transfer effects in an SOFC, barely accessible through experimentation. In addition, modeling the electrochemical performance of an SOFC is not possible without considering its thermal behavior, as the reaction rates and the material properties are highly dependent on temperature.

Many mathematical models for SOFCs are presented in the literature, for a wide range of geometries, designs, and operating conditions; few include heat transfer effects, and even fewer include a complete treatment of it. Excellent reviews by Bove and Ubertini, (2006); Colpan et al., (2008); Faghri and Guo, (2005); Kakac et al., (2007) summarize the ongoing efforts on the thermal modeling of SOFCs.

This model developed here is unique in several aspects. It presents one of the most comprehensive models developed for any type SOFC, not just the TμSOFC. Radiative heat transfer was modeled comprehensively on the anode and the cathode sides. The model included the reversible and irreversible heating effects in the SOFC. The reversible heating was modeled based on the single-electrode entropy generation, calculated locally within the volume of each electrode, as the volumetric reactions were assumed within the composite electrodes. The irreversible heat generation was also estimated within the volume of the SOFC layers. A novel approach was implemented for calculating the electromotive potential that can account for the thermoelectric effects in a non-isothermal electrochemical cell. The materials' physical properties were calculated based on the local conditions, i.e. temperature, pressure, and composition.

This work is especially distinguished as it presents the experimental results conducted on the TμSOFC, specifically to validate the mathematical model. This is the only modeling effort that has validated the model predictions both in terms of the cell's electrochemical performance as well as its detailed thermal behavior. In addition, special attention was paid to the validity of the simplifications assumed to develop the model, as well as the numerical consistency of the model.

No parameter fitting was required for this model, as the parameters form the isothermal study presented in chapter 3. The purely predictive simulation results were found to be consistent with the physical reality of the cell.

The validated model was used to investigate the thermal behavior of the TμSOFC. The temperature distribution profile was simulated in detail, and the significance of radiative heat transfer was investigated. In addition, the effect of the non-isothermal conditions on the cell potential was assessed. Validated for a single cell, the model can be further extended to model a stack of TμSOFCs, which can be a significant development tool.

4.2 Model development

The non-isothermal model includes the heat transfer model in addition the equations presented for the isothermal model. The isothermal model equations remain essentially unchanged once they account for the temperature dependency of the physical properties. The only exceptions are the electrochemical potential equations which have a different form for a non-isothermal electrochemical system, and are further discussed in the following. The buoyancy effect was ignored in the fluid flow model. The diffusion-thermo effects on the mass and the energy transport, i.e. thermal diffusion and Dufour effects, were also ignored, as their contributions are negligible (Bird et al., 2002).

The cell overall electrochemical reaction of hydrogen reacting with oxygen, as in Eq.(3.1)(a), is exothermic for an SOFC system. Therefore while current is drawn from the cell, heat must be taken away from the cell active length to preserve the steady-state conditions. Heat is transported by conduction, convection, and radiation. While there is no doubt that radiation is significant at the SOFC operating temperatures, including it in the thermal modeling of SOFCs has been debated in the literature. About 50 papers published from 2003 to 2009 have discussed the heat transfer effects in SOFCs or included it in their models; only about 20 included radiative heat transfer, half of which were directly dedicated to radiation. Interestingly enough, most of the models that include radiative heat transfer are those for the tubular geometry. Earlier models presented in the literature more often ignored radiative heat transfer (Ackmann et al., 2003; Chyou et al., 2005; Haberman and Young, 2004; Li et al., 2004; Lu et al., 2005b). An increasing number of studies suggest that including radiation is essential for an accurate thermal model of both tubular and planar geometries (Calise et al., 2007; Sanchez et al., 2006; Sanchez et al., 2007; VanderSteen and Pharoah, 2006). Some studies suggest that radiation can be ignored; any conclusion however should be investigated with special care. For example, a study suggested that including radiation is not inevitable for predicting the maximum temperature in a planar SOFC stack, and that the effect of radiation is small in its central part (Tanaka et al., 2007). However, they included radiation only on the outer surfaces of the stack to draw this conclusion, but not among the cells. Their conclusion therefore could be just a natural result of the well-known thermal radiation shielding phenomena (Holman, 2002). In another study, it has been suggested that including radiative heat transfer in a model is essential for analyzing the local temperature distribution; however ignoring it would still result in an acceptable evaluation of the overall electrochemical performance (Sanchez et al., 2007). Another study suggested that including radiative heat transfer lowers the maximum temperature by as much as 100°C, and mitigates the temperature non-uniformities within the stack (Burt et al., 2004). Some of the different conclusions about radiative heat transfer can be associated to the variations in geometries and designs studied, which can have a significant effect on the overall effect of radiative heat transfer. In fact, some have proposed designs which employ radiative heat transfer as the main mechanism for enhanced thermal management of their stacks (Krist and Jewulski, 2006).

Modeling radiative heat transfer is a challenging task. The data available on the radiative properties of materials used in the SOFC components are very limited (Faghri and Guo, 2005), which also faces the reproducibility issue associated with the SOFC fabrication. From the mathematical point of view, a comprehensive treatment of radiative heat transfer can be quite difficult. The integro-differential equations describing radiative heat transfer are highly non-linear, and must be solved numerically with schemes that are inherently very different from those implemented for solving the conventional transport equations. Including radiation can drastically increase the computational requirements of the numerical scheme and the solution time. Hence, radiative heat transfer, when modeled, is often treated with significant simplifying assumptions; i.e. using view factors for relatively large surface segments (Calise et al., 2007; Calise et al., 2009; Haberman and Young, 2008; Li and Suzuki, 2004; Nishino et al., 2006; Song et al., 2005), assuming radiation only in the radial direction for tubular geometries (Jia et al., 2007; Jia et al., 2008; Suwanwarangkul et al., 2006, 2007; Xue et al., 2005), or assuming radiative exchange with an environment at constant temperature (Serincan et al., 2008) . Verification of these assumptions is critical and often not straightforward, which leads to inaccuracies of unknown magnitude. It seems that these challenges have led some authors, even in very recent detailed modeling studies, to ignore radiative heat transfer altogether without any mentioning of it (Mounir et al., 2009; Ni, 2009; Suzuki et al., 2008; Wang et al., 2009; Yuan et al., 2009).

The definite conclusion about radiative heat transfer is that it is important in SOFCs, and any assumption should be made with special care, considering the geometrical design and operating conditions. In the model developed for this work, we include surface to surface radiation on both the air side and the fuel side; the assumptions made and the basis of their validity will be further discussed.

4.2.1 Conductive and convective heat transfer

The conductive and convective heat transfer can be modeled by the energy balance equation. Although these equations are well established, occasional mistakes in the SOFC modeling literature calls for a brief discussion of its development here to reinforce the correct formulation.

The steady state energy balance equation with no volumetric heat source is:

$$\nabla \bullet (\mathbf{N}_i^h) = 0 \tag{4.1}$$

The total heat flux, $\mathbf{N}_i^h$, includes thermal conduction and the energy transported by the mass flux of components:

$$\mathbf{N}_i^h = -\bar{\kappa} \nabla T + \sum_i \hat{H}_i \mathbf{N}_i^m \tag{4.2}$$

where $\bar{\kappa}$ is the overall thermal conductivity of the gas mixture. $\hat{H}_i$ is the partial enthalpy of the component *i*, where for an ideal gas mixture is equal to the pure component enthalpy. The total mass flux of the component *i*, $\mathbf{N}_i^m$, is the sum of its diffusive mass flux, $\mathbf{J}_i^m$,and convective mass flux, $\mathbf{c}_i^m$:

$$\mathbf{N}_i^m = \mathbf{J}_i^m + \mathbf{c}_i^m = \mathbf{J}_i^m + \omega_i \rho \mathbf{u} \tag{4.3}$$

where, ω_i represents the mass fraction of the component *i*. $\mathbf{u}$ and ρ are the average mass velocity and the density of the gas mixture respectively.

Combining Eqs. (4.1) to (4.3):

$$\nabla \bullet (-\bar{\kappa} \nabla T) + \sum_i (\hat{H}_i \nabla \bullet \mathbf{N}_i^m + \mathbf{N}_i^m \bullet \nabla \hat{H}_i) = 0 \tag{4.4}$$

The spatial gradient of enthalpy of each component can be related to its specific heat capacity and the spatial gradient of temperature:

$$\nabla \hat{H}_i = \frac{\partial}{\partial x_j} \hat{H}_i = \frac{\partial}{\partial T} \hat{H}_i \frac{\partial}{\partial x_j} T = c_{p,i} \nabla T \tag{4.5}$$

With no gas phase chemical reaction, the component mass balance equation dictates that:

$$\nabla \bullet \mathbf{N}_i^m = 0 \tag{4.6}$$

Therefore, from Eqs. (4.4) to (4.6):

$$\nabla \bullet (-\bar{\kappa} \nabla T) + \sum_i (\rho \omega_i c_{p,i} \mathbf{u} \bullet \nabla T + c_{p,i} \mathbf{J}_i^m \bullet \nabla T) = 0 \tag{4.7}$$

Considering the ideal gas mixture specific heat capacity defined as:

$$\bar{c}_p = \sum_i (\omega_i c_{p,i}) \tag{4.8}$$

the final form of the energy balance equation for an ideal gas mixture is:

$$\nabla \bullet (-\bar{\kappa} \nabla T) + \left(\rho \mathbf{u} \bar{c}_p + \sum_i \mathbf{J}_i^m c_{p,i} \right) \bullet \nabla T = 0 \tag{4.9}$$

The first term of Eq.(4.9) represents the thermal conduction when there is no mass transfer; the second term represents the heat transfer due to the convection of mass; and the third term represents the heat transfer by the diffusion of gas components, which may be significant (Bird et al., 2002). In some SOFC modeling literature (Lu et al., 2005b; Suwanwarangkul et al., 2006; Wang et al., 2009) the $\bar{c}_p$ was incorrectly included inside the divergence operator, which should be outside as in Eq.(4.9).

Heat transfer in the porous electrodes can be modeled by the volume averaged equations, in which the quantities of interest are averaged over a representative elementary volume (REV). A rigorous development of these equations for modeling battery systems is presented elsewhere (Gu and Wang, 2000) which can equally be applied to an SOFC porous electrode. A basic assumption made is that the local thermal equilibrium condition exists, which is the case for SOFC electrodes (Damm and Fedorov, 2006). The general form of the equation for a composite electrode comprising of *k* phases is (Gu and Wang, 2000):

$$\nabla\bullet(-\overline{\lambda}\nabla T)+\overline{\rho c_p\mathbf{u}}\bullet\nabla T=q_{h,gen} \tag{4.10}$$

$\overline{\rho c_p\mathbf{u}}$ and $\overline{\lambda}$ are the average heat convection and the average heat conductivity of REV calculated as $\overline{\rho c_p\mathbf{u}}=\sum_k\phi_k\rho_k c_{p,k}\mathbf{u}_k$ and $\overline{\lambda}=\sum_k(\lambda_k^{eff}+\lambda_{a,k})$. ϕ_k, ρ_k, $c_{p,k}$, and $\mathbf{u}_k$ are respectively the volume fraction, density, specific heat capacity and velocity of the phase *k*. The effective conductivity of the phase *k*, λ_k^{eff}, includes the tortuosity effects. $\lambda_{a,k}$ is the hydrodynamic dispersion and appears as an artifact due to the volume averaging of the equations – it represents the effect of velocity and temperature variations within the REV. $q_{h,gen}$ is the volumetric heat source, which includes the volumetric and the interfacial heat generation within the REV.

Within the SOFC porous electrodes, the gas phase contribution to heat transfer is quite small compared to the solid phase, because of its relatively small heat capacity and thermal conductivity. $\lambda_{a,k}$ is zero by definition for the solid phase. Therefore Eq.(4.10) for the porous electrode simplifies to:

$$\nabla\bullet(-\lambda_{solid}^{eff}\nabla T)=q_{h,gen} \tag{4.11}$$

λ_{solid}^{eff} is the effective thermal conductivity of the solid phase. The heat transported by the flow of oxygen ions, the ionic current, can be included in the model (Fischer and Seume, 2009). However, its effect is negligible as the Thomson coefficient, equivalent to the heat capacity, of the oxygen ions in YSZ is shown to be half of that of the oxygen gas (Ratkje and Tomii, 1993).

Therefore if the convection of oxygen gas can be neglected, the Thomson effect can be ignored as well.

The heat generated within an electrode results from the reversible and the irreversible effects. The reversible heat is generated due to the entropy change of the electrochemical reactions, which will be discussed further. The irreversible heat results from the heat generated due to the resistive heating within the electrically conducting solids, i.e. the ohmic overpotential, and the heat generated because of the irreversibly activated nature of the electrochemical reactions, i.e. the activation overpotential. The volumetric irreversible heat source, $q_{h,irr}$, is calculated as:

$$q_{h,irr} = \sigma_{ionic}^{eff} \nabla V_{ionic} \bullet \nabla V_{ionic} + \sigma_{elec}^{eff} \nabla V_{elec} \bullet \nabla V_{elec} + i_{gen} \eta_{act} \tag{4.12}$$

The first two terms on the RHS of Eq.(4.12) represent the resistive heating caused by the ionic and the electronic currents, while the third term represents heating due to the activation overpotential. Note that the irreversible heat would be zero for an ideal fuel cell.

4.2.2 Radiative heat transfer

Thermal radiation is significant at the SOFC operating temperature. Surfaces exchange heat through radiation, and gases can absorb and emit radiation. The significance of the gas participation in radiative heat transfer depends on the physical nature of the gas and the geometry of the gas enclosure. The non-polar molecules on the cathode side, nitrogen and oxygen, do not participate in radiative heat transfer at all and are transparent to radiation. On the other hand, H_2O on the anode side participates in the bulk gas radiation and absorption. However, for a narrow gas channel (<5 mm) the gas is optically so thin that makes it practically transparent to thermal radiation (Damm and Fedorov, 2005).Simulation results also have shown that the participation of the anode gas in thermal radiation can be safely ignored for the tubular and planar geometries when the aspect ratio of the gas channel is high (Sanchez et al., 2006; VanderSteen and Pharoah, 2006). Therefore surface to surface radiation is the only significant radiative heat transfer mode in an SOFC with a narrow anode gas channels. Radiative heat transfer not only occurs between the surfaces of the gas channels, but also between the surfaces within the porous electrodes. Radiative heat transfer within an optically thick porous medium can be approximated as an enhancement to its thermal conductivity, i.e. Rosseland approximation. However, the Rosseland thermal radiative conductivity of the SOFC porous electrodes is much smaller than its solid phases thermal conductivity, and therefore can be safely ignored (Damm and Fedorov, 2005).

It is noteworthy that the solid electrolyte, YSZ, is an optically thin medium (Damm and Fedorov, 2005), and therefore radiative heat transfer occurs within the electrolyte as a participating medium. Some have suggested that the thermal radiation within the electrolyte can play an important role in heat transfer (Murthy and Fedorov, 2003). However, a detailed modeling analysis has concluded that radiation within a thin electrolyte has an insignificant effect on the temperature distribution within the system (Daun et al., 2006).

Based on the arguments presented above, only the radiative heat exchange among the gas channel surfaces was modeled, while the gases were assumed transparent and non-participating. On the air side, the inner surface of the furnace tube exchanged radiative energy with itself and with the outer surface of the TμSOFC. Similarly, the inner surface of the TμSOFC exchanged radiation with itself and the outer surface of the fuel injector tube inside it. Finally, the inner surface of the fuel injector tube exchanged radiation with itself. In addition, surfaces could exchange radiation with the environment when possible through the outlet of the air and the fuel gas channels.

A simplified schematic of radiative heat transfer within an enclosure is shown in Figure 4.1. The net radiative heat flux leaving any point (*x*) on a surface, q^r_{net}, is the difference between the radiative flux leaving, the radiosity (q^r_{out}), and that arriving at that point, the irradiation (q^r_{in}):

$$q^r_{net}(x) = q^r_{out}(x) - q^r_{in}(x) \tag{4.13}$$

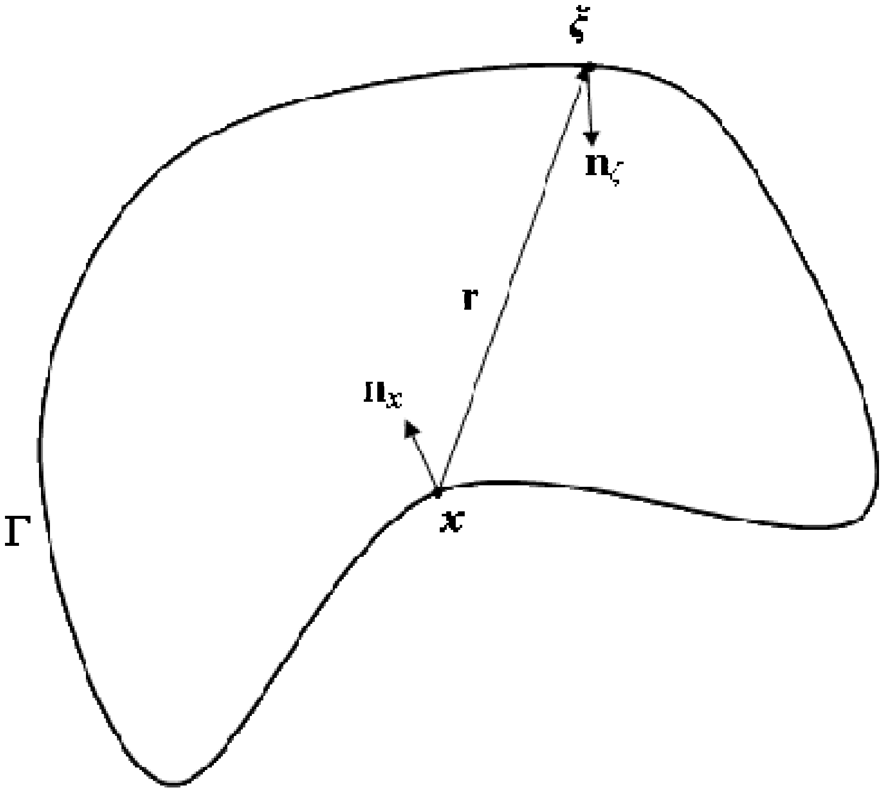

Figure 4.1. A schematic of the surface to surface radiation within an enclosure.

The radiosity of a surface consists of the emitted and the reflected radiation. For an opaque, gray, and diffuse surface it is:

$$q^r_{out}(x) = \varepsilon\sigma\left(T(x)\right)^4 + (1-\varepsilon)q^r_{in}(x) \tag{4.14}$$

The first term in Eq.(4.14) is the Stefan-Boltzmann expression for the radiative power of an opaque, diffuse, gray surface. ε is the emissivity of the surface, is a temperature dependent physical property, and can vary for different radiated wavelengths. σ is the Stefan-Boltzmann constant (5.67e-8 W.m^{-2}.K^{-4}).

The irradiation at any point (x) on the surface, is the sum of the radiative heat flux arriving to that point from every other point (ξ) on the surrounding surfaces (Γ):

$$q^r_{in} = \int_{\Gamma} q^r_{out}(\xi)\theta(x,\xi)\omega(x,\xi)d\xi \tag{4.15}$$

where ω is a geometric factor accounting for the effect of the surfaces relative orientation on the radiative power exchanged, and θ is the visibility factor:

$$\omega(x,\xi) = \frac{-(\mathbf{r}.\mathbf{n}_x)(\mathbf{r}.\mathbf{n}_\xi)}{\pi|\mathbf{r}|^4} \quad , \quad \theta(x,\xi) = \begin{cases} 1 & x \text{ and } \xi \text{ see each other} \\ 0 & \text{otherwise} \end{cases} \tag{4.16}$$

where **r** is the vector connecting the two points, and **n** is the normal vector at each point, as shown in Figure 4.1.

Equation (4.14) and (4.15) form a set of integro-differential equations on the radiating surfaces, the radiosity equation (Voigt et al., 2004), that models the surface to surface radiative exchange in an enclosure. The effect of radiative heat transfer is included in the model through Eq.(4.13) as a boundary condition which will be further discussed.

4.2.3 The thermodynamics of a non-isothermal electrochemical cell

Two aspects of the thermodynamics of a non-isothermal electrochemical cell are important for our model: the reversible heat generation and the non-isothermal electromotive force of a single-electrode. They should be calculated at each point within the electrode volume based on the local temperature, pressure, and composition. This is the only model to calculate electrochemical potentials locally within the SOFC electrodes experiencing temperature gradients.

4.2.3.1 The single-electrode reversible heat generation

Reversible heat generation is inherent to any fuel cell because the cell can only harvest the reaction Gibbs free energy change as electric power, not its enthalpy change. Therefore heat can be generated or consumed depending on the relative values of ΔH and ΔG. The overall reaction in an SOFC is exothermic, and the amount of heat released is significant; hence thermal management is a critical issue even in a very efficient SOFC.

Although the overall reaction in the SOFC is exothermic, the half-reactions occurring at each electrode are not necessarily exothermic. In fact, it has been shown that although the cathode reaction is always exothermic, the anode reaction can be endothermic (Ratkje and Mollerholst, 1993). This is in contrast with the assumption that the overall heat of reaction is released on the anode electrode, seen in some SOFC modeling literature (Li and Chyu, 2003; Li et al., 2004; Lu et al., 2005a, b; Yuan et al., 2009).

It is straightforward to calculate the reversible heat generation of the overall reaction from basic thermodynamics. In contrast, the estimation of the single-electrode reversible heat generation is not as simple. In this work, we calculate the reversible heat generation of each electrode individually as a function of the local temperature and pressure conditions, based on the entropy change of each half reaction:

$$q_h^{rev} = -T\Delta S(T, p_i) \tag{4.17}$$

The entropy change of the cathode reaction, Eq.(3.1)(c), per half a mole gaseous oxygen consumed is (Takehara et al., 1989):

$$\Delta S_{cathode}(T, p_i) = S^*_{O^{2-}}(T, p_i) - \frac{1}{2} S_{O_2}(T, p_i) - 2S^*_{e^-}(T, p_i) \tag{4.18}$$

where $S^*_{O^{2-}}$ and $S^*_{e^-}$ are the transported entropy of the oxygen ions and the electrons respectively, and S_{O_2} is the entropy of gaseous oxygen.

The challenging aspect of Eq.(4.18) is the estimation of the transported entropy of oxygen ions and electrons. They are not values reported in conventional thermodynamic references, unlike the entropy of neutral components. An excellent series of studies were conducted to experimentally estimate the transported entropy of the oxygen ions specifically in YSZ (Kanamura et al., 1991; Ratkje and Forland, 1991; Ratkje and Tomii, 1993; Takehara et al., 1989). This was done by the measurement of the thermoelectric effect that was induced between two oxygen electrodes by a temperature gradient held across a YSZ electrolyte. An excellent summary of these studies can be found elsewhere (Fischer and Seume, 2009). Based on irreversible thermodynamics, the Seebeck coefficient, which is the change in the electric potential difference between the two oxygen electrodes, divided by the temperature gradient across them, is related to the entropy change of the electrode half-reaction as:

$$\Delta S_{cathode}(T, p_{o_2}) = nF \frac{dE}{dT} \tag{4.19}$$

where $\frac{dE}{dT}$ is the Seebeck coefficient, F is the Faraday constant, and n is the number of electrons exchanged in the half reaction.

Experiments showed that the measured Seebeck coefficient was essentially independent of temperature (Ratkje and Tomii, 1993). In addition, the transported entropy of the oxygen ions was independent of the oxygen gas partial pressure (Ratkje and Forland, 1991). It was also found that the measured Seebeck coefficient was independent of the electrolyte sintering conditions, i.e. the electrolyte grain size, and the Yttria content of YSZ(Ratkje and Tomii, 1993).

We are interested in the reversible heat generation, or the entropy change, of the cathode reaction, within an electrode where temperature and oxygen concentration are not necessarily constant. Therefore, based on the available experimental data at a given condition, the terms on the RHS of Eq.(4.18) should be calculated for any temperature and oxygen partial pressure.

The first term on the RHS of Eq.(4.18), $S^*_{O^{2-}}$, was observed experimentally not to be a function of oxygen partial pressure, and therefore is only a function of temperature (Ratkje and Tomii, 1993):

$$S^*_{O^{2-}}(T, p_{o_2}) = S^*_{O^{2-}}(T^\circ) + \tau_{O^{2-}} \ln(\frac{T}{T^\circ}) \tag{4.20}$$

where $\tau_{O^{2-}}$ is the Thomson coefficient of the oxygen ion in YSZ.

The second term on the RHS of Eq.(4.18), the entropy of oxygen gas, can be calculated as a function of temperature and oxygen partial pressure, assuming ideal gas conditions:

$$S_{O_2}(T, p_{O_2}) = S_{O_2}(T^\circ, p^\circ_{O_2}) + c_{p,O_2} \ln(\frac{T}{T^\circ}) - R\ln(\frac{p_{O_2}}{p^\circ_{O_2}}) \tag{4.21}$$

The transported entropy of electrons, $S^*_{e^-}$, is relatively small compared to other terms on the RHS of Eq.(4.18), and its change with temperature and pressure is negligible. At 1000°C $S^*_{e^-}$ is estimated to be 2 (Pollock, 1985), 3 (Pollock, 1985), and 1 (Ahlgren and Poulsen, 1996) $J.K^{-1}.mol^{-1}$ for Pt, Ni and LSM respectively. These values are comparable to the measurement error of the Seebeck coefficient, and therefore not significant. Hence, the transported entropy of electrons was assumed to be equal to that of Pt, $S^*_{e^-}$=2 $J.K^{-1}.mol^{-1}$, in all of our calculations regardless of the type of the electrode electronic conductor.

Combining Eqs.(4.18), (4.20), and (4.21), one would obtain:

$$\Delta S_{cathode}(T, p_{o_2}) = S^*_{O^{2-}}(T^\circ) + \tau_{O^{2-}} \ln(\frac{T}{T^\circ}) - \frac{c_{p,O_2}}{2} \ln(\frac{T}{T^\circ}) - \frac{1}{2}\left(S_{O_2}(T^\circ, p^\circ_{O_2}) - R\ln(\frac{p_{O_2}}{p^\circ_{O_2}}) \right) - 2S^*_{e^-}(T^\circ) \quad (4.22)$$

Based on the observation that the measured Seebeck coefficient was independent of temperature, it can be concluded that $\tau_{O^{2-}} \simeq c_{p,O_2} / 2$. Therefore the entropy change of the cathode would be only a function of the partial pressure of oxygen and independent of temperature:

$$\Delta S_{cathode}(p_{o_2}) = S^*_{O^{2-}}(T^\circ) - \frac{1}{2} S_{O_2}(T^\circ, p^\circ_{O_2}) - 2S^*_{e^-}(T^\circ) + \frac{R}{2}\ln(\frac{p_{O_2}}{p^\circ_{O_2}}) \quad (4.23)$$

or

$$\Delta S_{cathode}(p_{o_2}) = \Delta S_{cathode}(T^\circ, p^\circ_{O_2}) + \frac{R}{2}\ln(\frac{p_{O_2}}{p^\circ_{O_2}}) \quad (4.24)$$

The Seebeck coefficient of a Pt/YSZ electrode was experimentally estimated to be -0.463 ± 0.004 mV.K^{-1} at 1273K and 1 atm pure oxygen (Ratkje and Tomii, 1993), which corresponds to $S^*_{O^{2-}} = -41 \pm 1$ J.K^{-1}.mol^{-1} and $\Delta S_{Cathode} = -89.3 \pm 1$ J.K^{-1}.mol^{-1}; $\Delta S_{Cathode}$ is per one mole of O^{2-} generated, equivalent to half a mole of O_2 consumed, as in Eq.(3.1)(c).

The final expression for calculating the volumetric reversible heat generation within the cathode is:

$$q^{rev}_{h,Ca} = \frac{-i_{gen}}{2F}(-T\Delta S_{cathode}(T, p^\circ_{O_2})) = \frac{i_{gen}T}{2F}\left(-89.3 + \frac{R}{2}\ln\left(\frac{p_{O_2}}{1\times 10^5} \right) \right) \quad (4.25)$$

Note that i_{gen} is the rate of electron generation, while electrons are consumed according to the stoichiometry of the half-reaction, as in Eq.(3.1)(b); hence the negative sign is used in Eq.(4.25).

Knowing the entropy change of the cathode electrode, one can conveniently calculate the entropy change of the anode half-reaction. The entropy change of the overall reaction, $\Delta S_{cell}(T, p_i)$, is the sum of the entropy changes of each half reaction:

$$\Delta S_{anode}(T, p_i) = \Delta S_{cell}(T, p_i) - \Delta S_{cathode}(T, p_i) \tag{4.26}$$

Based on the thermodynamics of an ideal gas system, we have:

$$\Delta S_{cell}(T, p_i) = \Delta S_{cell}(T, p_i^{\circ}) + R\ln\left(\frac{(p_{H_2} / p_{H_2}^{\circ})(p_{O_2} / p_{O_2}^{\circ})^{1/2}}{(p_{H_2O} / p_{H_2O}^{\circ})}\right) \tag{4.27}$$

From Eqs.(4.26) and (4.27):

$$\Delta S_{cell}(T, p_i) = \Delta S_{cell}(T, p_i^{\circ}) + R\ln\left(\frac{(p_{H_2} / p_{H_2}^{\circ})(p_{O_2} / p_{O_2}^{\circ})^{1/2}}{(p_{H_2O} / p_{H_2O}^{\circ})}\right) - \left(\Delta S_{Cathode}(T^{\circ}, p_{O_2}^{\circ}) + \frac{R}{2}\ln(\frac{p_{O_2}}{p_{O_2}^{\circ}})\right) \tag{4.28}$$

Assuming the same standard pressure for all the components, the entropy change of the anode reaction per mole of hydrogen consumed is:

$$\Delta S_{anode}(T, p_i) = \Delta S_{cell}(T, p_i^{\circ}) + R\ln\left(\frac{p_{H_2}}{p_{H_2O}}\right) - \Delta S_{Cathode}(T^{\circ}, p^{\circ}) \tag{4.29}$$

Note that, unlike the cathode, the anode reaction entropy change is a function of temperature.

The final working expression for calculating the volumetric heat source within the anode is:

$$q_{h,andoe}^{rev} = \frac{i_{gen}}{2F}\left(-T\Delta S_{anode}(T, p_{O_2}^{\circ})\right) = -\frac{i_{gen}T}{2F}\left(\Delta S_{cell}(T, p_i^{\circ}) + R\ln\left(\frac{p_{H_2}}{p_{H_2O}}\right) + 89.3\right) \tag{4.30}$$

where a polynomial expression for calculating the entropy change of the overall reaction at the standard pressure, $\Delta S_{cell}(T, p_i^{\circ})$, is given in the appendix. Note again that i_{gen} is the volumetric electron generation rate and electrons are generated according to the stoichiometry of the anode half-reaction, as in Eq.(3.1)(a), therefore its sign remains unchanged. Note also that in the above development it was implicitly assumed that the transported entropy of electrons within the anode and cathode conductor were the same, which is a valid approximation as discussed before.

The entropy change of the anode and the cathode reactions are plotted against the composition in Figure (4.2). It is clear that within the operating range of SOFCs, the cathode reaction is exothermic. The anode reaction however tends to become more endothermic at a higher partial pressure of hydrogen compared to oxygen. In fact, the anode reaction is endothermic even when the partial pressure of hydrogen is as small as a hundredth of that of gaseous water. Hence, the anode reaction is practically endothermic for SOFC systems, as fuel utilization is much less than those levels. Therefore it is more appropriate to assume that the overall heat of electrochemical reactions in an SOFC is released on the cathode side, if an assumption should be made. In this work that the reversible heat of each electrode is calculated within each electrode, the cathode would generate heat while the anode would absorb heat. Again, the overall reaction is exothermic at SOFC operating conditions; $\Delta S_{cell}(1073K, p_i^\circ)$ = -55.6 J.K^{-1}.mol^{-1}.

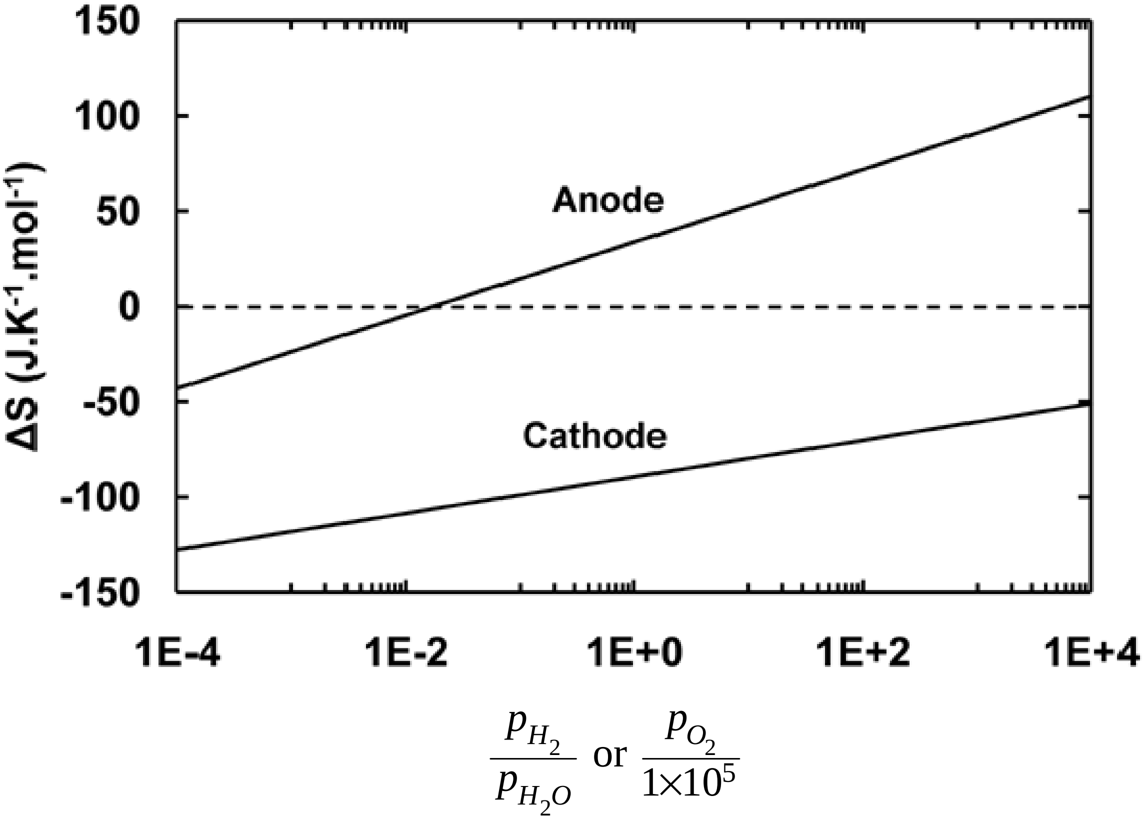

Figure 4.2. The entropy change of the anode and the cathode reactions as a function of partial pressure of the components.

4.2.3.2 The electromotive force of a non-isothermal electrochemical cell

The electromotive force of an isothermal cell can be calculated based on the change in the Gibbs free energy of the overall cell reaction according to the Nernst law:

$$-nF\varepsilon_{cell} = \Delta G_{cell}(T_a, p_i) \tag{4.31}$$

The Gibbs free energy change of the cell reaction, assuming an ideal gas system is:

$$\Delta G_{cell}(T, p_i) = \Delta G_{cell}(T, p_i^{\circ}) + RT \ln\left(\frac{(p_{H_2O} / p_{H_2O}^{\circ})}{(p_{H_2} / p_{H_2}^{\circ})(p_{O_2} / p_{O_2}^{\circ})^{1/2}}\right) \tag{4.32}$$

Calculation of the electromotive force of a non-isothermal cell is not as straightforward. The Gibbs free energy change of a cell with its anode and cathode at T_a and T_c, is the sum of the Gibbs free energy changes its electrodes each:

$$\Delta G_{cell} = \Delta G_{An}(T_a, p_i) + \Delta G_{Ca}(T_c, p_i) \tag{4.33}$$

From basic thermodynamic relations, one can rewrite Eq.(4.33) as:

$$\Delta G_{cell} = \Delta G_{An}(T_a, p_i) + \Delta G_{Ca}(T_a, p_i) - \int_{T_a}^{T_c} \Delta S_{Ca}(T, p_i) dT \tag{4.34}$$

and therefore:

$$\Delta G_{cell} = \Delta G_{cell}(T_a, p_i) - \int_{T_a}^{T_c} \Delta S_{Ca}(T, p_i) dT \tag{4.35}$$

In an alternative development, the electric work method can been applied to a non-isothermal electrochemical cell to obtain the exact same equation as Eq.(4.35) (Ratkje and Mollerholst, 1993).

In the previous section, $\Delta S_{Ca}(T, p_i)$ was shown to be independent of temperature; therefore the last term of Eq.(4.35) can be integrated analytically. For the overall cell reaction of Eq.(3.1)(c), and based on Eqs.(4.24), (4.32), and (4.35), the cell potential can be calculated as:

$$-2F\varepsilon_{cell} = \Delta G_{cell}(T_a, p_i) - (T_c - T_a)\left(\Delta S_{Cathode}(p^{\circ}) + \frac{R}{2}\ln(\frac{p_{O_2}}{p^{\circ}_{O_2}})\right) \tag{4.36}$$

The second term on the RHS of Eq.(4.36) shows that in non-isothermal cells, there is an added effect to the cell electromotive force, proportional to the temperature difference of the electrodes. As it was discussed before, $\Delta S_{Cathode}$ was experimentally estimated to be -89.3 J.K^{-1}.mol^{-1} for a YSZ based SOFC. Therefore a YSZ based SOFC that has its cathode at a higher temperature than its anode would have a higher electromotive force compared to an isothermal cell. Note however that ΔG_{cell} at 800°C and standard pressure is -188.6 kJ.mol^{-1}; therefore a 20°C difference between the anode and the cathode introduces a small difference, about 1%, in the electromotive force of a cell at 800°C and standard pressure. Add to that the fact that the temperature differences across the very thin TμSOFC layers is expected to be much smaller than 20°C, as it will be seen in the simulation results. Nonetheless, it is interesting to estimate how the temperature gradients within each electrode affect the cell's overall electromotive force, as the temperature gradients within the same electrode along the tubular cell can be quite significant.

It is clear that the electromotive force of an electrode is a function of the components partial pressures, as seen in Eq.(4.36), which is not constant within each electrode. Therefore variations in the local electromotive force within each electrode should be accounted for. The absolute value of the electromotive force of each electrode cannot be estimated, as the absolute Gibbs free energy change of each electrode cannot be determined. It is sufficient however to calculate the electromotive force of each point within the electrodes compared to a reference electrode at the standard conditions. Using the same reference for the anode and the cathode, the potential difference between them can be obtained properly. Therefore, we develop expressions for the anode electromotive force by pairing each point within the electrode with an oxygen electrode at the standard conditions as the reference electrode. We are interested in the cathodic half-potential of each electrode while Eq.(4.36) estimates the anodic potential, as the electrode of interest is the anode while the cathode is the reference electrode. Therefore the negative of the cell potential calculated from equation (4.36) is the cathodic potential of each electrode. For the anode:

$$-2F\left(-\varepsilon_{anode}(T,p_{H_2},p_{H_2O})\right)=\Delta G_{cell}(T,p_i^\circ)+RT\ln\left(\frac{p_{H_2O}}{p_{H_2}}\right)-(T^\circ-T)\Delta S_{Cathode}(p^\circ) \qquad (4.37)$$

Similarly for the cathode, we would have a concentration / thermoelectric cell against an oxygen reference electrode. Note that the last term in Eq.(4.36) is equal to zero, as the partial pressure of oxygen corresponds to that of the reference cathode electrode, which is at the standard conditions. The Gibbs free energy change would be that of a concentration cell:

$$\frac{1}{2}O_2(p_{O_2})\longrightarrow\frac{1}{2}O_2(p_{O_2}^\circ) \qquad \Delta G_{cell}(T_a,p_i)=\frac{RT}{2}\ln\left(\frac{p_{O_2}}{p_{O_2}^\circ}\right) \qquad (4.38)$$

The cathodic half-potential is negative of the potential calculated from Eq.(4.36); therefore:

$$-2F\left(-\varepsilon_{cathode}(T,p_{O_2})\right)=\frac{RT}{2}\ln\left(\frac{p_{O_2}}{p_{O_2}^\circ}\right)-(T^\circ-T)\Delta S_{Cathode}(p^\circ) \qquad (4.39)$$

Eqs. (4.37) and (4.39) are the working relations for calculating the local OCV within each electrode; they are consistent overall, as Eq.(3.36) can be recovered assuming constant partial pressures within electrodes and considering that $\varepsilon_{cell}=(\varepsilon_{cathode}-\varepsilon_{anode})$.

4.3 Model implementation

The model equations form a set of highly nonlinear interdependent differential equation that had to be solved simultaneously, with proper boundary conditions. Taking advantage of the axial symmetry of the system, the equations had to be solved numerically on a 2-dimensional domain, see Figure 3.2, without any loss in accuracy.

4.3.1 Model parameters

The model parameters included the thermo-physical properties and the kinetic constants, which were calculated using appropriate local conditions, i.e. pressure, temperature, and concentration. Expressions to estimate the thermo-physical properties, i.e. the heat capacities, the enthalpy, the entropy, and the Gibbs free energy change of the overall reaction, the thermal conductivity of the gases and the solids, and the emissivity of the solids are given in the appendix.

The reaction kinetic constants for each electrode are critical for the accuracy of the model predictions. For the isothermal model, the reaction kinetic parameters had been estimated by fitting the performance curve against the experimental results conducted at isothermal conditions in a three-zone furnace. For the purpose of the non-isothermal study, Arrhenius type functions were used to extrapolate the temperature dependence of the reaction kinetic constants estimated for the isothermal model in Chapter 3. The values are presented in Appendix A.

The exponential constant (the activation energy, E_a) of the cathode kinetic expression was estimated experimentally based on the electrochemical impedance spectroscopy technique (EIS) of symmetric electrodes on button-cell samples, as explained in Chapter 6. For the anode however, a value obtained from the literature was used. It was concluded in Chapter 3 that the cathode electrochemical kinetic is a major performance bottleneck, while the anode was highly active and influenced the overall performance marginally. Therefore using an anode activation energy value from the literature instead of an experimental estimation was not expected to introduce a significant error.

The temperature-dependent effective electronic conductivity of the cathode layer was also estimated experimentally, as explained in Chapter 6. The temperature dependent electric conductivities of the solids are presented in the appendix. The effective electronic conductivity of the anode support and the anode functional layer was extrapolated from the values estimated in our 800°C isothermal experiments, using nickel's activation energy obtained from the literature. The error introduced because of this estimation was of concern, as it was observed that the electronic conductivity of the anode support layer was unusually high and therefore could significantly influence the overall performance predictions; see Chapter 6. Although the experimental measurement of the ASL electronic conductivity was made at various temperatures, severe irreproducibility made them practically useless to be implemented in the model.

The fuel and air flowrates were 50 and 100 mL.s^{-1} at standard conditions for the experiments and the model.

4.3.2 Boundary conditions

A Dirichlet boundary condition was used at the inlet of the air and the fuel gas channels, prescribing the inlet temperature. Experiments showed that air was preheated before entering the system, due to the relatively low air velocity. Therefore the air inlet temperature was set to 625°C, consistent with experimental measurements (TC-5 in Figure 2.5). The hydrogen inlet temperature was assumed to be 25°C, as it was entering with a high velocity into the system.

On the outlet of the gas channels, a pure convection boundary condition was assumed, by setting the thermal conduction equal to zero:

$$\mathbf{n} \bullet \{-\bar{\kappa}\nabla T\}_{\text{gas outlet}} = 0 \tag{4.40}$$

A constant inward heat flux was assumed along the furnace's outer surface, representing the effect of the electric heating-coil:

$$\mathbf{n}^{\text{solid}} \bullet \{-\kappa \nabla T\}_{\text{furnace external boundary}} = \dot{q}_{\text{furnace}} \tag{4.41}$$

where $\mathbf{n}^{\text{solid}}$ is the unity vector normal to the boundary, facing toward the furnace wall.

The surface to surface radiation was implemented as a heat source on the solid/gas boundaries:

$$-\mathbf{n}^{\text{solid}}\bullet(\{-\kappa\nabla T\}^{\text{solid}}_{\text{solid/gas boundary}}-\{-\kappa\nabla T\}^{\text{gas}}_{\text{solid/gas boundary}})=q^{\text{r}}_{\text{net}} \tag{4.42}$$

where $\mathbf{n}^{\text{solid}}$ is the unity vector normal to the boundary facing inward the solid domain. $q^{\text{r}}_{\text{net}}$ is the net radiative out-flux at every point on the boundary, calculated from the radiation model.

For all the boundaries separating the domains, the continuity of temperature and conductive heat flux was assumed:

$$\mathbf{n}\bullet\left\{\mathbf{N}_i^{\,h}\right\}^{\text{solid 1}}_{\text{solid/solid boundary}}=-\mathbf{n}\bullet\left\{\mathbf{N}_i^{\,h}\right\}^{\text{solid 2}}_{\text{solid/solid boundary}} \tag{4.43}$$

$$\left\{T\right\}^{\text{solid 1}}_{\text{solid/solid boundary}}=\left\{T\right\}^{\text{solid 2}}_{\text{solid/solid boundary}} \tag{4.44}$$

Note that this boundary condition is valid at the interfaces with different porosities because superficial fluxes and intrinsic temperatures were used in the averaged transport equations within for the porous electrodes.

The flux along the geometry’s axis of symmetry was set to zero:

$$\mathbf{n}\bullet\{-\kappa\nabla T\}_{\text{axis of symmetry}}=0 \tag{4.45}$$

The boundary conditions for the rest of the equations are the same as those for the isothermal model, explained in Chapter 3.

4.3.3 Geometry discretization

The model geometry was discretized by a numerical mesh, as shown in Figure 3.2. As explained before, a structured multi-scale mesh was used to discretize the domain, as there was a significant length-scale difference within the modeled domains, from the micron thin electrodes to the centimeter wide gas channels. The mesh had 40 nodes in the cross section of the air channel, the diffuser tube, and the annular space between the diffuser and the cell. It had 320 nodes along the active length of the cell and a total number of 480 nodes along the furnace. 40 nodes were used to resolve the cross section of each layer of the active length. The mesh was finer where steeper changes were expected, i.e. close to the solid walls, as well as the electrode/electrolyte interface where most of the electrochemical reactions were expected to occur. Using a structured mesh drastically reduced the computational demand of the numerical scheme, as illustrated before. In addition, the numerical convergence was faster and much smoother due to alignment of transport fluxes with the mesh.

4.3.4 Equation discretization

The model equations formed an inter-coupled system of highly non-linear equations. A commercial finite element solver, COMSOL, was used to numerically discretize the model equations on the 2D axi-symmetric domain, and to iteratively solve it. Second order Lagrangian polynomials were used to discretize and approximate the solution on the numerical grid.

Note that unlike the transport equations, planar or axial symmetry does not exist for radiation models. Although there is no net heat flux across the symmetry boundary, the surfaces do “see” and exchange heat with each other across the symmetry plane. Therefore any geometrical symmetry is meaningless for radiation models, and they have to be solved on the complete geometry. Despite this, the symmetry boundary condition has been occasionally used for the radiation model (Sanchez et al., 2006; Suwanwarangkul et al., 2006) which would imply inaccuracies of unknown magnitude. The complete geometry of our model was generated by rotating the 2D domain around its axis of symmetry in 128 azimuthal sectors. The radiosity equation, Eq.(4.14), was discretized on the resulting mesh into surfaces that exchanged radiation with each other (Weichmann et al., 2004). The view factors between the surface elements were then calculated based on the hemi-cube method (Cohen and Greenberg, 1985). The hemi-cube method is commonly used in computer graphics to render geometrically complex environments, and can effectively handle the effect of objects blocking each other out. The view factors were calculated once and for all at the beginning of the solution. The resulting discretized radiosity equation was linear in terms of the radiosity, which had to be simultaneously solved with the rest of the model.

4.3.5 Numerical solution

The discretized equations were solved using the Newton's iterative method, with a direct solver, UMFPACK, to solve the linearized set of equations. The computations were performed on 16 Quad-Core AMD Opteron 8274 CPUs equipped with 66GB of RAM.

As the system of equations were highly non-linear, an appropriate solving strategy and a suitable initial solution were essential for obtaining a converged numerical solution. To solve the non-isothermal model, a solution for the isothermal model was used as the initial solution: the temperature of the entire domain was fixed at the temperature of the middle of the active length (TC-2). The solution strategy for the isothermal cell, to have a guaranteed and stable numerical convergence, was explained in Chapter 3. The furnace heat flux however was unknown and had to be found such that the temperature of the middle of the active length (TC-2) was equal to the desired value. This was done by solving a function that solved the non-isothermal model, and had furnace heat flux as its input variable and TC-2 as its output variable; Newton's method was used to find a solution for the heat flux.

4.4 Experimental validation

The model predictions were compared to the experimental results in two aspects: the overall cell performance, and the temperature distribution within the system. As it was mentioned before, no parameter fitting was done for this model; all the parameters were obtained experimentally or from the literature, and the kinetic parameters at 800°C were estimated in the isothermal model. Therefore all the results presented here are completely predictive.

The overall cell performance predicted by the model at various temperatures is compared to the experimental results in Figure 4.3. There is an excellent agreement between the predictions and the experimental results, indicating the predictive capacity of the model most notably for predictions at temperatures other than 800°C where no kinetic parameter fitting was done.

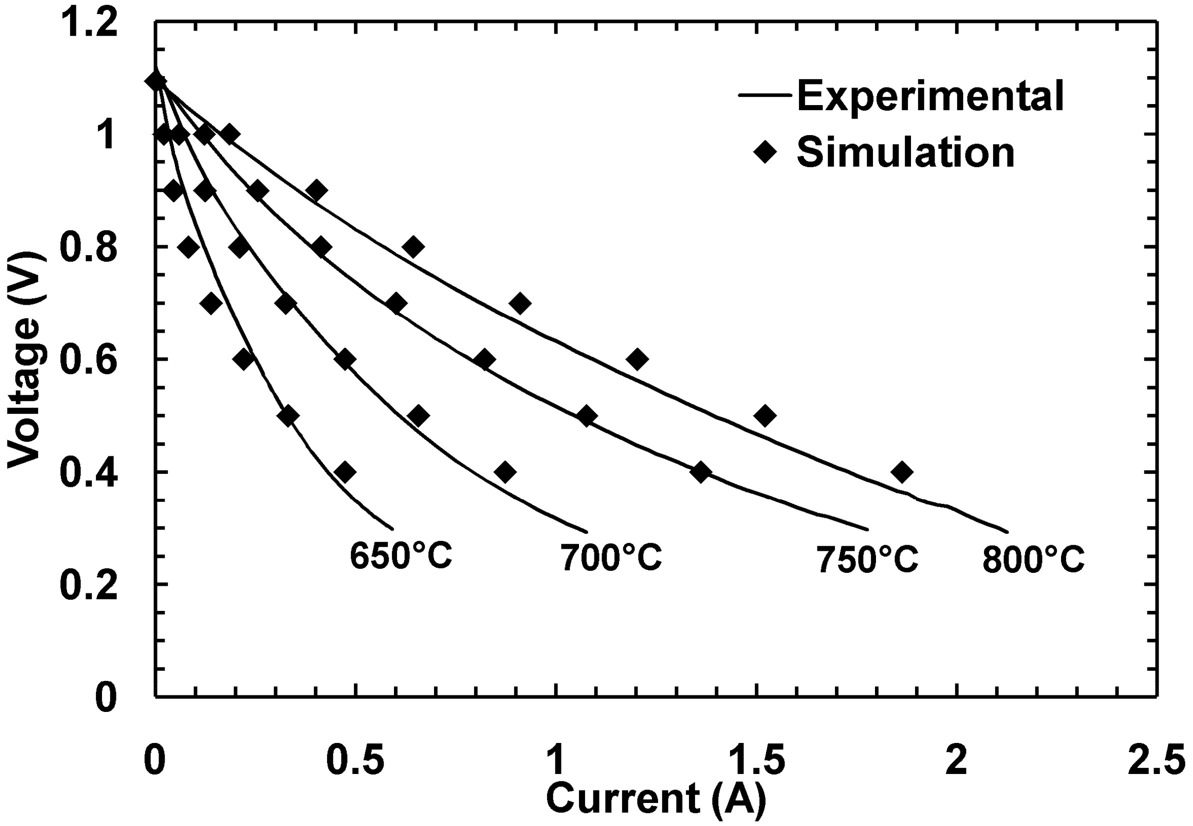

Figure 4.3. The overall performance prediction of the cell at various temperatures and the experimental results.

The predicted temperature distribution is compared to the experimental in Figure 4.4. As the three thermocouple rods attached to the cell had a thickness comparable to the TµSOFC's very thin wall, they influenced the temperature distribution around the cell within the furnace. The thermocouple rods enhanced the thermal conduction along the cell, acting similar to a thermal fin. The thermocouples could not be included in our 2D axi-symmetric model because it would not be symmetric anymore, requiring a full 3D simulation. Therefore the influence of the thermocouples was accounted for by enhancing the thermal conductivity of the anode support layer. This enhanced the radial conductivity of the anode support layer; however its effect on the radial temperature distribution was negligible; because as it will be shown by the simulation results, the radial temperature gradients across the wall were very small. Including the effect of thermocouple rods in fact did improve the predicted temperature distribution in the cell, as seen in Figure 4.4. This is especially true for TC-1, which was closest thermocouple to the furnace outlet, and therefore the thermal fin effect was the most among the other thermocouples. It can be concluded that the thermocouples did indeed affect the thermal distribution within the furnace. A similar effect has been reported to occur within monolith reactors, where the fin effect of the thermocouple rods interfered with the temperature readings (Rankin et al., 1995). Nonetheless, without the thermocouple effect, temperature distribution predictions and its trend were quite acceptable. As we were interested in the behavior of the cell itself, all the subsequent results are reported for the model that does not include the thermocouples effect.

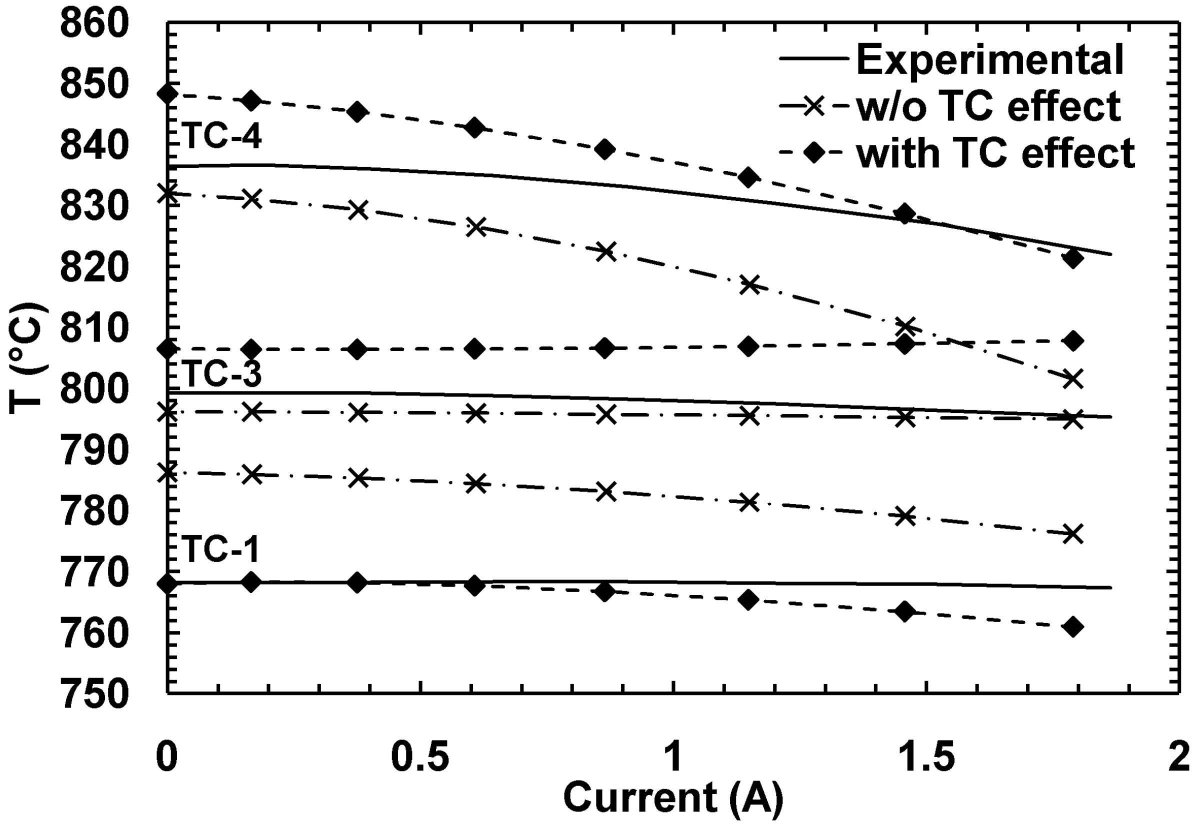

Figure 4.4. The temperature distribution prediction within the furnace versus the experimental.

4.5 Results and discussion

The model was numerically solved to obtain details of the temperature distribution, the fluid flow, the concentration profile within the gas channels and the porous electrodes, and the electrochemical reactions within the electrodes. We will focus mainly the thermal aspect of the model here; the essence of the results on the rest of the model was very similar to the isothermal results presented in Chapter 3.

4.5.1 Gas flow and concentration distribution

Hydrogen and oxygen were consumed as the flow passed by the active length of the cell, and their concentration decreased; see figure 4.5.

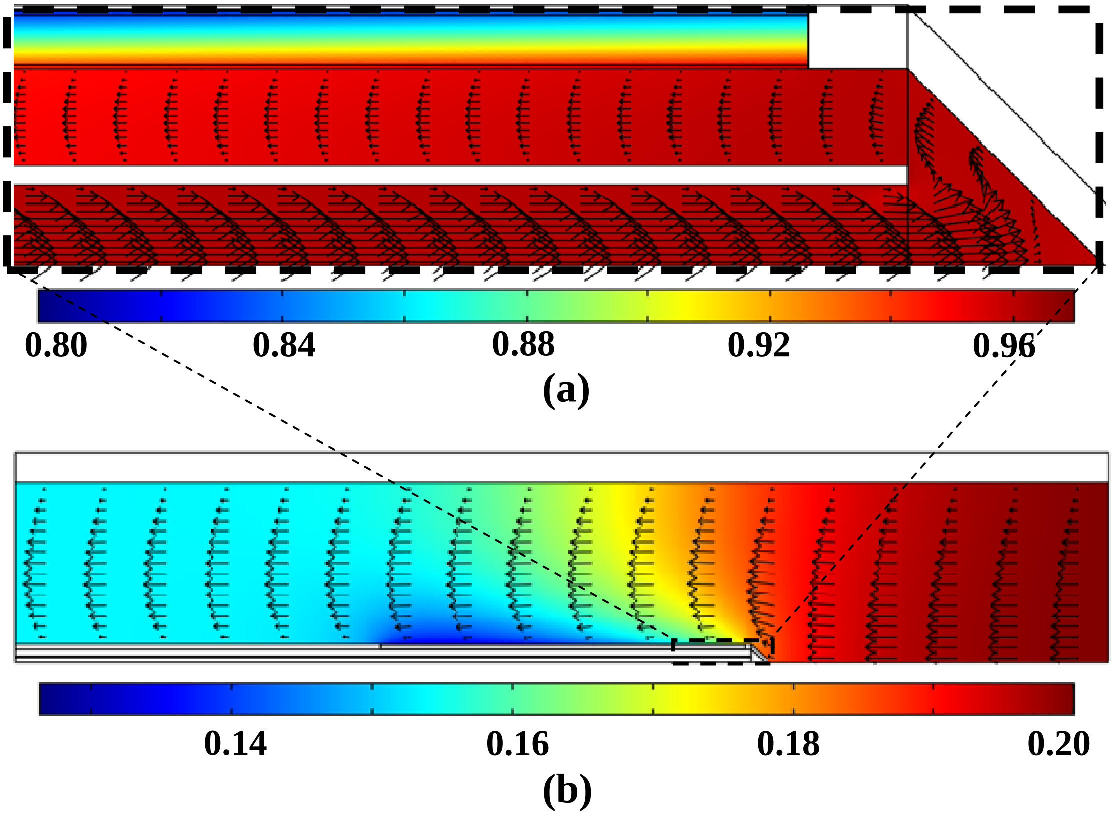

Figure 4.5. The simulated concentration distribution and the velocity profile: (a) the hydrogen mole fraction on the anode side; (b) the oxygen model fraction on the cathode side. The arrows show (a) the hydrogen, and (b) the air velocity profile.

Note that the velocity profile within the gas channels is shown by arrows, which are normalized within their own gas channel. The velocity in the fuel cell tube was much higher than the velocity in the air channel.

4.5.2 Volumetric current and heat generation within each electrode

Figure 4.6 shows the volumetric electron generation within the anode and the cathode, which corresponds to the rate of electrochemical reactions. The reaction rates were clearly higher at the electrode/electrolyte interface due to the lower ionic conductivity of YSZ compared to the electronic conductivity of LSM or Ni. Note that the reaction rate peaked much higher within the anode compared to the cathode and had a shorter extension within the electrode. These are because of the much higher electro-catalytic activity of the anode compared to the cathode.

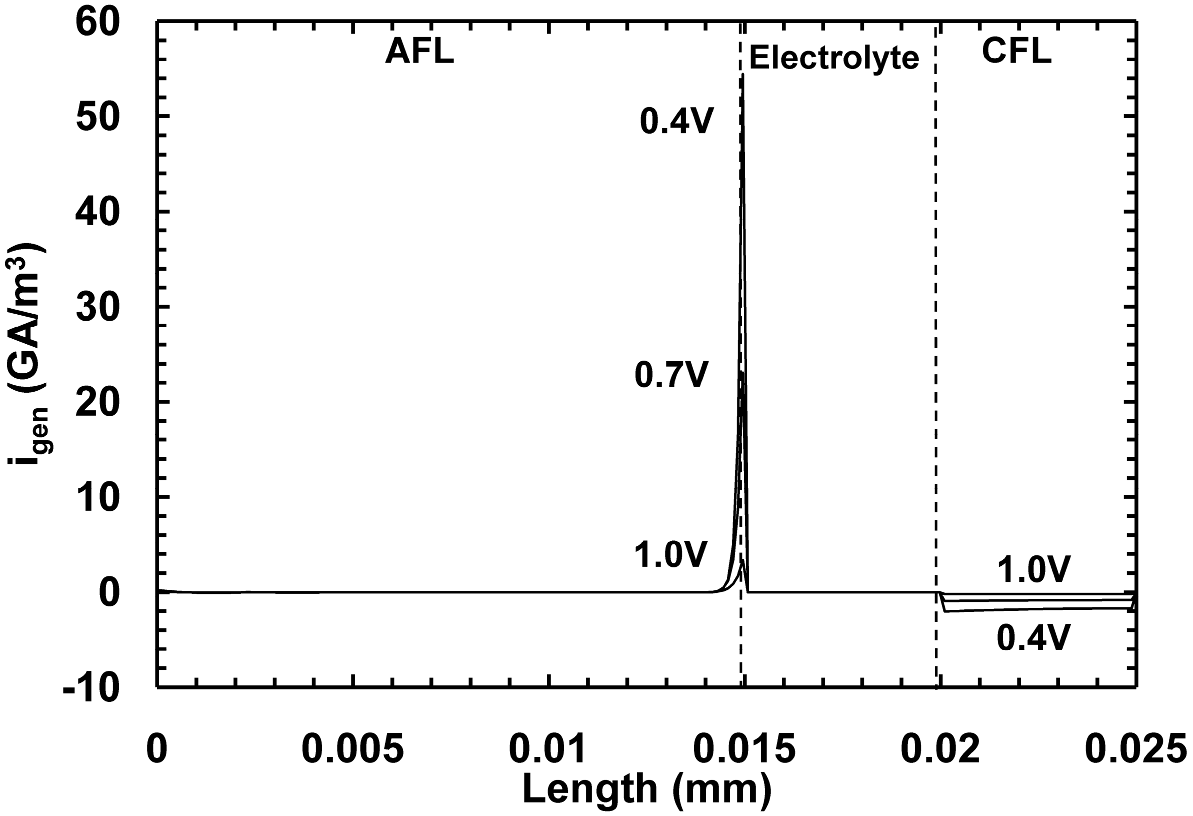

Figure 4.6. The volumetric electron generation within the anode and the cathode in the radial cross section at the middle of the active length.

Figure 4.7 shows the total volumetric heat generation within the cell layers. There are peaks at the electrolyte/electrode interface, corresponding to the peaks in the volumetric electron generation profile, as the reversible and the activation heat generation are proportional to the reaction rates. Clearly, heat was absorbed on the anode/electrolyte interface and was generated on the cathode/electrolyte interface.

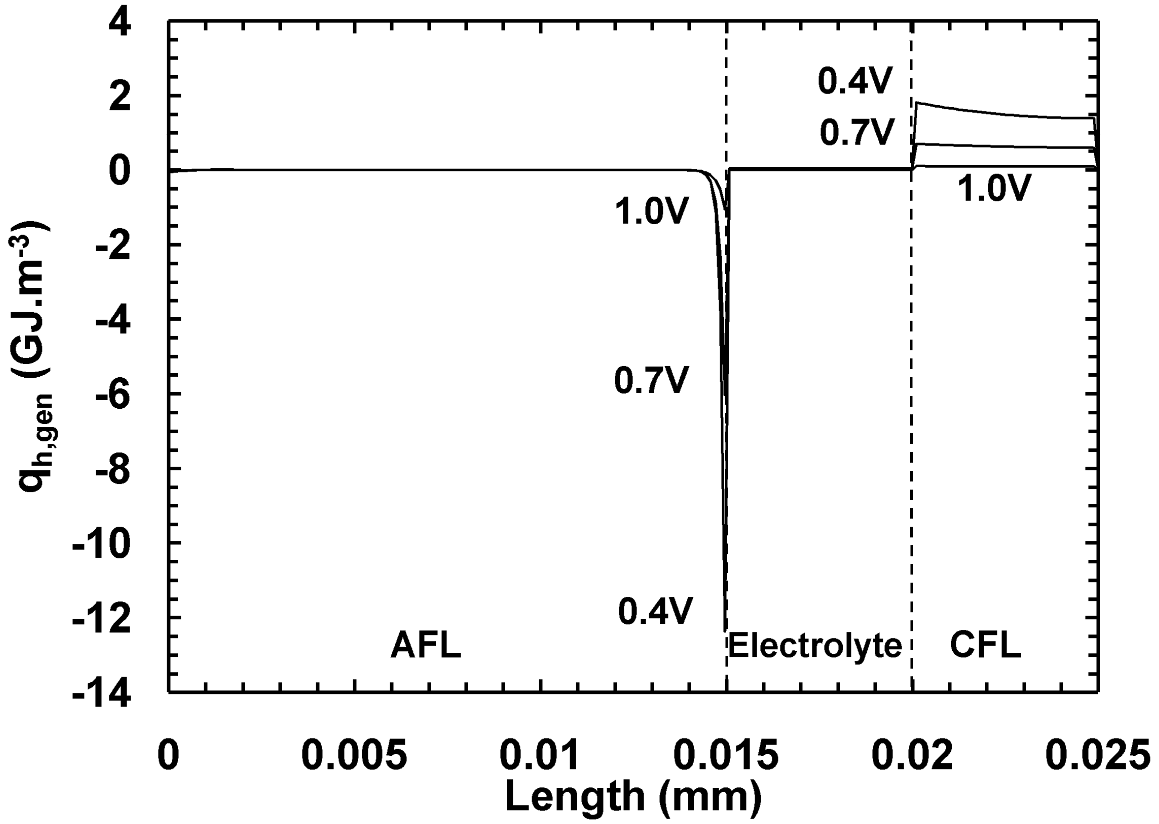

Figure 4.7. The volumetric heat generation within the cell layers in the radial cross section at the middle of the active length.

The total volumetric heat generation on the anode/electrolyte and the cathode/electrolyte interfaces along the cell active length are respectively presented in Figures 4.8 and 4.9. Although they changed along the cell, the anode remained endothermic, and the cathode remained exothermic. This is consistent with the conclusion made previously, based on Figure 4.2, that the anode and the cathode reactions are expected to always be endothermic and exothermic respectively, within the concentration range encountered in an SOFC.

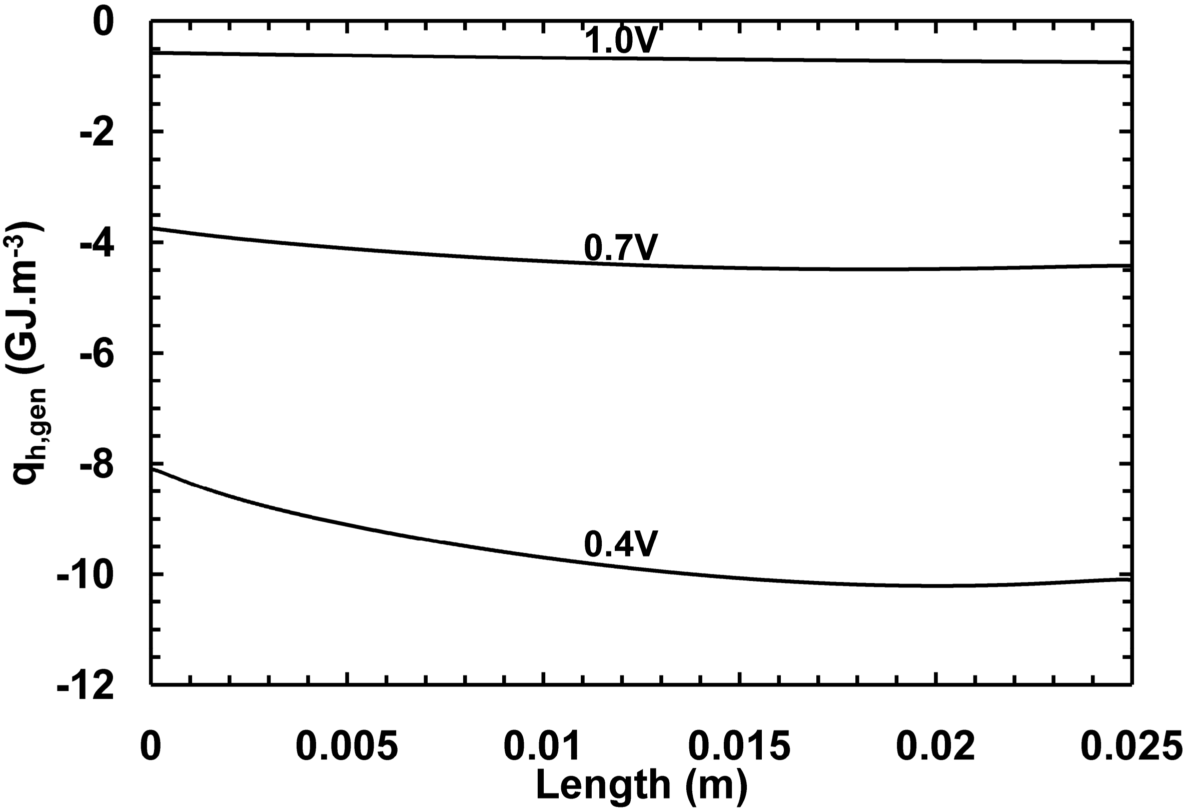

Figure 4.8. The volumetric heat generation along the active length at the anode/electrode interface.

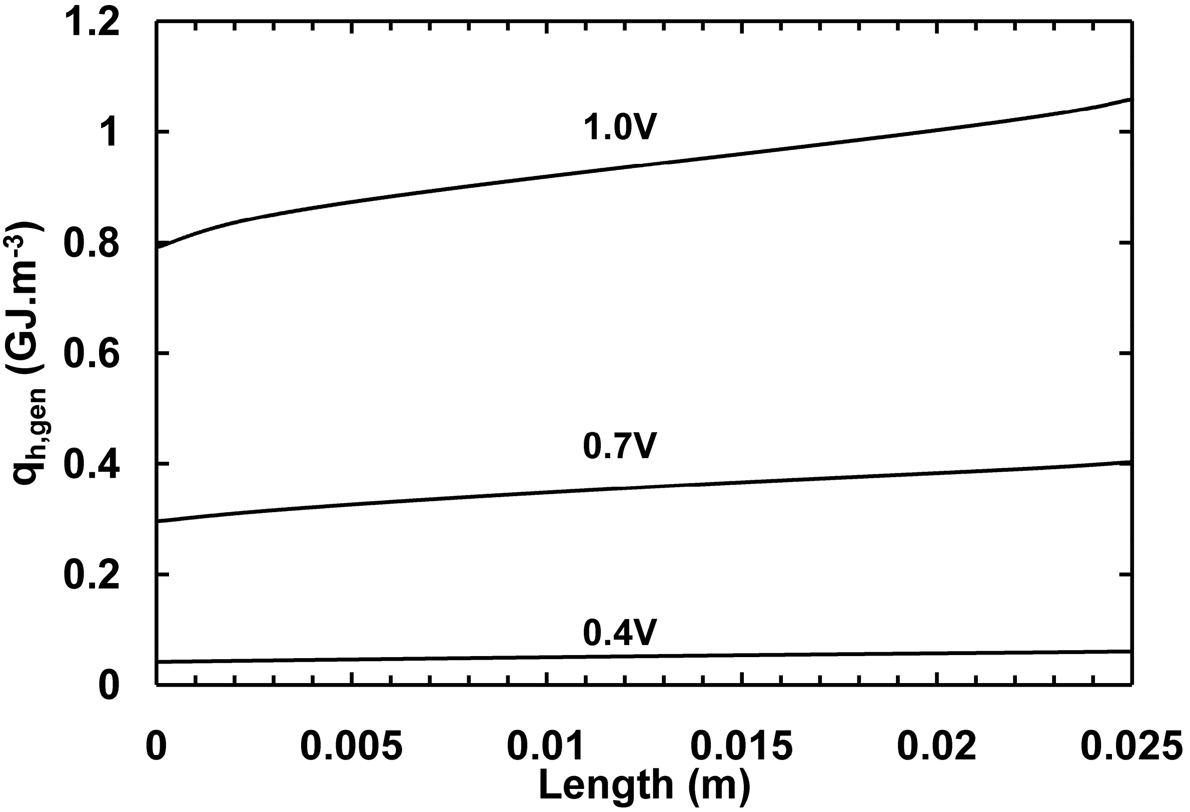

Figure 4.9. The volumetric heat generation along the active length at the cathode/electrode interface.

4.5.3 Temperature distribution within gas channels and cell layers

The predicted temperature profile within the furnace and the TμSOFC for a range of cell voltages is shown in Figure 4.10; a lower voltage corresponds to a higher current load, as shown in Figure 4.3. Note that the temperature decreased towards the outlet mainly due to the thermal radiation lost to the ambient, through the open end of the furnace. It is clear that the temperature profile had a complex pattern, which completely changed as the current load changed. At a low current load, the furnace heat flux kept the cell at its operating temperature, because not much heat was generated by the active length. The maximum temperature occurred around the middle of the furnace tube. At a high current load however, the shape of the temperature profile changed around the active length, and had a maximum at the middle of the active length. This is because of the significant heat released by the electrochemical reactions occurring within the active length of the cell. Note that these simulations are for the case were the furnace load was controlled to maintain TC-2 at 800°C; the furnace heating load was smaller at higher current levels as explained later in Figure 4.17.

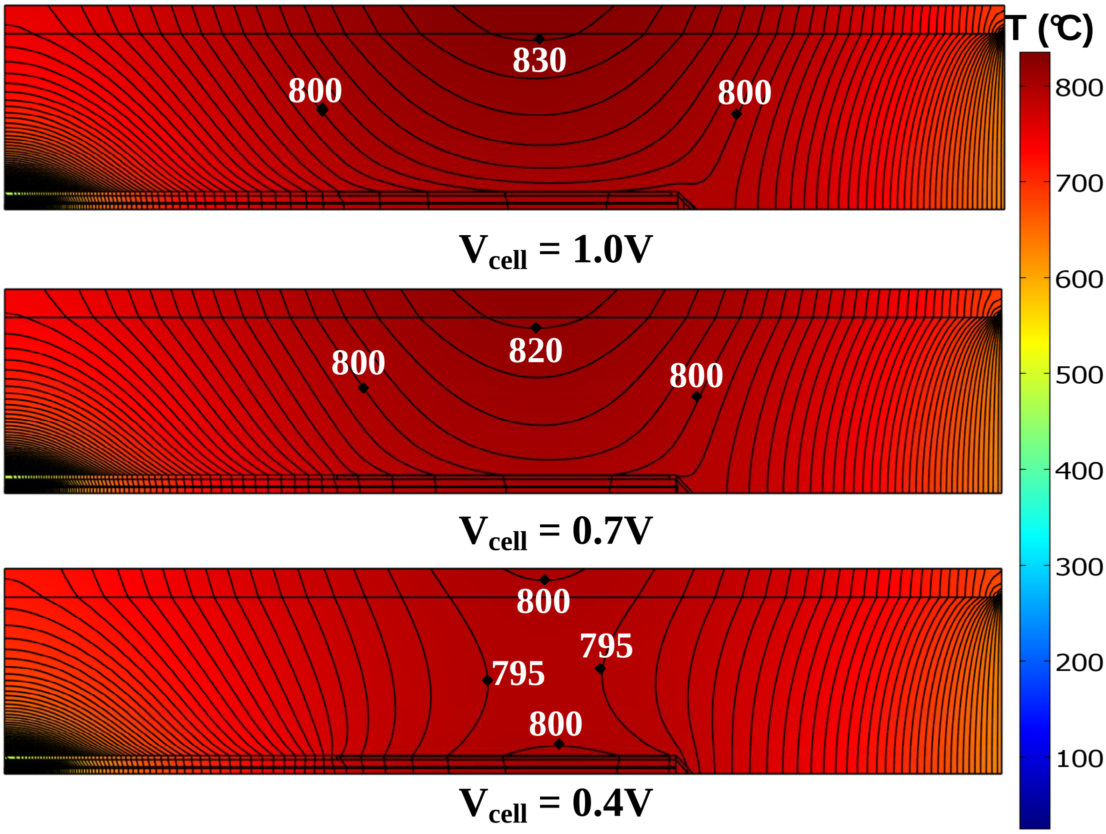

Figure 4.10. The predicted temperature distribution at various cell voltages. The adjacent contours are 5°C apart.

The temperature within the electrode and the electolyte increased because of the heat generation. It is of practical importance to know the magnitude of this temperature rise, and whether it is within the acceptable range. The temperature profile across the active length is shown in Figure 4.11, distinguishing the several cell layers. It is clear that the temperature rise within the cell active length was very small, less than 0.05°C, even at the highest current load. Interestingly, despite the small magnitude of the temperature changes, minute details are apparent in the temperature profile. The temperature profile slightly peaked at the cathode/electrolyte interface, where most of the heat was generated. The temperature had a flat peak within the anode support layert at the high current load, resulting from the ohmic heating. The temperaure within current collectors were very flat, due to the very high thermal conducitvity of gold.

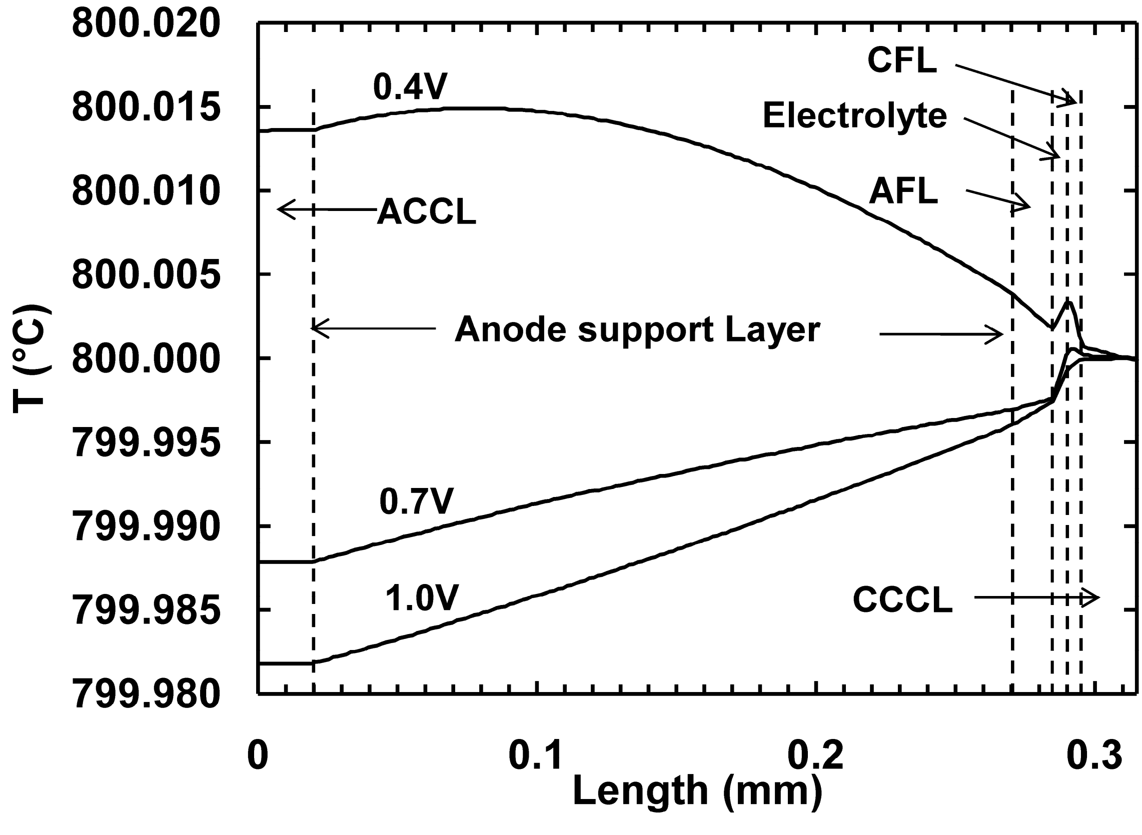

Figure 4.11. The temperature distribution within the cell layers in the radial cross section at the middle of the active length.

The temperature distribution in the radial direction at the middle of the furnace is shown in Figure 4.12. The temperature gradients were very small within the fuel channel, because of the strong convective heat transfer, resulting from the high gas velocity. The temperature difference between the cell surface and the furnace wall reached as high as 30°C.

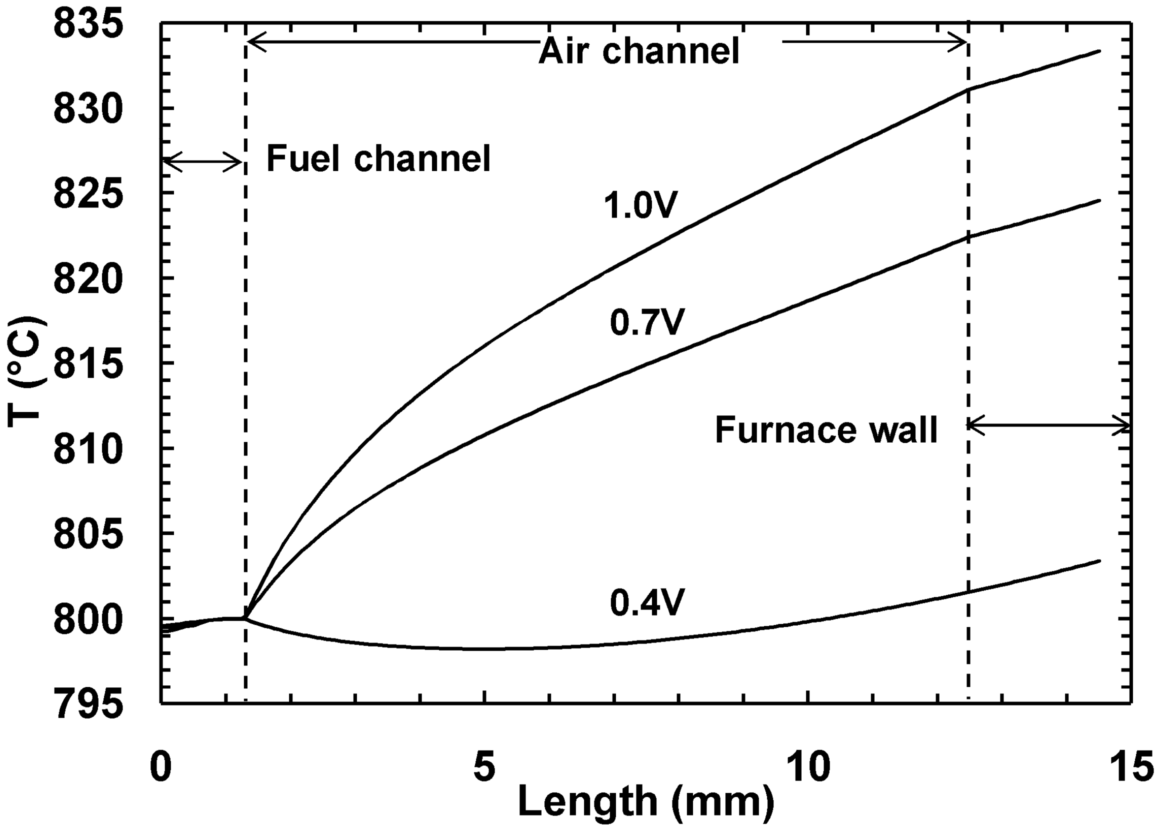

Figure 4.12. The temperature distribution within the furnace in the radial cross section at the middle of the active length.

Figure 4.13 shows the temperture profile along the active length of the cell at the cathode/gas channel interface; the temperature across the layers is the same as discussed before. Temperature gradienst were higher at higher current loads, but always less than about 25°C. All curves intersect at the same point at the middle of the active length, which corresponts to TC-2 being kept at 800°C by the furnace controller.

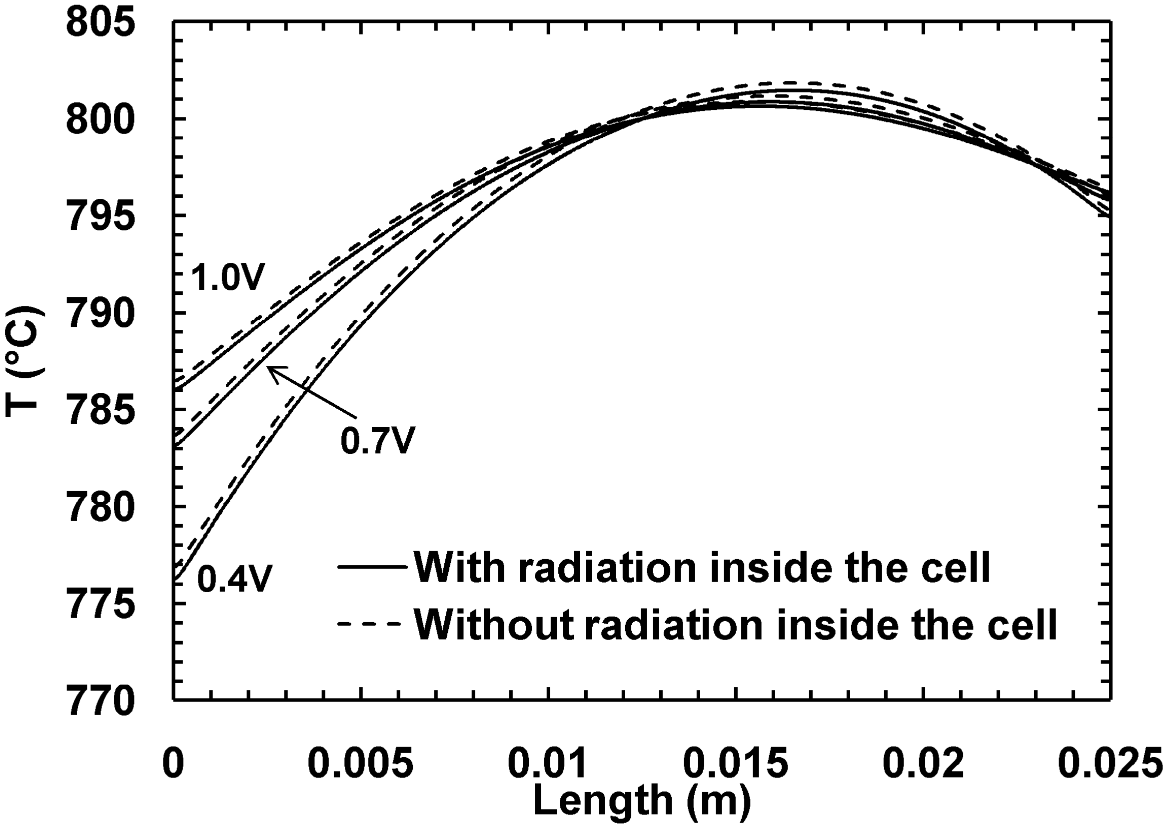

Figure 4.13. Temperature distribution along the active length at the cathode/air interface.

Figure 4.13 also shows that the temperature distribution along the active length of the cell changed negligibly when radiative heat transfer within the cell was ignored. This is because of the strong thermal convection inside the cell, which significantly reduced the temperature gradients and therefore the effect of thermal radiation inside the cell.

4.5.4 Overall reversible and irreversible heat generation

The total electric power and the total heat generation rate by the cell, as well as the contribution of irreversible and reversible effect to the total heat are presented in Figure 4.14. The electric power produced by the cell peaked around 1.5 A. It declined at higher current levels as a result of the increased performance losses. The total heat generated by the cell increased with a higher rate at higher current loads. The enthalpy of reaction was almost equally split between electric power and heat generation around 1.1 A. In contrast to reversible heat generation, irreversible heat generation increased significantly with the current load.

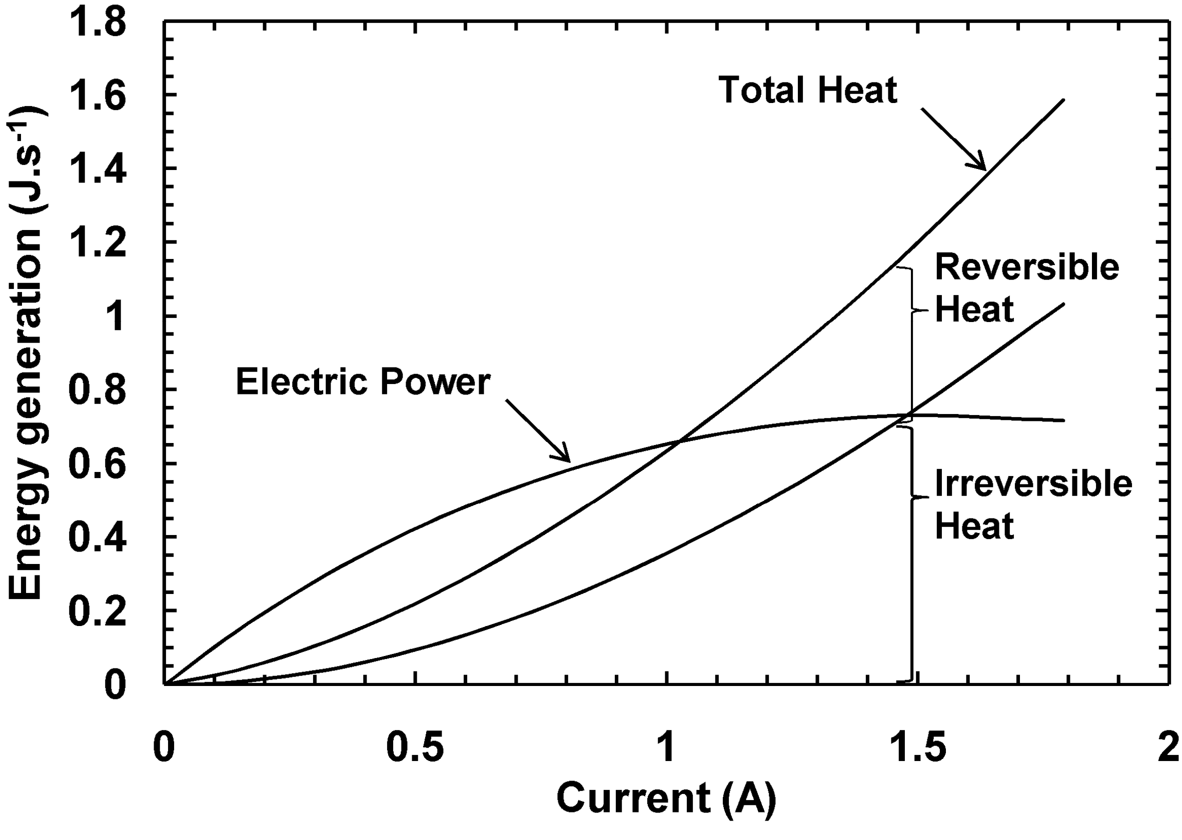

Figure 4.14. The cell overall electric power and heat generation rate.

The overall heat generation rate by each electrode and the contribution of the reversible and irreversible effects to each is presented in Figure 4.15. The irreversible heat generation was always positive for the anode and the cathode. The reversible heat of the anode was negative, while it was positive for the cathode. Therefore the cathode was exothermic overall. The anode however was endothermic, as the magnitude of the irreversible heat generated was less than the reversible heat absorbed. The total heat generated on the anode side had a minimum as current increases, and was less endothermic at higher current levels as the effect of irreversible heat generation became greater.

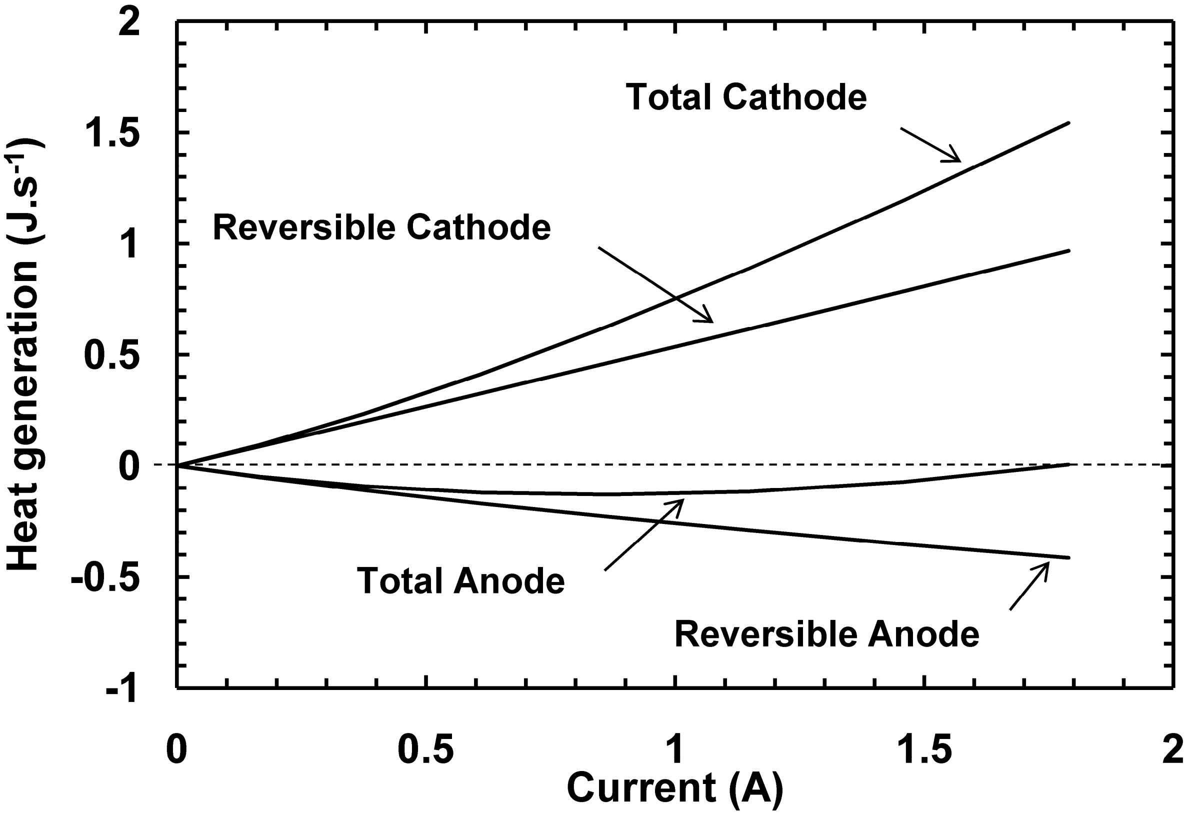

Figure 4.15. The overall heat generation rate within the electrodes.

The temperature of the cell would increase due to heat generation as it operates if the furnace heat flux is constant. This is shown in Figure 4.16. The temperature of the middle of the active length (TC-2) was 800°C, initially when no current was drawn from the cell. Keeping the furnace heat flux constant, the temperature rose by about 40°C when ~2A (corresponding to V_{cell}=0.4) current was drawn from the cell.

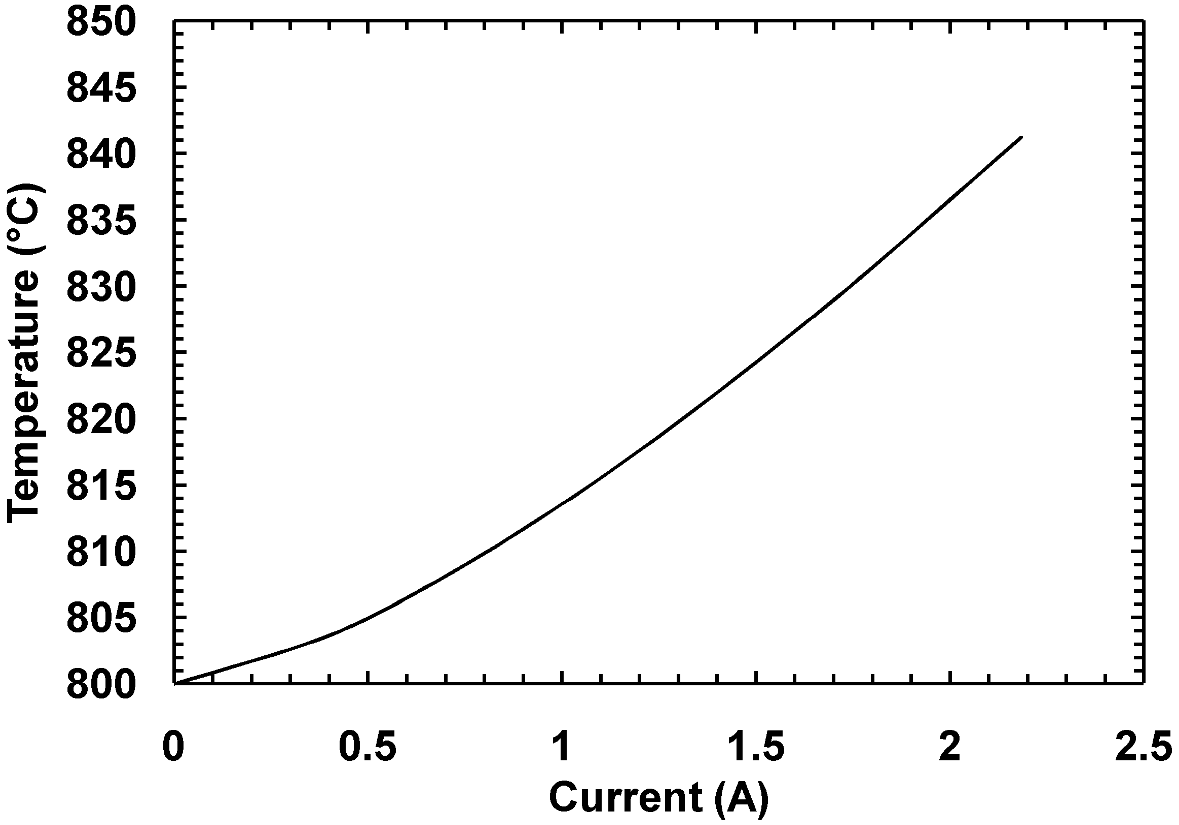

Figure 4.16. The temperature of the middle of the active length (TC-2) as current is drawn from the cell.

4.5.5 The significance of modeling heat transfer

The performance predictions of the isothermal model at 800°C and the non-isothermal model are compared in Figure 4.16. The predicted performance curves are very close. This is due to the fact that the temperature of the active length was higher than 800°C at some regions, and less than 800°C at some other regions. Therefore for our system, an isothermal model predicted the cell overall performance quite accurately. This observation is consistent with a previous modeling study concluding that isothermal models can be acceptably used for the overall performance prediction (Sanchez et al., 2007). Figure 4.16 also shows that including the effect of temperature gradients in the electromotive force of the cell did not affect the overall performance of the cell predictions at all, as its curve overlaps with the non-isothermal model curve.

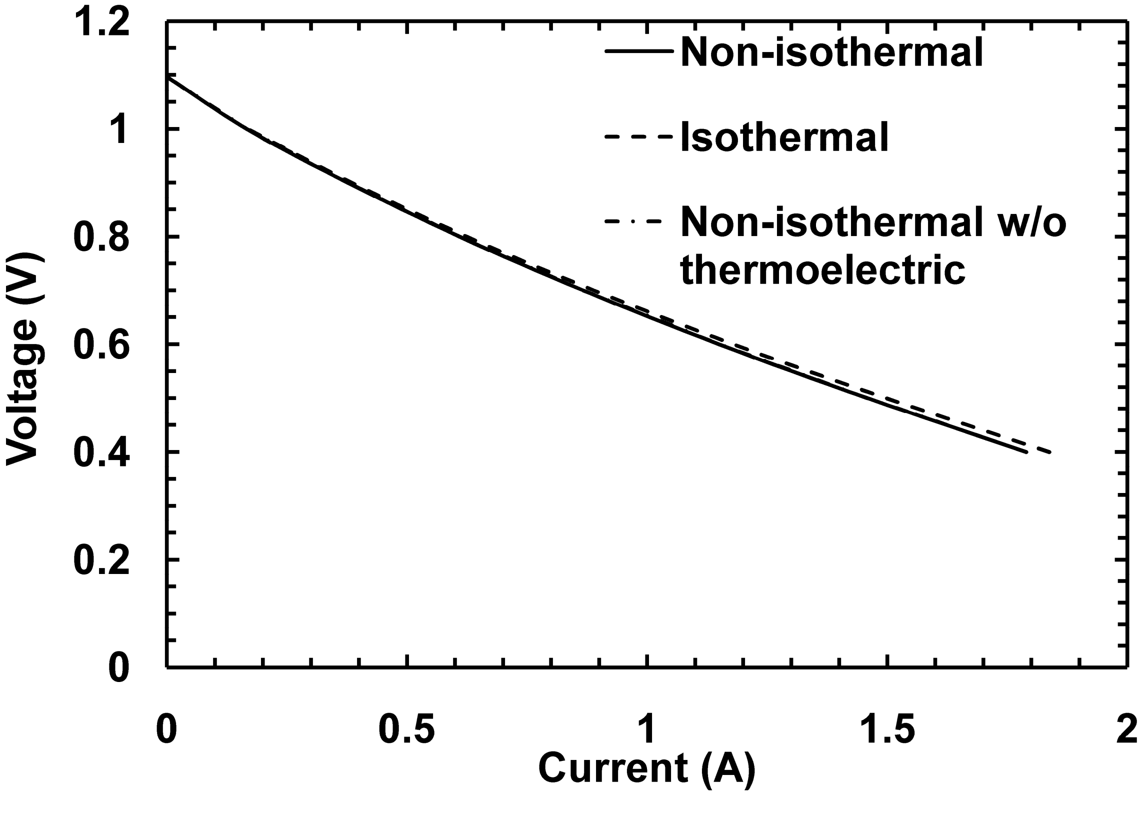

Figure 4.16. The overall performance curves predicted by the isothermal model, the non-isothermal model, and the non-isothermal model without the effect of temperature gradients on the cell electromotive force.

Heat should be always provided to the system to keep it at its operating temperature, as the numerically estimated furnace heat flux was always positive; see Figure 4.17. These values should be lower than real values, as in reality the furnace tube loses heat to the environment despite the insulation around it. The trend shows that at higher current loads, when the cell was generating more heat, less heat flux had to be provided by the furnace.

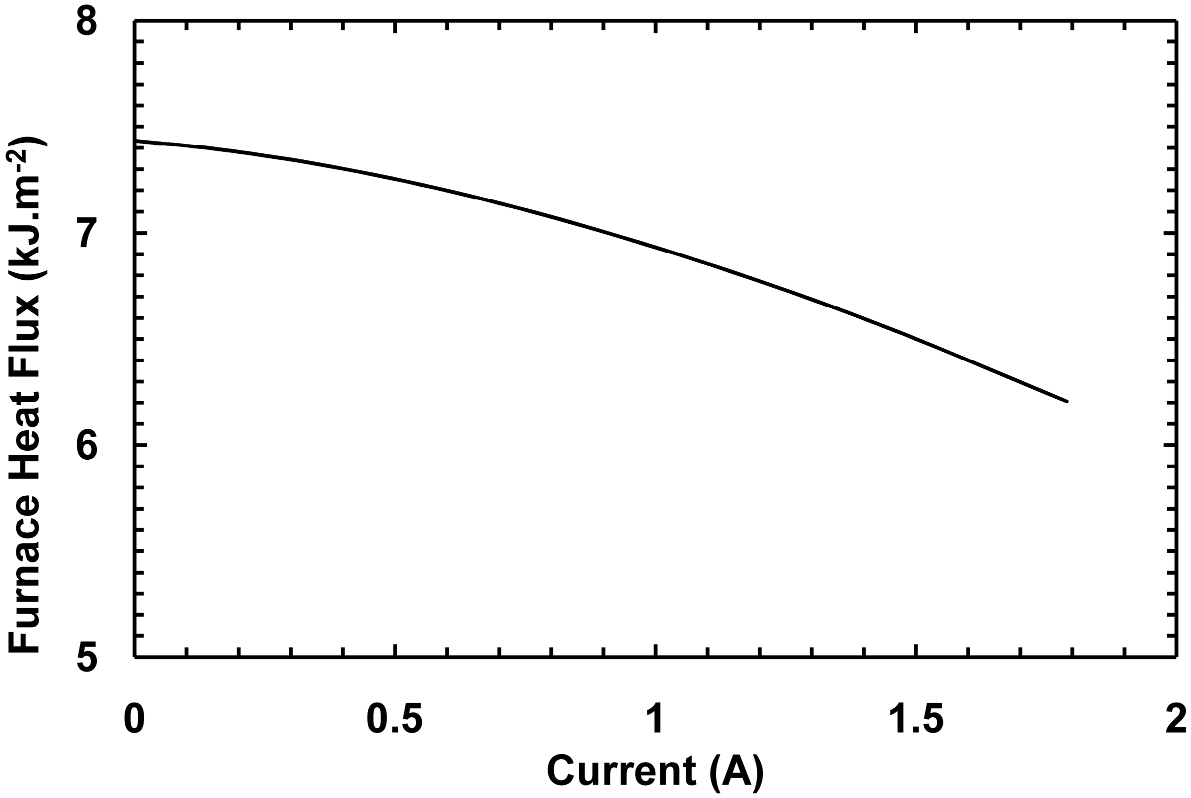

Figure 4.17. The estimated furnace heat flux at various current loads.

4.5.6 The significance of radiative heat transfer

The heat transferred from the cathode at the cathode/gas interface, due to thermal radiation and thermal conduction were relatively comparable at low current loads, see Figure 4.18. At high current levels radiation became much more significant than thermal conduction, practically becoming the main mechanism for heat transfer. The outward radiative flux was positive all along the active length, indicating that the cathode was losing heat to the surfaces around it. Figure 4.18 illustrates how complex the interaction of the heat transfer mechanisms can become, making it difficult to draw general conclusions without a detailed assessment.

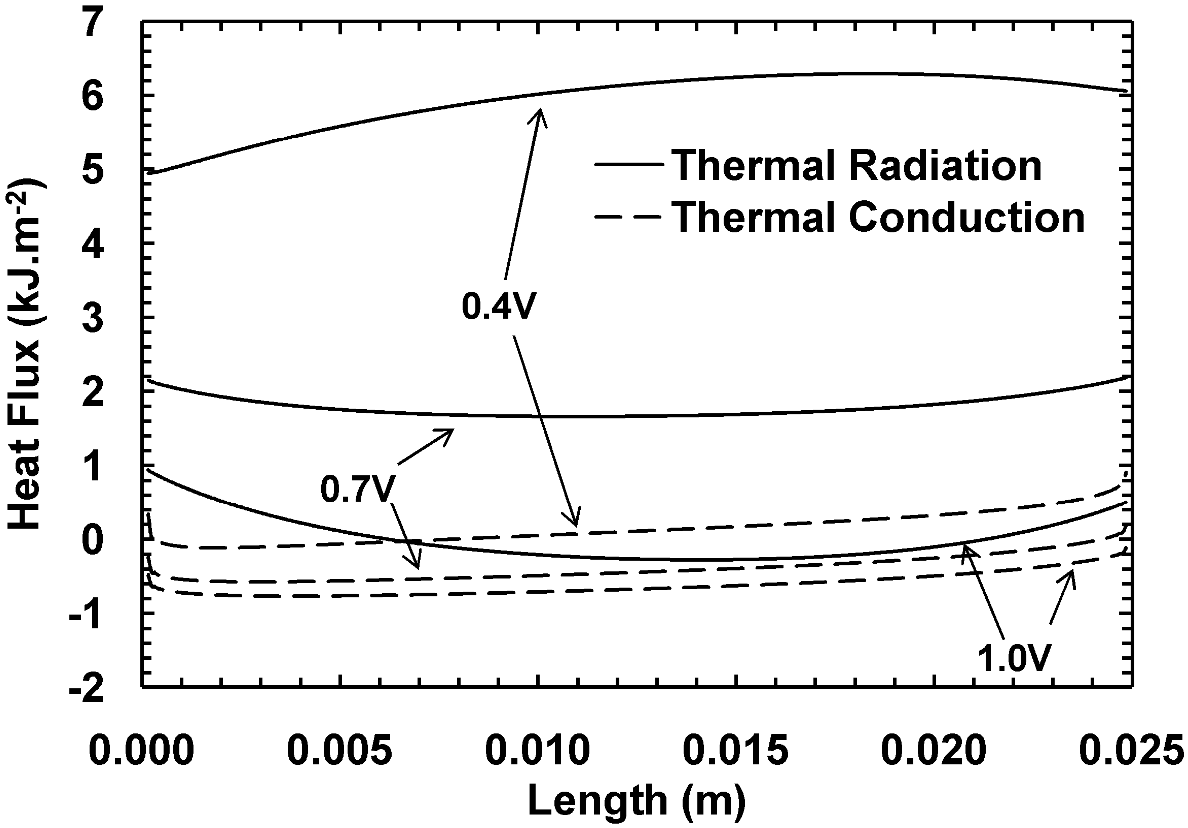

Figure 4.18. The heat transferred away from the cathode by thermal radiation and thermal conduction at the cathode/gas interface.

The effect of ignoring radiation was studied for a cell operating at 0.4V. The initial effort to model heat transfer without including radiation was unsuccessful, as the numerical solver did not numerically converge to a solution. In a transient simulation, which started from the converged steady-state isothermal simulation at 800°C, the temperature of the active length increased from 800°C in a run-away fashion. This was because the conductive and the convective heat transfer could not dissipate enough heat from the cell to maintain a steady state, even when the heat flux provided by the furnace was zero. Higher temperatures in turn increased the current generation, as the reaction kinetics were faster at higher temperature, causing an unrealistic reaction run-away. To avoid the temperature run-away in the no-radiation model, a hypothetical simulation was conducted where the kinetic and the material properties were decoupled from temperature, and evaluated at 800°C. The result is shown in Figure 4.19. The cell active length still experienced a maximum temperature of about 850°C, despite zero furnace heat flux. This again indicates that not including radiation in the heat transfer can result in a non-physical situation. In practice, the cell rapidly cooled down and lost power as soon as the furnace was turned off. Radiative heat transfer on the anode side had an insignificant impact on the temperature distribution along the active length, as shown in Figure 4.13, due to the high convective heat transfer inside the cell. Therefore radiation on the air side was the significant heat transfer mechanism which could not be ignored.

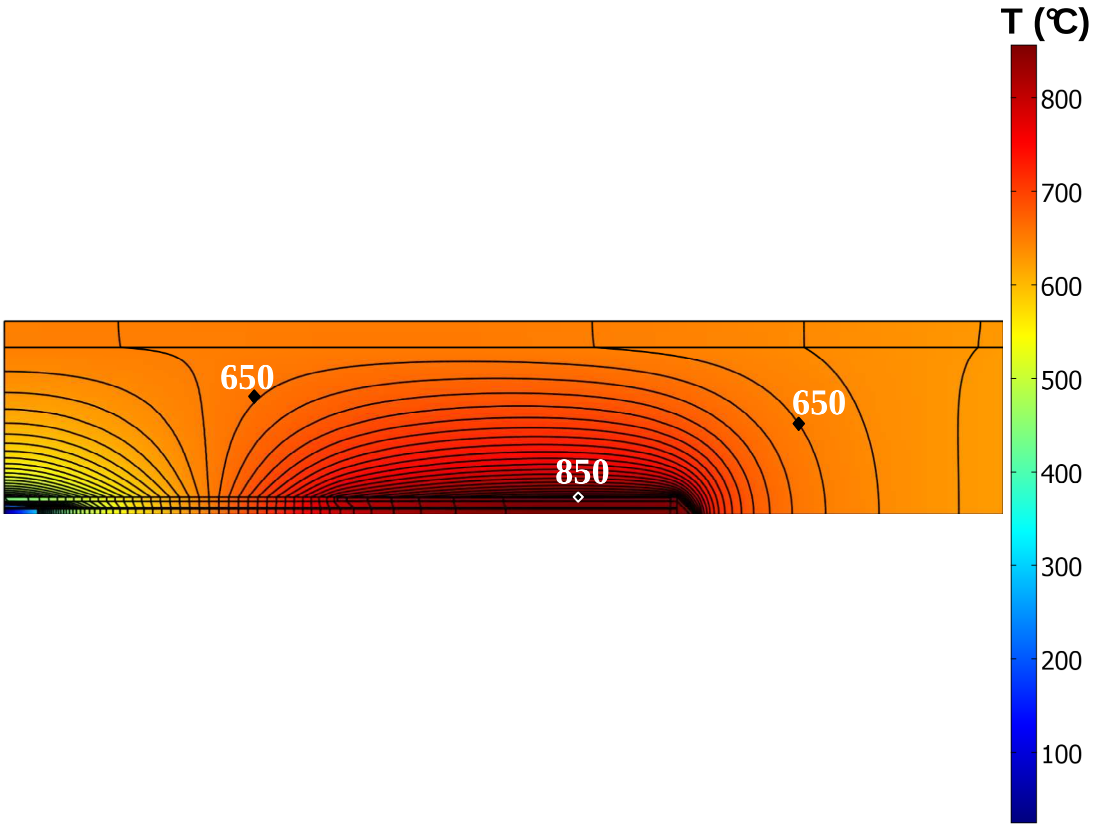

Figure 4.19. The simulated temperature distribution when radiative heat transfer is not included; V_{cell} = 0.4V and no heat is provided by the furnace.

4.5.7 Sensitivity analysis

As it was mentioned before, the knowledge available on the emissivity of various fuel cell components is very limited. In this work, the emissivity was assumed to be 0.5 for the furnace's alumina wall, and 0.9 for all the fuel cell components regardless of their material. It is of interest to know the sensitivity of the simulations to the emissivity values. The cell operating at a high current load, i.e. V_{cell}=0.4 V was investigated. Two cases were studied: the first case where the emissivity of the furnace wall was high, i.e. 0.9; the second case where the emissivity of the cell was low, i.e. 0.5.

The furnace heat flux in the model was estimated such that TC-2 was at the desired value, i.e. 800°C. By changing the emissivity at constant furnace heat flux, the temperature profile completely changed, hence TC-2 was not the same. Therefore the sensitivity analysis was conducted for two cases, one where the heat flux was kept constant, and second where the heat flux was re-estimated to maintain TC-2 at 800°C. The estimated furnace heat flux when the cell emissivity was low was 5.7 kW.m^{-2}, while it was 6.2 kW.m^{-2} for the base case. This is because the cell active length remained hotter as less heat was dissipated by thermal radiation which also required the furnace to provide less heat to keep TC-2 at 800°C. The furnace heat flux was estimated to be higher at 6.3 kW.m^{-2} when its emissivity was high, as it lost more radiative heat to the ambient through its open end, requiring more heat flux to keep TC-2 at 800°C.

The temperature distribution along the cell active length was naturally more sensitive to its own emissivity than the furnace wall emissivity; see Figure 4.20. The temperature gradients along the active length increased by reducing its emissivity, which is consistent with previous studies concluding that radiative heat transfer decreases thermal gradients within the system.

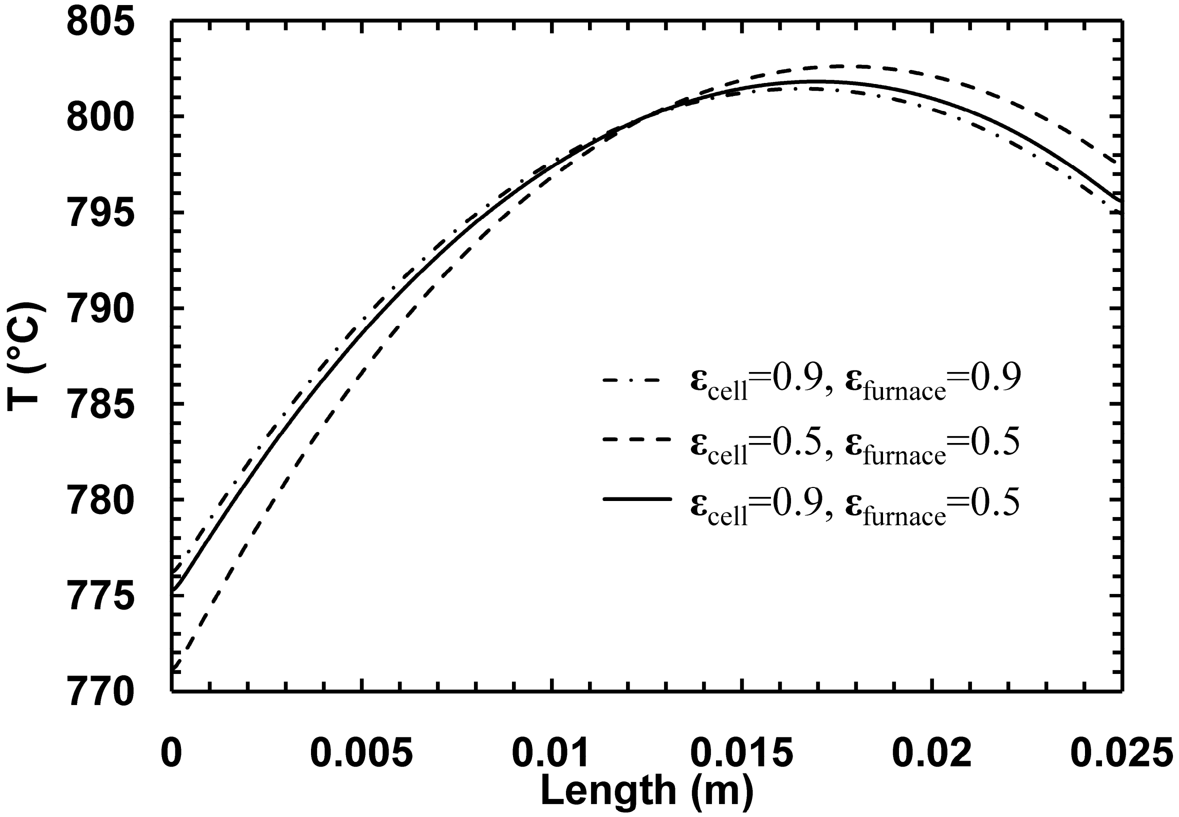

Figure 4.20. The sensitivity of the temperature distribution along the cell active length to the surfaces emissivities, when the furnace heat was re-estimated.

When the furnace heat flux was re-estimated, decreasing the cell emissivity decreased the furnace wall temperature, as shown in Figure 4-21. This is because the furnace provided less heat for the same temperature at TC-2, as explained before. On the other hand, the furnace wall remained cooler when its emissivity was higher, as it could more effectively heat the active length through radiation, requiring a lower temperature.

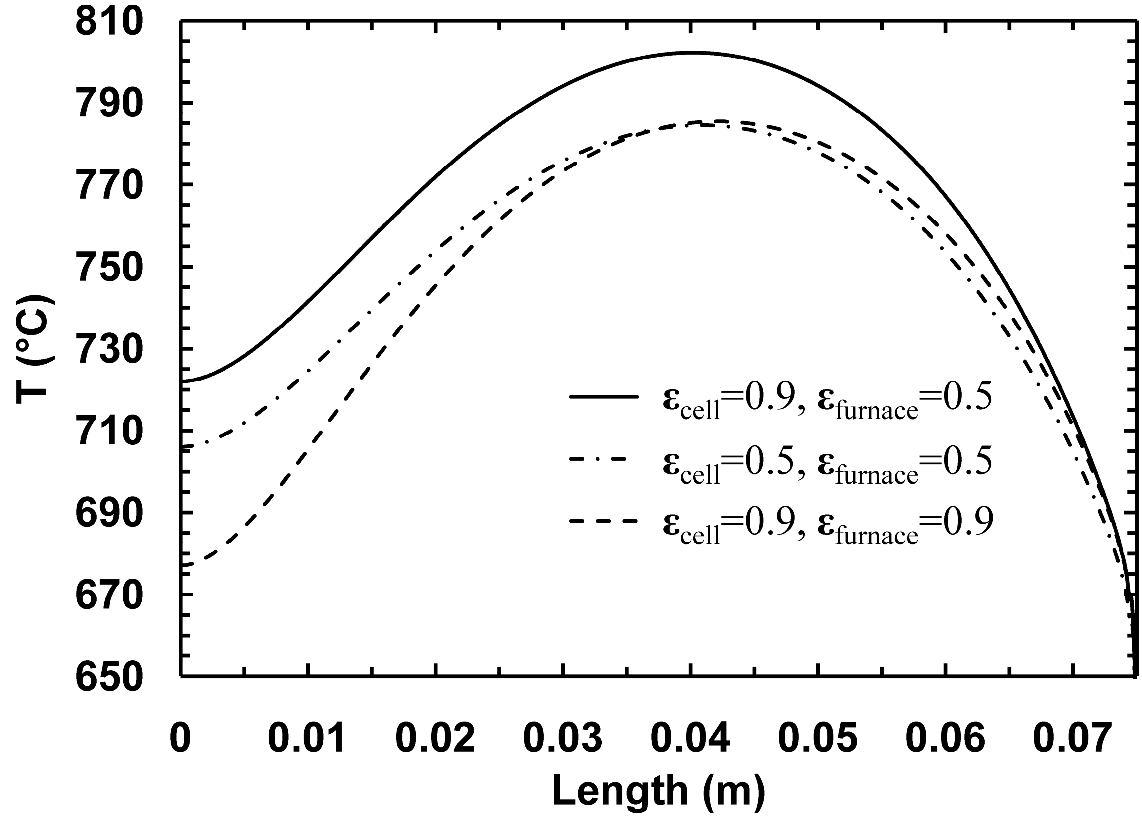

Figure 4.21. The sensitivity of the temperature distribution along the furnace wall to the surfaces emissivities, when the furnace heat was re-estimated.

When the furnace heat flux was not re-estimated, decreasing the emissivity of the cell increased the temperature along the active length noticeably; see Figure 4.22. This indicates again that thermal radiation is a significant mechanism in dissipating the heat generated by the cell.

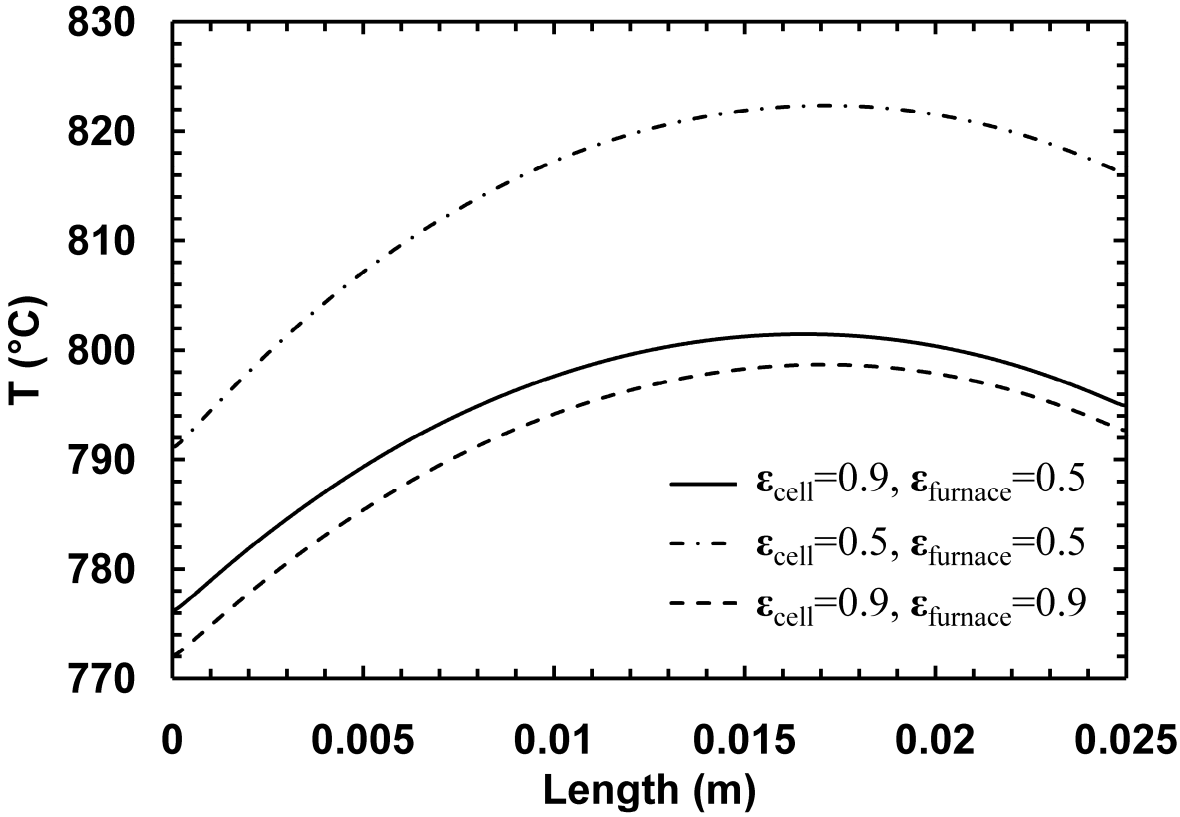

Figure 4.22. The sensitivity of the temperature distribution along the cell active length to the surfaces emissivities, when the furnace heat was kept constant.

Higher emissivity of the furnace wall decreased the temperature along the active length, as more heat was lost to the ambient; see Figure 4.23. Reducing the emissivity of the active length had a minimal effect on furnace wall temperature, which is trivial.

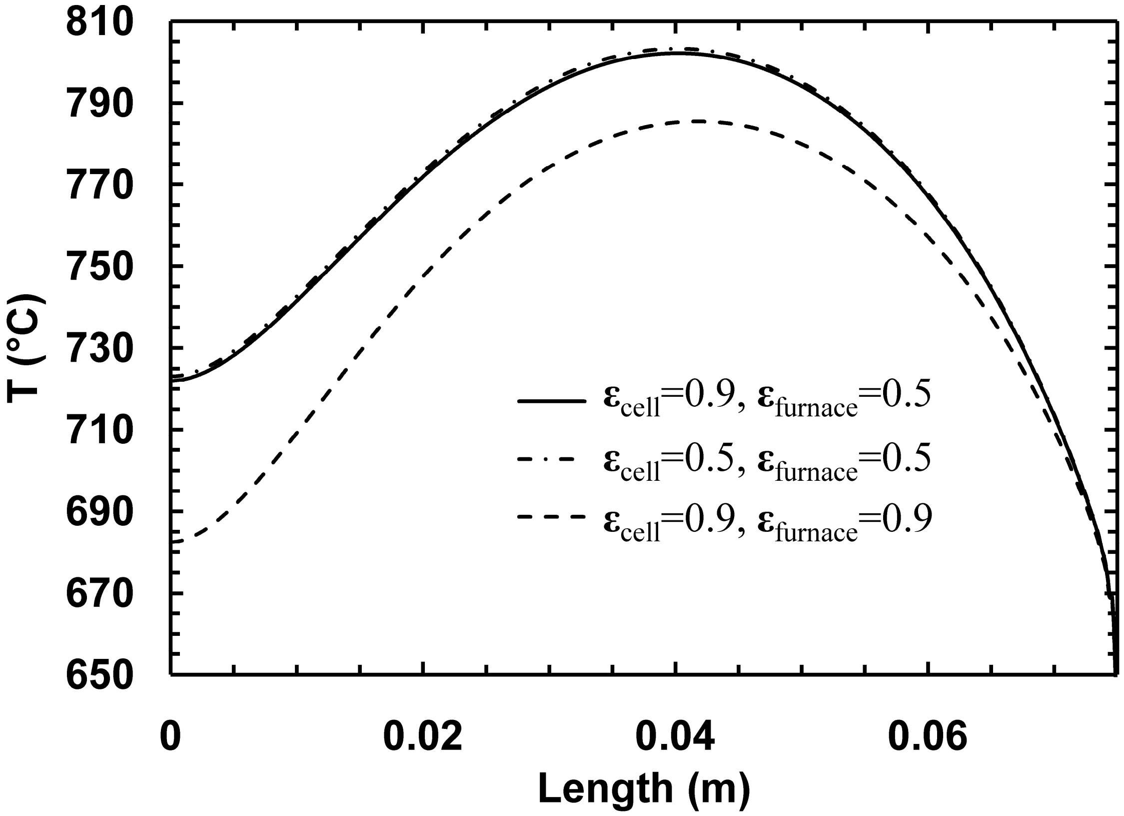

Figure 4.23. The sensitivity of the temperature distribution along the furnace wall to the surfaces emissivities, when the furnace heat was kept constant.

4.5.8 The overall energy balance and the overall thermoelectric effect in the non-isothermal electrodes

A detailed energy balance of the non-isothermal cell operating at 0.4 V is presented in Table 4.1, breaking down various contributions for each electrode. The overall values in Table 4.1 were obtained by integrating local expressions over the appropriate domains. The current generated by integrating the volumetric electron generation rate, as before:

$$I_{cell} = \int_{CFL} i_{gen,Ca} \mathrm{dv} \tag{4.46}$$

The overall ionic current ohmic heating rate on the cathode side was calculated as:

$$\int_{CFL} \left(\sigma_{ionic}^{eff} \nabla V_{ionic} \bullet \nabla V_{ionic} \right) \mathrm{dv} \tag{4.47}$$

The overall ionic current ohmic heating rate on the anode side was calculated as:

$$\int_{AFL+ASL} \left(\sigma_{ionic}^{eff} \nabla V_{ionic} \bullet \nabla V_{ionic} \right) \mathrm{dv} \tag{4.48}$$

The overall electronic current ohmic heating rate on the cathode side included the contribution of the cathode and its current collector:

$$\int_{CFL+CCCL} \left(\sigma_{elec}^{eff} \nabla V_{elec} \bullet \nabla V_{elec} \right) \mathrm{dv} \tag{4.49}$$

Similarly, the overall electronic current ohmic heating rate on the anode side was calculated as:

$$\int_{AFL+ASL+ACCL} \left(\sigma_{elec}^{eff} \nabla V_{elec} \bullet \nabla V_{elec} \right) \mathrm{dv} \tag{4.50}$$

The heat generation rate due to activation losses on the cathode side was calculated as:

$$\int_{CFL} i_{gen,Ca}\eta_{act}\mathrm{dv} \tag{4.51}$$

The heat generation rate due to activation losses on the anode side was calculated as:

$$\int_{AFL+ASL} i_{gen,An}\eta_{act}\mathrm{dv} \tag{4.52}$$

The reversible heat generated on the cathode side was calculated as:

$$\int_{CFL} q_{h,Ca}^{rev}\mathrm{dv} \tag{4.53}$$

where $q_{h,Ca}^{rev}$ is the local rate of reversible heat generation on the cathode side, as defined in Eq. (4.25).

The reversible heat generated on the anode side was:

$$\int_{AFL+ASL} q_{h,An}^{rev}\mathrm{dv} \tag{4.54}$$

Where $q_{h,An}^{rev}$ is the local rate of reversible heat generation on the anode side, as defined in Eq. (4.30).

Adding up the total heat generation, and the overall electric power of the cell, the total chemical energy converted is accurately comparable to the net rate of enthalpy change due to the reaction. This indicates that the model was consistent and the numerical solution was conservative. The net rate of enthalpy change was calculated based on the ΔH_{rxn} at 800°C, and then accounting for the integral of the enthalpy change of reactants from 800°C to their local temperature within the electrodes.

The rate of change in enthalpy due to electrochemical reactions at 800°C calculated as:

$$\frac{I_{cell}}{2F}\times\Delta H(800°C) \tag{4.55}$$

The actual rate of change in enthalpy of reaction included the effect of reactants not being at 800°C:

$$\frac{I_{cell}}{2F}\times\Delta H_{rxn}(800°C)+\int_{CFL}\left(-\frac{i_{gen}^{Ca}}{4F}\int_{800}^{T}c_{p,O_2}\,dT\right)\mathrm{dv}+\int_{AFL+ASL}\left(\frac{i_{gen}^{An}}{2F}\int_{800}^{T}(-c_{p,H_2}+c_{p,H_2O})dT\right)\mathrm{dv} \tag{4.56}$$

The two biggest sources of the irreversible heat generation were the anode ohmic heating and the cathode activation heating, consistent with the conclusion of chapter 3 that those two effects were the major contributors to the overall performance loss. The anode reaction was endothermic, while the cathode reaction was exothermic. Although the irreversible heating of the electrodes were equal, the total heat generated within the anode was much smaller than the cathode, in fact negative, due to the anode’s negative reversible heat generation.

The integral of the electromotive force resulting from the temperature gradients within the electrodes, the last term on the RHS of Eqs.(4.37) and (4.39), cancelled each other out. This indicates the thermoelectric electromotive force was negligible for this cell, because the temperature gradients across the layers are very small, and the temperature gradients within each electrode did not have a significant impact whatsoever.

Table 4.1. The energy balance of the TμSOFC operating at 0.4V; units are all in watts.

	Anode	Cathode	Total (An.+Ca.)
I.1. Ohmic losses			
I.1.a. Ionic current	0.001558	0.039942	0.082439 *
I.1.b. Electronic current	0.457647	0.027531	0.485178
I.2. Activation Losses	0.001499	0.555198	0.556697
I. Total Irreversible (I.1 + I.2)	0.460704	0.622671	1.124314
II. Reversible heating	-0.474128	1.013761	0.539633
Total Heat generated (I + II)	-0.013424	1.636432	1.663947
III. Electric power (I_{cell}×V_{cell})			0.750767
Total energy converted (I+II+III)			**2.414715**
ΔH_{rxn} rate at 800°C,			-2.414977
Effect of the reactants not being at 800°C	-0.001864 (H_2O) -0.00135(H_2)	7.70969e-4 (O_2)	-0.000257
ΔH of the non-isothermal reaction			**-2.414720**

* Includes the electrolyte ohmic losses of 0.040939 watts.

4.6 Conclusion

A detailed non-isothermal model was developed for a TuSOFC. The model predictions were found to be consistent with the experimental results on the cell overall performance as well as temperature distribution. The temperature profile was found to be a complex outcome of various effects, especially radiation. If the furnace heat flux was constant, the heat generated by the cell could raise its temperature as much as 40°C.

It was found that including thermal radiation is essential for any meaningful heat transfer modeling of our system. In fact, for our case, not modeling heat transfer at all was closer to reality than modeling heat transfer without thermal radiation. The prediction of the cell overall performance by the isothermal model was very close to the non-isothermal model. Thermal radiation was the main mechanism of transporting away the generated heat by the electrodes. Thermal radiation inside the cell, in our system, was found to be negligible because of the strong convection flow inside the cell. The thermal radiation on the air side was the main mechanism for the dissipation of the heat generated by the cell.

The effect of emissivity of the cell components was studied for a wide range of values, i.e. 0.5 to 0.9, as there is limited data in the literature. For that range of values, a maximum temperature difference of 50°C was observed in the predicted temperature profile. Not including thermal radiation however resulted in the temperature of the electrode to run-away, inconsistent with the experimental.

It was also found that the cathode reaction is exothermic, while the anode reaction is endothermic for our cell and for SOFCs in general. In addition, the effect of temperature gradients within electrodes on the overall electromotive force of the cell was found to be negligible, as the temperature gradients across the cell layers were less than 0.05°C.

Chapter 5. TµSOFC transient simulation

5.1 Introduction

The transient behavior of an SOFC is of practical importance, especially as the technology approaches commercialization. Transients are an inseparable aspect of SOFC operation; the current and voltage of an actual SOFC system change significantly during its operation depending on the load requirements. The control and power conditioning components, one of the major elements of any SOFC based power generation system, are designed to regulate its transients. The changes in load require changes in various operating parameters to keep the SOFC running effectively and within the acceptable range. For example, an increase in SOFC load would require a higher flowrate of reactants to keep the same utilization and efficiency. In addition, to avoid excessive temperatures, the extra heat generated at the higher loads must be removed for example by increasing the air flow. Thermal transients are also important during the start-up and shut-down cycles, as the thermal stresses must be managed to ensure the mechanical stability and the safe operation of the SOFC.

Computer simulation is a powerful tool to gain a better understanding of the SOFC transients, to predict them, and to effectively control them. Several dynamic SOFC models have been developed which vary in their details, designs, and purpose. A nice review can be found by (Bhattacharyya and Rengaswamy, 2009). The control of SOFCs is one of the main focuses of transient modeling, and a large number of dynamic models are developed for studying and optimizing control strategies. A model that correlates the input parameters of an SOFC to parameters that need to be controlled, such as power, voltage, current, and temperature can be sufficient for this purpose. Therefore the control based models are usually simplified zero (Lin and Hong, 2009; Gaynor et al., 2008; Wang and Nehrir, 2007; Haynes, 2002) or one dimensional (Pradhan et al., 2007; Gemmen and Johnson, 2005; Aguiar et al., 2005). Transient models are also developed for studying the systems aspect of the SOFC operation, i.e. the balance of plant, which focus on the interaction of the components, and the control and optimization of the overall system (Mueller et al., 2009; Vijay et al., 2009; Ferrari et al., 2005, Li et al., 2007; Mazumder et al., 2007; Kaneko et al., 2006). On the other hand, physic-based dynamic models have been developed that capture the detailed phenomena occurring in an SOFC, such as models developed that simulate the impedance response of electrodes (Bessler, 2006; Bessler and Gewies, 2007; Jacobsen et al., 2008; Sasaki et al., 2002; Zhu and Kee, 2006).

The various phenomena occurring in the fuel cell have different transient time-scales. The electrochemical reaction steps are very fast and have time constants of milliseconds. The mass transport phenomena have larger time scales, of the order of seconds. The thermal transients of SOFCs are the slowest of the order or minutes to hours. The transient time constants, especially those for mass and heat transport are very dependent on the design and operating conditions of the cell. For example cells with thicker electrodes or slower gas velocities would have slower mass transport transients. The thermal transients are often the controlling transient and therefore of the most importance from a practical point of view - which has led some models to only include only the thermal transients in their transient models. In fact, one of the earliest dynamic SOFC only modeled temperature distribution and electrochemical reactions (Achenbach, 1994, 1995). Nonetheless, there are transient models assuming isothermal conditions (Murshed et al., 2007; Bhattacharyya et al., 2009).

In this chapter we extend the steady-state model to predict the transient behavior of the TμSOFC. The validated steady-state model being one of the most detailed models presented for any type of SOFC, the transient model is unique in the phenomena it captures compared to other transient models. It includes the transient transport phenomena occurring within the gas channels and the electrodes. The transient model presented here is unique because of its experimental validation. This is significant because little work has been done on experimental validation of the transient models (Bhattacharyya et al., 2009).

5.2 Model development

The equations used in the transient model are similar to the steady state equation, while they account for transient accumulation or depletion as source terms.

The unsteady continuity equation is:

$$\nabla.(\rho\mathbf{u}) = -\frac{\partial\rho}{\partial t} \tag{5.1}$$

The unsteady component mass balance equation is:

$$\nabla.(\mathbf{N}_i^m) = -\frac{\partial(w_i\rho)}{\partial t} \tag{5.2}$$

The unsteady momentum equation is:

$$\rho(\mathbf{u}.\nabla)\mathbf{u} - \nabla.[-p\mathbf{I} + \mu(\nabla\mathbf{u} + (\nabla\mathbf{u})^T) - \frac{2}{3}\mu(\nabla.\mathbf{u})\mathbf{I}] = -\rho\frac{\partial\mathbf{u}}{\partial t} \tag{5.3}$$

The unsteady heat transfer is:

$$\nabla.(\mathbf{N}_i^h) = -\rho c_p\frac{\partial T}{\partial t} \tag{5.4}$$

where $\mathbf{N}_i^m$ and $\mathbf{N}_i^h$ are the mass and heat flux vectors of component *i* respectively. **u** and **I** are the mass velocity and the unity vector respectively. w_i is the mass fraction of the component *i*. *p*, *μ*, and c_p are the gas pressure, viscosity, and specific heat capacity.

All the physical properties were calculated as discussed for the steady-state model. The solids specific heat capacities are given in the appendix. Note that within the porous electrodes, the heat and mass fluxes as well as the velocity are the superficial ones.

5.3 Experimental validation

The model predications of the thermal transients were compared with the experimental results when a step occurred in the cell current and in the air flowrate. The transient experiments were conducted by disabling the feedback loop of the PID controller, hence keeping the furnace heating load constant. The furnace heating load in the simulations was estimated for the steady state conditions, as explained for the non-isothermal simulations. The mild drift in the temperature observed in the open-loop experiments was ignored in the simulations. In the model, the step was applied as a Heaviside function that changed over a 0.001 second time period. The use of the Heaviside function, which is a smoothened step with continuous first and second order derivatives, enhanced the numerical convergence for the very fast steps.

The validation simulations were conducted for the two cases with and without the thermocouples effect. The thermocouples attached along the cell in the experimental, affected the temperature distribution within the furnace, as it was explained for the non-isothermal mode. Note that for the dynamic model, the thermocouples affected the system due to their thermal mass in addition to their thermal conductivity. These effects were mimicked by enhancing the thermal conductivity and the heat capacity of the cell as for the steady-state non-isothermal simulations. Notice that a change in the heat capacity affects unsteady simulations, but not the steady-state results.

The experimental and the predicted transient response of the temperature at the middle of the active length (TC-2 in Figure 2.5) is compared in Figures 5.1 and 5.2, when the cell current stepped from 0 A to 0.5 A, and 0 A to 1 A. Note that after a while, the current was switched back to 0 A for the experimental curve, which was not included in the results shown in Figures 5.1 and 5.2. Naturally, including the effect of thermocouples increased the simulated cell response time, which is more consistent with the experimental results. The experimental response has a time constant of ~30 seconds. The simulated curves seem to have two constants, which is very clear in the case where TC effects are not modeled; this will be further discussed. Nonetheless, the initial rise of the predictions, i.e. the fast transient, is consistent with the experimental for both 1A and 0.5A steps responses when TC effect is included.

The new steady state predicted by the model was 813°C for the 1A step compared to the experimental value of 808°C, and was the same regardless of the TC effect. For the 0.5A step, the predicted new steady state was 805°C not including the TC effect and 805°C including the TC effect, while experimentally it was 803°C. Therefore, the heat transfer model overestimated the temperature rise in the cell. This can be an indicator that heat transfer was under-estimated by the model, which will be further discussed.

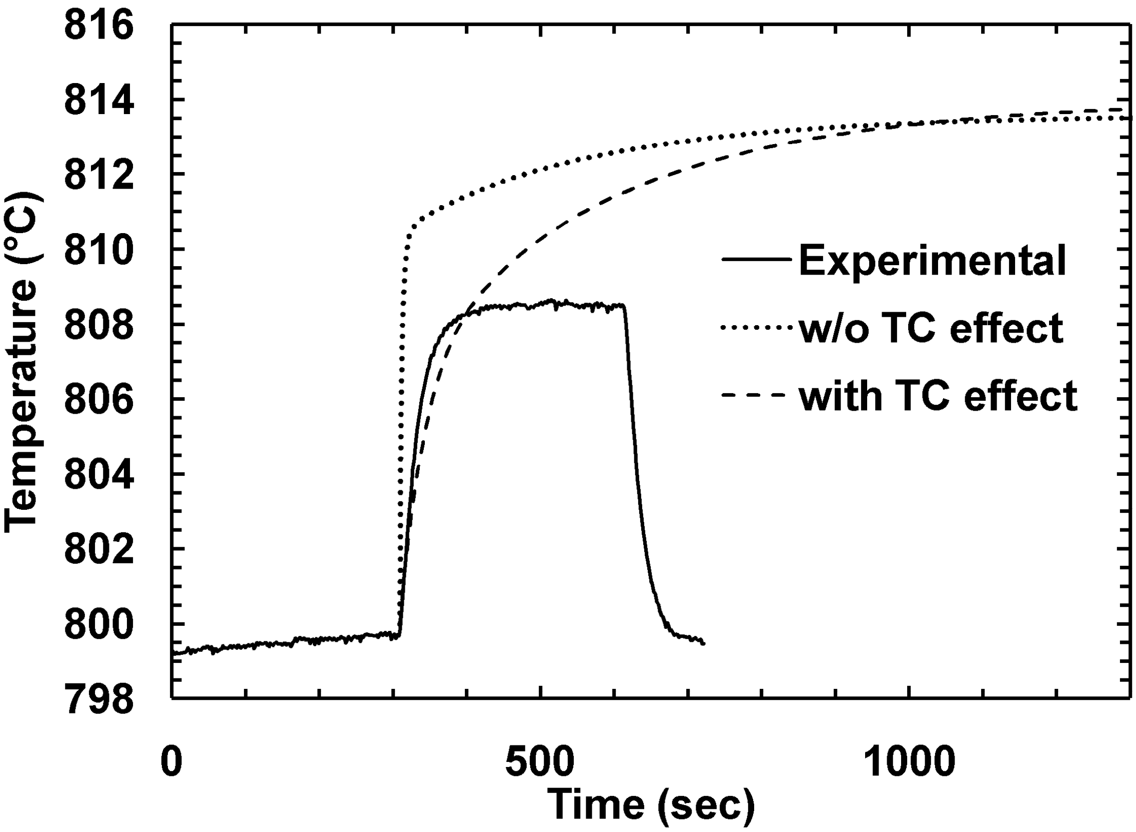

Figure 5.1. The temperature transients for a current step of 0 A to 1 A.

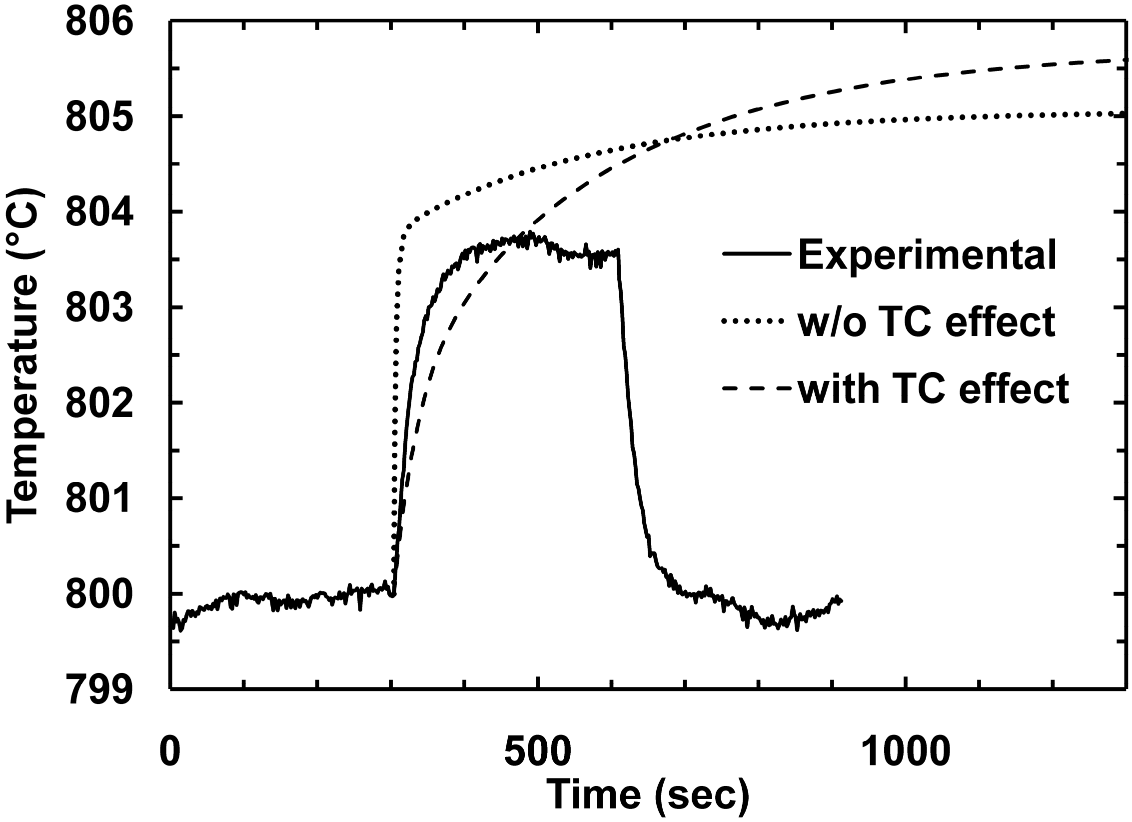

Figure 5.2. The temperature transients for a current step of 0 A to 0.5 A.

The slow temperature transients predicted by the model, as it will be discussed in the next section, is caused by the furnace wall. In the model, only the furnace tube, but not the insulation and the structure around it, was modeled. It will be shown that increasing the furnace wall heat capacity makes the slow transient very sluggish and flat looking. When the thermal mass of the furnace wall was included, the slow response time was very long, essentially making it look flat in the time-frame of our experiments. Considering this, a second set of validation simulations, including the TC effect, was conducted where the furnace wall specific thermal conductivity was multiplied by 100; see Figure 5.3. The outcome clearly is more consistent with the experimental.

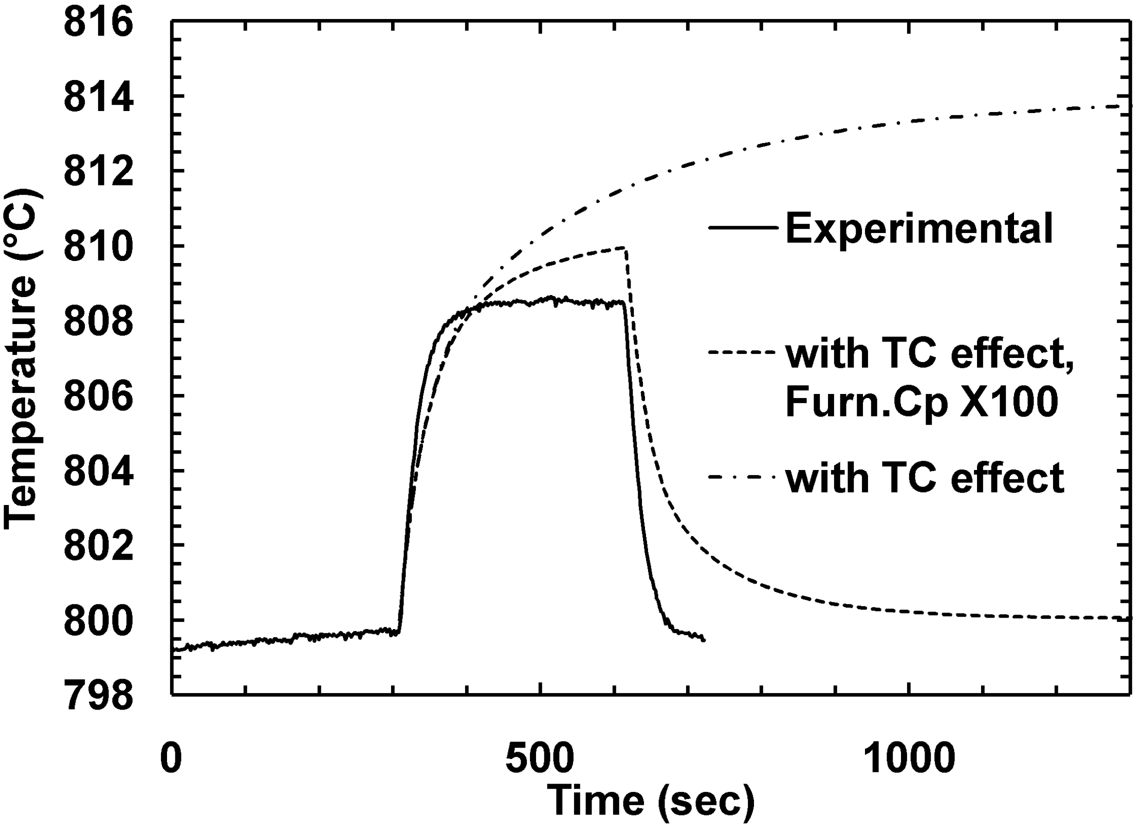

Figure 5.3. The temperature transients for a current step of 0 A to 1 A. Note that the second step from 1 A back to 0 A was only modeled for the case where Cp was multiplied by 100.

The experimental and predicted thermal response of the cell to a step in the air flowrate from 300 mL.s^{-1} to 400 mL.s^{-1} and back to 300 mL.s^{-1} is shown in Figure 5.4. The predicted temperature clearly changed less than the experimental. This can be an indicator that the convective heat transfer is underestimated in the model, which is consistent with the observations in Figures 5.2 and 5.3. This can be due to the fact that the airflow in the experimental was not perfectly distributed by the inlet diffuser and its velocity was higher in the centre of the furnace along the cell; this in turn caused higher heat transfer rate and lower temperatures. Figure 5.4 shows the temperature transient for a bigger step in airflow, i.e. higher gas velocity, which confirms the effect of higher velocity.

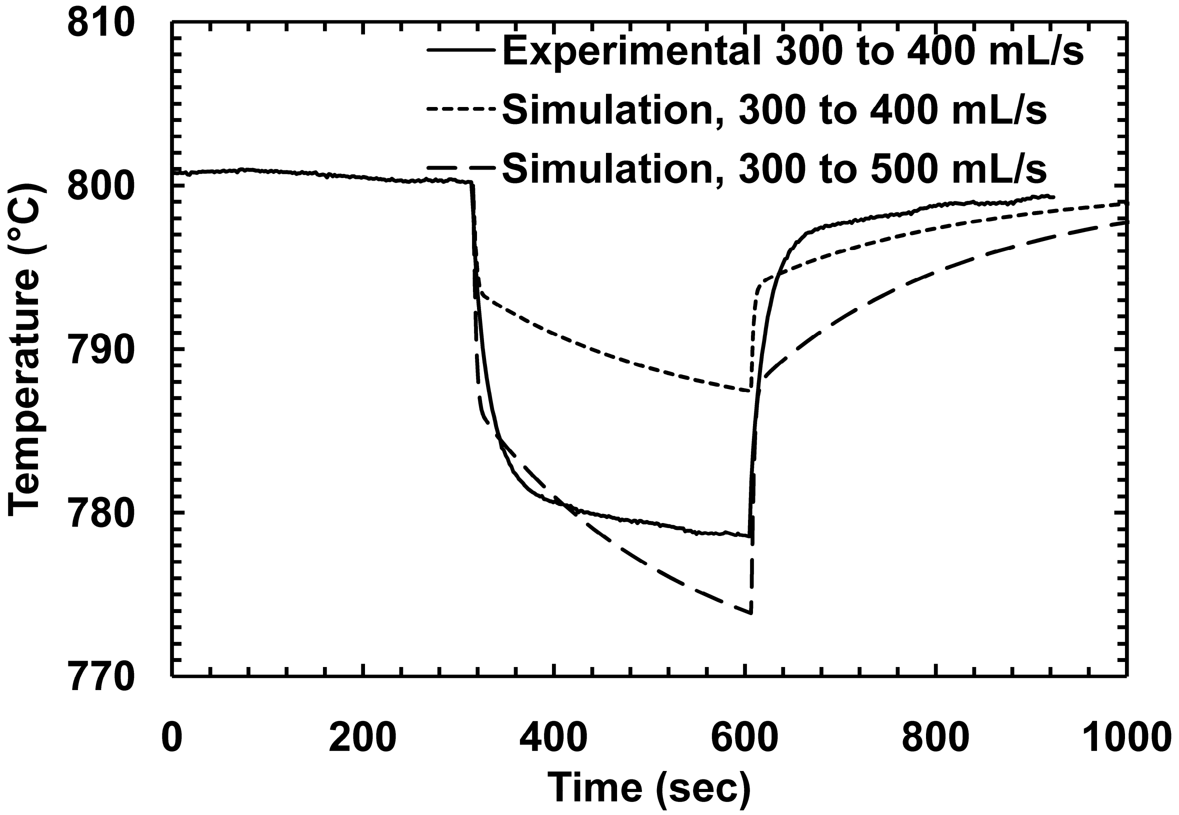

Figure 5.4. The temperature transients for a current step of 0 A to 0.5 A.

5.4 Results and discussion

The effect of various parameters on the thermal and voltage transients to a step in the current load from 0 A to 1 A was studied. Because the behavior of the TµSOFC itself is of importance, the results presented are for the case with no TC effect.

In general, the time constant of a transient thermal system is proportional to its thermal mass, mc_p, and to the inverse of the heat transfer coefficient. The thermal transient response of a lumped system can be written as:

$$\Delta T(t) = \Delta T(0) e^{-\frac{t}{\tau}} \quad ; \qquad \tau = \frac{mc_p}{U} \tag{5.5}$$

where m, c_p, and U are the mass, the specific heat capacity, and the heat transfer coefficient and τ is the time constant of the system. Eq.5.5 indicates that the transient response of the system becomes slower by increasing its heat capacity, and faster by increasing its heat transfer coefficient. The heat transfer coefficient is higher when factors such as the thermal conductivity, the gas velocity, and the thermal radiation are higher.

With no TC effect, the fast transient had a time constant of 2 seconds with a temperature rise of ~10°C; see Figure 5.5. The slow transient however had a time constant of 230 second with a temperature rise of ~3°C. The combined time constant for the thermal transients was 4 seconds.

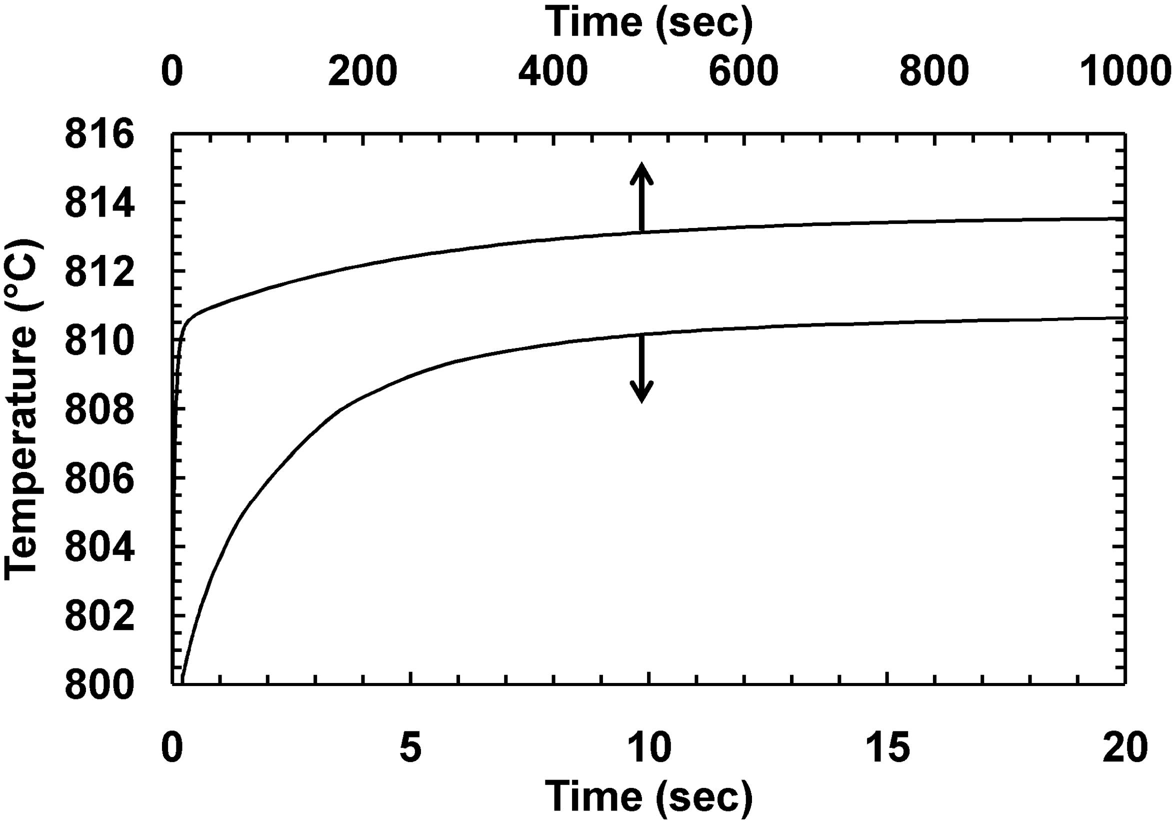

Figure 5.5. The predicted fast and slow temperature transients; I= 0 to 1 A.

Changing the specific heat capacity of the furnace wall only changed the slow segment of the temperature response, indicating that it is associated with the furnace wall. Note that changing the heat capacity of the furnace wall did not change the final steady-state of the system; therefore all the responses eventually converged to the same value. However, by increasing the furnace heat capacity by ten times, the slow response became so sluggish that its steady-state was well beyond the time-frame simulated in Figure 5.6.

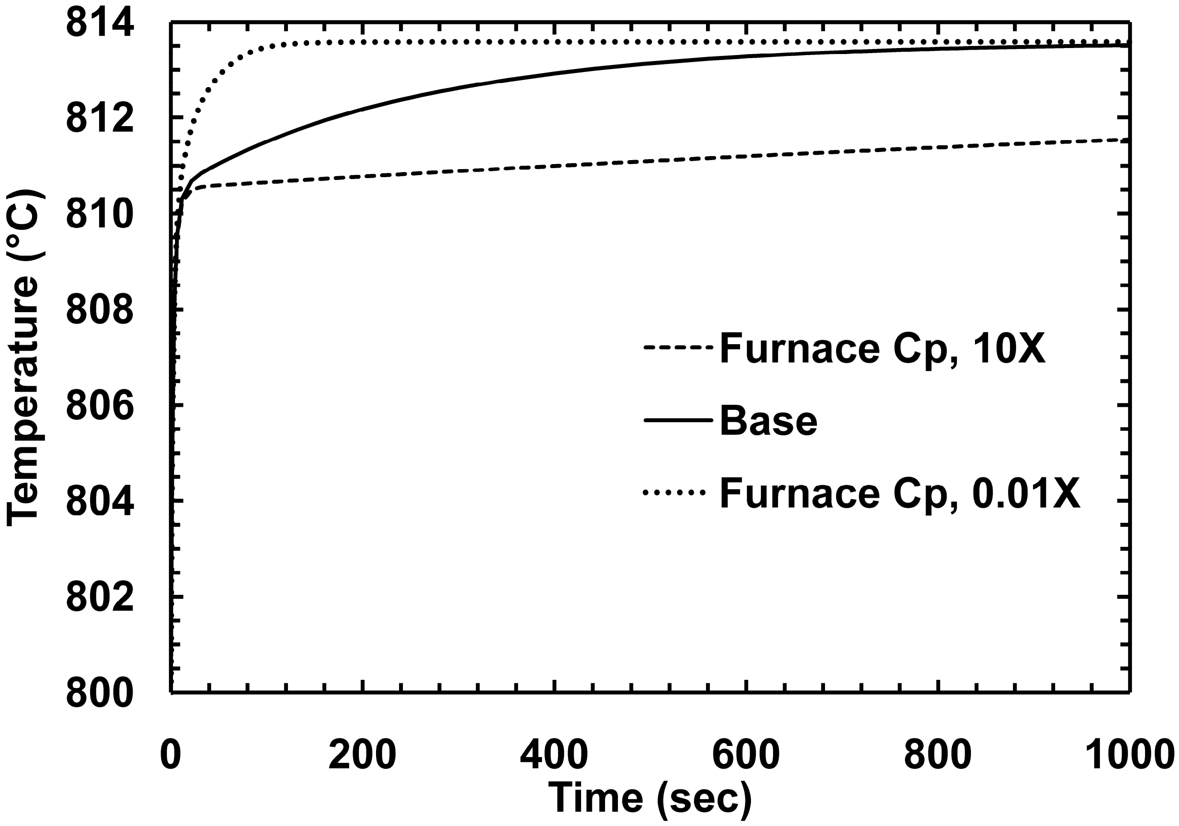

Figure 5.6. The sensitivity of the cell thermal transients to the furnace wall heat capacity; I= 0 A to 1 A.

Changing the heat capacity of the cell changed the fast transient of temperature, see Figure 5.7. This indicates that the fast response is associated with the cell itself. As the cell had a very small thermal mass, decreasing its heat capacity affected the fast response negligibly. However, increasing the heat capacity of the cell significantly slowed down the overall thermal response of the cell.

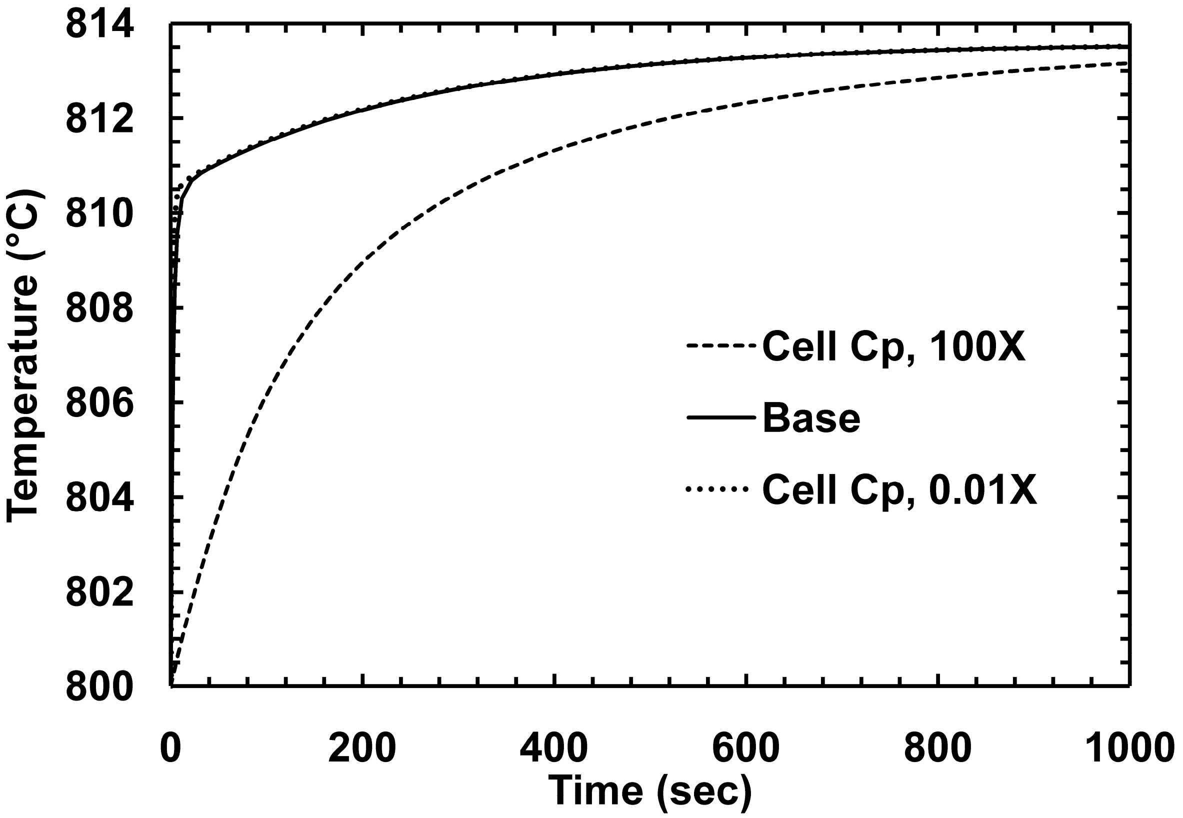

Figure 5.7. The sensitivity of the cell thermal transients to the cell heat capacity; I= 0 to 1 A.

The effect of cell components emissivity on the temperature transients are presented in Figure 5.8. Reducing the emissivity of the cell increased its final steady-state temperature. However the rate of changes, i.e. the time constant of the response, changed negligibly. Changing the emissivity of the furnace wall had a negligible effect of the transient response and the final steady-state of the cell.

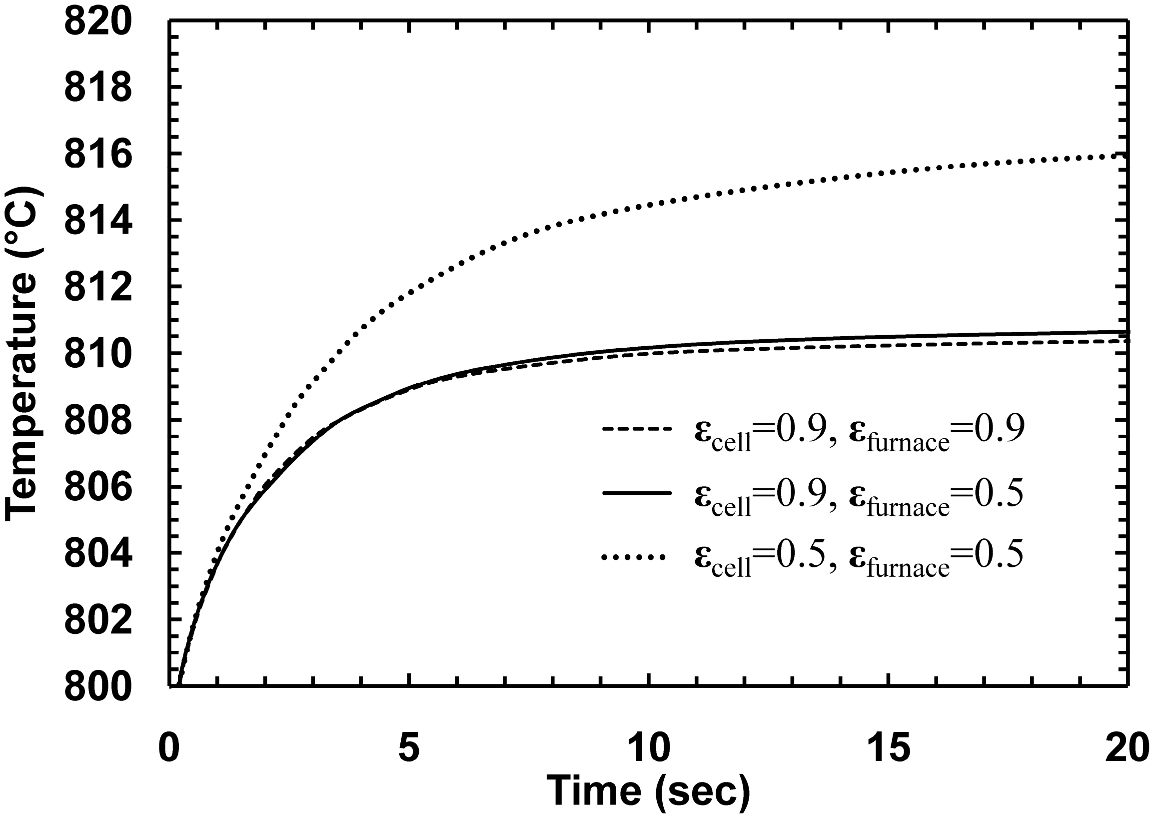

Figure 5.8. The sensitivity of the cell thermal transients to the surface emissivity of components; I= 0 to 1 A.

Increasing or decreasing the air flowrate by three times slightly changed the final steady-state temperature, without affecting its transient noticeably; see Figure 5.9. This is because the thermal convection on the air side was not significant due to the low velocities. Increasing the fuel flowrate by 10 times had a more significant effect on the steady-state temperature of the cell, but its transient was again affected negligibly.

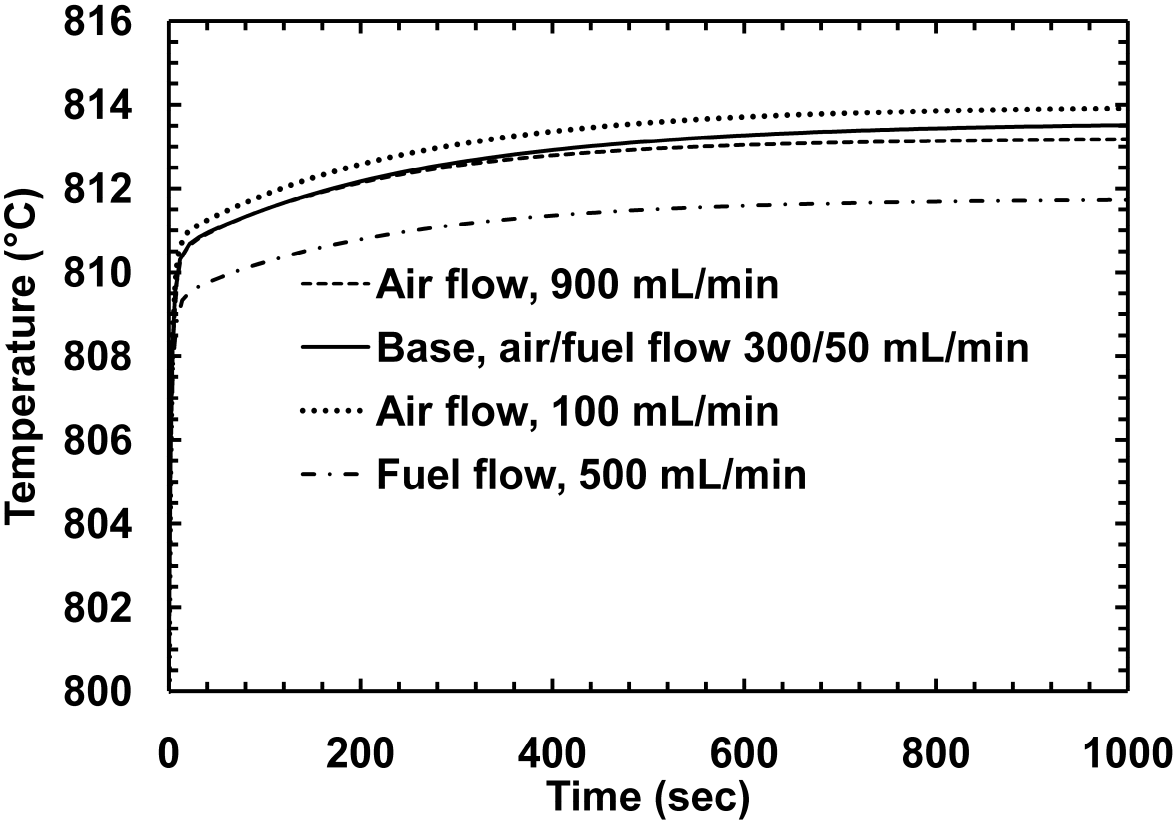

Figure 5.9. The sensitivity of the cell thermal transients to the gas velocity; I= 0 to 1 A.

Changing the thermal conductivity of the cell slightly changed the final steady-state temperature of the cell, with no noticeable effect on its transient; see Figure 5.10.

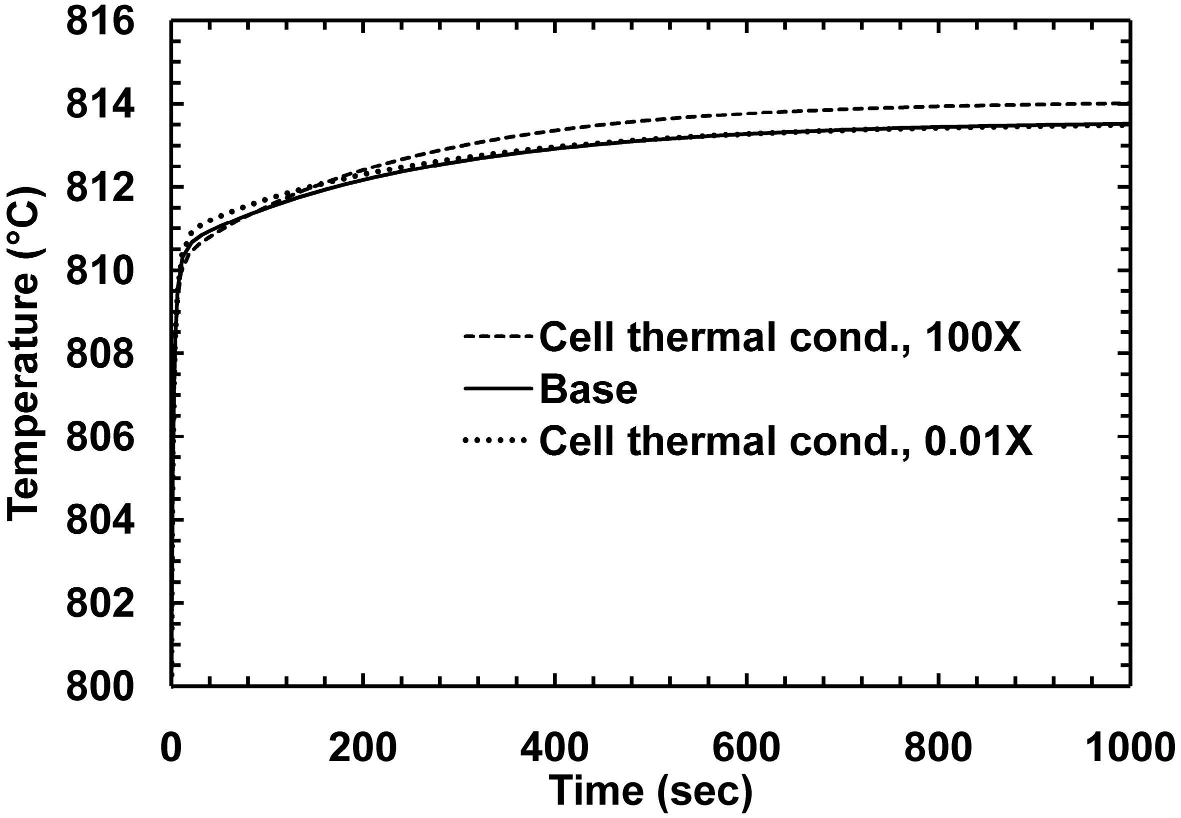

Figure 5.10. The sensitivity of the cell thermal transients to its thermal conductivity; I= 0 to 1 A.

Increasing the thermal conductivity of the furnace wall decreased the final steady-state temperature of the cell and resulted in a faster overall transient, as shown in Figure 5.11. Decreasing the thermal conductivity of the furnace wall slightly increased the final steady-state temperature.

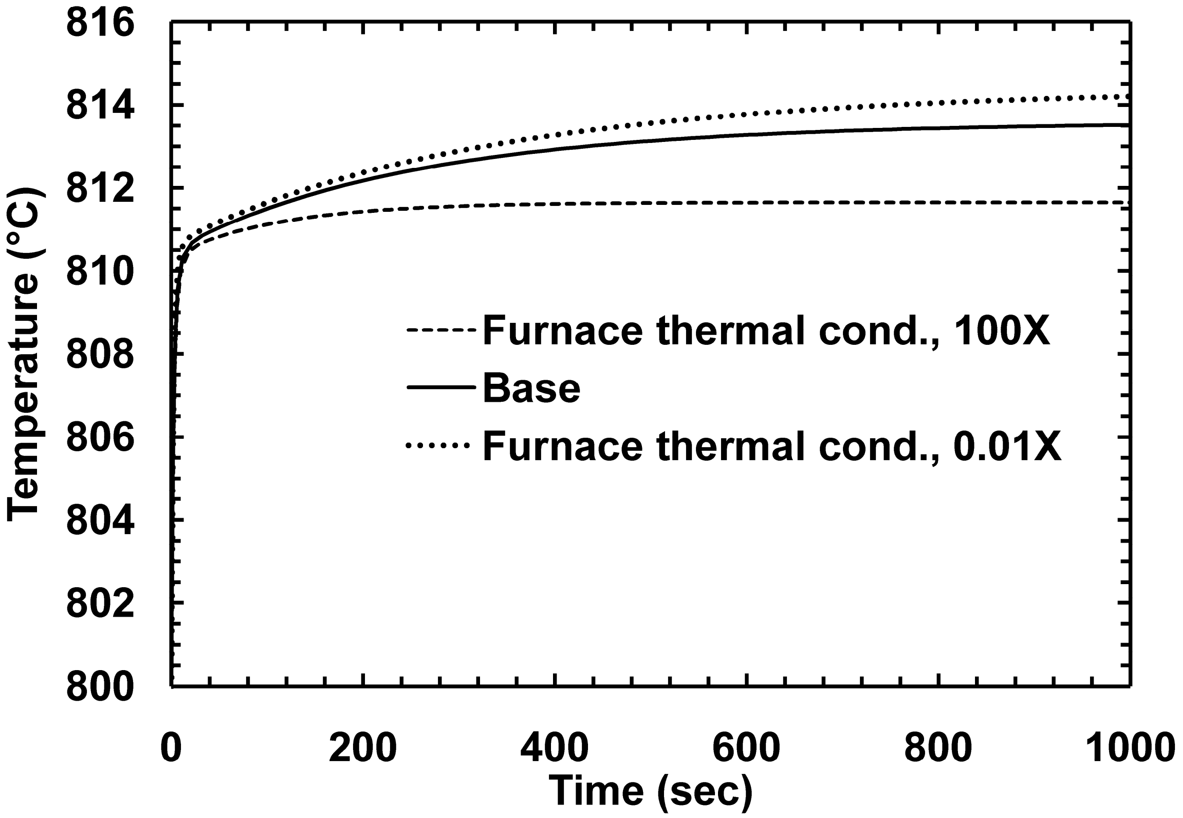

Figure 5.11. The sensitivity of the cell thermal transients to the furnace thermal conductivity; I= 0 to 1 A.

The transients of hydrogen concentration within the electrodes at three point along the active length is shown in Figure 5.12. It is clear that the transient of hydrigen concentration were very fast. Note that they become slower in the direction of the flow, from the top of the active length to the bottom, close to the open end. The time constants for the top, middle and the bottom of the active length were 0.007, 0.023, and 0.040 seconds respectively.

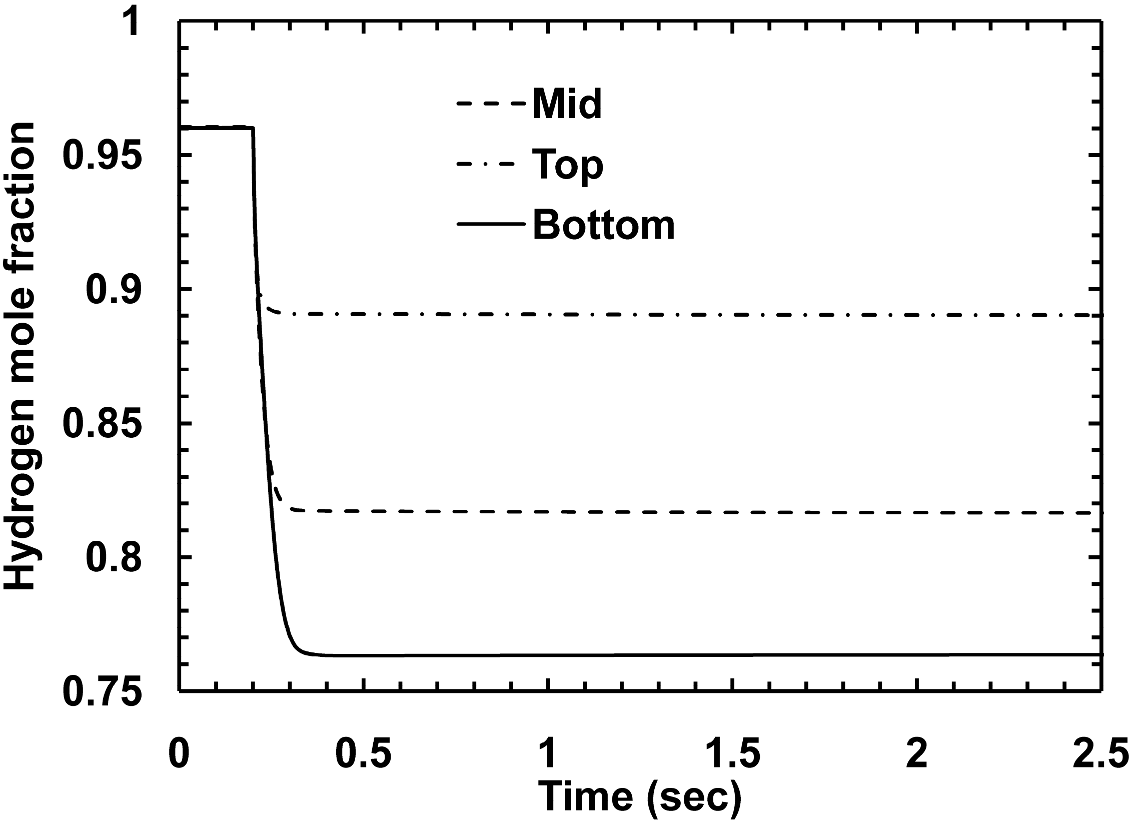

Figure 5.12. The concentration transient at the anode/electrolyte interface; I= 0 to 1 A.

The oxygen concentration transient became slower in the direction of the flow, towards the bottom of the active length and closer to the open end. The time constants for the top, mid and bottom of the active length were 0.010, 0.044, and 0.198 seconds respectively. The time constants of oxygen transient on the cathode side were greater than that of hydrogen on the cathode side. This is due to the much slower gas velocities on the cathode side.

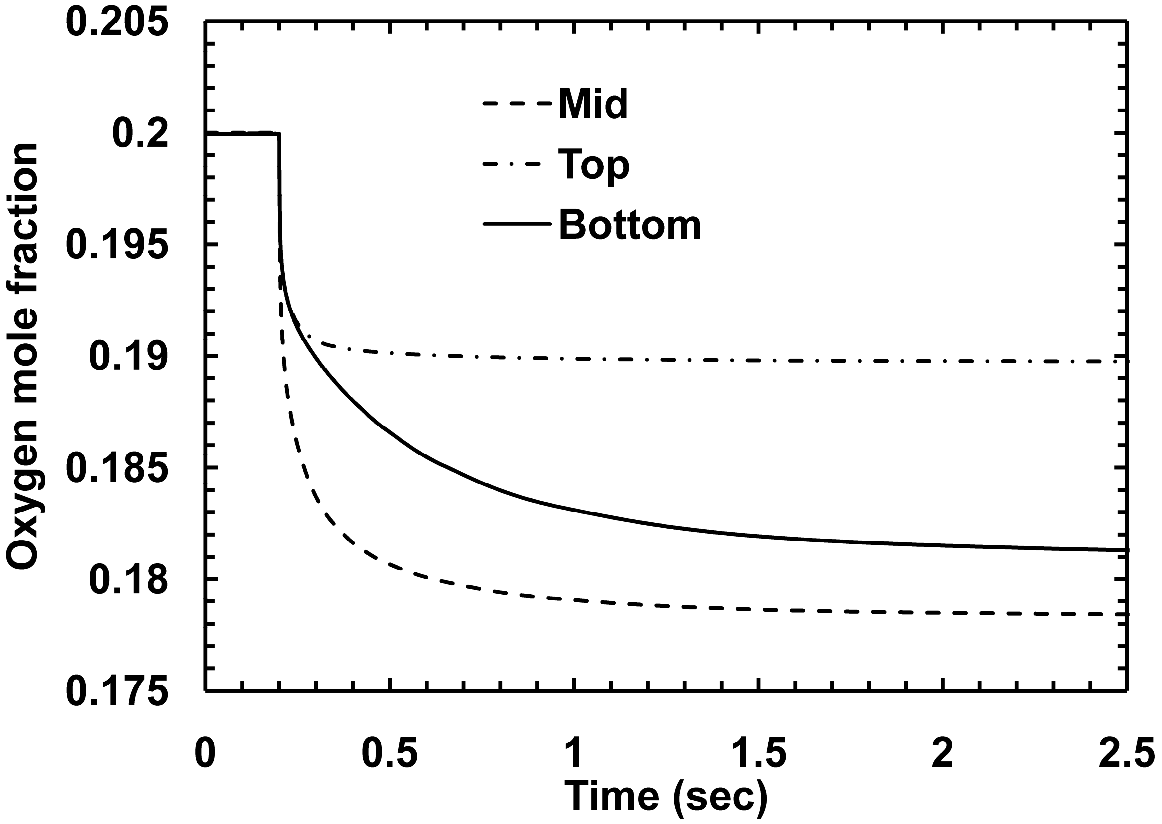

Figure 5.13. The concentration transient at the cathode/electrolyte interface; I= 0 to 1 A.

The voltage transient for a 1 A and 0.5 step as well as the expanded views are shown in Figures 5.14, 5.15, and 5.16. For both of the steps, the voltage dipped rapidly, and then gradually increased. The increase is because of the temperature rise of the electrodes. The electrodes have higher performance at higher temperatures, i.e. lower overpotential. Therefore, as the temperature of the electrode rose, the cell potential increased as well. The time constant of the 0.5 A and 1 A step were 4.8 and 5.7 seconds, consistent with the time constant of the cell thermal transients as discussed before. The 1 A step resulted in a larger voltage recovery compared to the 0.5 A step, as the increase in the electrode temperature was higher for the 1 A step.

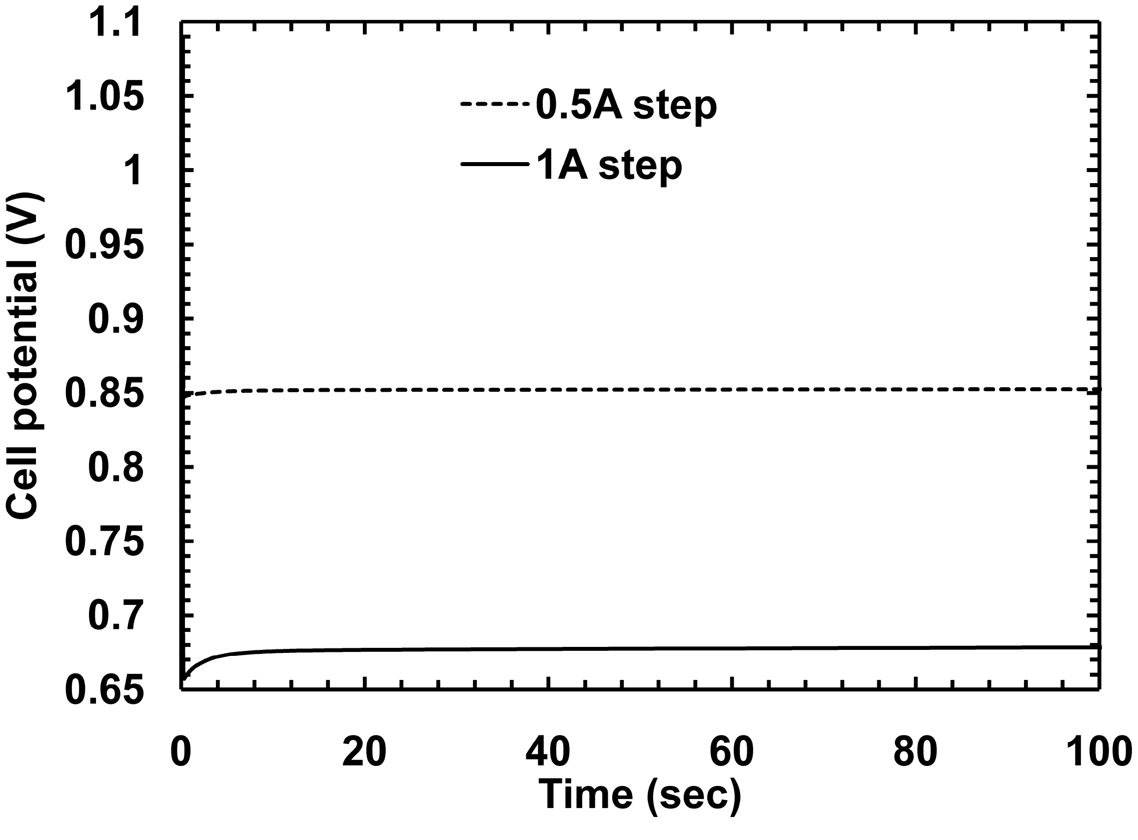

Figure 5.14. The cell potential transient as the current stepped from 0 A.

The pattern of an initial dip followed by a gradual recovery can be found in other modeling papers as well (Jia et al., 2008; Saarinen et al., 2007; Xi and Sun, 2008; Jia et al., 2007; Magistri et al., 2006; Lu et al., 2006; Nehter, 2006; Sedghisigarchi and Feliachi, 2004).

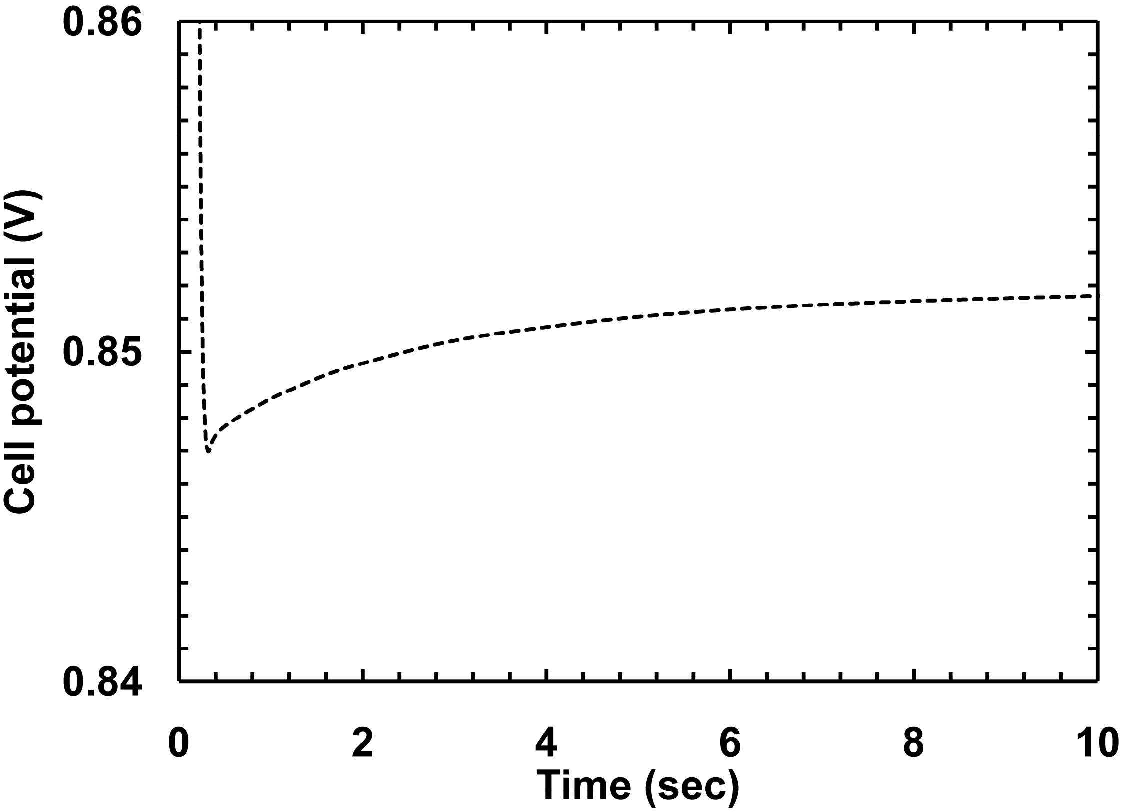

Figure 5.15. The expanded cell potential transient; I= 0 to 0.5 A.

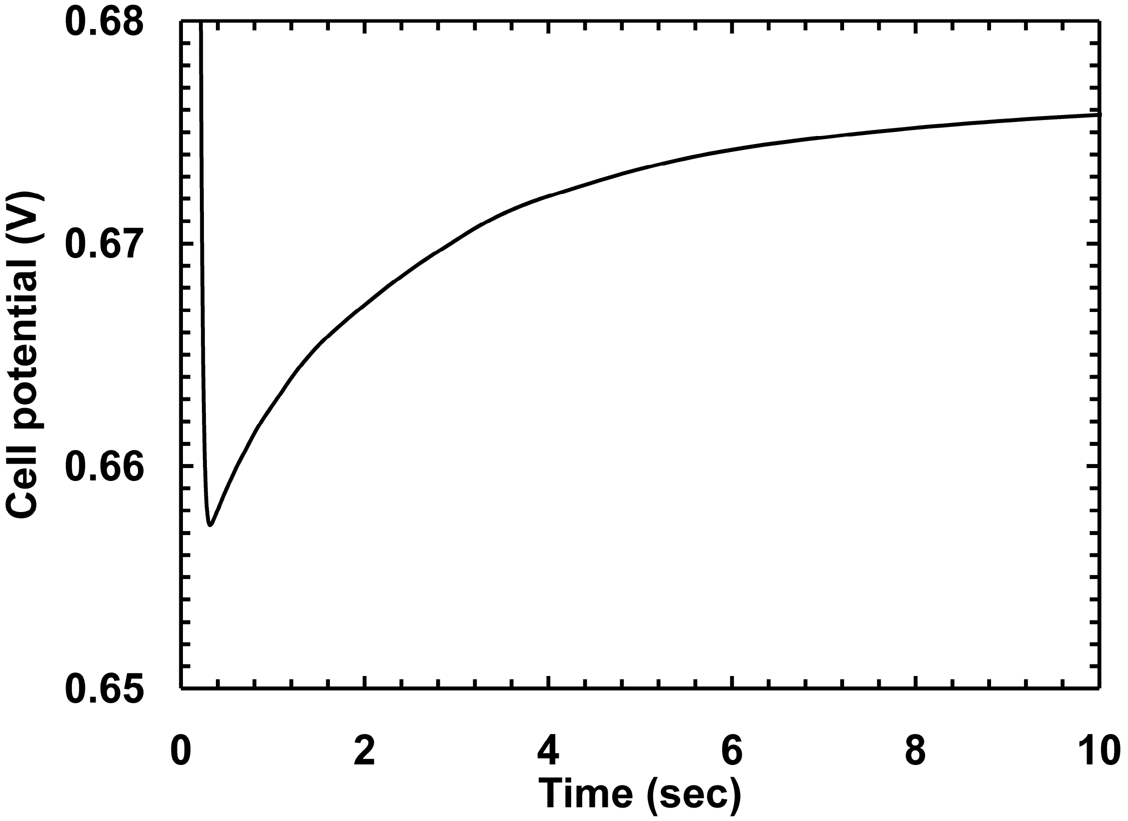

Figure 5.16. The expanded cell potential transient; I= 0 to 1 A.

The effect of the gas flow on the voltage transients is shown in Figure 6.17. The time constants of all the curves were negligibly affected by the gas flowrate. The initial dip was different because of the different flow pattern and temperature distribution within the system.

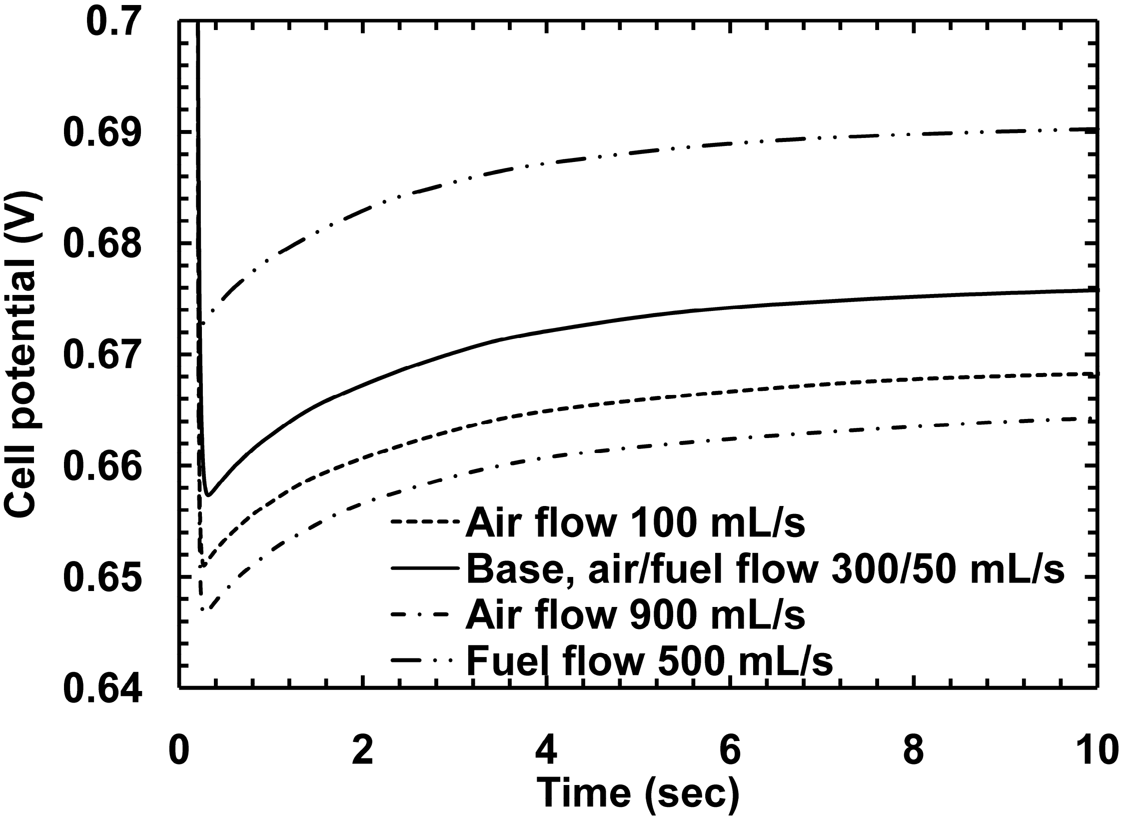

Figure 5.17. The effect of gas flowrate on the cell potential transient; I= 0 to 1 A.

5.5 Conclusion

The transient model was compared with the experimental results and was found to be consistent in its predictions. Similar to the steady-state non-isothermal simulations, including the effect of thermocouples attached to the cell resulted in model predictions closer to the experimental.

Two transients could be identified for the thermal transient of the system; a faster transient which corresponded to the cell, and a slow transient which corresponded to the furnace wall. The fast thermal transients had a time constant of about 2 seconds, consistent with the expected advantage of the TμSOFC for rapid heating and cooling. While it was not included in the model, the insulation covering the furnace wall made its transients even slower by adding a significant amount of thermal mass.

The transients in the concentration were very fast, with time constants of a fraction of a second. It was faster for the anode due to higher velocities in its gas channel.

The cell's voltage transient was control by the thermal transients, with a time constant of ~5 seconds. Therefore the small thermal mass of the TμSOFC, or in other words it fast thermal response, is directly translated into a faster electric response. As current was drawn from the cell, its voltage had a rapid dip and a gradual recovery. The gradual recovery was due to the increase in cell temperature.

Chapter 6. TµSOFC characterization and performance diagnostic

6.1 Introduction

The very thin electrolyte layer is an important advantage of the TµSOFC design, which should result in superior cell performance due to significantly lower ohmic losses in the electrolyte layer. It was suspected that the cell was suffering from an unidentified performance bottleneck.

Another group studied (Soderberg) the same type of cell to identify the cause of its underperformance by characterizing each electrode using EIS. They found that the electrochemical activity of the electrodes was normal, and in fact the anode was too active to be accurately characterized. Their study concluded that the ohmic resistance of the cell was higher than expected, potentially due to high contact resistance.

The contact resistance between the current collector layer and the electrode could indeed be the problem. The gold current collector did not adhere very strongly to the electrode surfaces inside and outside the cell, and could be peeled off relatively easily. The issue of contact resistance is more pronounced for tubular designs compared to planar, because no direct pressure can be applied to the current collectors to ensure their firm attachment to the electrode surface. The contact resistance is more concerning for the TμSOFC design, as it is impossible to even visually inspect the attachment quality inside the cell. Other current collector materials were tried, such as silver/palladium. Ag/Pd attached very well to electrode surfaces but shrank significantly after sintering such that the current collector layer was completely detached, forming a hollow tube of smaller diameter inside the cell.

In addition to the cell performance being lower than expected, it varied from cell to cell, changed with time, and from cycle to cycle when the cell was cooled down to room temperature and heated up again to its operating temperature. In addition, some cells suffered from severe performance degradation, especially during the first testing cycle; see Figure 6.1. Nonetheless, that the issue of irreproducibility and performance degradation is common in SOFCs.

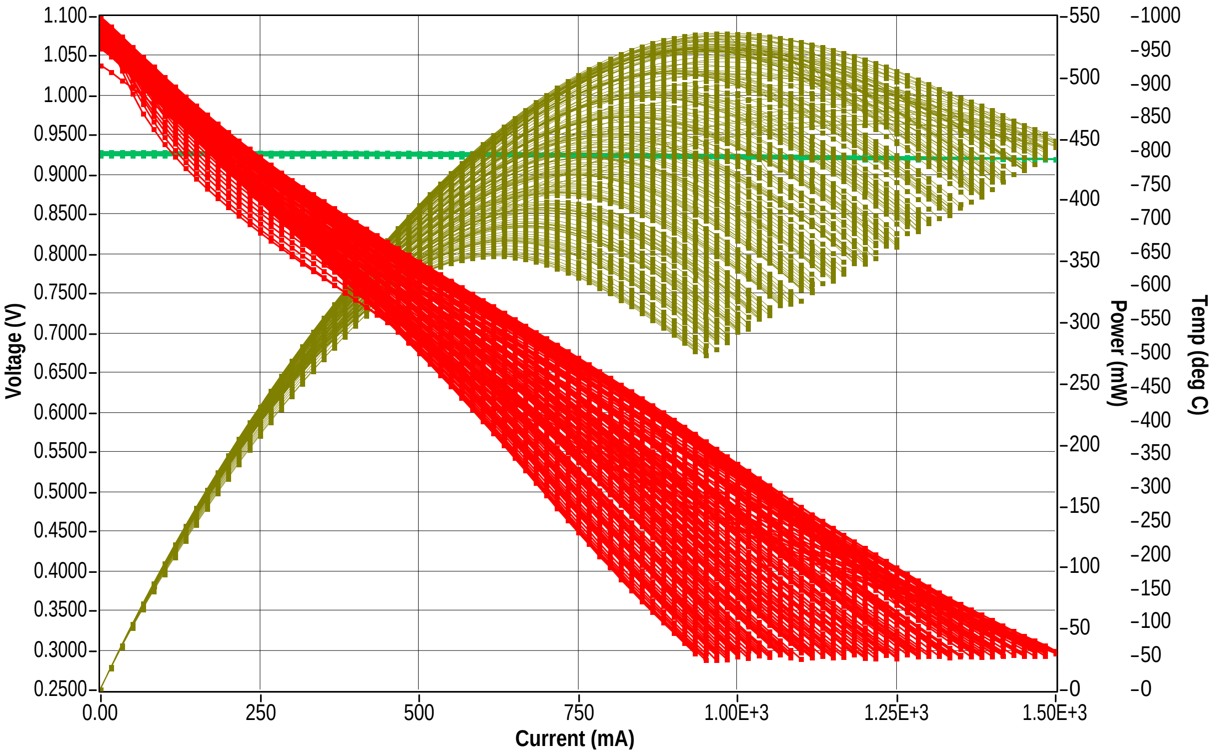

Figure 6.1. An experimental example of severe performance degradation in a TμSOFC. Each of the 176 I-V cycles lasted ~3 minutes, 1000 mA/min, with a 1 minute break after each cycle.

Therefore, an experimental study was conducted to find the cause of the underperformance and its irreproducibility issue, by characterizing cell components and the variability associated with them. The electrochemical performance of the cathode and its electronic conductivity was measured initially, as it is the main contributor to performance losses in a TμSOFC. The results were normal, although the electronic resistance was lower than theoretical values. Next, it was attempted to identify and measure the contact resistance of the current collectors. This was done by fabricating samples that only had an anode support layer (ASL) between two current collector layers (CCL). It was found that the resistance of the samples was much higher than expected, potentially because of the high contact resistance. However, further investigation using computer simulation indicated that not the contact resistance, but the resistance of the anode support layer itself could be the main cause of the high resistance. Therefore the conductivity of the ASL tubes was measured directly, and found to be several orders of magnitude lower than expected. In addition, the ASL conductivity significantly changed with temperature and time, taking several hours for the changes to settle once it was at 800°C.

In this chapter, the experimental results on the electronic conductivity of the electrodes, the cathode electrochemical performance, and their changes with time are presented and discussed. It is concluded that the low ASL conductivity and its variation is the main cause for the TμSOFC lower than expected and varying performance.

6.2 Experimental

6.2.1 The cathode effective conductivity measurements

The effective electronic conductivity of the cathode functional layer (CFL), a porous LSM-YSZ composite, was measured by the van der Pauw method (Pauw and J. 1958). This method is used to measure the specific conductivity of a flat, uniformly thin sheet of conductor. A thin layer of the cathode paste was screen-printed on a YSZ disk, and was sintered according to the TµSOFC cathode fabrication method. The current and voltage probes of a four-probe ohmmeter were connected to four small contact points on the periphery of the CFL layer. Note that the contact points do not necessarily have to be symmetric for the van der Pauw method. The resistance was measured for two configurations, shown in Figure 6.2. In practice, instead of measuring resistance, the voltage was measured at five current levels from 1 mA to 5 mA in 1 mA intervals. The resistance of the sheet in each configuration was obtained from the slope of the line passing through voltage versus current plot. Hence, more accurate data were obtained as measuring the resistant with just an ohmmeter was significantly fluctuating.

The effective electronic conductivity of the sheet (σ^{eff}) can be calculated by numerically solving the van der Pauw equation:

$$e^{-\pi R_A d \sigma^{eff}} + e^{-\pi R_B d \sigma^{eff}} = 1 \tag{6.6}$$

where d is the thickness of the layer and R_A and R_B is the resistance measured for each configuration.

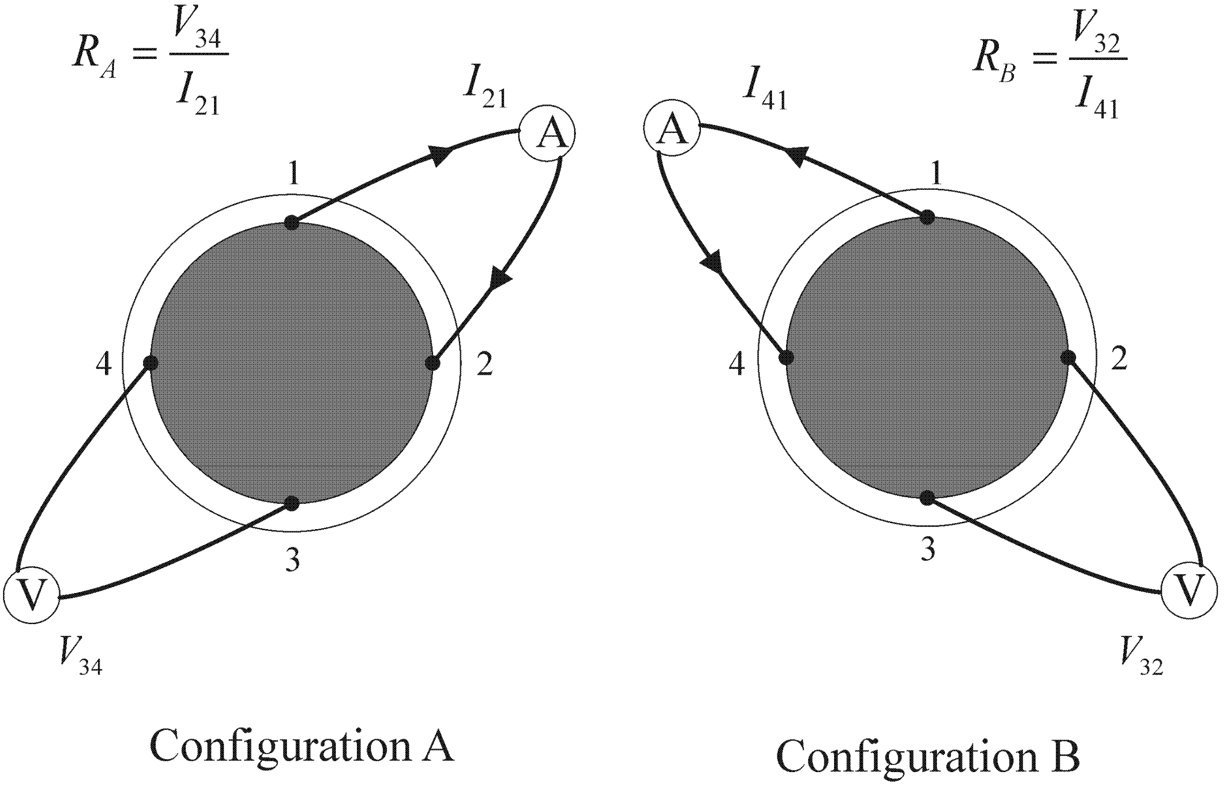

Figure 6.2. The two configurations used for the van der Pauw conductivity measurements method.

6.2.2 The cathode electrochemical performance measurements

The performance of the cathode was characterized by the electrochemical impedance spectroscopy technique (EIS) of symmetric button cells. The cells had circular electrodes (area = 1 cm^2, thickness = 30 μm), symmetrically deposited on each side of a thick YSZ disk (Fuel Cell Materials, thickness = 250 μm). The electrodes were fabricated by screen-printing of the cathode paste on both sides of the YSZ disk followed by sintering. The gold current collectors were paint-brushed on the top of each electrode followed by sintered. The sintering steps were according to the TμSOFC fabrication programs, given in tables 2.1 and 2.2.

The activation polarization of the cell was measured under air atmosphere using a Solartron 1255 Frequency response analyzer connected to a Solartron 1287 potentiostat. The impedance spectra were measured at OCV with a 10 mV AC perturbation signal at frequencies ranging from 0.1 Hz to 1 MHz.

6.2.3 The anode support layer effective conductivity measurements

The effective electronic conductivity of a porous Ni-YSZ composite can significantly change by the arrangement of the particles within its structure. A thin flat sheet of Ni-YSZ composite fabricated by EPD or by screen printing does not necessarily result in a micro-structure similar to the actual TμSOFC anode. Therefore a four-probe conductivity measurement was performed on bare tubes of the anode functional layer (AFL) and the anode support layer (ASL) fabricated by EPD, exactly the same way they were fabricated for the TμSOFC. The fabrication of AFL samples with EPD was challenging, as they frequently were fractured or destroyed during the sintering stage. The fabricated samples were very fragile. This was not a problem for the actual TμSOFC, as ASL was deposited on the graphite rod by EPD and supported the AFL deposited on top of it.

The tubes were 4-5 cm long. A conductive Ag/Pd paste was applied to firmly attach the wrapped connecting wires to each end of the tube. The paste covered the edges of the tubes to eliminate the possibility of results being affected by any accumulation of YSZ particles on the surface of the tubes.

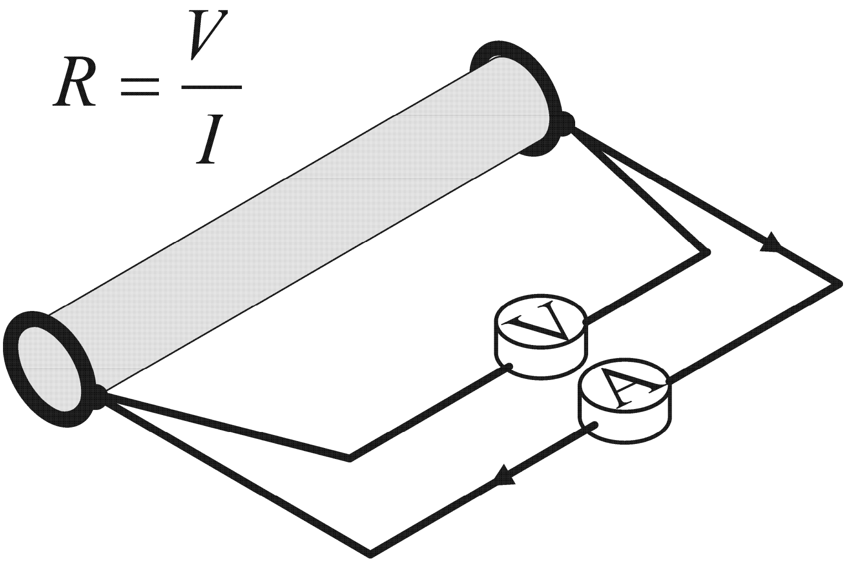

Figure 6.3. A schematic of the four-probe measurement of the ASL and the AFL tubular samples.

The samples were tested in a tubular electric furnace (L = 50 cm, ID = 2.5 cm), and were heated and cooled at 5°C/min. A PID controller maintained the temperature of the thermocouple attached to the samples inside the furnace at the desired level. The reducing atmosphere was maintained by flowing 100 $mL.s^{-1}$ of hydrogen, humidified at room temperature, through the furnace tube. The resistance was measured at various temperatures in a four-probe configuration by an Agilent 34970A DAQ switch equipped with a 34901A multiplexer module. Several samples could be placed in the furnace and tested at the same time.

The effective specific electronic conductivity of the ASL and AFL composites were calculated as:

$$\sigma^{eff} = \frac{L}{2\pi dR} \tag{6.7}$$

where d, R, and L are the thickness, inner radius, and length of the tube.

6.2.4 The contact resistance measurement

Samples with only the ASL and the gold current collectors layers (CCL) were used to measure the contact resistance between the ASL and the CCL. The CCL covered the exact same areas as the TμSOFC current collectors. It covered inside the cell to the open end, and a length of 2.5 cm outside the tube close to its close end - similar to the active length in the actual TμSOFC. Once the ASL was reduced, there was a complete electronically conducting path between the electrodes. The resistance measured across the electrodes included the resistance of the CCLs, the ASL, and the contact resistances between the layers; see Figure 6.4.

The experimental setup and procedures were the same as the ASL effective conductivity measurement, described in section 6.2.3. The samples were reduced prior to the actual measurement at 800°C for 2 hours under humidified hydrogen atmosphere, and were cooled down to room temperature.

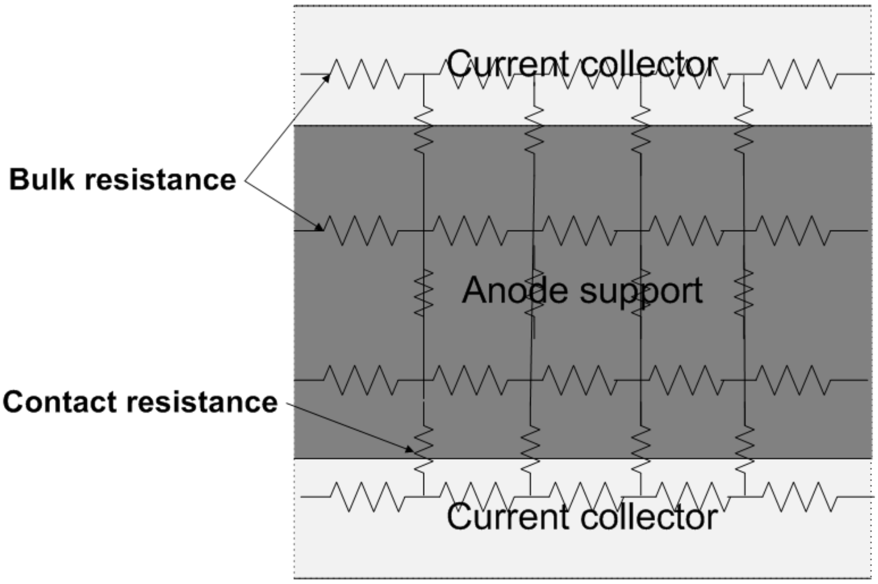

Figure 6.4. A schematic of the various contributions to the overall resistance of the contact resistance samples.

6.3 Results and discussion

6.3.1 The cathode electrochemical polarization resistance and its degradation

The polarization resistance of each electrode (R_p) was calculated as the half of the horizontal distance between the two x-axis intercepts of the impedance curve, shown in Figure 6.5. This implied the assumption that the electrodes had the same R_p, or in other words the calculated R_p, was the average of the two electrodes. R_p is an indicator of the electrode performance and represents the activation resistance and diffusion limitation of the electrode, but not the ohmic losses. Figure 6.6 shows the calculated R_p as a function of temperature. The activation energy of the cathode was estimated to be ~128 $kJ.mol^{-1}$, compared to other values reported in the literature, 200 $kJ.mol^{-1}$ (Shi et al., 2007), 120 $kJ.mol^{-1}$ (Costamagna and Honegger, 1998) (Nehter, 2006), and 160 $kJ.mol^{-1}$ (Costamagna and Honegger, 1998). The long term R_p of the cathode at 800°C settled within 20 hours, a less than 10% change; see Figure 6.7.

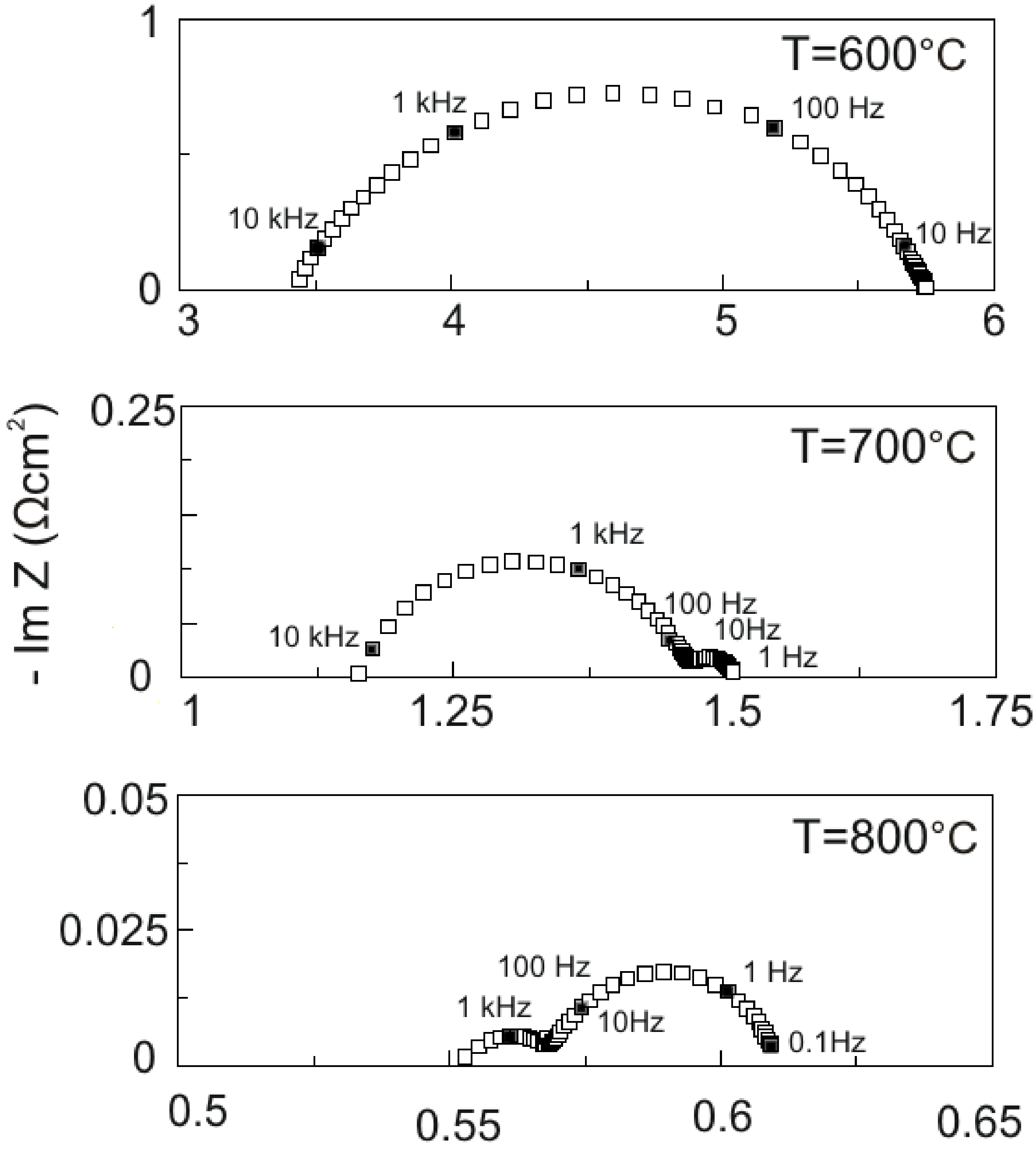

Figure 6.5. The impedance spectra of the symmetric planar cell at various temperatures; the high frequency tail below x-axis is truncated.

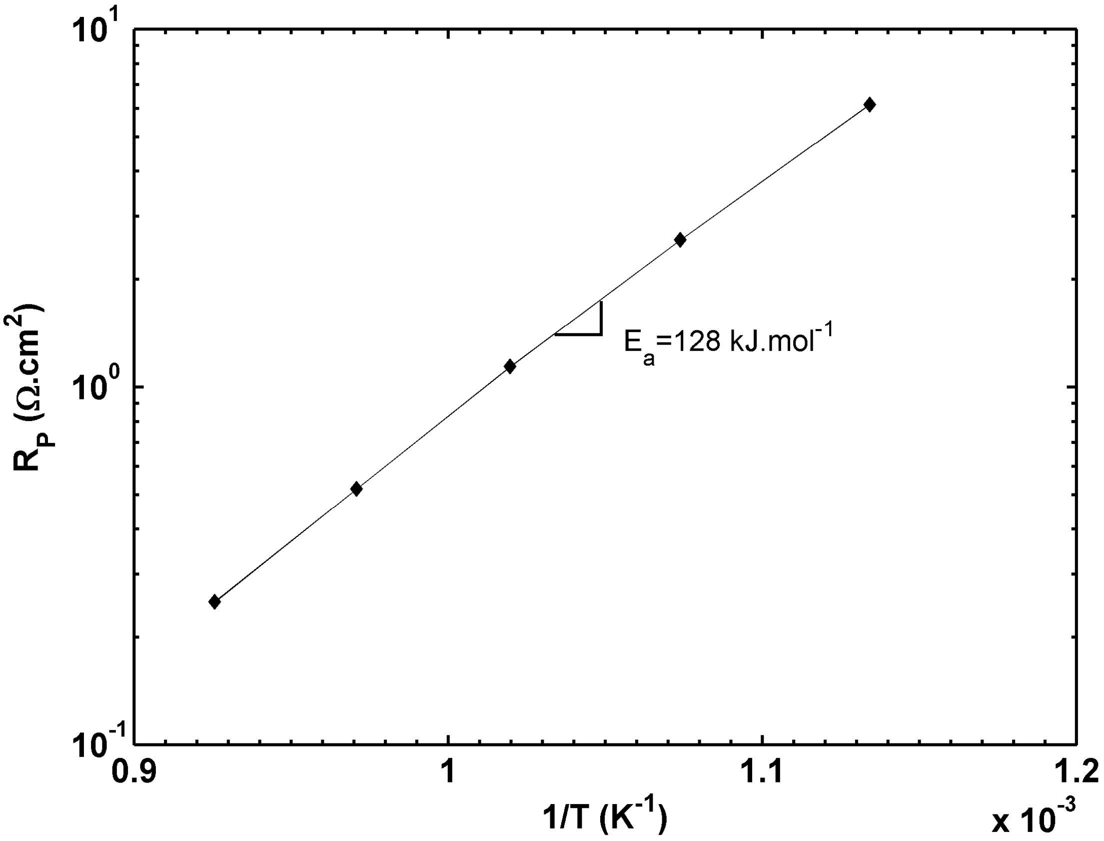

Figure 6.6. The temperature dependence of the cathode polarization resistance, R_p.

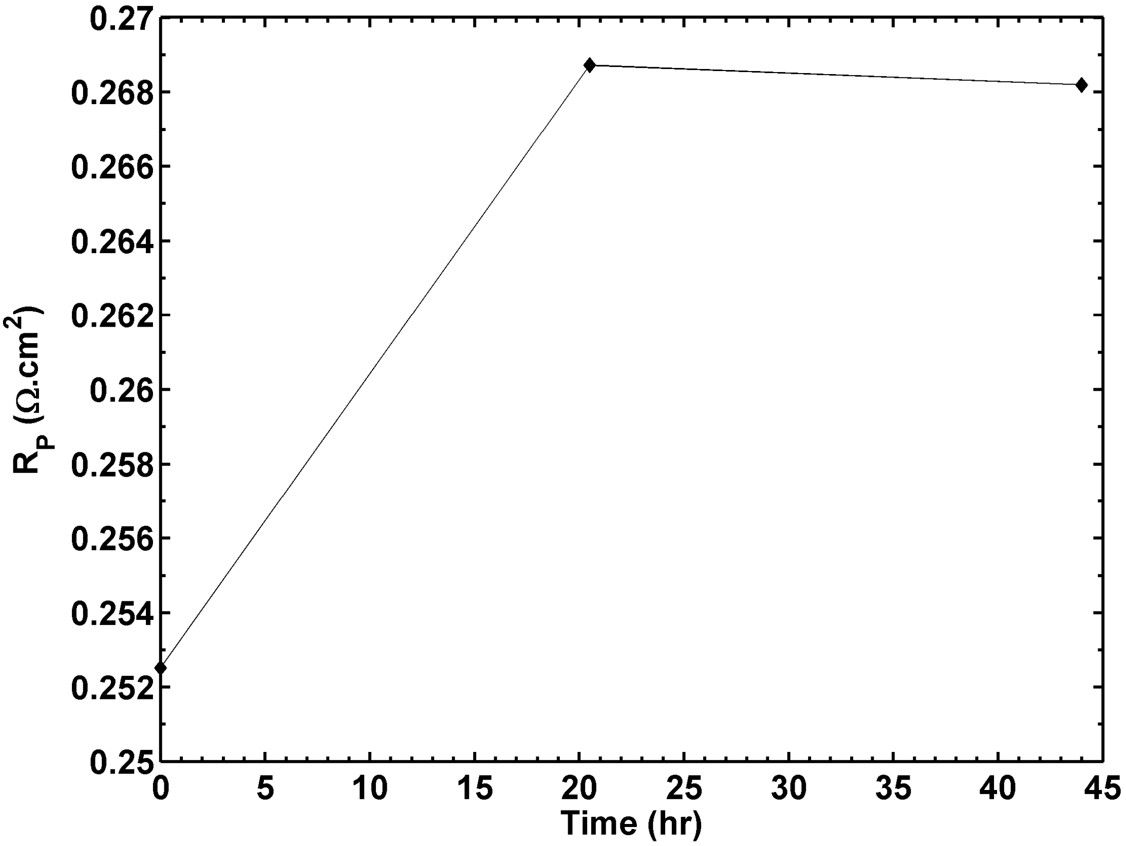

Figure 6.7. The change in the polarization resistance of the LSM-YSZ cathode with time.

6.3.2 Electronic conductivity of the cathode and its degradation

The electronic conductivity of the LSM-YSZ cathode was measured at various temperatures, as shown in Figure 6.8. The effective electronic conductivity of the cathode at 800°C did not change significantly with time; see Figure 6.9. The conductivity at the end of the test, after ~30 hours at 800°C, was ~242 $S.m^{-1}$ compared to 13400 $S.m^{-1}$ (Shi et al., 2007), 12800 $S.m^{-1}$ (Ferguson et al., 1996) and a theoretical value of 4500 $S.m^{-1}$ based on the percolation theory.

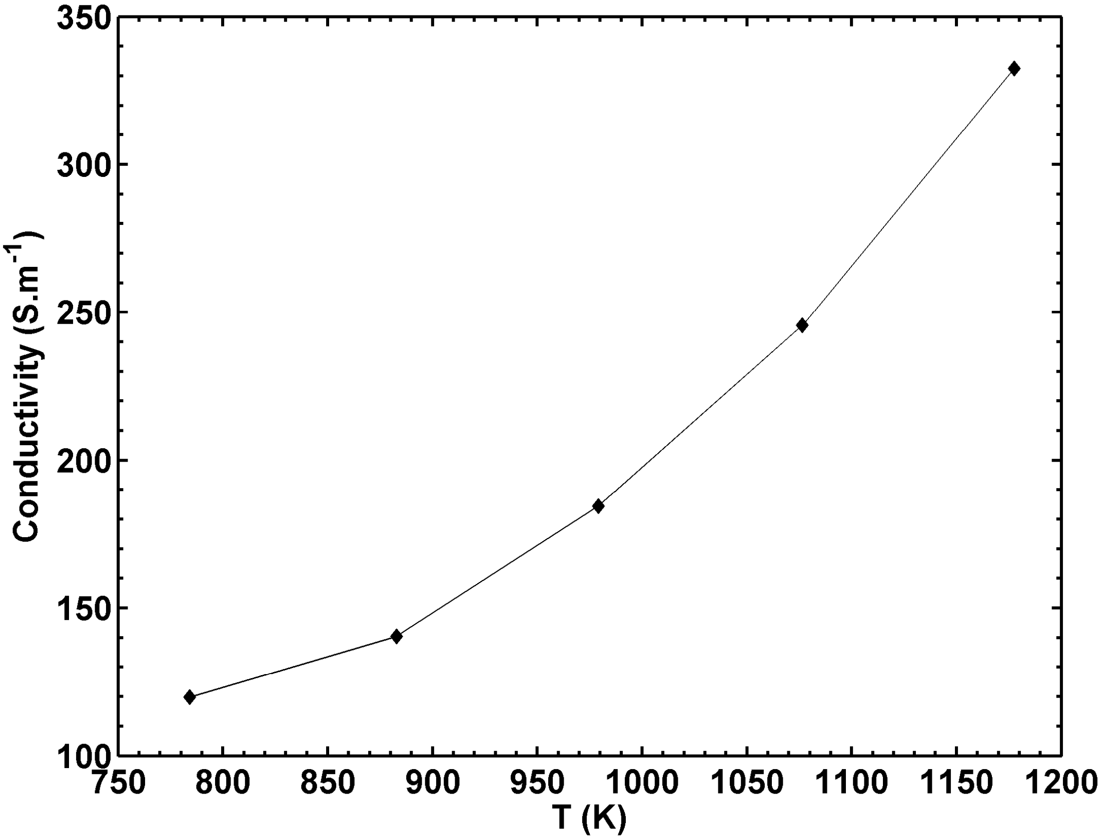

Figure 6.8. The effective electronic conductivity of the LSM-YSZ electrode versus temperature.

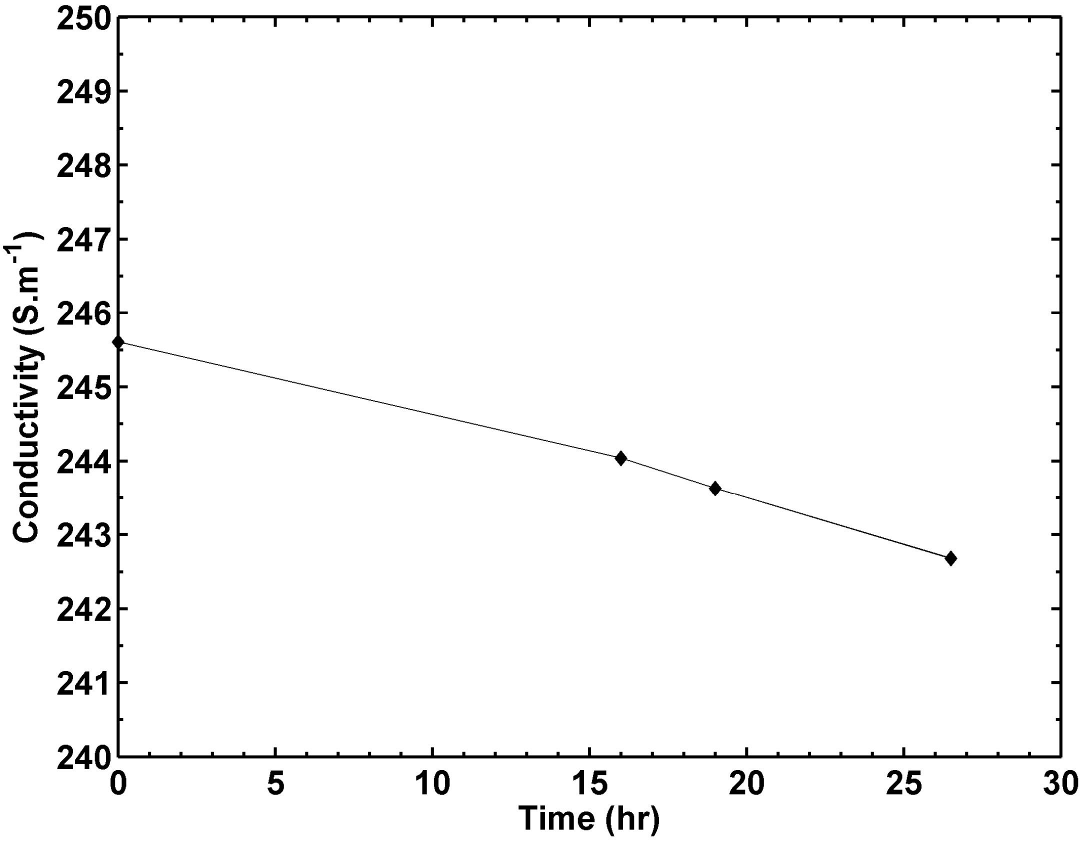

Figure 6.9. The change in the effective electronic conductivity of the LSM-YSZ electrode at 800°C versus time.

6.3.3 The contact resistance measurement

The resistances of the "contact resistance" samples at various temperatures are shown in Figure 6.10. To have a better sense of the resistance values, note that the ASL ohmic contribution to the performance loss simulated for the isothermal cell, Figure 3.5, was equivalent to 0.12 Ω. An initial calculation indicated that the resistances of the samples were higher than expected. Therefore contact resistance could indeed be an issue. However, contact resistance should not change with temperature if the sample microstructure remains unchanged, while Figure 6.10 shows the overall resistance changes with temperature. It was noticed that the resistance changes were consistent with the change in the conductivity of gold and nickel. To further confirm this, the overall resistance was predicted with the mathematical model as a function of temperature.

The current conduction within the samples was mathematically modeled using Ohm's law, similar to the TμSOFC model, which included ASL and the inner and outer current collector layers. Temperature dependent conductivities were used for the ASL and the CCLs, and therefore the resistance of the samples could be predicted at various temperatures. Values found for the ASL effective conductivity are subject to significant uncertainty, due to the percolation effects in the Ni-YSZ composite; 3e4 S.m^{-1} (Ferguson et al., 1996), 2e6 S.m^{-1} (Shi et al., 2007), and a theoretical value of 7e5 S.m^{-1} based on the percolation theory. Using the first value as a conservative estimate of the ASL conductivity, the overall resistance of the sample at 800°C was estimated to be ~0.025 Ω, which is smaller than the experimental values shown in Figure 6.10.

Further developing the model, the effective conductivity of ASL was estimated as the temperature dependent Ni conductivity, multiplied by a factor. The factor was estimated such that at 800°C the predicted overall resistance matched that of the experimental. Using the same factor, the overall resistance was predicted for the complete temperature range of the experimental, see Figure 6.10. The predicted resistance followed the experimental trend very well and captured the changes in the sample resistance with temperature. This led to the conclusion that the ASL low effective conductivity could be the main cause of the high resistance, not the contact resistance. Therefore the conductivity of ASL samples were measured experimentally, which confirmed this hypothesis, as it will be discussed in the next section.

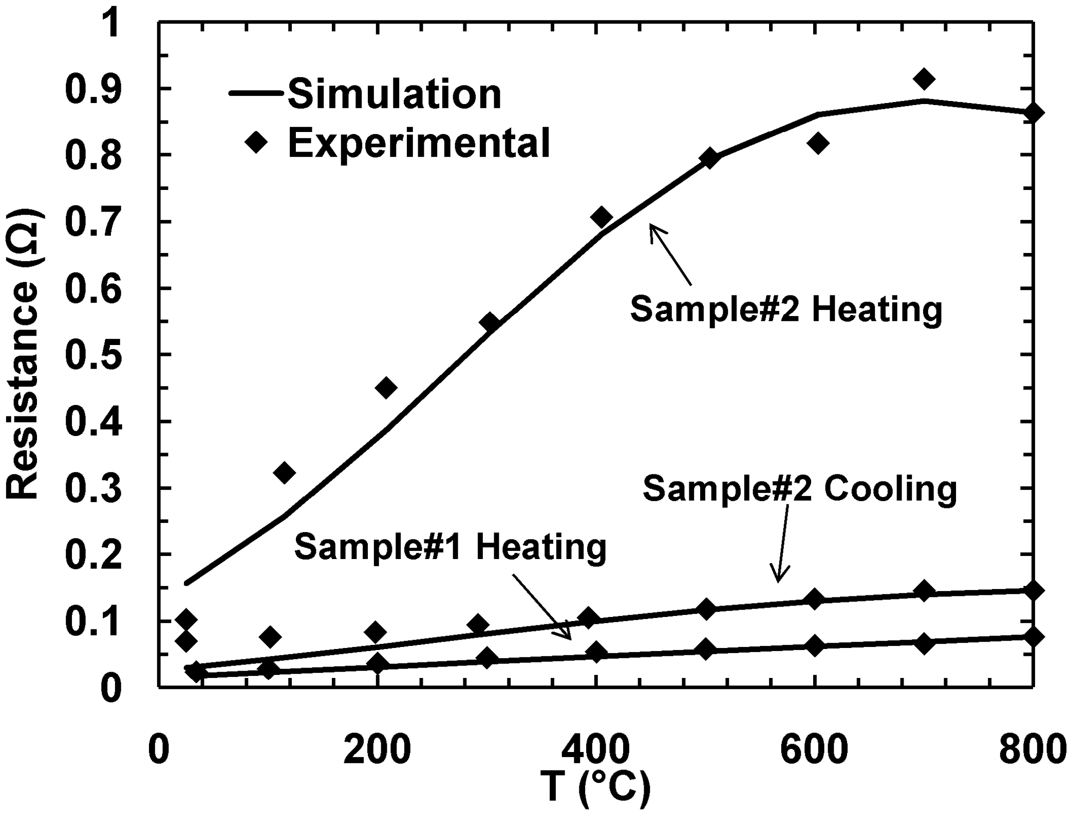

Figure 6.10. The experimental and simulated overall resistance of the contact resistance samples versus temperature.

The effective conductivity of the ASL for the simulated overall resistance of the samples shown in Figure 6.10 at 800°C were estimated, by fitting, to be 1.8, 24, and 1305 $S.m^{-1}$ for an overall resistance of 0.86, 0.15, and 0.077 Ω, respectively. Clearly, the effect of ASL conductivity on the overall resistance becomes more significant at lower ASL conductivities. Therefore changes in the ASL conductivity at those low conductivity values, which would normally have a minor effect on the overall resistance, can become a major bottleneck that cause large changes in the overall performance of the cell.

The resistance of the ACCL was predicted by the model to be 0.034 Ω at 25°C, which is consistent with the experimental value. The resistance of the sintered CCL layer inside the unreduced cell was measured experimentally to be ~0.03 Ω (the conductivity of the inner CCL layer, as the unreduced ASL was non-conducting), which further validates the conduction model. It was mentioned earlier that the model predicted the overall resistance of the samples ~0.025Ω, using an expected value for the ASL conductivity, lower than the resistance of the inner CCL even at room temperature – note that the resistance increased with temperature. This is because a highly conductive ASL layer would contribute to current conduction, hence reducing the overall resistance of the sample. In other words, when the conductivity of ASL is high, it conducts the current along the gold CCL. On the other hand, when the ASL conductivity is low, only CCL conducts the current along the cell. In that case current would flow across the ASL to get to the CCL, while negligible current passes along the ASL due to its high resistance.

At 800°C, the overall resistance of the samples changed significantly with time; see Figure 6.11. The sample resistance reduced to a fifth of its initial value within 10 hours.

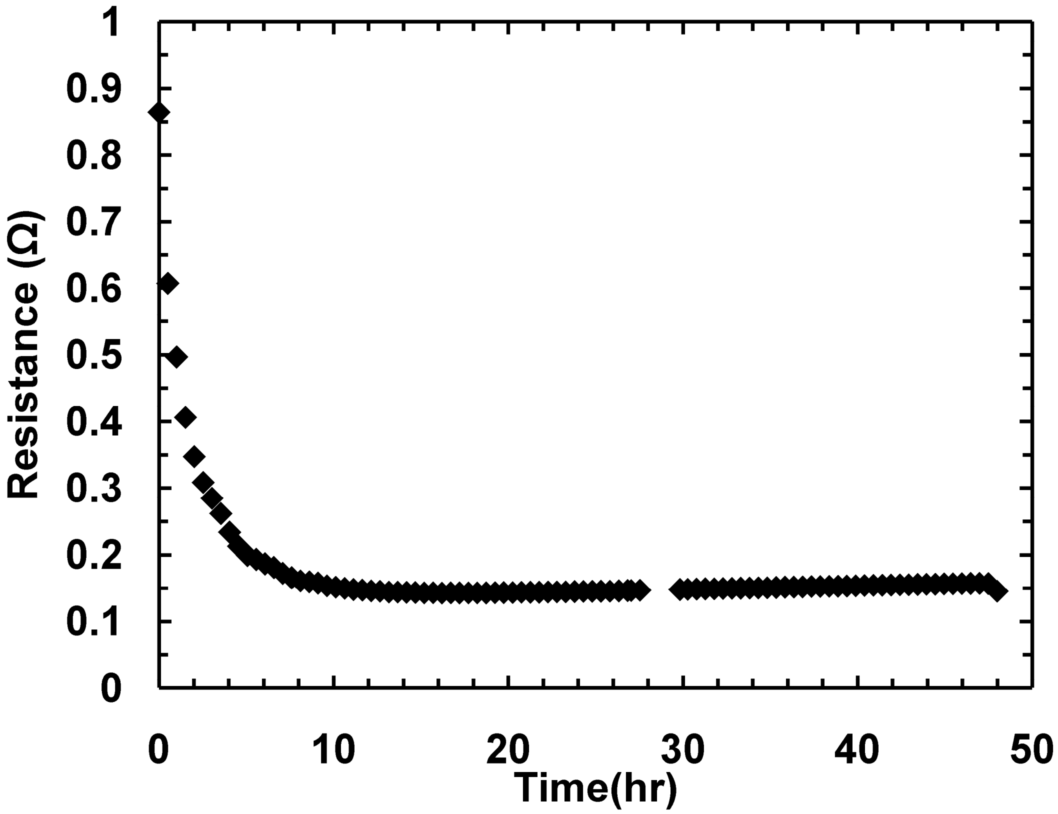

Figure 6.11. The overall resistance changes in the contact resistance samples versus time.

6.3.4 The anode support layer effective electronic conductivity

The conductivity of the ASL tubular samples was measured to be much lower than expected and changed significantly with time and with temperature. The tests were conducted under a reducing atmosphere, i.e. humidified hydrogen. Some selected results are presented in this section, as shown in Figures 6.12 to 6.20.

Figure 6.12 shows the conductivity of four ASL samples, ASR87-1, ASR87-2, ASR89-1, and ASR89-2. All four samples were tested together to expose them to the exact same temperature history and therefore to minimize the variations that could be caused by testing them individually. In addition, each pair of samples was half of a longer ASL tube, ASR87 and ASR89. Therefore the samples ASR87-1 and ASR87-2 were fabricated on the same EPD rod, and had the exact same fabrication history; similarly for ASR89-1&2. This minimized the variations in the microstructure of each pair of samples as much as possible. Despite the variations observed in the measurements of these four samples, they have a common trend and share several distinct characteristics. The samples were initially non-conducting. As the temperature rose, an abrupt increase in the conductivity of all the samples can be seen around 450°C, which indicated the reduction of non-conducting NiO to metallic Ni. The initial conductivity of all the samples was about 1e5 $S.m^{-1}$, as expected for Ni-YSZ composite electrodes. This shows that the Ni particles were well-percolating and formed a full path for electronic conduction. However, the conductivity of the samples dropped significantly, by 1000 times, as the temperature rose to and stayed at 800°C. The temperature ramp took about 2 hours to complete and reach 800°C. Note that the x-axis in most figures are in log scale to expand the initial time-frame, when most changes occurred. It took from 20 minutes to 40 hours for the conductivity of different samples to settle. Three of the samples showed significant oscillation in their conductivities during that period. After ~100 hours at 800°C, the conductivities of all the samples were about 50 to 100 $S.m^{-1}$ and had a gradual decreasing trend.

Once the samples were cooled down to room temperature, the samples had conductivities varying from 10 to 1e4 $S.m^{-1}$; see Figure 6.13. During the second heating cycle, the conductivity of all the samples experienced a sharp drop as seen in Figure 6.13. Although the sharp drop occurred for all the samples, its time and temperature varied for different samples from 20 minutes to 2 hours into the experiment at temperatures ranging from 100°C to 450°C. The magnitude of the drop on the log scale varied for samples, and was less for those with a higher initial conductivity. After the drop, the conductivity of all the samples gradually increased to values ranging from 1 to 10 S.m^{-1}, 10 hours into the experiment at 800°C. Figure 6.14 shows that the conductivities of the samples after 120 hours at 800°C were about 5 to 30 S.m^{-1}. As the samples were cooled down for the second cycle, their conductivity dropped significantly, making the samples essentially non-conducting.

Figures 6.15 and 6.16 show the conductivities of the two samples ASR89-1 and ASR89-2 throughout their second testing cycle, as a function of temperature. Both samples share similar features, as their conductivity went through the cycle, starting at a low value, increasing with temperature, and decreasing to levels below their initial value when they are cooled down to room temperature. A significant observation is that the conductivity of the samples experience step-like changes, which occurred around the same temperatures for the heating and the cooling stages.

Figure 6.17 shows the conductivity of the sample ASR40, which was reduced under humidified hydrogen for 2 hours prior to the actual experiment. Therefore it was essentially the second heating cycle for the sample. The sample conductivity increased by about 100 times from room temperature to 800°C. No sharp drop in the conductivity was observed unlike the second heating cycle of ASR87&89-1&2. At 800°C, the conductivity had a decreasing trend with a final value of about 8 S.m^{-1} after 50 hours into the experiment. The step-like changes can be observed in the heating and cooling curves, Figures 6.17 and 6.18. A large step in the conductivity can be seen in Figure 6.19, which occurred around the same temperature during the heating and cooling ramps. The final conductivity of the sample was ~0.01 S.m^{-1}, lower than its initial value before the testing cycle.

The conductivity of the sample ASR39, which was reduced for 2 hours before the experiment, is shown in Figure 6.20. The conductivity of the sample had a sharp drop as it was heated up, similar to the second testing cycle of the ASR87&89 samples. Similarly, the conductivity increased as the temperature rose. The final conductivity of the sample at 800°C was about 2 S.m^{-1}, ten times higher than its value of 0.2 S.m^{-1}.

Therefore, a significant variation was observed in the ASL conductivity measurements, even for samples made from the same tubes and tested together, as discussed above. However, the following common observations can be identified:

1- The samples were highly conductive, as expected for a Ni-YSZ composite, right after they were reduced.
2- The conductivity degraded very rapidly to values several orders of magnitude below the initial values.
3- Significant oscillation in the conductivity was observed during the early stages of the first cycle, just after reduction, and it took tens of hours for the changes to settle. The conductivity did not have these oscillations during the second heating cycle and beyond.
4- Once the initial changes were settled, the conductivity had a very gradual decline.
5- In general, the conductivity decreased from one cycle to the next.
6- After the first cycle, the conductivity of the samples increased with temperature. In fact, some samples were essentially non-conducting at room temperature, became conductors as their temperature was increased, and became non-conducting again once they were cooled down to room temperature.
7- Step-like changes occur in the conductivity, especially during the heating and cooling stages, and frequently around the same temperature.

Observation 1 indicates that the Ni particles were well percolated and initially well connected in the composite. Observations 2 and 3 show that the Ni network microstructure in the composite experienced significant changes once the NiO was reduced to Ni. This should be mainly due to the significant agglomeration of Ni particles, which is a well known issue for high temperature Ni-YSZ electrodes. In addition, the NiO particles shrink when they are reduced to Ni. This would introduce transients in the microstructure and hence its effective conductivity. The agglomeration effects are faster for smaller particles, while it slows down as more as the agglomerates grow. Therefore the slow reduction of conductivity is still present in long term and from cycle to cycle; i.e. observations 4 and 5.

Observations 6 and 7 are more difficult to explain. Note that the intrinsic conductivity of Ni decreases with increasing temperature. Therefore the increase in the effective conductivity of the Ni-YSZ composite should be due to changes in the microstructure of the Ni network in the composite. A theory can be presented to consistently explain observations 6 and 7. The Ni microstructure, formed and agglomerated at 800°C, shrinks relative to the YSZ structure due to the higher thermal expansion coefficient of Ni compared to YSZ. This causes mechanical stresses on the Ni network, which can lead to the detachment of some of the contacts, and therefore reduce the effective conductivity of the composite at lower temperatures. When temperature is increased again, the Ni particles expand relative to the YSZ structure, forming new contacts and hence increasing the conductivity of the network. If the percolation of the network is low enough, or if the microstructure of the Ni network is such that “bottleneck” bridges are present for electron conduction, breakage of those few bottleneck contacts will result in a significant drop in the effective conductivity of the sample. This can explain the step-like changes in the conductivity versus temperature curves, and the fact that they occur around the same temperature during the heating and cooling cycles.

Figures 6.21 to 6.27 show SEM images of the ASR39 microstructure, after the conductivity tests. Note the spherical Ni particles trapped in cavity like enclosure of the YSZ structure, and the clearance that exists between the sphere and its surrounding, especially in Figures 6.23, 6.24, and 6.27. Also, note the gap between the spherical particles sitting by each other. In addition, the nickel particles appear as discrete cavities scattered throughout the relatively continuous microstructure of YSZ; see Figure 6.21. The precursor powder of the ASL had NiO particles of 0.65 μm, and YSZ particles of 0.35 μm, which explains why the YSZ structure is more continuous after sintering.

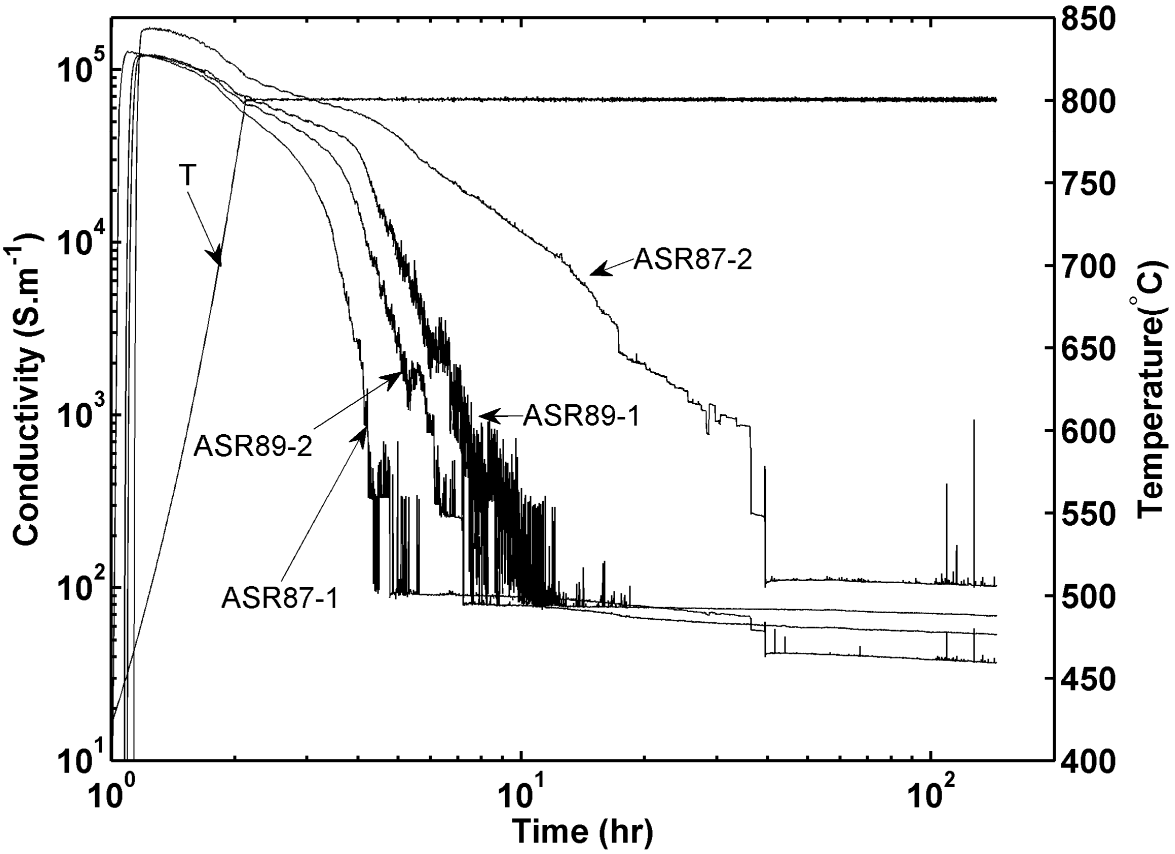

Figure 6.12. The conductivity of the ASL samples during the first cycle of heating and long-term testing. The samples were tested together under a humidified hydrogen atmosphere, and were initially unreduced. ASR87-1 and ASR87-2 were made from the same longer tube; same for ASR89-1 and ASR89-2.

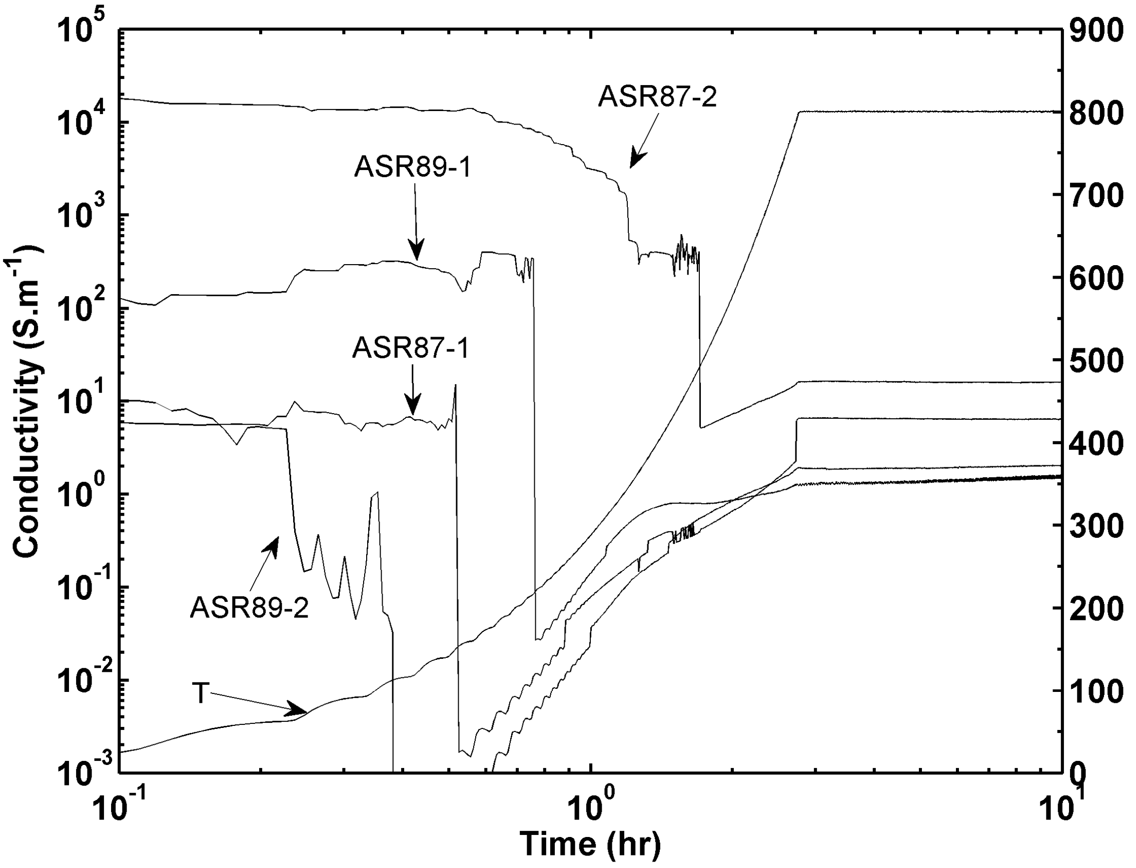

Figure 6.13. The conductivity of the ASL samples during the second cycle of heating and long-term testing. ASR87-1 and ASR87-2 were from the same longer tube; same for ASR89-1 and ASR89-2.

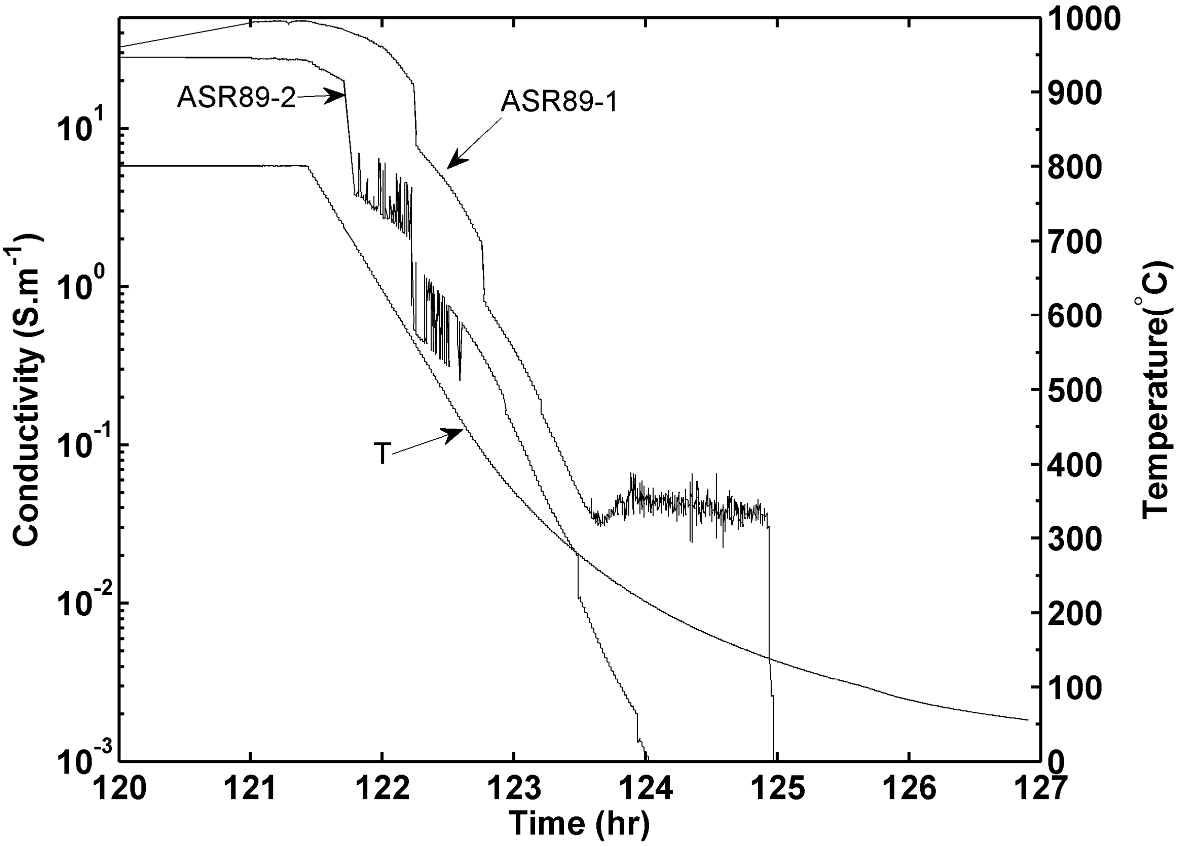

Figure 6.14. The conductivity of ASR89-1&2 during the cooling stage of the second cycle. They were from the same longer tube.

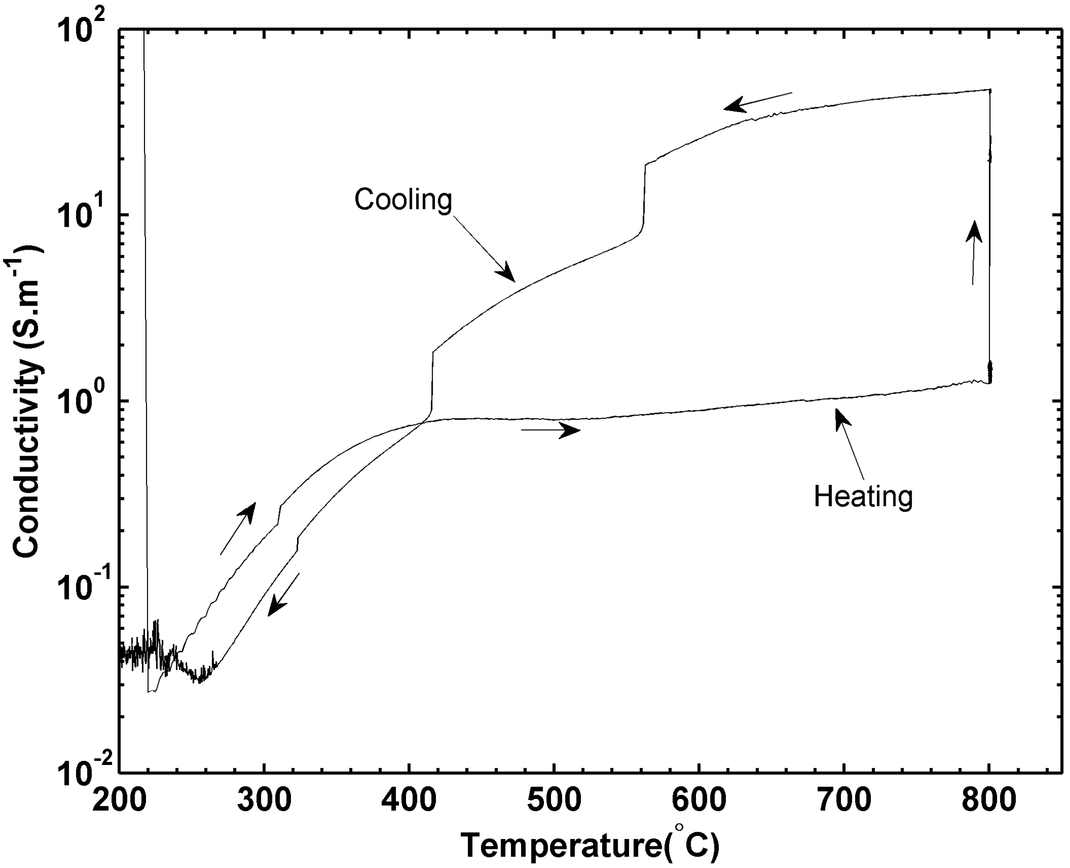

Figure 6.15. The conductivity of ASR89-1 as a function of temperature during the heating, long-term and cooling stages of the second testing cycle.

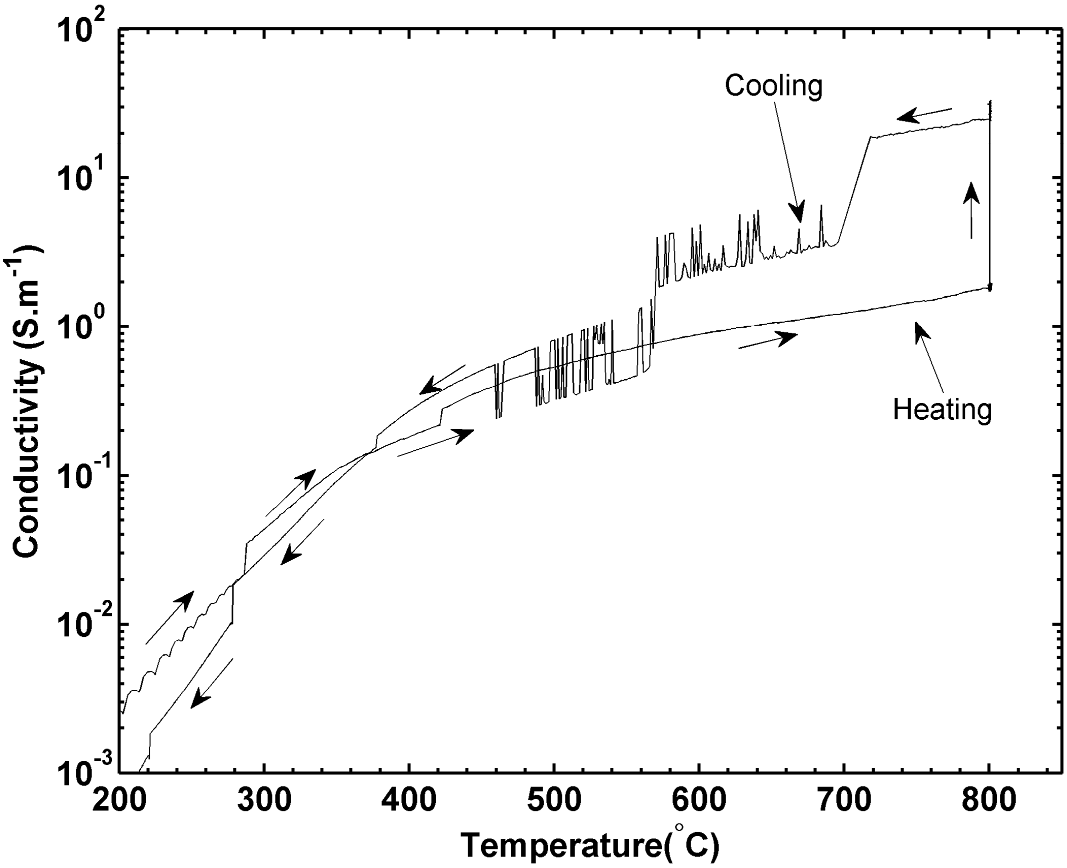

Figure 6.16. The conductivity of ASR89-2 as a function of temperature during the heating, long-term and cooling stages of the second testing cycle.

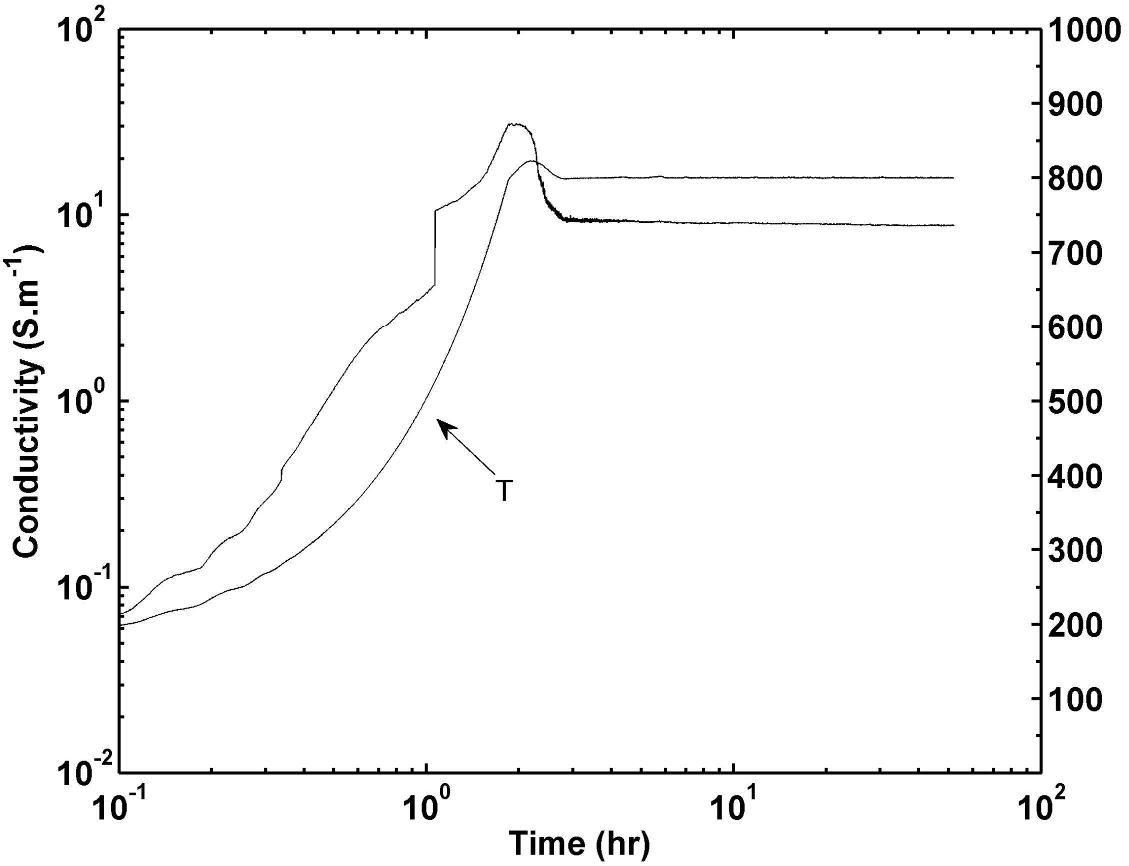

Figure 6.17. The conductivity of ASR40 during the heating and long-term testing. The sample was reduced for 2 hours prior testing.

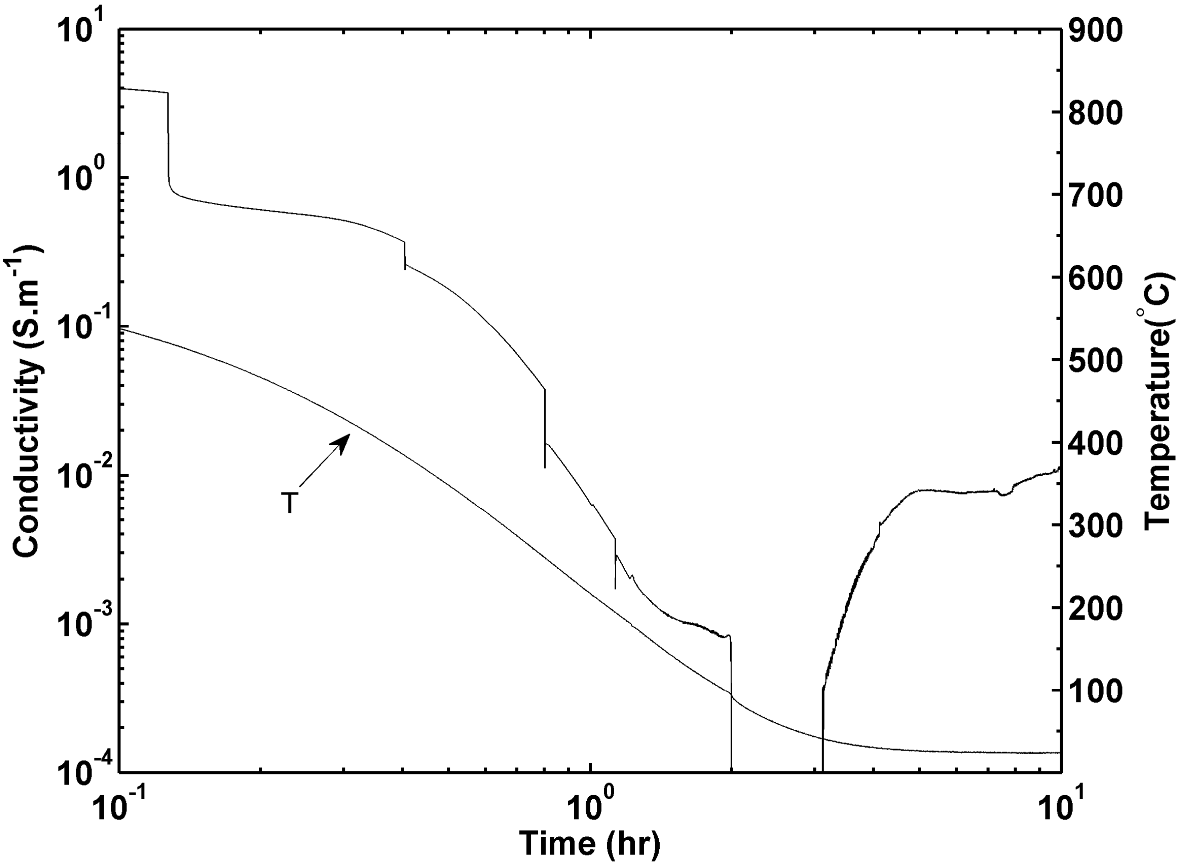

Figure 6.18. The conductivity of ASR40 during the cooling stage of its first testing cycle (second heating cycle).

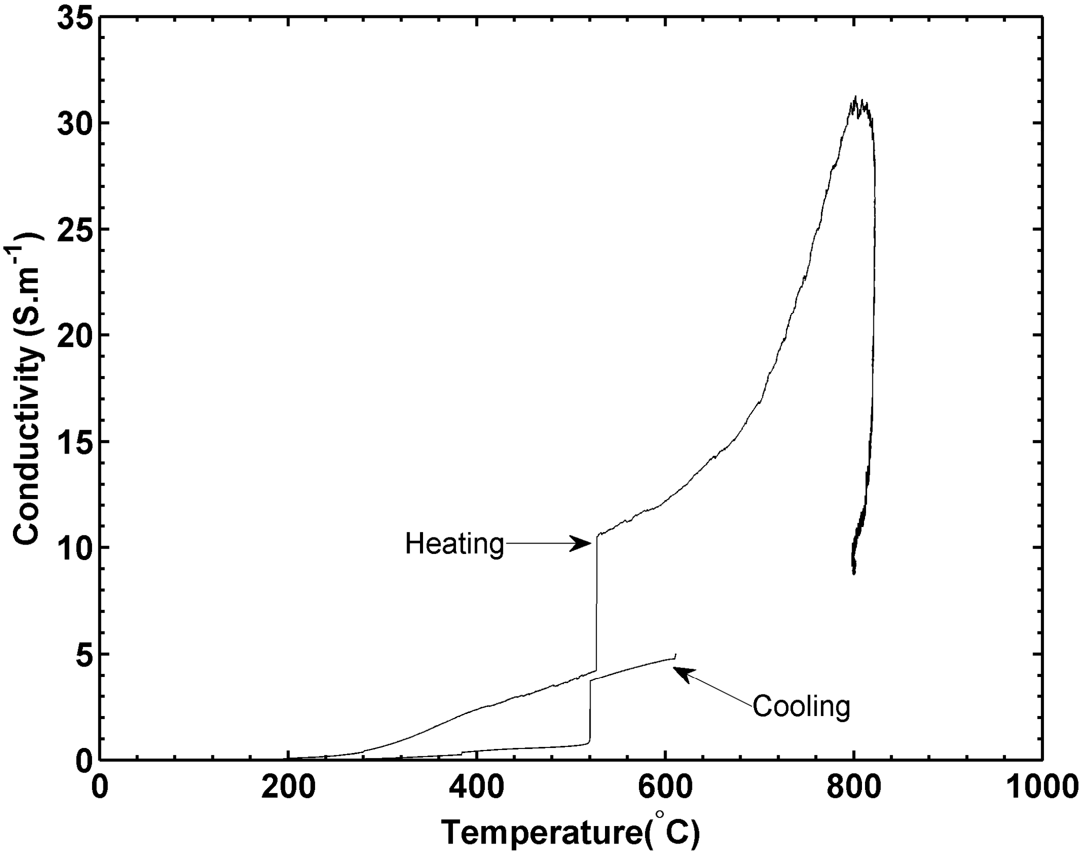

Figure 6.19. The conductivity of ASR40 as a function of temperature during the heating, long-term and cooling stages.

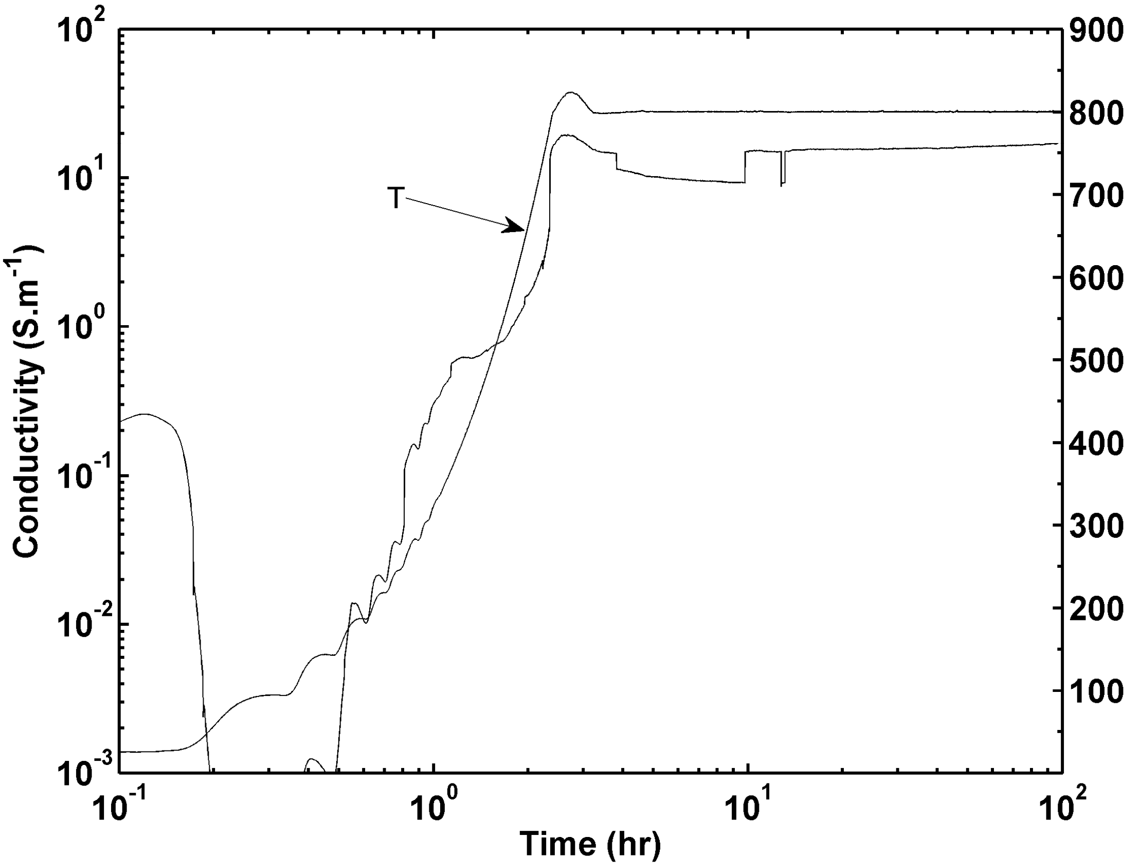

Figure 6.20. The conductivity of ASR39 during the heating and long-term testing stages. The sample was reduced for 2 hours prior testing.

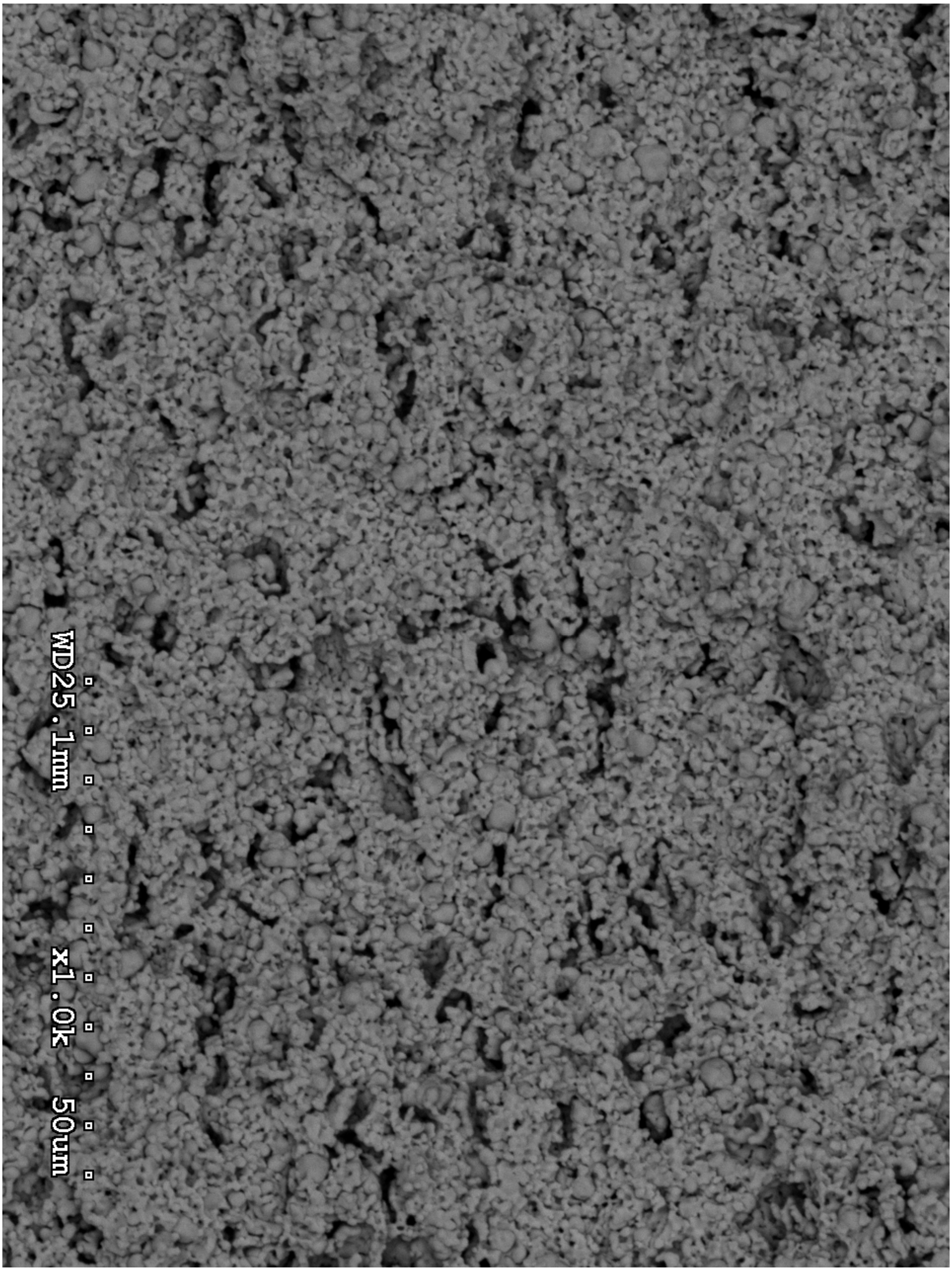

Figure 6.21. The SEM microstructure of ASR39 after the conductivity measurements.

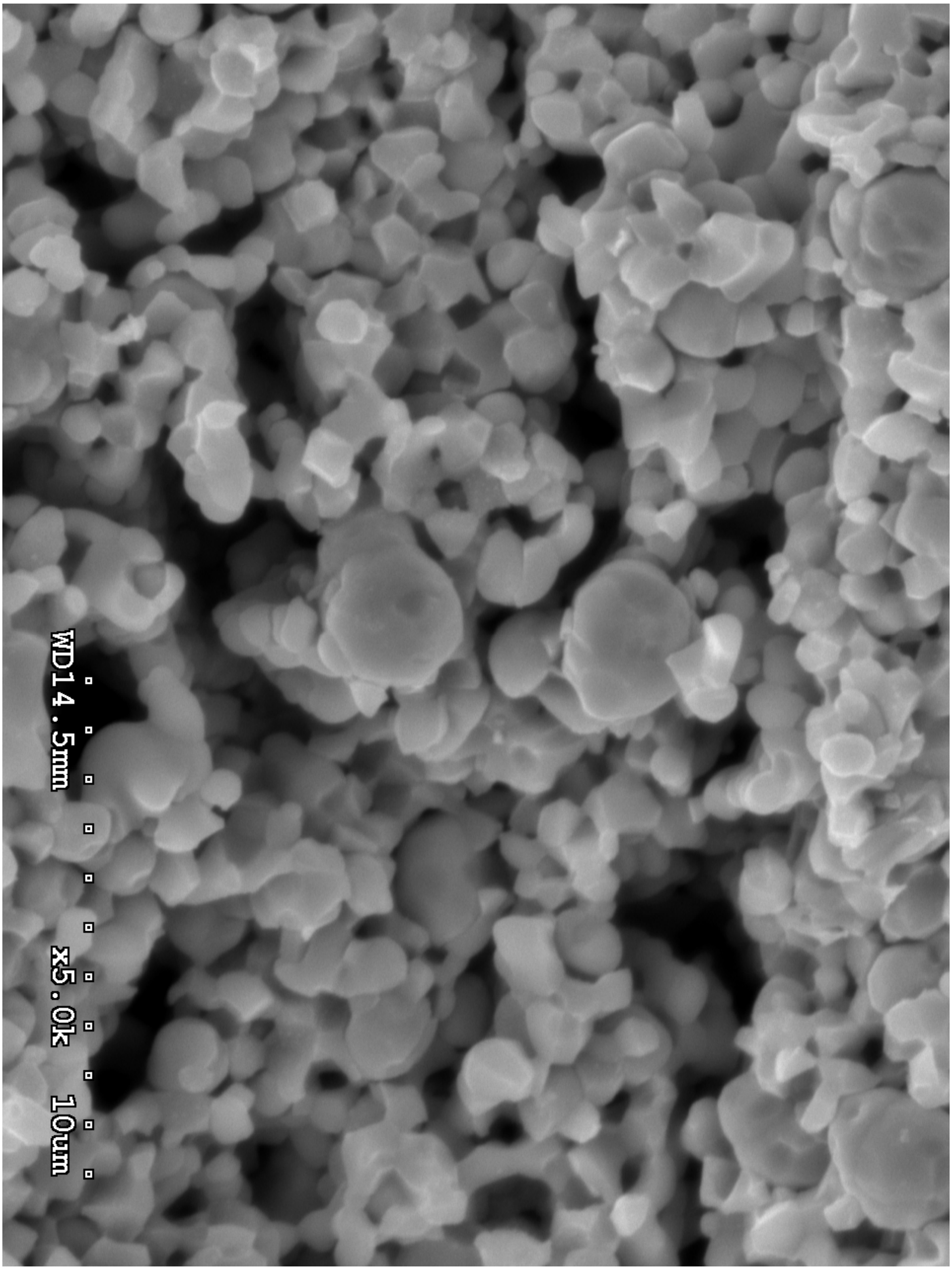

Figure 6.22. The SEM microstructure of ASR39 after the conductivity measurements.

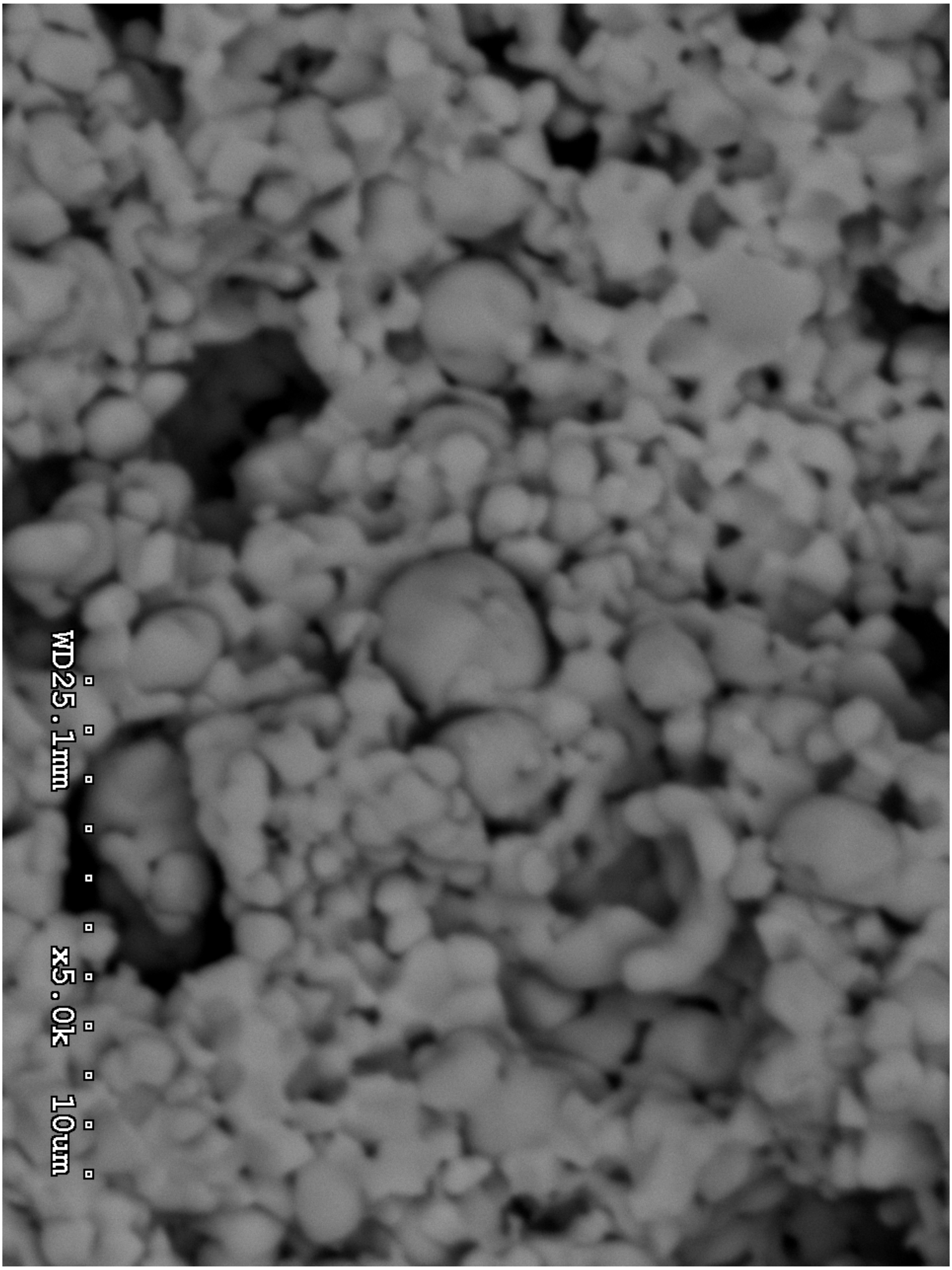

Figure 6.23. The BSE microstructure of ASR39 after the conductivity measurements.

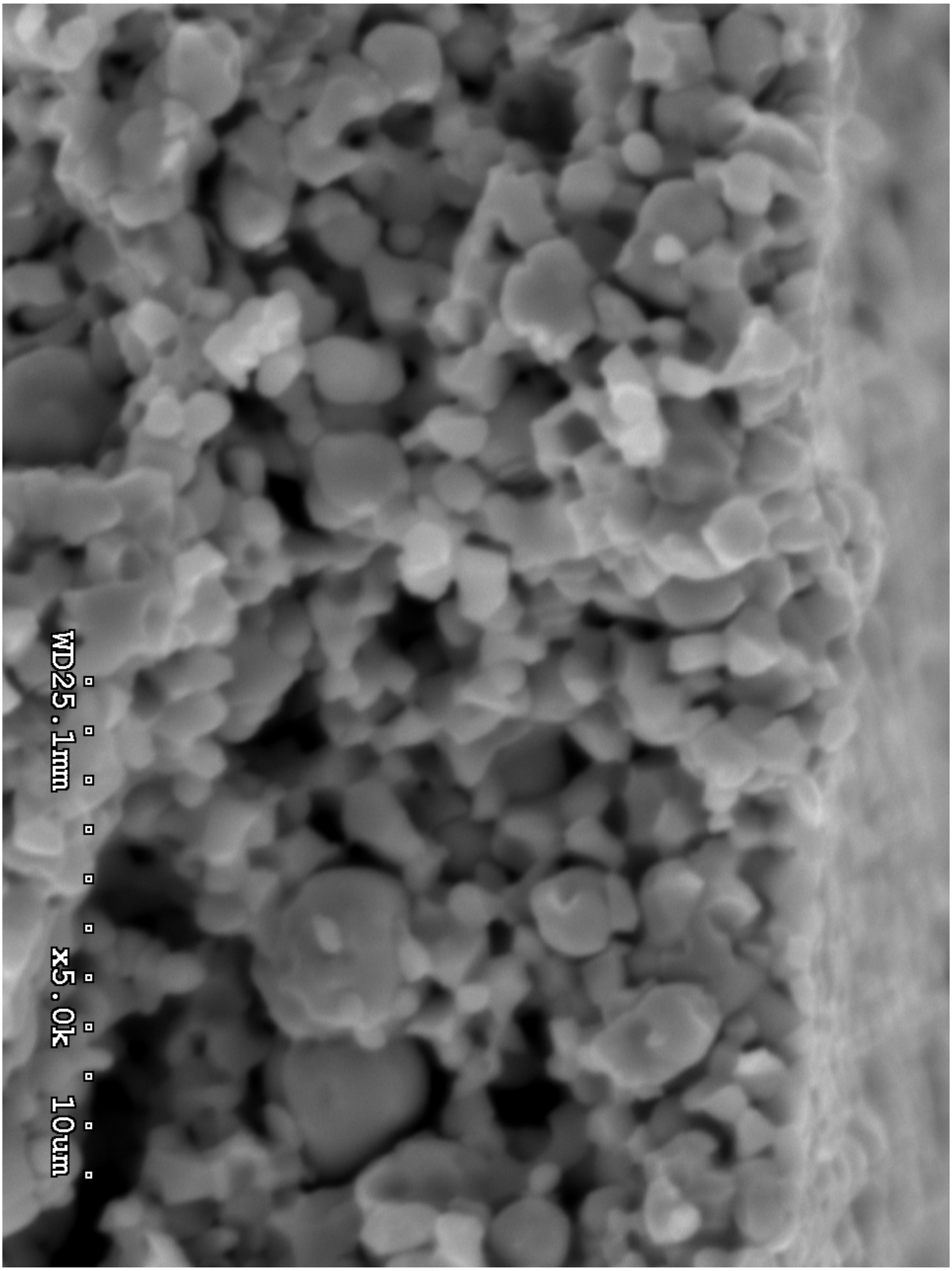

Figure 6.24. The SEM microstructure of ASR39 after the conductivity measurements.

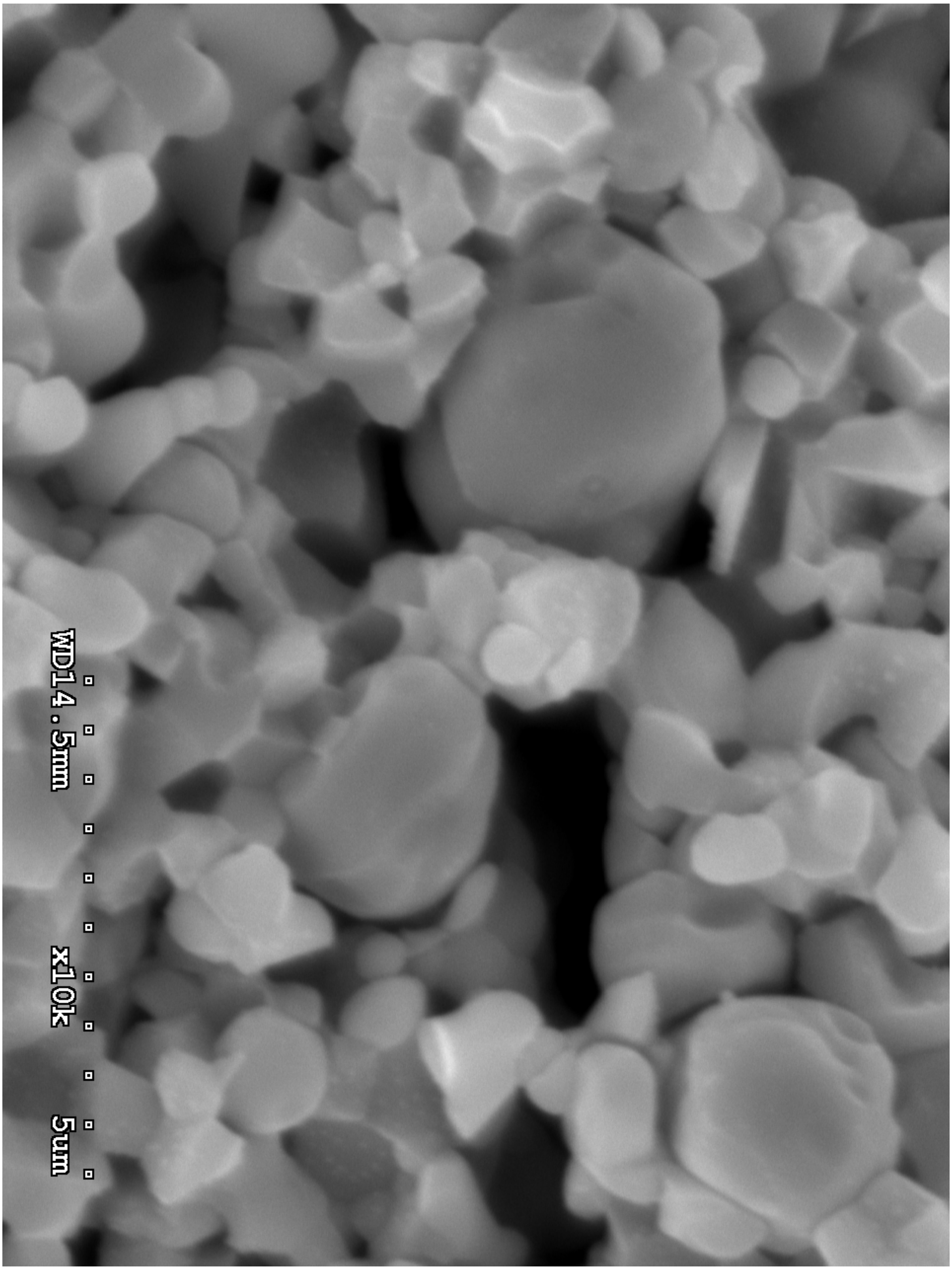

Figure 6.25. The SEM microstructure of ASR39 after the conductivity measurements.

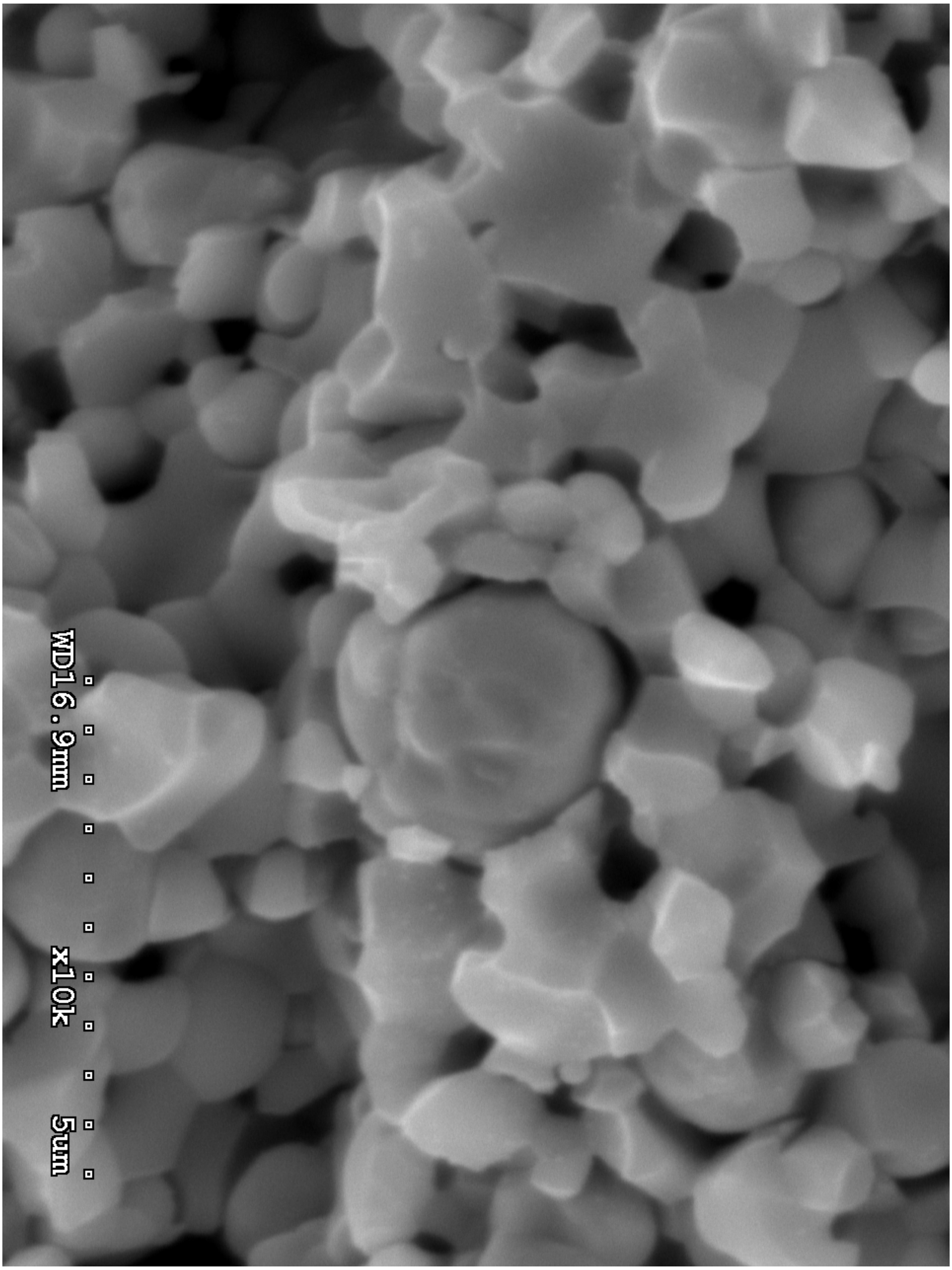

Figure 6.26. The SEM microstructure of ASR39 after the conductivity measurements.

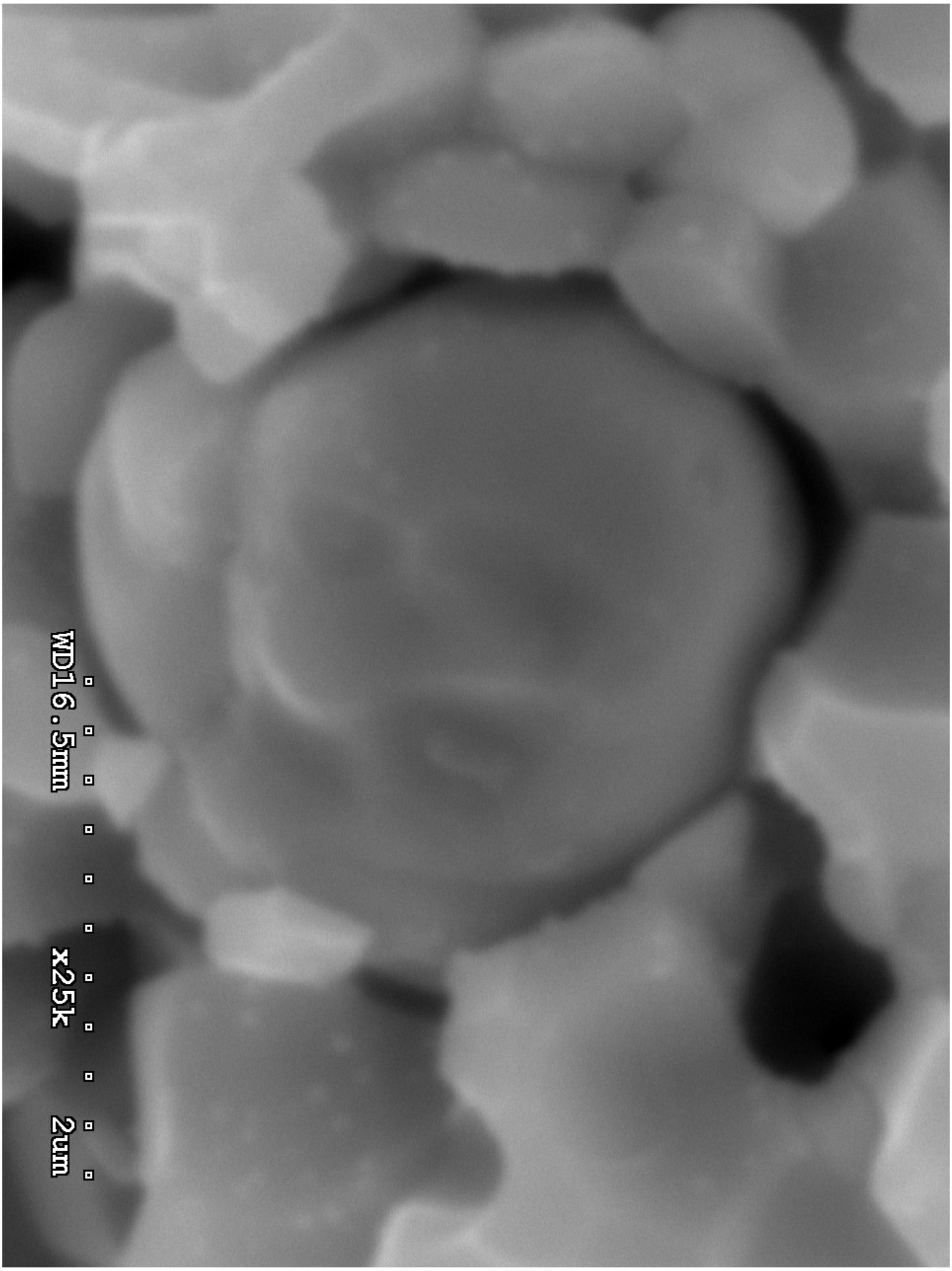

Figure 6.27. The SEM microstructure of ASR39 after the conductivity measurements.

6.3.5 The anode functional layer effective electronic conductivity

Figure 6.28 shows the conductivity measurement of an anode functional layer (AFL) tubular sample, which was reduced before the experiment. The reduced sample was very conductive at room temperature, however its conductivity dropped by about 1000 times as it was heated up to 800°C. The final conductivity rose to a final value of 7000 $S.m^{-1}$ after ~100 hours at 800°C still more than 10 times lower than its room temperature conductivity. Note that the settled conductivity of the AFL is still much higher than that of the ASL, indicating the significance of the microstructure and particle size ratio of Ni and YSZ on the percolation of the Ni network. The precursor powder used for fabricating the AFL had 0.3 μm NiO particles compared to the 0.65 μm used for the ASL. The ASL precursor power contained pore former to create extra porosity, while for AFL no pore former was added. Several studies have shown that composites Ni-YSZ have a higher conductivity when the particles sizes are closer to each other.

Significant oscillation can be seen in the AFL sample conductivity in the first 30 hours of the experiment, as seen in Figure 6.28. This behavior is unlike the second heating cycle for the ASL samples, but similar to the first heating cycle of ASL samples just after reduction. This indicates that the major changes in the network formed by the finer Ni particles did settle within the first cycle, i.e. reduction for 2 hours at 800°C. It is known that finer particles agglomerate more.

Figures 6.29 to 6.31 show the SEM images of the AFL microstructure after the conductivity tests. Note the smaller spherical Ni particles in the AFL compared to what was seen for the ASL, and their more homogenous distribution within the structure - they still appear as spheres loosely trapped in their enclosures.

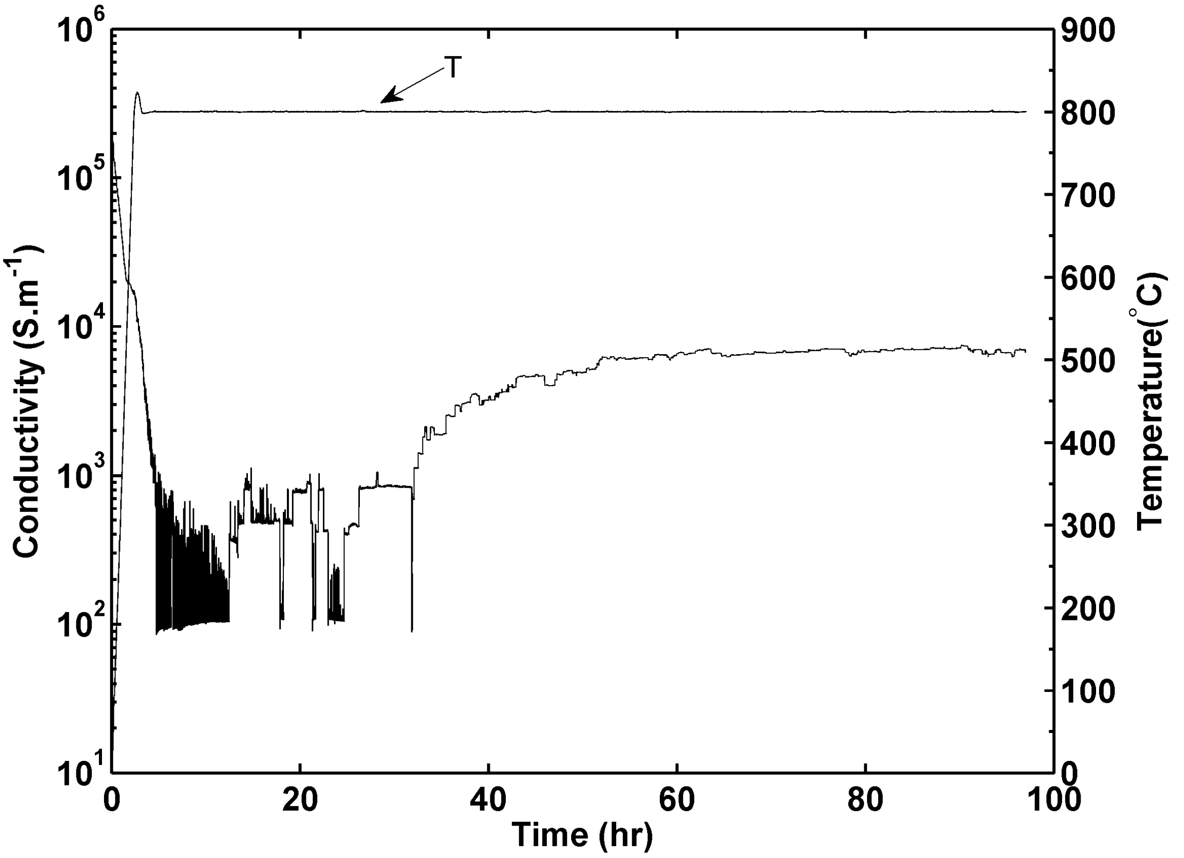

Figure 6.28. The conductivity of ASR40 during the heating and long-term testing. The sample was reduced for 2 hours prior testing.

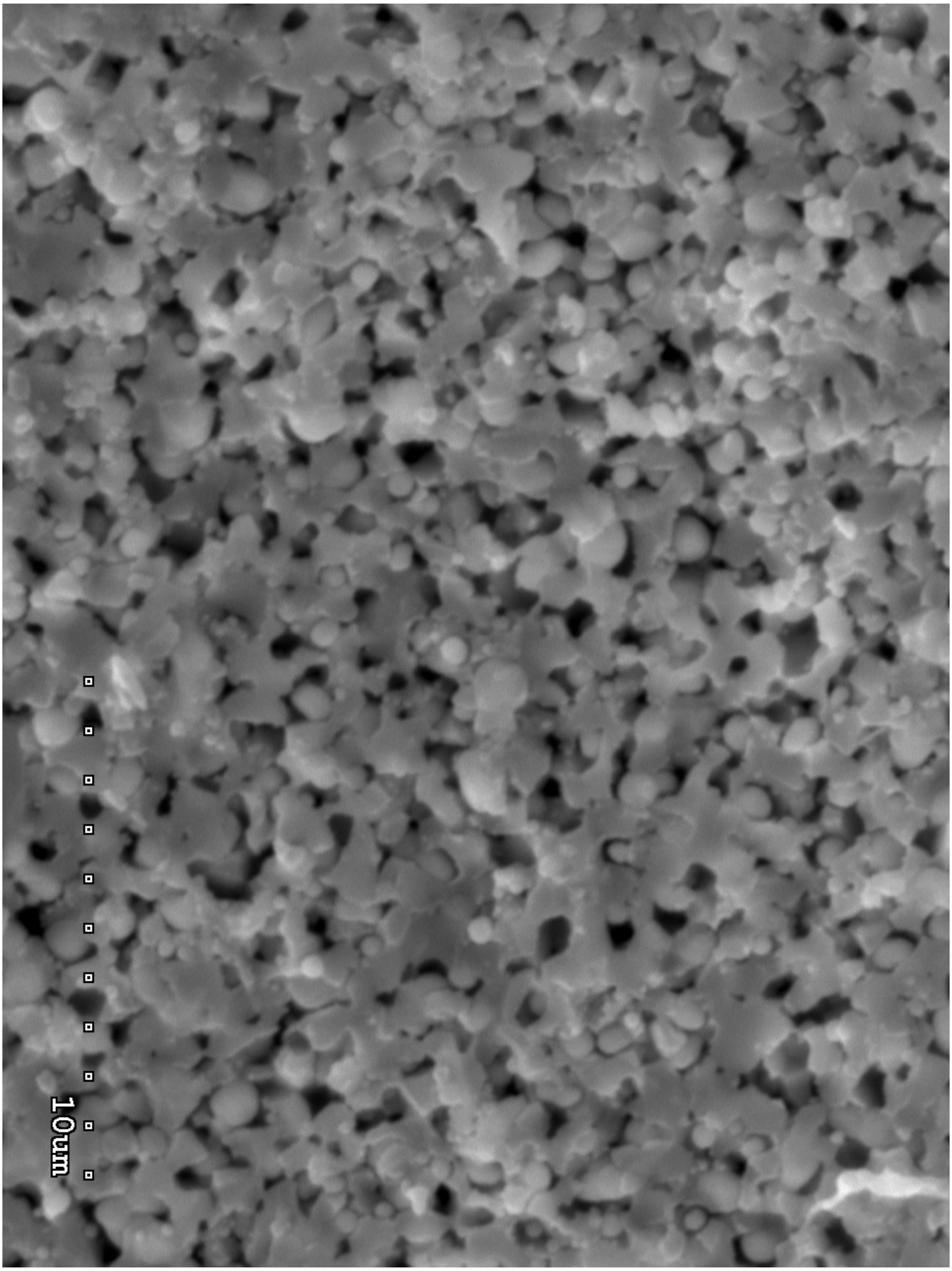

Figure 6.29. The SEM microstructure of AFR2 after the conductivity measurements.

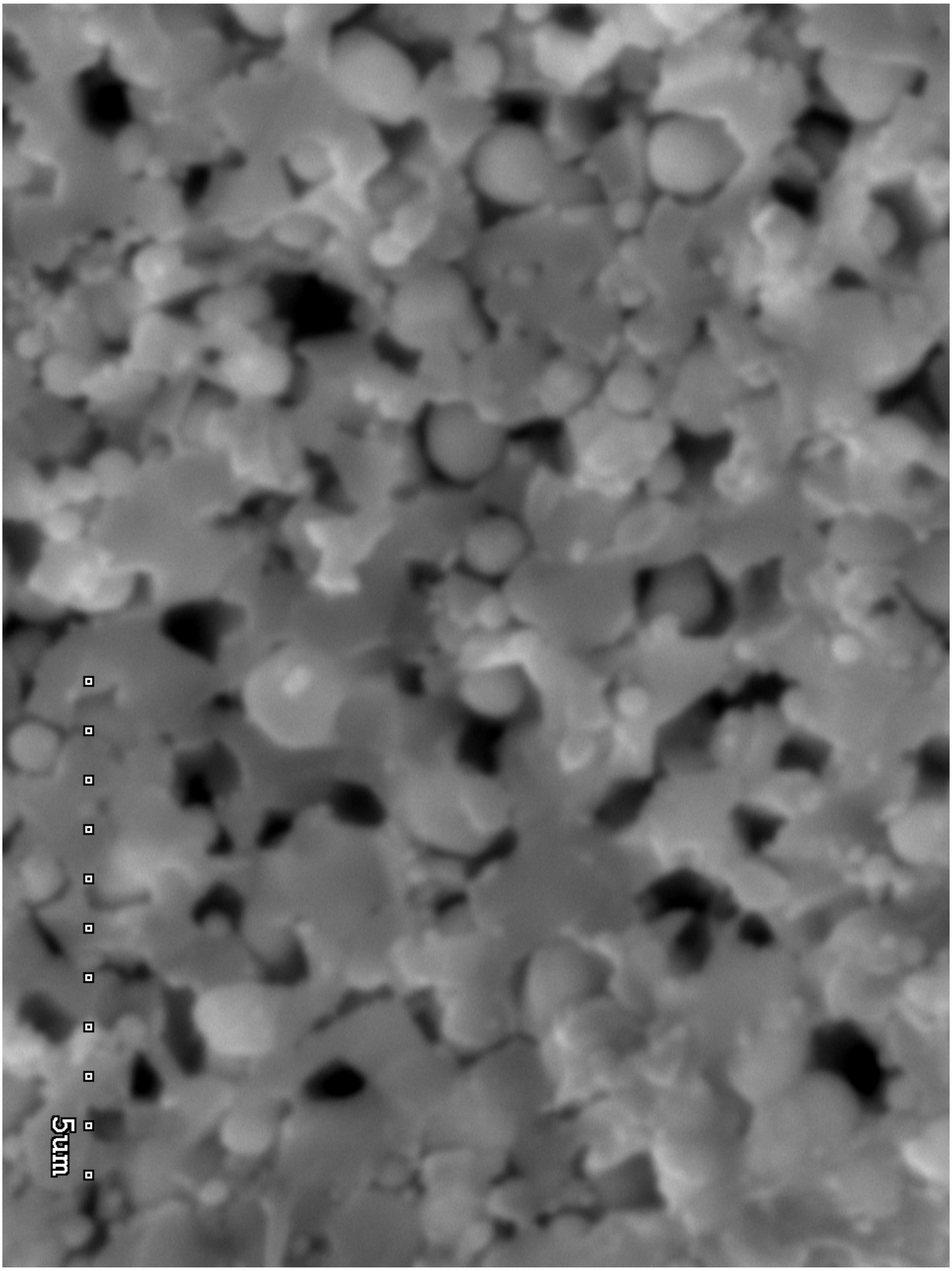

Figure 6.30. The SEM microstructure of AFR2 after the conductivity measurements.

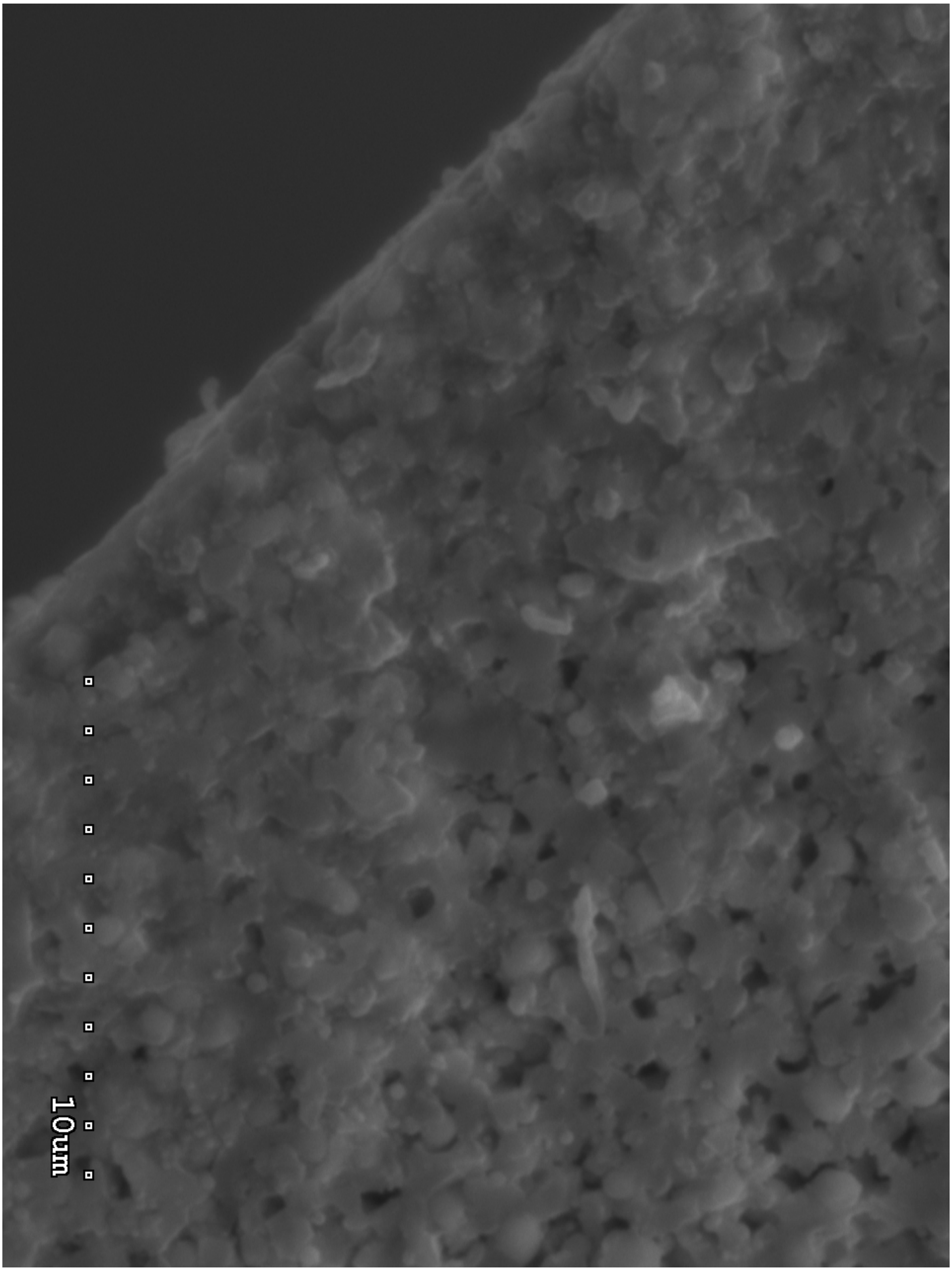

Figure 6.31. The outer surface of AFR2 after the conductivity measurements.

6.4 The use of computer simulation as a diagnostic tool

As it was mentioned briefly in the isothermal model section, when the typical physical properties reported in the literature were used in the isothermal model, the optimization procedure could not find the Butler-Volmer kinetic parameters that resulted in I-V curve predictions that satisfactorily match the experimental data. Figure 6.32 shows a typical case, where the ASL electronic conductivity was taken from the literature, much higher than the actual measurements made later on. An I-V curve is primarily dominated by activation effects at lower currents, i.e. reaction kinetics. However, ohmic resistance dominates the behavior of the curve at higher currents, and eventually concentration limitations. When the kinetic parameters were optimized for low current levels, i.e. 1 V & 0.7 V, the model predicted a much higher performance at higher current levels. This was due to the underestimation in the ASL conductivity in the model. The estimated kinetic parameters were close to the actual values, as the initial slope of the I-V curve which reflects the kinetics, matches for the simulation and experimental results. On the other hand, when the high current level experimental data point at 0.3 V was used for parameter fitting, the kinetic parameters were underestimated - note the sharp slope of the I-V curve at low current levels. This was because the underperformance caused by the high cell resistance, and not included in the model, was compensated by lower kinetic performance. The result was an underestimation of the cell performance for the cell potentials higher than 0.3 V.

To conclude, the model indicated signs of the unusually high cell resistance. Parameter optimization is often an inseparable part of mathematical modeling. However, not every experimental trend can be arbitrarily fitted if the model captures enough details of the system. Therefore a detailed model can be used to diagnose and identify unusual experimental results. In addition to I-V performance simulation, the mathematical model developed for current conduction in the contact resistance samples, led to suspecting the ASL high resistance rather than contact resistance, as discussed earlier in section 6.3.3.

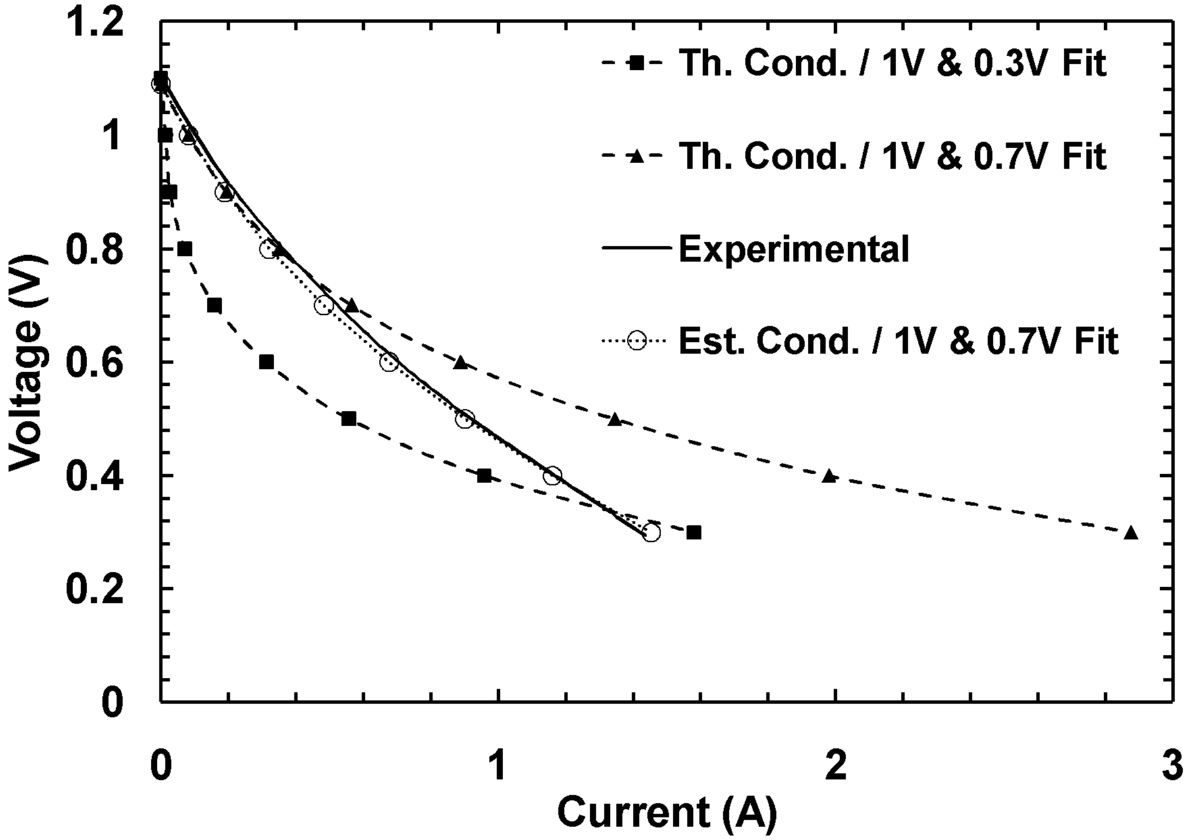

Figure 6.32. Model predictions resulting from the kinetic parameters based on various fitting points.

6.5 Conclusion

The electronic conductivity of the anode and the cathode as well as the electrochemical activity of the cathode and their temporal changes were investigated, to identify the cause of the lower than expected and occasionally degrading TμSOFC performance. It was found that the effective conductivity of the anode support composite was orders of magnitude lower than expected, and changed significantly with temperature. In addition, it took tens of hours for the ASL conductivity to settle once it was at 800°C, especially during the first cycle after the reduction of NiO to Ni. It can be concluded that the microstructure of the Ni network in the composite changed significantly with temperature. There are several indicators that the Ni particles in the Ni-YSZ composite form or lose their connection as a result of thermal expansion and contraction, which leads to changes in the overall conductivity with temperature. The average value of 1.56 ± 0.40 was found for the logarithm of the effective conductivity of the ASL, based on long term tests of several samples over several testing cycles. The low conductivity of the ASL causes the ohmic resistance to be a performance bottleneck for the cell. In addition, the performance of the cell becomes quite sensitive to variations in ASL conductivity. This can explain why cell performance changes over time and from cycle to cycle: if the ASL resistance is low enough to be a performance bottleneck, its variations result in significant variations in the I-V curve.

The effective conductivity of the AFL changed much less with temperature and time, with a final conductivity several orders of magnitude higher than ASL. This indicates the significance of particle size ratio of the precursor powders on the microstructure behavior of the composite. In this case, the bigger NiO particle size compared to YSZ used for fabricating ASL resulted in a microstructure that was more vulnerable to changes cause by agglomeration and thermal stresses compared to the smaller AFL which was fabricated with NiO particle size close to YSZ.

The change in the effective conductivity of ASL with temperature can be explained by the contact formed and broken among the Ni particles within the composite, as a result of the thermal expansion. At higher temperatures Ni particles are bigger, and form connections, while at lower temperatures they shrink some of the contacts may break. An indicator of this phenomenon is the step-like changes in the conductivity of ASL, which occur consistently around the same temperature when the sample is heated and then cooled. Another indicator is SEM images which show the Ni particles appear as individual spheres trapped within the YSZ enclosures with a bigger diameter.

Chapter 7. Concluding remarks

A detailed model was developed for the TμSOFC to gain a better insight into its performance. The isothermal and non-isothermal steady-state as well as the transient performance of the cell was simulated and was successfully validated against the experimental results.

The following highlights the conclusions of this work:

1- Detailed modeling can result in numerous parameters that reflect the physical reality of the system in the model. These parameters are often estimated based the available data. While this is a commonplace approach, special attention should be paid to the values used. Nothing can reliably replace the experimental measurement of a parameter. Identifying which parameters should be measured, and which can be assumed is the art of effective modeling. For the TμSOFC, the much lower conductivity of the anode support layer and its variation with time was the most troublesome issue, while it was one of the least suspected.

2- For our specific system, modeling radiation was essential for a proper heat transfer model, such that without it no physically meaningful simulation was possible. In fact, not modeling heat transfer at all was a better representation of the reality, compared to including it without radiation. This again indicates the critical task of making valid assumptions.

3- Modeling indicates that the heat generated by the cell can increase its temperature by as much as 40°C.

4- The surface emissivities were found to have a significant effect on the temperature distribution and the dissipation of the heat generated by the cell. In general, higher emissivity results in more uniform temperatures. Hence, thermal radiation has a great capacity for effective thermal management.

5- The overall thermal behavior of the cell was found to be a complex pattern. Modeling is an effective tool for gaining an insight about the thermal behavior of the system, as the experimental characterization may be difficult and sometimes misleading. In our case, the thermocouples used to measure the temperature, significantly altered the thermal behavior of the system due to the TμSOFC low "thermal footprint".

6- A thermodynamic framework was developed to estimate the single-electrode reversible heat generation within the volume of the composite electrodes. The cathode reaction was found to be exothermic, while the anode reaction was endothermic. The predicted temperature gradients across the cell layers were less than 0.05°C.

7- A thermodynamic framework was developed to estimate the local electromotive force within non-isothermal electrodes. The simulations showed that the thermoelectric effects caused by the temperature gradients had a negligible effect on the overall cell performance. This was due to the very small temperature gradients across the cell layers.

8- The transients of the TμSOFC were very fast with a time constant less than 5 seconds. The overall transient of the system was found to be controlled by the thermal transients, which was very fast because of the small thermal mass of the cell.

9- The furnace wall and its insulation induced a slow thermal transient on the cell, with a time constant of several hundreds of seconds.

10- The experimental measurements revealed that the effective conductivity of the anode support composite was several orders of magnitude lower than expected. In fact initially, for a short period of time after the reduction of NiO to Ni, the effective conductivity of the anode support was very high, indicating that the composite was well-percolated. However, at 800°C the conductivity dropped by several orders of magnitude which indicates significant change in the microstructure of Ni particles within the composite.

11- It was consistently observed that the reduced anode support samples had a very low conductivity at room temperature, essentially insulating in several cases, while it increased by several orders of magnitude when the sample was at higher temperatures. This anomalous behavior, along with few other observations, indicates the significant change in the microstructure of Ni within the composite, by changes in temperature. This can be explained by considering that the Ni particles thermal expansion can result in the particles to touch and to form a conducting path.

12- The ohmic resistance of the anode support was a major performance bottleneck for this cell, due to its very low conductivity. This also made the overall performance of the cell very sensitive to the changes in the thermal conductivity of the anode support, which normally would not be noticeable. This can explain the severe performance degradation observed for some cells.

13- The anode functional layer also showed significant changes in its electronic conductivity. However, its conductivity was much higher than the anode support layer, which indicates the significance of particle size ratio on the composite behavior.

14- Detailed modeling, if used effectively, can be a significant diagnostic tool. Modeling was used in this capacity at least in two cases for the current study: the model’s prediction of a much higher cell performance if the anode support had its expected conductivity, and the modeling of current flow in the contact resistance samples.

Recommendations and future work

The TμSOFC is practically an outstanding cell. It is mechanically very robust, and can effectively withstand severe thermal shocks. It is convenient to seal and to operate. It has an ideal electrolyte, very thin but impermeable, which minimizes its ohmic resistance. In terms of electrochemical performance however, the cell cannot effectively take advantage of its strengths. This study suggests that the ohmic loss of the anode support, and activation losses of the cathode are the two major performance bottlenecks. Enhancing the conductivity of the anode support to have its expected conductivity should be the first and foremost objective in further developing the TμSOFC. This is an objective within reach, as the anode support was indeed very conductive initially after reduction. Parameters such as porosity and particle size ratio should be investigated to optimize the anode support conductivity. Another aspect of improving the cell performance is the cathode, which involves developing more active catalyst material.

This work concludes that by mathematical modeling one can accurately predict the TμSOFC performance. Therefore the model can be extended to 3D for designing a stack, especially for studying and optimizing its thermal management and flow configuration.

Bibliography

Abbaspour, A., K. Nandakumar, J. L. Luo, and K. T. Chuang, 2006, A novel approach to study the structure versus performance relationship of SOFC electrodes: Journal of Power Sources, v. 161, p. 965-970.

Achenbach, E., 1994, 3-DIMENSIONAL AND TIME-DEPENDENT SIMULATION OF A PLANAR SOLID OXIDE FUEL-CELL STACK, p. 333-348.

Achenbach, E., 1995, Response of a solid oxide fuel cell to load change: Journal of Power Sources, v. 57, p. 105-109.

Ackmann, T., L. G. J. de Haart, W. Lehnert, and D. Stolten, 2003, Modeling of mass and heat transport in planar substrate type SOFCs: Journal of the Electrochemical Society, v. 150, p. A783-A789.

Aguiar, P., C. S. Adjiman, and N. P. Brandon, 2005, Anode-supported intermediate-temperature direct internal reforming solid oxide fuel cell - II. Model-based dynamic performance and control: Journal of Power Sources, v. 147, p. 136-147.

Aguiar, P., D. Chadwick, and L. Kershenbaum, 2002, Modelling of an indirect internal reforming solid oxide fuel cell: Chemical Engineering Science, v. 57, p. 1665-1677.

Ahlgren, E. O., and F. W. Poulsen, 1996, Thermoelectric power and electrical conductivity of strontium-doped lanthanum manganite: Solid State Ionics, v. 86-8, p. 1173-1178.

Bessler, W. G., 2006, Gas concentration impedance of solid oxide fuel cell anodes I. Stagnation point flow geometry: Journal of the Electrochemical Society, v. 153, p. A1492-A1504.

Bessler, W. G., and S. Gewies, 2007, Gas concentration impedance of solid oxide fuel cell anodes: Journal of the Electrochemical Society, v. 154, p. B548-B559.

Bhattacharyya, D., and R. Rengaswamy, 2009, A Review of Solid Oxide Fuel Cell (SOFC) Dynamic Models: Industrial & Engineering Chemistry Research, v. 48, p. 6068-6086.

Bhattacharyya, D., R. Rengaswamy, and C. Finnerty, 2009, Dynamic modeling and validation studies of a tubular solid oxide fuel cell: Chemical Engineering Science, v. 64, p. 2158-2172.

Bird, R. B., W. E. Stewart, and E. N. Lightfoot, 2002, Transport phenomena: New York, J. Wiley.

Bove, R., and S. Ubertini, 2006, Modeling solid oxide fuel cell operation: Approaches, techniques and results: Journal of Power Sources, v. 159, p. 543-559.

Burt, A. C., I. B. Celik, R. S. Gemmen, and A. V. Smirnov, 2004, A numerical study of cell-to-cell variations in a SOFC stack: Journal of Power Sources, v. 126, p. 76-87.

Calise, F., M. D. d'Accadia, and G. Restuccia, 2007, Simulation of a tubular solid oxide fuel cell through finite volume analysis: Effects of the radiative heat transfer and exergy analysis: International Journal of Hydrogen Energy, v. 32, p. 4575-4590.

Calise, F., G. Ferruzzi, and L. Vanoli, 2009, Parametric exergy analysis of a tubular Solid Oxide Fuel Cell (SOFC) stack through finite-volume model: Applied Energy, v. 86, p. 2401-2410.

Chan, S. H., X. J. Chen, and K. A. Khor, 2004, Cathode micromodel of solid oxide fuel cell: Journal of the Electrochemical Society, v. 151, p. A164-A172.

Chan, S. H., K. A. Khor, and Z. T. Xia, 2001, A complete polarization model of a solid oxide fuel cell and its sensitivity to the change of cell component thickness: Journal of Power Sources, v. 93, p. 130-140.

Chan, S. H., and Z. T. Xia, 2001, Anode micro model of solid oxide fuel cell: Journal of the Electrochemical Society, v. 148, p. A388-A394.

Chemical Rubber Company., Handbook of chemistry and physics, Cleveland,, Chemical Rubber Pub. Co.

Chyou, Y. P., T. D. Chung, J. S. Chen, and R. F. Shie, 2005, Integrated thermal engineering analyses with heat transfer at periphery of planar solid oxide fuel cell: Journal of Power Sources, v. 139, p. 126-140.

Cohen, M. F., and D. P. Greenberg, 1985, HEMI-CUBE - A RADIOSITY SOLUTION FOR COMPLEX ENVIRONMENTS, v. 19, p. 31-40.

Colpan, C. O., I. Dincer, and F. Hamdullahpur, 2008, A review on macro-level modeling of planar solid oxide fuel cells: International Journal of Energy Research, v. 32, p. 336-355.

Costamagna, P., and K. Honegger, 1998, Modeling at solid oxide heat exchanger integrated stacks and simulation at high fuel utilization: Journal of the Electrochemical Society, v. 145, p. 3995-4007.

Costamagna, P., M. Panizza, G. Cerisola, and A. Barbucci, 2002, Effect of composition on the performance of cermet electrodes. Experimental and theoretical approach: Electrochimica Acta, v. 47, p. 1079-1089.

Costamagna, P., A. Selimovic, M. Del Borghi, and G. Agnew, 2004, Electrochemical model of the integrated planar solid oxide fuel cell (IP-SOFC): Chemical Engineering Journal, v. 102, p. 61-69.

Curtiss, C. F., and R. B. Bird, 1999, Multicomponent diffusion: Industrial & Engineering Chemistry Research, v. 38, p. 2515-2522.

Damm, D. L., and A. G. Fedorov, 2005, Radiation heat transfer in SOFC materials and components: Journal of Power Sources, v. 143, p. 158-165.

Damm, D. L., and A. G. Fedorov, 2006, Local thermal non-equilibrium effects in porous electrodes of the hydrogen-fueled SOFC: Journal of Power Sources, v. 159, p. 1153-1157.

Daubert, T. E., R. P. Danner, and Design Institute for Physical Property Data (U.S.), 1989, Physical and thermodynamic properties of pure chemicals : data compilation: New York, Hemisphere Pub. Corp.

Daun, K. J., S. B. Beale, F. Liu, and G. J. Smallwood, 2006, Radiation heat transfer in planar SOFC electrolytes: Journal of Power Sources, v. 157, p. 302-310.

Duplessis, J. P., and J. H. Masliyah, 1988, MATHEMATICAL-MODELING OF FLOW THROUGH CONSOLIDATED ISOTROPIC POROUS-MEDIA: Transport in Porous Media, v. 3, p. 145-161.

Faghri, A., and Z. Guo, 2005, Challenges and opportunities of thermal management issues related to fuel cell technology and modeling: International Journal of Heat and Mass Transfer, v. 48, p. 3891-3920.

Ferguson, J. R., J. M. Fiard, and R. Herbin, 1996, Three-dimensional numerical simulation for various geometries of solid oxide fuel cells: Journal of Power Sources, v. 58, p. 109-122.

Ferrari, M. L., A. Traverso, L. Magistri, and A. F. Massardo, 2005, Influence of the anodic recirculation transient behaviour on the SOFC hybrid system performance: Journal of Power Sources, v. 149, p. 22-32.

Fischer, K., and J. R. Seume, 2009, Location and Magnitude of Heat Sources in Solid Oxide Fuel Cells: Journal of Fuel Cell Science and Technology, v. 6, p. 11.

Gaynor, R., F. Mueller, F. Jabbari, and J. Brouwer, 2008, On control concepts to prevent fuel starvation in solid oxide fuel cells: Journal of Power Sources, v. 180, p. 330-342.

Gemmen, R. S., and C. D. Johnson, 2005, Effect of load transients on SOFC operation-current reversal on loss of load: Journal of Power Sources, v. 144, p. 152-164.

Gu, W. B., and C. Y. Wang, 2000, Thermal-electrochemical modeling of battery systems: Journal of the Electrochemical Society, v. 147, p. 2910-2922.

Haberman, B. A., and J. B. Young, 2004, Three-dimensional simulation of chemically reacting gas flows in the porous support structure of an integrated-planar solid oxide fuel cell: International Journal of Heat and Mass Transfer, v. 47, p. 3617-3629.

Haberman, B. A., and J. B. Young, 2008, A detailed three-dimensional simulation of an IP-SOFC stack: Journal of Fuel Cell Science and Technology, v. 5.

Haynes, C., 2002, Simulating process settings for unslaved SOFC response to increases in load demand: Journal of Power Sources, v. 109, p. 365-376.

Hellwege, K.-H., and J. L. Olsen, 1982: Landolt-Börnstein - Group III Condensed Matter, v. 15a.

Ho, C. K., and S. W. Webb, 2006, Gas transport in porous media: Dordrecht ; [London], Springer.

Holman, J. P., 2002, Heat transfer: New York, McGraw-Hill.

Jacobsen, T., P. V. Hendriksen, and S. Koch, 2008, Diffusion and conversion impedance in solid oxide fuel cells: Electrochimica Acta, v. 53, p. 7500-7508.

Jia, J. X., A. Abudula, L. M. Wei, R. Q. Jiang, and S. Q. Shen, 2007, A mathematical model of a tubular solid oxide fuel cell with specified combustion zone: Journal of Power Sources, v. 171, p. 696-705.

Jia, J. X., R. Q. Jiang, S. Q. Shen, and A. Abudula, 2008, Effect of operation parameters on performance of tubular solid oxide fuel cell: Aiche Journal, v. 54, p. 554-564.

Kakac, S., A. Pramuanjaroenkij, and X. Y. Zhou, 2007, A review of numerical modeling of solid oxide fuel cells: International Journal of Hydrogen Energy, v. 32, p. 761-786.

Kanamura, K., S. Yoshioka, and Z. I. Takehara, 1991, DEPENDENCE OF ENTROPY CHANGE OF SINGLE ELECTRODES ON PARTIAL-PRESSURE IN SOLID OXIDE FUEL-CELLS: Journal of the Electrochemical Society, v. 138, p. 2165-2167.

Kaneko, T., J. Brouwer, and G. S. Samuelsen, 2006, Power and temperature control of fluctuating biomass gas fueled solid oxide fuel cell and micro gas turbine hybrid system: Journal of Power Sources, v. 160, p. 316-325.

Keil, F. J., 1999, Diffusion and reaction in porous networks: Catalysis Today, v. 53, p. 245-258.

Kerkhof, P., 1996, A modified Maxwell-Stefan model for transport through inert membranes: The binary friction model: Chemical Engineering Journal, v. 64, p. 319-343.

Kerkhof, P., and M. A. M. Geboers, 2005, Analysis and extension of the theory of multicomponent fluid diffusion: Chemical Engineering Science, v. 60, p. 3129-3167.

Kim, J. D., G. D. Kim, J. W. Moon, Y. I. Park, W. H. Lee, K. Kobayashi, M. Nagai, and C. E. Kim, 2001, Characterization of LSM-YSZ composite electrode by ac impedance spectroscopy: Solid State Ionics, v. 143, p. 379-389.

Krishna, R., and J. A. Wesselingh, 1997, Review article number 50 - The Maxwell-Stefan approach to mass transfer: Chemical Engineering Science, v. 52, p. 861-911.

Krist, K., and J. Jewulski, 2006, A radiation-based approach to planar solid oxide fuel cell modules: Journal of Materials Engineering and Performance, v. 15, p. 468-473.

Leng, Y. J., S. H. Chan, K. A. Khor, S. P. Jiang, and P. Cheang, 2003, Effect of characteristics of Y2O3/ZrO2 powders on fabrication of anode-supported solid oxide fuel cells: Journal of Power Sources, v. 117, p. 26-34.

Li, P. W., and M. K. Chyu, 2003, Simulation of the chemical/electrochemical reactions and heat/mass transfer for a tubular SOFC in a stack: Journal of Power Sources, v. 124, p. 487-498.

Li, P. W., L. Schaefer, and M. K. Chyu, 2004, A numerical model coupling the heat and gas species' transport processes in a tubular SOFC: Journal of Heat Transfer-Transactions of the Asme, v. 126, p. 219-229.

Li, P. W., and K. Suzuki, 2004, Numerical modeling and performance study of a tubular SOFC: Journal of the Electrochemical Society, v. 151, p. A548-A557.

Li, Y. H., S. Rajakaruna, and S. S. Choi, 2007, Control of a solid oxide fuel cell power plant in a grid-connected system: Ieee Transactions on Energy Conversion, v. 22, p. 405-413.

Lin, P. H., and C. W. Hong, 2009, Cold start dynamics and temperature sliding observer design of an automotive SOFC APU: Journal of Power Sources, v. 187, p. 517-526.

Lu, N., Q. Li, X. Sun, and M. A. Khaleel, 2006, The modeling of a standalone solid-oxide fuel cell auxiliary power unit: Journal of Power Sources, v. 161, p. 938-948.

Lu, Y. X., L. Schaefer, and P. W. Li, 2005a, Numerical simulation of heat transfer and fluid flow of a flat-tube high power density solid oxide fuel cell: Journal of Fuel Cell Science and Technology, v. 2, p. 65-69.

Lu, Y. X., L. Schaefer, and P. W. Li, 2005b, Numerical study of a flat-tube high power density solid oxide fuel cell - Part I. Heat/mass transfer and fluid flow: Journal of Power Sources, v. 140, p. 331-339.

Magistri, L., F. Trasino, and P. Costamagna, 2006, Transient analysis of solid oxide fuel cell hybrids - Part I: Fuel cell models: Journal of Engineering for Gas Turbines and Power-Transactions of the Asme, v. 128, p. 288-293.

Mason, E. A., and A. P. Malinauskas, 1983, Gas transport in porous media : the dusty-gas model: Amsterdam ; New York, Elsevier.

Mazumder, S. K., S. K. Pradhan, J. Hartvigsen, M. R. von Spakovsky, and D. F. Rancruel, 2007, Effects of battery buffering on the post-load-transient performance of a PSOFC: Ieee Transactions on Energy Conversion, v. 22, p. 457-466.

Mounir, H., A. El Gharad, M. Belaiche, and M. Boukalouch, 2009, Thermo-fluid and electrochemical modeling of a multi-bundle IP-SOFC - Technology for second generation hybrid application: Energy Conversion and Management, v. 50, p. 2685-2692.

Mueller, F., F. Jabbari, and J. Brouwer, 2009, On the intrinsic transient capability and limitations of solid oxide fuel cell systems: Journal of Power Sources, v. 187, p. 452-460.

Murshed, A., B. Huang, and K. Nandakumar, 2007, Control relevant modeling of planer solid oxide fuel cell system: Journal of Power Sources, v. 163, p. 830-845.

Murthy, S., and A. G. Fedorov, 2003, Radiation heat transfer analysis of the monolith type solid oxide fuel cell: Journal of Power Sources, v. 124, p. 453-458.

Nehter, P., 2006, Two-dimensional transient model of a cascaded micro-tubular solid oxide fuel cell fed with methane: Journal of Power Sources, v. 157, p. 325-334.

Ni, M., 2009, Three-Dimensional Computational Fluid Dynamics Modeling of a Planar Solid Oxide Fuel Cell: Chemical Engineering & Technology, v. 32, p. 1484-1493.

Nishino, T., H. Iwai, and K. Suzuki, 2006, Comprehensive numerical modeling and analysis of a cell-based indirect internal reforming tubular SOFC: Journal of Fuel Cell Science and Technology, v. 3, p. 33-44.

Noordman, T. R., and J. A. Wesselingh, 2002, Transport of large molecules through membranes with narrow pores - The Maxwell-Stefan description combined with hydrodynamic theory: Journal of Membrane Science, v. 210, p. 227-243.

Petruzzi, L., S. Cocchi, and F. Fineschi, 2003, A global thermo-electrochemical model for SOFC systems design and engineering, p. 96-107.

Poling, B. E., J. M. Prausnitz, and J. P. O'Connell, 2001, The properties of gases and liquids: New York, McGraw-Hill.

Pollock, D. D., 1985, Thermoelectricity : theory, thermometry, tool: Philadelphia, PA, ASTM.

Pradhan, S. K., S. K. Mazumder, J. Hartvigsen, and M. Hollist, 2007, Effects of electrical feedbacks on planar solid oxide fuel cell: Journal of Fuel Cell Science and Technology, v. 4, p. 154-166.

Purdue University. Thermophysical Properties Research Center., and Y. S. Touloukian, 1970, Thermophysical properties of matter; [the TPRC data series; a comprehensive compilation of data: New York,, IFI/Plenum, 13 v. in 14 p.

Rankin, A. J., R. E. Hayes, and S. T. Kolaczkowski, 1995, ANNULAR-FLOW IN A CATALYTIC MONOLITH REACTOR - THE SIGNIFICANCE OF CENTERLINE PROBE TEMPERATURES: Chemical Engineering Research & Design, v. 73, p. 110-121.

Ratkje, S. K., and K. S. Forland, 1991, THE TRANSPORTED ENTROPY OF OXYGEN ION IN YTTRIA-STABILIZED ZIRCONIA: Journal of the Electrochemical Society, v. 138, p. 2374-2376.

Ratkje, S. K., and S. Mollerholst, 1993, EXERGY EFFICIENCY AND LOCAL HEAT-PRODUCTION IN SOLID OXIDE FUEL-CELLS: Electrochimica Acta, v. 38, p. 447-453.

Ratkje, S. K., and Y. Tomii, 1993, TRANSPORTED ENTROPY IN ZIRCONIA WITH 3 TO 12 MOLE PERCENT YTTRIA: Journal of the Electrochemical Society, v. 140, p. 59-66.

Saarinen, J., M. Halinen, J. Ylijoki, M. Noponen, P. Simell, and J. Kiviaho, 2007, Dynamic model of 5 kW SOFCCHP test station: Journal of Fuel Cell Science and Technology, v. 4, p. 397-405.

Sanchez, D., R. Chacartegui, A. Munoz, and T. Sanchez, 2006, Thermal and electrochemical model of internal reforming solid oxide fuel cells with tubular geometry: Journal of Power Sources, v. 160, p. 1074-1087.

Sanchez, D., A. Munoz, and T. Sanchez, 2007, An assessment on convective and radiative heat transfer modelling in tubular solid oxide fuel cells: Journal of Power Sources, v. 169, p. 25-34.

Sarkar, P., L. Yamarte, H. S. Rho, and L. Johanson, 2007, Anode-supported tubular micro-solid oxide fuel cell: International Journal of Applied Ceramic Technology, v. 4, p. 103-108.

Sasaki, K., Y. Hori, R. Kikuchi, K. Eguchi, A. Ueno, H. Takeuchi, M. Aizawa, K. Tsujimoto, H. Tajiri, H. Nishikawa, and Y. Uchida, 2002, Current-voltage characteristics and impedance analysis of solid oxide fuel cells for mixed H-2 and CO gases: Journal of the Electrochemical Society, v. 149, p. A227-A233.

Sedghisigarchi, K., and A. Feliachi, 2004, Dynamic and transient analysis of power distribution systems with fuel cells - Part I: Fuel-cell dynamic model: Ieee Transactions on Energy Conversion, v. 19, p. 423-428.

Serincan, M. F., U. Pasaogullari, and N. M. Sammes, 2008, Computational thermal-fluid analysis of a microtubular solid oxide fuel cell: Journal of the Electrochemical Society, v. 155, p. B1117-B1127.

Shackelford, J. F., and W. Alexander, 2001, CRC materials science and engineering handbook: Boca Raton, FL, CRC Press.

Shi, Y. X., N. S. Cai, and C. Li, 2007, Numerical modeling of an anode-supported SOFC button cell considering anodic surface diffusion: Journal of Power Sources, v. 164, p. 639-648.

Soderberg, J., 2008, Improving the performance of microtubular solid oxide fuel cells, MSc Thesis, University of Calgary, Calgary.

Song, T. W., J. L. Sohn, J. H. Kim, T. S. Kim, S. T. Ro, and K. Suzuki, 2005, Performance analysis of a tubular solid oxide fuel cell/micro gas turbine hybrid power system based on a quasi-two dimensional model: Journal of Power Sources, v. 142, p. 30-42.

Suwanwarangkul, R., E. Croiset, M. W. Fowler, P. L. Douglas, E. Entchev, and M. A. Douglas, 2003, Performance comparison of Fick's, dusty-gas and Stefan-Maxwell models to predict the concentration overpotential of a SOFC anode: Journal of Power Sources, v. 122, p. 9-18.

Suwanwarangkul, R., E. Croiset, M. D. Pritzker, M. W. Fowler, P. L. Douglas, and E. Entchev, 2006, Mechanistic modelling of a cathode-supported tubular solid oxide fuel cell: Journal of Power Sources, v. 154, p. 74-85.

Suwanwarangkul, R., E. Croiset, M. D. Pritzker, M. W. Fowler, P. L. Douglas, and E. Entchev, 2007, Modelling of a cathode-supported tubular solid oxide fuel cell operating with biomass-derived synthesis gas: Journal of Power Sources, v. 166, p. 386-399.

Suzuki, M., N. Shikazona, K. Fukagata, and N. Kasagi, 2008, Numerical analysis of coupled transport and reaction phenomena in an anode-supported flat-tube solid oxide fuel cell: Journal of Power Sources, v. 180, p. 29-40.

Takehara, Z., K. Kanamura, and S. Yoshioka, 1989, THERMAL-ENERGY GENERATED BY ENTROPY CHANGE IN SOLID OXIDE FUEL-CELL: Journal of the Electrochemical Society, v. 136, p. 2506-2511.

Tanaka, T., Y. Inui, A. Urata, and T. Kanno, 2007, Three dimensional analysis of planar solid oxide fuel cell stack considering radiation: Energy Conversion and Management, v. 48, p. 1491-1498.

Taylor, R., and R. Krishna, 1993, Multicomponent mass transfer: New York, Wiley.

Todd, B., and J. B. Young, 2002, Thermodynamic and transport properties of gases for use in solid oxide fuel cell modelling: Journal of Power Sources, v. 110, p. 186-200.

Vafai, K., 2005, Handbook of porous media: Boca Raton, Taylor & Francis, xviii, 752 p. p.

VanderSteen, J. D. J., and J. G. Pharoah, 2006, Modeling radiation heat transfer with participating media in solid oxide fuel cells: Journal of Fuel Cell Science and Technology, v. 3, p. 62-67.

Vijay, P., A. K. Samantaray, and A. Mukherjee, 2009, On the rationale behind constant fuel utilization control of solid oxide fuel cells: Proceedings of the Institution of Mechanical Engineers Part I-Journal of Systems and Control Engineering, v. 223, p. 229-251.

Voigt, A., N. Hanssen, and C. Weichmann, 2004, The radiosity equation for solving global heat transfer in industrial furnaces: Mathematical and Computer Modelling, v. 39, p. 145-150.

Wang, C., and M. H. Nehrir, 2007, Load transient mitigation for stand-alone fuel cell power generation systems: Ieee Transactions on Energy Conversion, v. 22, p. 864-872.

Wang, Q., L. Li, and C. Wang, 2009, Numerical study of thermoelectric characteristics of a planar solid oxide fuel cell with direct internal reforming of methane: Journal of Power Sources, v. 186, p. 399-407.

Weber, A. Z., and J. Newman, 2005, Modeling gas-phase flow in porous media: International Communications in Heat and Mass Transfer, v. 32, p. 855-860.

Weichmann, C., R. Backofen, and A. Voigt, 2004, Time dependent 3D heat radiation calculation in high temperature furnaces, p. 313-322.

Wesselingh, J. A., and R. Krishna, 2000, Mass transfer in multicomponent mixtures: Delft, Netherland, Delft University Press.

Whitaker, S., 1999, The method of volume averaging: Dordrecht ; Boston, Kluwer Academic, xvi, 219.

Wilson, J. R., A. T. Duong, M. Gameiro, H. Y. Chen, K. Thornton, D. R. Mumm, and S. A. Barnett, 2009, Quantitative three-dimensional microstructure of a solid oxide fuel cell cathode: Electrochemistry Communications, v. 11, p. 1052-1056.

Wilson, J. R., W. Kobsiriphat, R. Mendoza, H. Y. Chen, J. M. Hiller, D. J. Miller, K. Thornton, P. W. Voorhees, S. B. Adler, and S. A. Barnett, 2006, Three-dimensional reconstruction of a solid-oxide fuel-cell anode: Nature Materials, v. 5, p. 541-544.

Wood, J., L. F. Gladden, and F. J. Keil, 2002, Modelling diffusion and reaction accompanied by capillary condensation using three-dimensional pore networks. Part 2. Dusty gas model and general reaction kinetics: Chemical Engineering Science, v. 57, p. 3047-3059.

Xi, H. D., and J. Sun, 2008, A Low-Order Dynamic Model for Planar Solid Oxide Fuel Cells Using Online Iterative Computation: Journal of Fuel Cell Science and Technology, v. 5.

Xue, X., J. Tang, N. Sammes, and Y. Du, 2005, Dynamic modeling of single tubular SOFC combining heat/mass transfer and electrochemical reaction effects: Journal of Power Sources, v. 142, p. 211-222.

Yakabe, H., M. Hishinuma, M. Uratani, Y. Matsuzaki, and I. Yasuda, 2000, Evaluation and modeling of performance of anode-supported solid oxide fuel cell, p. 423-431.

Yuan, J. L., Y. Huang, B. Sunden, and W. G. Wang, 2009, Analysis of parameter effects on chemical reaction coupled transport phenomena in SOFC anodes: Heat and Mass Transfer, v. 45, p. 471-484.

Zhu, H. Y., and R. J. Kee, 2006, Modeling electrochemical impedance spectra in SOFC button cells with internal methane reforming: Journal of the Electrochemical Society, v. 153, p. A1765-A1772.

Zhu, H. Y., R. J. Kee, V. M. Janardhanan, O. Deutschmann, and D. G. Goodwin, 2005, Modeling elementary heterogeneous chemistry and electrochemistry in solid-oxide fuel cells: Journal of the Electrochemical Society, v. 152, p. A2427-A2440.

Zinovik, I., and D. Poulikakos, 2009, Modeling the temperature field in the reforming anode of a button-shaped solid oxide fuel cell: Electrochimica Acta, v. 54, p. 6234-6243.

Appendix A. Physical properties

A.1 The gas mixture density

The density of gases at low pressures can be calculated based on the ideal gas law:

$$\rho_g = \frac{P}{RT} M_g \tag{A.8}$$

$$M_g = \sum_i x_i M_i = \frac{1}{\sum_i \frac{w_i}{M_i}} \tag{A.9}$$

where ρ_g is the gas density (kg.m^{-3}); P is the total pressure (Pa); T is temperature (K); M_g is the gas mixture average molecular mass (kg.mol^{-1}); R is the ideal gas constant, 8.314 J.K^{-1}.mol^{-1}; x_i, w_i, and M_i are the mole fraction, the mass fraction, and the molecular mass (kg.mol^{-1}) of the component i respectively.

A.2 The gas mixture viscosity

The viscosity of a low pressure gas mixture is a function of its composition and temperature. A semi-empirical and widely tested Wilke equation (Poling et al., 2001), developed based on the kinetic theory of gases, is used:

$$\mu_g = \sum_i \frac{x_i \mu_i}{\sum_j x_j \phi_{ij}} \tag{A.10}$$

$$\phi_{ij} = \frac{\left(1 + \left(\frac{\mu_i}{\mu_j}\right)^{1/2} \left(\frac{M_j}{M_i}\right)^{1/4}\right)^2}{\left(8\left(1 + \frac{M_j}{M_i}\right)\right)^{1/2}} \tag{A.11}$$

$$\phi_{ji} = \frac{\mu_j}{\mu_i}\frac{M_i}{M_j}\phi_{ij} \tag{A.12}$$

For a binary system this would be:

$$\mu_m = \frac{y_1 \mu_1}{y_1 + y_2 \phi_{12}} + \frac{y_2 \mu_2}{y_2 + y_1 \phi_{21}} \tag{A.13}$$

$$\phi_{12} = \frac{\left(1 + \left(\frac{\mu_1}{\mu_2}\right)^{1/2} \left(\frac{M_2}{M_1}\right)^{1/4}\right)^2}{\left(8\left(1 + \frac{M_1}{M_2}\right)\right)^{1/2}} \tag{A.14}$$

$$\phi_{21} = \frac{\mu_2}{\mu_1}\frac{M_1}{M_2}\phi_{12} \tag{A.15}$$

The pure component viscosities can be calculated based on a polynomial correlation (Todd and Young, 2002):

$$\mu_i = 10^{-7} \times \sum_i A_i \left(\frac{T}{1000} \right)^i \tag{A.16}$$

where μ_i is the viscosity (Pa.s) of component *i*. The polynomial coefficients A_i for each component can be found in Table A.1.

Table A.1. The polynomial coefficients of the viscosity correlation.

	A_0	A_1	A_2	A_3	A_4	A_5	A_6	Error %	μ (1473K , µP)
H_2	15.553	299.78	-244.34	249.41	-167.51	62.966	-9.9892	10	270.13
H_2O	-6.7541	244.93	419.5	-522.38	348.12	-126.96	19.591	3	553.28
N_2	1.2719	771.45	-809.2	832.47	-553.93	206.15	-32.43	3	533.02
O_2	-1.6918	889.75	-892.79	905.98	-598.36	221.64	-34.754	5	632.36

A.3 The gas mixture thermal conductivity

The average thermal conductivity, $\bar{\kappa}$, of a gas mixture can be calculated based on the equations developed by Wassiljewa(Todd and Young, 2002):

$$\bar{\kappa} = \sum_{i=1}^{n} \frac{x_i \kappa_i}{\sum_{j=1}^{n} x_i B_{ij}} \tag{A.17}$$

$$B_{ij} = \frac{\left[1 + \left(\lambda_i^{tr} / \lambda_j^{tr}\right)^{1/2} \left(M_i / M_j\right)^{1/4}\right]^2}{\left[8(1 + M_i / M_j)\right]^{1/2}} \tag{A.18}$$

$$\lambda_i^{tr} = \frac{\mu_i M_j}{\mu_j M_i} \tag{A.19}$$

where μ_i and M_i are respectively the dynamic viscosity and the molar mass of the component i.

The thermal conductivity of a pure gas, κ ($W.m^{-1}.K^{-1}$), can be calculated as (Todd and Young, 2002):

$$\kappa = 0.01 \sum_{i=0}^{6} b_i \left(\frac{T}{1000}\right)^i \tag{A.20}$$

where T is in the absolute temperature (K). The polynomial coefficients for each component, b_i, are listed in Table A.2.

Table A.2. The polynomial coefficients of the pure component thermal conductivity correlation.

	b_0	b_1	b_2	b_3	b_4	b_5	b_6	Error %	κ (1473K)
H_2	1.504	62.892	-47.19	47.763	-31.939	11.972	-1.8954	5	57.705
H_2O	2.0103	-7.9139	35.922	-41.39	35.993	-18.974	4.1531	1	16.303
N_2	-0.3216	14.81	-25.473	38.837	-32.133	13.493	-2.2741	5	9.4124
O_2	-0.1857	11.118	-7.3734	6.713	-4.1797	1.491	-0.2278	10	9.9832

A.4 The gas mixture specific heat capacity

The specific mass heat capacity of an ideal gas mixture, $\overline{c}_p$, can be calculated as a function of its composition as:

$$\overline{c}_p(T) = \sum_{species} \omega_i \frac{c_{p,i}(T)}{M_i} \tag{A.21}$$

where M_i and ω_i are the molecular mass (kg.mol^{-1}) and mass fraction of component *i*. The specific molar heat capacity of a pure component, $c_{p,i}$, can be calculated as a polynomial function of temperature(Todd and Young, 2002):

$$c_p(T) = \sum_{i=0}^{6} b_i \left(\frac{T}{1000} \right)^i \tag{A.22}$$

where c_p is in (J.mol^{-1}.K^{-1}) and T is in (K); the polynomial coefficients in Eq.(A.15), b_i, are listed in Table A.3.

Table A.3. The polynomial coefficients of the pure component heat capacity correlation.(Todd and Young, 2002).

	b_0	b_1	b_2	b_3	b_4	b_5	b_6	Error %	C_p (1473K)
H_2	21.157	56.036	-150.55	199.29	-136.15	46.903	-6.4725	1	32.146
H_2O	37.373	-41.205	146.01	-217.08	181.54	-79.409	14.015	1	46.831
N_2	29.027	4.8987	-38.04	105.17	-113.56	55.554	-10.35	1	34.756
O_2	34.85	-57.975	203.68	-300.37	231.72	-91.821	14.776	1	36.469

A.5 The gas binary diffusion coefficients

The binary diffusion coefficients were calculated based on the Chapman and Enskog relations (Poling et al., 2001):

$$D_{ij} = \frac{0.00266T^{3/2}}{P\sigma_{ij}^2\Omega_{D,ij}}\sqrt{\left(\frac{1}{M_i}+\frac{1}{M_j}\right)} \tag{A.23}$$

$$\sigma_{ij} = \frac{1}{2}(\sigma_i + \sigma_j) \tag{A.24}$$

$$\Omega_{D,ij} = \frac{1.06036}{(\mathrm{T^*})^{0.15610}} + \frac{0.19300}{\exp(0.47635\mathrm{T^*})} + \frac{1.03587}{\exp(1.52996\mathrm{T^*})} + \frac{1.76474}{\exp(3.89411\mathrm{T^*})} \tag{A.25}$$

$$\mathrm{T^*} = \frac{\mathrm{k}_b\mathrm{T}}{\varepsilon_{ij}} \tag{A.26}$$

$$\varepsilon_{ij} = \sqrt{\varepsilon_i\varepsilon_j} \tag{A.27}$$

where D_{ij} is the binary diffusion coefficient (cm^2.s^{-1}); T and P are the gas temperature (K) and pressure (bars); M_i is in the molecular mass of the component i (g.mol^{-1}).

$\Omega_{D,ij}$ is the collision integral for diffusion. σ and ε are the characteristic Lennard-Jones energy and length respectively, and can be found in Table A.4.

Table A.4. The constants of the Chapman and Enskog relations for various components.

Component	σ_i (Å)	ε_i / k_b (K)
H_2	2.827	59.7
H_2O	2.641	809.1
O_2	3.467	106.7
N_2	3.798	71.4

A.6 The reaction specific enthalpy, entropy, and Gibbs free energy change

The specific enthalpy change (ΔH_{rxn}) and specific entropy change (ΔS_{rxn}) of the overall chemical reaction ($H_2 + \frac{1}{2}O_2 \longrightarrow H_2O$) at any given temperature, assuming ideal gas conditions, can be calculated as:

$$\Delta H_{rxn}(T) \equiv H_{H_2O}(T) - H_{H_2}(T) - \frac{1}{2}H_{O_2}(T) = \Delta H_{rxn}(T^\circ) + \int_{T^\circ}^{T} \Delta c_{p,rxn}(\tau)d\tau \qquad \text{(A.28)}$$

and

$$\Delta S_{rxn}(T, p^\circ) \equiv S_{H_2O}(T, p^\circ) - S_{H_2}(T, p^\circ) - \frac{1}{2}S_{O_2}(T, p^\circ) = \Delta S_{rxn}(T^\circ, p^\circ) + \int_{T^\circ}^{T} \frac{\Delta c_{p,rxn}(\tau)}{\tau} d\tau \qquad \text{(A.29)}$$

where $\Delta c_{p,rxn} = c_{p,H_2O} - c_{p,H_2} - \frac{1}{2}c_{p,O_2}$.

Based on Eqs. (A.21) and (A.22), and considering ΔH°_{rxn}= -241820 (J/mol) and ΔS°_{rxn}=-44.37 (J.mol^{-1}.K^{-1}) at standard conditions (25°C and 1bar)(Daubert et al., 1989), the following working expressions can be obtained:

$$\Delta H_{rxn}(T) = \sum_{i=0}^{7} b_i \left(\frac{T}{1000}\right)^i \qquad \text{(A.30)}$$

$$\Delta S_{rxn}(T, p_i = 1\text{bar}) = \sum_{i=0}^{6} b_i \left(\frac{T}{1000}\right)^i + b_7 \ln\left(\frac{T}{1000}\right) \qquad \text{(A.31)}$$

where ΔH_{rxn} in (J.mol^{-1}) and ΔS_{rxn} in (J.mol^{-1}.K^{-1}) are based on one mole of hydrogen consumed. T is the absolute temperature (K). The coefficients for Eqs. (A.23) and (A.24) are listed in Table A.5.

Table A.5. The polynomial coefficients of the ΔH_{rxn} and ΔS_{rxn} correlation polynomials.

	b_0	b_1	b_2	b_3	b_4	b_5	b_6	b_7
ΔH_{rxn}	-239706	-1.209	-34.1268	64.90667	-66.54625	40.366	-13.4003	1.871357
ΔS_{rxn}	-32.1487	-68.2535	97.3600	-88.72833	50.4575	-16.0803	2.183250	-1.209

The specific Gibbs free energy change of reaction (ΔG_{rxn}) at any temperature and standard pressure can be simply calculated as:

$$\Delta G_{rxn}(T, p_i = 1\,\mathrm{bar}) = \Delta H_{rxn}(T) - T\Delta S_{rxn}(T, p_i = 1\,\mathrm{bar}) \tag{A.32}$$

A.7 The thermal conductivity of solids

Table A.6. Thermal Conductivity of the solids.

Thermal conductivity of solids (W.K^{-1}.m^{-1})	
Cathode, effective (Li and Chyu, 2003)	6
Anode, effective (Li and Chyu, 2003)	11
YSZ(Li and Chyu, 2003)	2.7
Gold(Shackelford and Alexander, 2001)	$-0.0583T + 336.08$
Alumina(Shackelford and Alexander, 2001)	$3.6919e^{\frac{568.71}{T}}$

* T in (K)

A.8 The specific heat capacity of solids

Table A.7. Specific heat capacity of the solids.

Specific heat capacity (J.kg^{-1})	
LSM (Petruzzi et al., 2003)	573
Nickel**	$293 + 0.496T \quad T < 630$ K $489 + 0.061T \quad T > 630$ K
YSZ**	$686 - \frac{6.91 \times 10^{4}}{T}$
Gold**	$145 - 2.62 \times 10^{-2} T + 4.15 \times 10^{-5} T^{2}$
Alumina**	$1413.6 - \frac{189613}{T}$

* T in (K) **(Purdue University. Thermophysical Properties Research Center. and Touloukian, 1970)

A.9 The emissivity of solids

Table A.8. Emissivity of the solids.

Emissivity of solids	
All components	0.7(Calise et al., 2007); 0.9 (Fischer and Seume, 2009)
Alumina(Purdue University. Thermophysical Properties Research Center. and Touloukian, 1970)	0.5 at 1073K

A.10 The electric conductivity of solids

Table A.9. Electric conductivity of the solids.

Electric conductivity (S·m^{-1})	
Anode support, effective † experimental ††(Ferguson et al., 1996)	$\frac{3.77\times10^{4\dagger}}{T}e^{-\frac{1150^{\dagger\dagger}}{RT}}$
Anode functional, effective † experimental ††(Ferguson et al., 1996)	$\frac{2.17\times10^{7\dagger}}{T}e^{-\frac{1150^{\dagger\dagger}}{RT}}$
Cathode functional, effective (Experimental)	$\frac{6.10\times10^{6}}{T}e^{-\frac{3350}{RT}}$
Electrolyte (Ferguson et al., 1996)	$3.34\times10^{4}e^{-\frac{10300}{RT}}$
Gold, fitted(Chemical Rubber Company.)	$\frac{1}{9.22\times10^{-11}T-5.3710^{-9}}$
Nickel(Hellwege and Olsen, 1982)	$\log(\sigma)=8.2475-4.9\times10^{-3}T+4\times10^{-6}T^{2}-1\times10^{-5}T^{3}$

* T in (K)

A.11 Temperature dependent reaction kinetic parameters

Table A.10. Temperature dependent kinetic parameters.

Reaction kinetics; volumetric electron generation (A/m^3)	
Anode (Zhu et al., 2005) † experimental	$i_{gen,An} = i_{\circ,An}\left(e^{\frac{1.5F}{RT}\eta_{An}} - e^{-\frac{0.5F}{RT}\eta_{An}}\right)$ $\eta_{An} = V_{elec,An} - V_{ion,An} - \varepsilon_{An}$ $i_{\circ,An} = i_{*,An}\dfrac{(p_{H_2}/p^*_{H_2})^{1/4}(p_{H_2O})^{3/4}}{1+(p_{H_2}/p^*_{H_2})^{1/2}}$ $p^*_{H_2} = 1.22\times10^{8}T^{1/2}\,e^{-\frac{88120}{RT}}$ $i_{*,An} = 5.08\times10^{13\dagger}\,e^{-\frac{88000^{\dagger\dagger}}{RT}}$
Cathode (Zhu et al., 2005) † experimental ††experimental, 200000 by (Zhu et al., 2005)	$i_{gen,Ca} = i_{\circ,Ca}\left(e^{\frac{0.5F}{RT}\eta_{Ca}} - e^{-\frac{0.5F}{RT}\eta_{Ca}}\right)$ $\eta_{Ca} = V_{elec,Ca} - V_{ion,Ca} - \varepsilon_{Ca}$ $i_{\circ,Ca} = i_{*,Ca}\dfrac{(p_{O_2}/p^*_{O_2})^{1/4}}{1+(p_{O_2}/p^*_{O_2})^{1/2}}$ $i_{*,Ca} = 1.47\times10^{15\dagger}\,e^{-\frac{128000^{\dagger\dagger}}{RT}}$

* T in (K)